PB85-137362

Continued Research in Mesoscale Air Pollution Simulation Modeling. Volume 5 Refinements in Numerical Analysis, Transport, Chemistry, and Pollutant Removal

Systems Applications, Inc., San Rafael, CA

Prepared for

Environmental Sciences Research Lab.
Research Triangle Park, NC

Dec 84

U.S. Department of Commerce
National Technical Information Service
NTIS

EPA-600/3-84-095a
December 1984

PB85-137362

CONTINUED RESEARCH IN MESOSCALE AIR POLLUTION SIMULATION MODELING

VOLUME V -- Refinements in Numerical Analysis, Transport, Chemistry, and Pollutant Removal

by

J.P. Killus, J.P. Meyer, D.R. Durran, G.E. Anderson,
T.N. Jerskey, S.D. Reynolds, and J. Ames

Systems Applications, Incorporated
101 Lucas Valley Road
San Rafael, California 94903

Contract No. 68-02-2216

Project Officer

Kenneth L. Demerjian
Meteorology and Assessment Division
Environmental Sciences Research Laboratory
Research Triangle Park, North Carolina 27711

ENVIRONMENTAL SCIENCES RESEARCH LABORATORY
OFFICE OF RESEARCH AND DEVELOPMENT
U.S. ENVIRONMENTAL PROTECTION AGENCY
RESEARCH TRIANGLE PARK, NORTH CAROLINA 27711

REPRODUCED BY
NATIONAL TECHNICAL
INFORMATION SERVICE
U.S. DEPARTMENT OF COMMERCE
SPRINGFIELD, VA. 22161

TECHNICAL REPORT DATA

(Please read Instructions on the reverse before completing)

1. REPORT NO. EPA-600/3-84-095a	2.	3. RECIPIENT'S ACCESSION NO. PB85 137362
4. TITLE AND SUBTITLE CONTINUED RESEARCH IN MESOSCALE AIR POLLUTION SIMULATION MODELING Volume V -- Refinements in Numerical Analysis, Transport, Chemistry, and Pollutant Removal		5. REPORT DATE December 1984 6. PERFORMING ORGANIZATION CODE
7. AUTHOR(S) J.P. Killus, J.P. Meyer, D.R. Durran, G.E. Anderson, T.N. Jerskey, S.D. Reynolds, and J. Ames		8. PERFORMING ORGANIZATION REPORT NO.
9. PERFORMING ORGANIZATION NAME AND ADDRESS Systems Applications, Inc. 101 Lucas Valley Road San Rafael, CA 94903		10. PROGRAM ELEMENT NO. CDWA1A/02-2260 (FY-84) 11. CONTRACT/GRANT NO. Contract No. 68-02-2216
12. SPONSORING AGENCY NAME AND ADDRESS Environmental Sciences Research Laboratory-RTP, NC Office of Research and Development U.S. Environmental Protection Agency Research Triangle Park, NC 27711		13. TYPE OF REPORT AND PERIOD COVERED Final (10/79 - 7/82) 14. SPONSORING AGENCY CODE EPA/600/09

15. SUPPLEMENTARY NOTES

Vol. I (EPA-600/4-76-016a, PB 257526/AS); Vol. II (EPA-600/4-76-016b, PB 257527/AS)
Vol. III (EPA-600/4-76-016c, PB 257528/AS) and Vol. IV (EPA-600/4-76-016d, PB 257529/AS)

16. ABSTRACT

Two numerical integration methods identified as having features that provided significant improvements over the technique originally embedded in the Airshed Model have been evaluated. Of particular concern was the treatment of horizontal transport. In the evaluation of the schemes, the predictions resulting from the SHASTA method differed no more than about 20 percent from those generated using the original method. In addition, SHASTA possesses the better blend of computational speed and minimum error propagation. An objective analysis technique for obtaining a gridded, time-varying, fully three-dimensional wind field for the Airshed Model from available measurements has been developed. The technique accounts for urban heat island effects and should be directly applicable to relatively flat areas. A 42-step chemical kinetic mechanism for describing the chemical transformations of organics, NO_x, O_3, and SO_2 and the production of sulfate, nitrate, and organic aerosols is presented. A unique feature of this mechanism is the explicit consideration given to the carbon bonds making up each organic molecule. An algorithm that relates the effective deposition velocity to the stability of the atmosphere and the type of surface has been implemented in the Airshed Model. Surface removal processes may significantly affect the concentrations of O_3, NO_2, and SO_2.

17. KEY WORDS AND DOCUMENT ANALYSIS

a. DESCRIPTORS	b. IDENTIFIERS/OPEN ENDED TERMS	c. COSATI Field/Group
Dis		

18. DISTRIBUTION STATEMENT RELEASE TO PUBLIC	19. SECURITY CLASS *(This Report)* UNCLASSIFIED	21. NO. OF PAGES 238
	20. SECURITY CLASS *(This page)* UNCLASSIFIED	22. PRICE

EPA Form 2220-1 (9-73)

ATTENTION

AS NOTED IN THE NTIS ANNOUNCEMENT, PORTIONS OF THIS REPORT ARE NOT LEGIBLE. HOWEVER, IT IS THE BEST REPRODUCTION AVAILABLE FROM THE COPY SENT TO NTIS.

NOTICE

This document has been reviewed in accordance with U.S. Environmental Protection Agency policy and approved for publication. Mention of trade names or commercial products does not constitute endorsement or recommendation for use.

ABSTRACT

Two numerical integration methods identified as having features that provided significant improvements over the technique originally embedded in the Airshed Model have been evaluated. Of particular concern was the treatment of horizontal transport. In the evaluation of the schemes, the predictions resulting from the SHASTA method differed no more than about 20 percent from those generated using the original method. In addition, SHASTA possesses the better blend of computational speed and minimum error propagation. An objective analysis technique for obtaining a gridded, time-varying, fully three-dimensional wind field for the Airshed Model from available measurements has been developed. The technique accounts for urban heat island effects and should be directly applicable to relatively flat areas. A 42-step chemical kinetic mechanism for describing the chemical transformations of organics, NO_x, O_3, and SO_2 and the production of sulfate, nitrate, and organic aerosols is presented. A unique feature of this mechanism is the explicit consideration given to the carbon bonds making up each organic molecule. An algorithm that relates the effective deposition velocity to the stability of the atmosphere and the type of surface has been implemented in the Airshed Model. Surface removal processes may significantly affect the concentrations of O_3, NO_2, and SO_2.

CONTENTS

ABSTRACT iii

LIST OF AUTHORS viii

LIST OF ILLUSTRATIONS ix

LIST OF TABLES vii

LIST OF EXHIBITS xv

I INTRODUCTORY COMMENTS 1

  A. Overview of This Volume 2

  B. Status of the SAI Urban Airshed Model 4

II EVALUATION OF THE SUITABILITY OF THE SHASTA, PRICE ET AL., EGAN AND MAHONEY INTEGRATION METHODS IN PHOTOCHEMICAL SIMULATION PROGRAMS 8

  A. Description of the Methods 10

    1. The Price Method 11
    2. The SHASTA Method 11
    3. Non-Flux-Limited SHASTA 16
    4. Standard Explicit (Flux-Limited) SHASTA 17
    5. Phoenical SHASTA 19
    6. Non-Flux-Limited, Non-Mass-Conservative SHASTA 19
    7. The Method of Egan and Mahoney 20

  B. Test Results 20

    1. One-Dimensional Advection 21
    2. Two-Dimensional Advection in a Nonreactive System . . . 23
    3. Two-Dimensional Advection with Chemical Reactions . . . 32
    4. Airshed Simulations 42

  C. Numerical Analysis 55

  D. Recommendations and Conclusions 63

III SURFACE SINKS 66

  A. Overview 66

  B. The Deposition Velocity 66

  C. Other Models for Treating Surface Sinks 81

Preceding page blank

III SURFACE SINKS (Continued)

D. Measurements of Deposition Velocities. 82
    1. Surface Deposition of SO_2. 82
    2. Surface Deposition of O_3, NO, and NO_2. 88
    3. Surface Deposition of Hydrocarbons 91
    4. Surface Deposition of HNO_2, H_2O_2, and Aldehydes. 92
    5. Surface Deposition of CO 93
    6. Summary of Results 96

E. Estimation of the Importance of Various Surface Sinks. 97
    1. Sinks of CO. 97
    2. Sinks of SO_2 98
    3. Sinks of Photochemical Pollutants. 98
    4. Sinks of H_2O_2 and HNO_2 111

F. Incorporation of Surface Sinks Into the Airshed Model. 111
    1. Determination of the Diffusional Resistance Through the Bottom Cell. 112
    2. Determination of the Surface Uptake Characteristics of Each Grid Square. 112
    3. The Treatment of NO Release from NO_2 Uptake 115

G. The Effects of Averaging Surface Uptake Rates and Concentrations Over Grid Squares 117

H. Summary and Conclusions. 118

IV OBJECTIVE CONSTRUCTION OF THREE-DIMENSIONAL WINDFIELDS 120

A. Background 120

B. Wind Measurements. 127

C. Objective Analysis Techniques. 128
    1. Statistical Fits 130
    2. Influence Factor Fits. 130
    3. Spectral Fits. 135
    4. Boundary Value Fits. 135

D. Constraints on the St. Louis Windfield 137

E. The Windfield Algorithm Developed in This Study 140

F. Computer Solution. 144

G. Summary. 145

V IMPROVED TREATMENT OF ATMOSPHERIC CHEMISTRY 147

A. Introduction 147

B. Hydrocarbon NO_x/O_3 Chemistry 147

1. Overview 147
2. Rate Constants for Hydrocarbon Classes 153
3. Sources of Radicals in the Carbon-Bond Mechanism. 160

C. Considerations in the Treatment of Hydrocarbon Emissions 163

D. Aerosol Chemistry. 167

1. Organic Aerosol. 169
2. Nitrate Aerosol. 172
3. Sulfate Aerosol and SO_2 Chemistry 175

VI THE ESTIMATION OF PHOTOLYSIS RATE CONSTANTS 184

A. Introduction 184

B. The Multi-Layer Light-Scattering Model 188

C. Application of the Model 193

D. Prediction of Photolysis Rate Constants. 201

E. Variations in Photolysis Rate Constants With Height and Atmospheric Conditions. 203

F. Parameterization of the Effects of Light Scattering on Photolysis 207

REFERENCES 211

AUTHORS

CHAPTER I - Steven D. Reynolds

CHAPTER II - James P. Meyer and Dale R. Durran

CHAPTER III - James P. Killus and Terry N. Jerskey

CHAPTER IV - Gerald E. Anderson

CHAPTER V - Gary Z. Whitten, Terry N. Jerskey, and James P. Killus

CHAPTER VI - James P. Killus

FIGURES

1 Advection of a Trapezoidal Fluid Element 12

2 Advection of Two Fluid Elements 13

3 Influence of the Flux-Limitation Step 18

4 One-Dimensional Comparison of the Price, Egan-Mahoney, and SHASTA Algorithms 22

5 Average Absolute Error as a Function of ε 27

6 Maximum Absolute Error as a Function of ε 28

7 Execution Time as a Function of ε 29

8 The Product of the Average Absolute Error and the Execution Time as a Function of ε 30

9 Peak Concentration of CO as a Function of Time 34

10 Peak Concentration of NO as a Function of Time 35

11 Peak Concentration of NO_2 as a Function of Time 36

12 Peak Concentration of O_3 as a Function of Time 37

13 Steepest Gradient Concentration of CO as a Function of Time 38

14 Steepest Gradient Concentration of NO as a Function of Time 39

15 Steepest Gradient Concentration of NO_2 as a Function of Time 40

16 Steepest Gradient Concentration of O_3 as a Function of Time 41

17 CO Concentration at Pomona on 29 September 1969 as a Function of Time 43

18 Ozone Concentration at Pomona on 29 September 1969 as a Function of Time. 44

19 CO Concentration at Commerce on 29 September 1969 as a Function of Time. 45

20 Ozone Concentration at Commerce on 29 September 1969 as a Function of Time. 46

21 CO Concentration at Anaheim on 29 September 1969 as a Function of Time. 47

22 Ozone Concentration at Anaheim on 29 September 1969 as a Function of Time. 48

23 CO Concentration at Long Beach on 29 September 1969 as a Function of Time. 49

24 Ozone Concentration at Long Beach on 29 September 1969 as a Function of Time. 50

25 CO Concentration at Burbank on 29 September 1969 as a Function of Time. 51

26 Ozone Concentration at Burbank on 29 September 1969 as a Function of Time. 52

27 CO Concentration in Downtown Los Angeles on 29 September 1969 as a Function of Time. 53

28 Ozone Concentration in Downtown Los Angeles on 29 September 1969 as a Function of Time 54

29 Carbon Monoxide Concentration Profiles in the Los Angeles Basin at 1000 PST on 29 September 1969. 56

30 Ozone Concentration Profiles in the Los Angeles Basin at 1200 PST on 29 September 1969 57

31 1/L as a Function of Pasquill Classes and z_r. 77

32 Ozone Fluxes Measured and Calculated Assuming a Surface Resistance of 0.3 cm/sec. 78

33 Ozone Fluxes Measured and Calculated Assuming a Surface Resistance of 0.4 cm/sec. 79

34 Ozone Fluxes Measured and Calculated Assuming a Surface Resistance of 0.6 cm/sec. 80

35 Ozone Deposition Velocities Over Different Surfaces Assuming a Partial Ozone Density of 40 μg/m^3 89

36 Response of CO Removal to CO Concentration in Field and Forest Soils. A--Cheshire Fine Sandy Loam (Field Soil) and B--Charlton Fine Sandy Loam (Forest Soil) 95

37 Ground-level SO_2 Concentrations in pphm at Start of Simulations (12:00 a.m.) 99

38 Ground-Level SO_2 Concentrations in pphm After 1 Hour of Simulation Using $v_d = 0$ 100

39 Ground-Level SO_2 Concentrations in pphm After 1 Hour of Simulation Using v_d = 4 cm sec^{-1} Over Water and 1 cm sec^{-1} Over Land 101

40 Ground-Level SO_2 Concentrations in pphm After 1 Hour of Simulation Using v_d = 1.0 cm sec^{-1} Over Water and 0.25 cm sec^{-1} Over Land 102

41 Ground-Level SO_2 Concentrations in pphm After 2 Hours of Simulation Using v_d = 1 cm sec^{-1} Over Water and 0.25 cm sec^{-1} Over Land 103

42 Ground-Level SO_2 Concentrations After 2 Hours of Simulation Using v_d = 4 cm sec^{-1} Over Water and 1 cm sec^{-1} Over Land 104

43 Predicted Profiles of Pollutant Concentrations at 1300 PST 29 September 1969 for Various Sinks Incorporated in the Trajectory Model 107

44 Persistence of Oxidant Reduction Due to Sinks. 110

45 Values of $\sum_k \alpha_{jk}\beta_k$ for Grid Squares in the Los Angeles Basin 116

46 Three Wind Patterns Consistent With Two Measured Wind Vectors 123

47 Wind Rose Variations at a Connecticut Site 125

48 Wind Rose Variations at a Connecticut Site 126

49 Isotherms (°F x 10^{-2}) in the Los Angeles Basin 138

50 Pathways for Formation of Nitrate Aerosols 173

TABLES

1 Results of the Parametric Analysis. 25

2 Amplification Factors as a Function of Stability Parameter for the Price Method. 61

3 Surface Resistance of an Alfalfa Canopy 75

4 Key to Pasquill Stability Categories. 76

5 Average Values of Flux and Deposition Velocity for the Three Surfaces Under Three Stability Classes. 83

6 Deposition of SO_2 Onto Grass. 84

7 Measurements of the Deposition Velocity of SO_2 on Short Grasses at Cardington, England. 86

8 Estimated Surface Fluxes and Net Bulk Deposition Velocities. 87

9 Summary of Deposition Velocity Measurements (and Calculated Resistances) 88

10 Measured Values of Ozone Decomposition Rates for Several Common Surfaces 90

11 Deposition Velocities of Selected Pollutants. 91

12a Comparison of the CO Uptake Capacity of Soils Under Cultivation and Soils Under Natural Vegetation. 94

12b Soil Activity at Sites Alongside a 20-Mile Stretch of the Bayshore Freeway (U.S. 101) Preselected on the Basis of Representative Vegetation or Ground Cover 94

13 Range of Deposition Velocities for Various Pollutants. 96

14 Differences in Predicted Concentrations at 1300 Hrs Due to Inclusion of Deposition Velocities. 106

15 Chemical Reactions in the SAI Urban Airshed Model . . . 148

16 Reactivities Towards OH· of Several Alkanes . . . 154

17 Rate Constants Per Double Bond for the Reactions of Some Olefins With OH· at 300°K . . . 156

18 Comparison of the Reactivities of $O(^3P)$ Atoms, Ozone, and NO_3 Toward Olefins . . . 157

19 Hydrocarbon Emissions in the Los Angeles Basin by Source Category, Weight, and Weight Fraction . . . 164

20 Hydrocarbon Emissions in the Los Angeles Basin by Source Category and Bond Fraction . . . 165

21 Assumed Weights of Hydrocarbon Groups in the Carbon-Bond Mechanism . . . 166

22 Hydrocarbon Emissions in the Los Angeles Basin by Weight Fraction in Categories Used in the SAI Urban Airshed Model . . . 168

23 Major Homogeneous Reactions Involving Nitrates in Photochemical Smog . . . 174

24 Rate Constants for SO_2 Oxidation ($ppm^{-1}min^{-1}$) . . . 178

25 Rates of SO_2 Oxidation by Various Oxidants for the Battelle Simulation . . . 183

26 MRI Data From Flight Ending at 17:28 on 25 July 1973 at Riverside, California . . . 189

27 MRI Data From Flight Ending at 16:58 on 28 September 1973 at Riverside, California . . . 190

28 Parameters Used in Model Calculations . . . 194

29 Calculated and Measured Irradiances in $Watts/M^2$ at 360 nm . . . 196

30 Ratio of Sky to Direct Irradiance at 360 nm . . . 197

51 Predicted and Observed Volumetric UV Intensity as a Function of Solar Zenith Angle. 198

52 Attenuation of UV in the Polluted Layer as a Function of Height 200

53 Predicted and Measured NO_2 Photolysis Rate Constants as a Function of Time of day. 202

54 Variation of NO_2 Photolysis Rate Constant With Solar Zenith Angle--Unpolluted Case 204

55 Variation of NO_2 Photolysis Rate Constant with Solar Zenith Angle--Polluted Case 205

56 Variation of Formaldehyde Photolysis Rate Constant With Solar Zenith Angle--Polluted Case. 206

57 Estimated Ground-Level NO_2 Photolysis Rate Constant as a Function of Solar Zenith Angle for Unpolluted Case. 208

EXHIBITS

1 Observations on Iterative Method of Hovland, Dartt, and Gage (1976) 133

I INTRODUCTORY COMMENTS

by Steven D. Reynolds

This report comprises seven volumes. Volumes I through IV discuss evaluative and research studies carried out for the EPA from June 1973 to April 1975. Much of this work was exploratory; it was an attempt to lay the groundwork for various refinements to the Urban Airshed Model developed by Systems Applications, Inc. (SAI). Volumes V through VII cover work from June 1975 to March 1977, during which time these studies were completed and the refinements incorporated into the SAI model.

This volume (V) contains details of model refinement activities concerned with the improvement of numerical integration techniques, the incorporation of surface removal processes, the development of automated, objective procedures for preparing wind inputs, the treatment of atmospheric chemical reactions, and the estimation of rate constants for photolysis reactions. Volume VI discusses microscale modeling efforts aimed at the estimation of eddy diffusivities and the improved treatment of point and line sources. Progress in the development of aerosol modeling capabilities is presented in Volume VII.

In the next section, we highlight the findings of the model refinement activities, which are discussed in detail in Chapters II through VI of this volume. We conclude this chapter with a broad overview of the present status of the SAI Urban Airshed Model, indicating its general capabilities and characteristics.

A. OVERVIEW OF THIS VOLUME

Chapter II presents an evaluation of two numerical integration methods identified in Volume II as significant improvements over the technique originally embedded in the SAI model. Of particular concern was the treatment of horizontal transport. The methods examined were the SHASTA and Egan-Mahoney methods. In several numerical experiments involving the transport of an inert pollutant in both one and two dimensions we found that the SHASTA method seems to possess the best blend of computational speed coupled with minimum error propagation. Further tests with a problem involving both transport and chemical transformations confirmed the enhanced reliability of this method over that used previously. In a final set of experiments, the SHASTA method was employed in an actual airshed simulation of the Los Angeles Basin. The resulting predictions differed no more than about 20 percent from those generated using the original method. Our conclusion is that implementing the SHASTA method in the SAI model will enhance the reliability of the model's predictions and will allow longer-term integrations to be performed before numerical error propagation becomes unacceptable.

Uptake by the ocean, ground, and biota is generally acknowledged to be of considerable importance for some air pollutants, especially when they are transported over long distances. Chapter III deals with the possible importance of including these processes in an urban-scale air quality model. Our review of the literature showed that little information exists regarding the rates of uptake of photochemical pollutants by characteristic urban materials. We parameterized uptake rates through use of the deposition velocity concept, in which the rate of uptake is assumed to be proportional to the pollutant concentration just above the surface. The proportionality constant (i.e., the deposition velocity) is influenced by the stability of the atmosphere and the type of surface. In Chapter III we present an algorithm that relates the overall effective deposition velocity to these two influences. Sensitivity studies using our best estimates of the deposition velocities indicate that surface removal processes may significantly affect the concentrations of O_3, NO_2, and SO_2 in the Los Angeles Basin. The specification of uptake parameters for the Los Angeles Basin is discussed in detail to aid model users in estimating these inputs for other urban areas.

Theoretical assessments and model sensitivity studies reported in Volumes I and II indicated the importance of treating the full three-dimensional nature of the windfield. As a result, we modified the SAI model to accept time-varying, fully three-dimensional wind inputs (namely, a one-hour-average wind speed and direction for each grid cell). In Chapter IV we present an objective analysis technique to prepare such a windfield using available measurements both at the surface and aloft. This technique also attempts to account for urban heat island effects. It should be directly applicable to relatively flat areas, such as St. Louis. We note, however, that it would be possible to extend the technique for application to areas with greater relief.

A chemical kinetic mechanism is one of the most important components of any model capable of predicting the concentrations of secondary air contaminants. Chapter V presents the features of a 42-step mechanism suitable for describing the chemical transformations of organics, nitrogen oxides, ozone, and sulfur dioxide, and the production of sulfate, nitrate, and organic aerosols. The organic/NO_x/O_3 mechanism consists of 32 steps. A unique feature of this mechanism is the explicit consideration given to the carbon bonds making up each organic molecule. In simulations of smog chamber experiments, this mechanism overcomes some deficiencies exhibited by reaction schemes previously employed in the Urban Airshed Model. For the addition of SO_2 and sulfate aerosol prediction capabilities to the model, we assembled a seven-step mechanism describing the conversion of SO_2 to sulfate aerosol. And finally, three reaction steps were postulated to describe the formation of organic and nitrate aerosols.

Chapter VI concludes this volume with a discussion of the treatment of rate constants for photolysis reactions. The chemical mechanism described in Chapter V includes photolysis reactions of NO_2, HNO_2, H_2O_2, and aldehydes. Through the use of our Multi-Layer Light-Scattering Model, we examined the influence of aerosols on the attenuation of sunlight within a column of polluted air. The results of this work led to the formulation of a linear relationship with height above the terrain for the photolysis rate constants. In effect, the total integrated aerosol mass in a column of grid cells is used in conjunction with nominal estimates of the clean air values of the photolysis rate constants to calculate values of the rate constants for each grid cell in that column.

B. STATUS OF THE SAI URBAN AIRSHED MODEL

Since the original version of the SAI model was published in 1973, a number of modifications have been implemented in the computer codes to account more fully for the physical and chemical phenomena believed to be important in influencing urban air quality. In this section we synopsize the current features of the model. As appropriate, we cite pertinent sections of the seven-volume report that may be referred to for a more comprehensive discussion.

Basically, the SAI model accepts emissions, meteorological, chemical, and air quality data as inputs and produces predictions of pollutant concentrations during specified time intervals within the cells of a three-dimensional grid encompassing the region of interest. Thirteen chemical species are considered: ozone (O_3), nitrogen dioxide (NO_2), nitric oxide (NO), sulfur dioxide (SO_2), carbon monoxide (CO), peroxyacetylnitrate (PAN), total aerosol, olefins (other than ethylene), paraffins, aromatics and ethylene, aldehydes, nitrous acid (HNO_2), and hydrogen peroxide (H_2O_2). The aerosol component consists of primary particulate and secondary nitrate, sulfate, and organic aerosols (see Volume V, Chapter V, and Volume VII).

The model simulates pollutant transport through the action of advection and turbulent dispersion. As mentioned above, wind inputs are time-varying and fully three-dimensional. Only horizontal wind components are input; appropriate vertical velocities are calculated using a mass balance constraint. Thus, the influence of convergence and divergence zones in the windfield can be handled properly. Eddy diffusivity coefficients are estimated from an algorithm that accounts for the effects of atmospheric stability, surface roughness, wind speed, and inversion height (see Volume VI).

Chemical transformations are represented by the 41-step chemical mechanism mentioned above. Organics are segmented into four classes that are based primarily on carbon bond characteristics and to a lesser extent on reactivity and reaction products. The mechanism can account for the effects of hourly temperature variations on reaction rate constants through the use of the Arrhenius relationship. Photolysis rate constants are allowed to vary in time as well as in space. Aerosol predictions in a column of grid cells are used to estimate the effect of light scattering on the photolysis rate constants in each grid cell of that column (see Volume V, Chapters V and VI).

Removal of pollutants by surface sinks is treated by means of the deposition velocity concept. The effects of both atmospheric turbulence and surface uptake characteristics are considered. Model inputs include a spatial array of surface types corresponding to the land use in each grid cell (see Volume V, Chapter III).

Several microscale features are incorporated in the model. As noted in Volume III, subgrid-scale concentration variations arising from the spatial characteristics of point and line sources can affect the spatially averaged predictions obtained from a grid model. However, these effects are only important when a contaminant emitted from a point or line source reacts rapidly with another pollutant. One such example is the reaction of NO with O_3 to form NO_2 and O_2.

To account for the subgrid-scale influences of line sources, the model treats the lowest layer of grid cells in a special manner. First, this layer is considered to have a depth of only about 20 meters. Second, NO emissions from motor vehicles are allowed to react immediately with only the O_3 in close proximity to the roadway. This treatment of the lowest layer also considers ground-level emissions from areal sources and surface removal processes. In addition to predicting "ground-level" concentrations, the algorithm developed for the lowest layer also predicts the net flux of each pollutant into the second layer of grid cells (see Volume VI).

Emissions from large point sources are distributed in grid cells aloft through the use of a plume rise algorithm. Consideration is given to whether a plume penetrates an elevated inversion layer, and, if so, whether it ultimately breaks through the layer (see Volume VI).

The governing equations of the model are solved through the use of finite difference relationships. The three-dimensional equation is split into the following four fractional steps:

> Advection and diffusion in the x-direction
> Advection and diffusion in the y-direction
> Advection and diffusion in the z-direction
> Chemistry.

Emissions, removal, and microscale considerations are included in the third step. The SHASTA algorithm is employed to calculate pollutant transport, and the trapezoidal rule is used in the chemistry step (see Volume V, Chapter II).

Efforts are currently underway to adapt the SAI model for application to the St. Louis area with the Regional Air Pollution Study (RAPS) data base. Model development activities to date have not had the benefit of feedback from definitive model applications to urban areas. The St. Louis study may provide a better understanding of the reliability and accuracy of the model. Even more important, it should help to elucidate any shortcomings in the model and to identify those areas in which future model development activities should be focused.

II EVALUATION OF THE SUITABILITY OF THE SHASTA, PRICE ET AL., AND EGAN AND MAHONEY INTEGRATION METHODS IN PHOTOCHEMICAL SIMULATION PROGRAMS

by James P. Meyer and Dale R. Durran

The SAI airshed model described by Reynolds et al. (1973) employs a finite difference numerical integration method to solve the species continuity equation:

$$\frac{\partial}{\partial t}(\Delta H c_i) + \frac{\partial}{\partial x}(u \Delta H c_i) + \frac{\partial}{\partial y}(v \Delta H c_i) + \frac{\partial}{\partial \rho}(W c_i)$$

$$= \frac{\partial}{\partial x}\left(K_H \Delta H \frac{\partial c_i}{\partial x}\right) + \frac{\partial}{\partial y}\left(K_H \Delta H \frac{\partial c_i}{\partial y}\right) + \frac{\partial}{\partial \rho}\left(\frac{K_V}{\Delta H} \frac{\partial c_i}{\partial \rho}\right) + R_i \Delta H + S_i \Delta H \quad , \qquad (1)$$

where

$$W = w - u\left(\frac{\partial h}{\partial x} + \rho \frac{\partial \Delta H}{\partial x}\right) - v\left(\frac{\partial h}{\partial y} + \rho \frac{\partial \Delta H}{\partial y}\right) - \rho \frac{\partial \Delta H}{\partial t}$$

$$\rho = \frac{z - h(x,y)}{\Delta H}$$

c_i = concentration of species i

ΔH = vertical extent of the modeling region

u,v,w = wind components in the x, y, and z directions, respectively

K_H, K_V = horizontal and vertical diffusivities

R_i = reaction rate term for species i

S_i = volumetric source term for species i

$h(x,y)$ = terrain elevation.

Reynolds et al. (1973, 1976) estimated the errors associated with integrating the horizontal transport terms of this equation using a difference method adapted from the work reported by Price et al. (1966) (hereafter referred to as the Price method) and identified other integration techniques that might provide more accuracy at a comparable cost. The SHASTA method (Boris and Book, 1973, 1975; Boris et al., 1975) and the method developed by Egan and Mahoney (1971, 1972) showed promise in providing the increase in accuracy necessary to warrant their substitution into the SAI airshed model. This chapter thus explores the strengths and weaknesses of these methods and describes ways of enhancing their use in the airshed model.

Throughout this study the method of fractional steps (Yanenko, 1971) was used to solve the multidimensional transport problem. In essence, this technique subdivides the original four-dimensional problem in (x,y,ρ,t,) into a series of three two-dimensional problems in (x,t), (y,t), and (ρ,t):

$$\frac{\partial}{\partial t}\left(\Delta H c_i\right) + \frac{\partial}{\partial x}\left(u \Delta H c_i\right) = \frac{\partial}{\partial x}\left(K_H \Delta H \frac{\partial c_i}{\partial x}\right) \quad , \tag{2}$$

$$\frac{\partial}{\partial t}\left(\Delta H c_i\right) + \frac{\partial}{\partial y}\left(v \Delta H c_i\right) = \frac{\partial}{\partial y}\left(K_H \Delta H \frac{\partial c_i}{\partial y}\right) \quad , \tag{3}$$

$$\frac{\partial}{\partial t}\left(\Delta H c_i\right) + \frac{\partial}{\partial \rho}\left(W c_i\right) = \frac{\partial}{\partial \rho}\left(\frac{K_V}{\Delta H} \frac{\partial c_i}{\partial \rho}\right) + R_i \Delta H + S_i \Delta H \quad , \tag{4}$$

which are solved sequentially. Not only does this method make the problem tractable, but also it generates forms of the equation compatible with the SHASTA, Price, and Egan-Mahoney methods.

Of fundamental interest in this study is the reduction in error associated with the integration of the horizontal transport steps (x,t) and (y,t). Since the effects of horizontal diffusion are, in general, much weaker than those of horizontal advection, each numerical method should be capable of developing accurate solutions to problems in which horizontal diffusion does not occur:

$$\frac{\partial}{\partial x}\left(K_H \Delta H \frac{\partial c_i}{\partial x}\right) = 0 \qquad (5)$$

and

$$\frac{\partial}{\partial y}\left(K_H \Delta H \frac{\partial c_i}{\partial y}\right) = 0 \quad . \qquad (6)$$

This stipulation has the effect of transforming the fractionalized step expressions in the x and y directions into the forms

$$\frac{\partial \Delta H c_i}{\partial t} + \frac{\partial u \Delta H c_i}{\partial x} = 0 \quad , \qquad (7)$$

$$\frac{\partial \Delta H c_i}{\partial t} + \frac{\partial v \Delta H c_i}{\partial y} = 0 \quad , \qquad (8)$$

which, if the quantity $\Delta H c_i$ is considered as a single variable, have the identical form needed for solution by both the SHASTA and Egan-Mahoney algorithms. In actual computational cycles, the horizontal diffusion process is treated as a secondary effect once the advection step has been simulated.

This chapter presents the various numerical integration methods studied, the results of our tests of them, our numerical analyses of these results, and our recommendations and conclusions regarding these methods.

A. DESCRIPTION OF THE METHODS

The following subsections synopsize the methods considered in this study. For the SHASTA algorithm, the original method and its variations are described in considerable detail because one of these variants is the most promising alternative. In contrast, the Egan-Mahoney method is treated only briefly; the interested reader is referred to the original articles for a more complete presentation.

1. The Price Method

The Price method, currently used in the SAI airshed model, is based on a finite difference approach involving forward time and backward distance differencing. For a uniform grid, the computational module for Eq. (7) is given by[*]

$$c_j^{n+1} = c_j^n + \frac{u^n_{j-\frac{1}{2}}\Delta t}{2\Delta x}\left(3c^n_{j-1} - c^n_{j-2}\right) - \frac{u^n_{j+\frac{1}{2}}\Delta t}{2\Delta x}\left(3c^n_j - c^n_{j-1}\right) \tag{9}$$

for the case in which the u velocity component is positive. The method is essentially first order in time (Δt) and second order in space $[(\Delta x)^2]$; special considerations are needed to handle boundary conditions.

2. The SHASTA Method

The SHASTA method was developed by Boris and Book to provide solutions to the advection equation

$$\frac{\partial c}{\partial t} + \frac{\partial uc}{\partial x} = 0 \tag{10}$$

that would minimize the errors associated with numerical diffusion in other solution methods. In doing so, they found that a two-stage (transport followed by antidiffusion) algorithm could provide results superior to those obtained using one-stage algorithms.

The transport stage is similar to a standard finite difference technique, except that an unusually large amount of numerical diffusion is introduced in the SHASTA formulation. In general, numerical diffusion tends to enhance the stability properties of an algorithm at the expense of degrading its accuracy. To counteract this effect, Boris and Book designed the antidiffusion stage to eliminate most of the error caused by numerical diffusion while retaining most of the stability benefits produced by it.

---

[*] In this section, subscripts and superscripts will be used to denote space and time discretizations, respectively.

a. The Transport Stage

The transport stage of SHASTA can be developed from purely geometrical considerations. We derive below the algorithm in its most general form--one that allows variable grid spacing and a nonuniform velocity field.

Let the grid points j and j+1 and the concentrations at time $t = n\Delta t$ define a trapezoidal fluid element that is advected so that after a time Δt it is still trapezoidal in shape and its total mass (or the area of the trapezoid) is conserved (see Figure 1). One nonunique way of expressing c_a and c_b in terms of c_j^n and c_{j+1}^n in a way in which the mass of the fluid element is conserved is

$$c_a = \frac{c_j^n \Delta x_j}{\Delta x_j + \Delta t\left(u_{j+1}^{\frac{1}{2}} - u_j^{\frac{1}{2}}\right)} \quad , \quad c_b = \frac{c_{j+1}^n \Delta x_j}{\Delta x_j + \Delta t\left(u_{j+1}^{\frac{1}{2}} - u_j^{\frac{1}{2}}\right)} \quad , \tag{11}$$

where $u_j^{\frac{1}{2}}$ denotes the velocity at grid location j at time $t = [(n+\frac{1}{2})\Delta t]$.

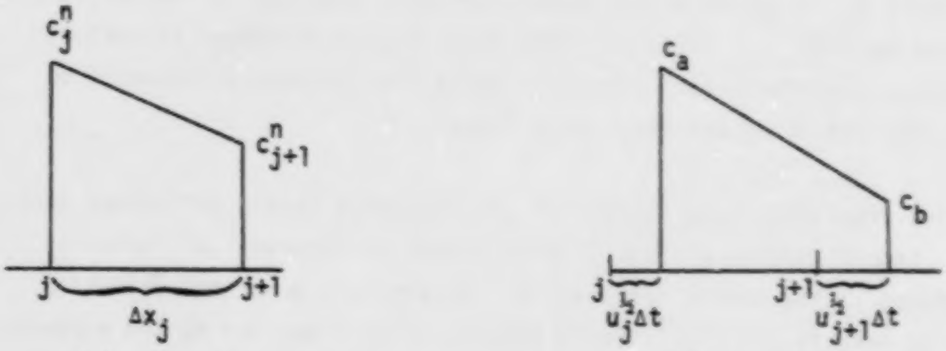

(a) $t = n\Delta t$ (b) $t = (n+1)\Delta t$

FIGURE 1. ADVECTION OF A TRAPEZOIDAL FLUID ELEMENT

To determine the concentration c_j^{n+1}, we consider the two fluid elements advected as shown in Figure 2. The previous discussion of the motion of a single fluid element suggests the following expressions:

$$c_a^1 = \frac{c_{j-1}^n \, \Delta x_{j-1}}{\Delta x_{j-1} + \Delta t\left(u_j^{\frac{1}{2}} - u_{j-1}^{\frac{1}{2}}\right)} \quad , \qquad c_b^1 = \frac{c_j^n \, \Delta x_{j-1}}{\Delta x_{j-1} + \Delta t\left(u_j^{\frac{1}{2}} - u_{j-1}^{\frac{1}{2}}\right)} \quad ,$$

$$c_a^2 = \frac{c_j^n \, \Delta x_j}{\Delta x_j + \Delta t\left(u_{j+1}^{\frac{1}{2}} - u_j^{\frac{1}{2}}\right)} \quad , \qquad c_b^2 = \frac{c_{j+1}^n \, \Delta x_j}{\Delta x_j + \Delta t\left(u_{j+1}^{\frac{1}{2}} - u_j^{\frac{1}{2}}\right)} \quad . \tag{12}$$

The final concentration c_j^{n+1} is estimated as the average concentration over the shaded regions and is expressed in terms of the areas of the two shaded trapezoids as

$$\frac{1}{2}\left(\Delta x_{j-1} + \Delta x_j\right) c_j^{n+1} = \left(\frac{1}{2}\,\Delta x_j - \Delta t u_j^{\frac{1}{2}}\right)\left(\frac{c_a^2 + c^{**}}{2}\right) + \left(\frac{1}{2}\,\Delta x_{j-1} + \Delta t u_j^{\frac{1}{2}}\right)\left(\frac{c_b^1 + c^{*}}{2}\right) \quad . \tag{13}$$

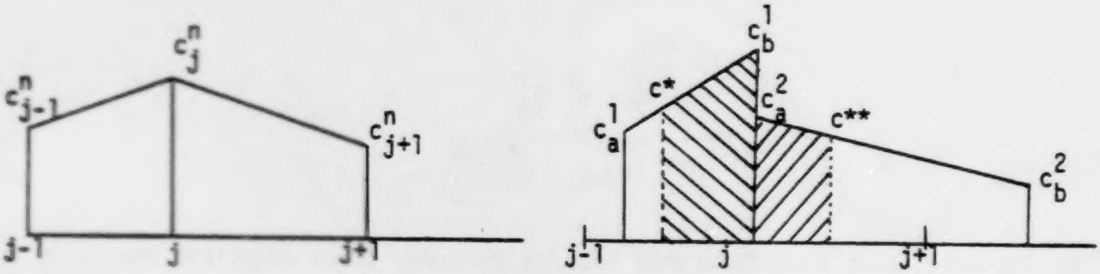

(a) $t = n\Delta t$ (b) $t = (n+1)\Delta t$

FIGURE 2. ADVECTION OF TWO FLUID ELEMENTS

To compute c* and c**, we use linear interpolation to obtain the expressions

$$c^{*} = c_b^1 + \frac{\left(c_a^1 - c_b^1\right)\left(\frac{1}{2}\,\Delta x_j - \Delta t u_j^{\frac{1}{2}}\right)}{\left[\Delta x_{j-1} + \Delta t\left(u_j^{\frac{1}{2}} - u_{j-1}^{\frac{1}{2}}\right)\right]} \quad , \qquad (14)$$

$$c^{**} = c_a^2 + \frac{\left(c_b^2 - c_a^2\right)\left(\frac{1}{2}\,\Delta x_j - \Delta t u_j^{\frac{1}{2}}\right)}{\left[\Delta x_j + \Delta t\left(u_{j+1}^{\frac{1}{2}} - u_j^{\frac{1}{2}}\right)\right]} \quad , \qquad (15)$$

which when substituted into the previous expression give the following result:

$$\begin{aligned} c_j^{n+1} = \frac{1}{\Delta x_{j-1} + \Delta x_j}\Big[&\left(c_{j+1}^n - c_j^n\right)\Delta x_j Q_+^2 + \left(c_{j-1}^n - c_j^n\right)\Delta x_{j-1} Q_-^2 \\ &+ 2c_j^n\left(\Delta x_j Q_+ + \Delta x_{j-1} Q_-\right)\Big] \quad , \qquad (16) \end{aligned}$$

where

$$Q_- = \frac{\frac{1}{2} + u_j^{\frac{1}{2}}\,\frac{\Delta t}{\Delta x_{j-1}}}{1 + \left(u_j^{\frac{1}{2}} - u_{j-1}^{\frac{1}{2}}\right)\frac{\Delta t}{\Delta x_{j-1}}} \quad ,$$

$$Q_+ = \frac{\frac{1}{2} - u_j^{\frac{1}{2}}\,\frac{\Delta t}{\Delta x_j}}{1 + \left(u_{j+1}^{\frac{1}{2}} - u_j^{\frac{1}{2}}\right)\frac{\Delta t}{\Delta x_j}} \quad .$$

In the event that a uniform grid spacing is used, these equations reduce to

$$c_j^{n+1} = \frac{1}{2}\,Q_-^2\left(c_{j-1}^n - c_j^n\right) + \frac{1}{2}\,Q_+^2\left(c_{j+1} - c_j^n\right) + \left(Q_+ + Q_-\right)c_j^n \quad , (17)$$

where

$$Q_{\pm} = \frac{\frac{1}{2} \mp u_j^{\frac{1}{2}} \frac{\Delta t}{\Delta x}}{1 \pm \left(u_{j\pm 1}^{\frac{1}{2}} - u_j^{\frac{1}{2}}\right)\frac{\Delta t}{\Delta x}} \quad .$$

In the special case of a uniform velocity, this result further simplifies to

$$c_j^{n+1} = c_j^n + \frac{\varepsilon}{2}\left(c_{j-1}^n - c_{j+1}^n\right) + \left(\frac{1}{8} + \frac{\varepsilon^2}{2}\right)\left(c_{j+1}^n - 2c_j^n + c_{j-1}^n\right) \quad , \tag{18}$$

where

$$\varepsilon = \frac{u\Delta t}{\Delta x} \qquad \left(0 < \varepsilon < \frac{1}{2}\right) \quad .$$

In comparison, the second-order Lax-Wendroff algorithm is given by

$$c_j^{n+1} = c_j^n + \frac{\varepsilon}{2}\left(c_{j-1}^n - c_{j+1}^n\right) + \frac{\varepsilon^2}{2}\left(c_{j+1}^n - 2c_j^n + c_{j-1}^n\right) \quad . \tag{19}$$

For this unique case, the transport stage of SHASTA is identical to this standard method except that it incorporates a much larger diffusion term.

b. The Antidiffusion Stage

As previously mentioned, the antidiffusion stage of SHASTA is designed to minimize the errors that would otherwise develop as a result of strong numerical diffusion. The term

$$\left(\frac{1}{8} + \frac{\varepsilon^2}{2}\right)\left(c_{j+1}^n - 2c_j^n + c_{j-1}^n\right)$$

in the previous expressions is referred to as numerical diffusion because its inclusion gives a finite difference approximation to the partial differential equation

$$\frac{\partial c}{\partial t} + \frac{\partial uc}{\partial x} = K\frac{\partial^2 c}{\partial x^2} \quad , \tag{20}$$

where

$$K = \frac{\Delta x^2}{8\Delta t} + \frac{u^2\Delta t}{2} \quad .$$

Several options are available for removing or minimizing the diffusional errors associated with the transport algorithm. They are discussed below.

3. Non-Flux-Limited SHASTA

In the simplest version of SHASTA, referred to here as non-flux-limited SHASTA, an attempt is made to cancel the effects of numerical diffusion by subtracting from the intermediate solution given by the transport stage a simple estimate of the diffusional error. This is performed as follows

Transport stage:

$$c_j^* = c_j^n + \frac{\varepsilon}{2}\left(c_{j-1}^n - c_{j+1}^n\right) + \left(\frac{1}{8} + \frac{\varepsilon^2}{2}\right)\left(c_{j+1}^n - 2c_j^n + c_{j-1}^n\right) \quad , \tag{21}$$

Antidiffusion stage:

$$c_j^{n+1} = c_j^* - \eta\left(c_{j+1}^* - 2c_j^* + c_{j-1}^*\right) \quad , \tag{22}$$

η = Antidiffusion Coefficient.

An obvious choice for η would be $[(1/8) + (\epsilon^2/2)]$, but, as shown later, for constant velocity problems $\eta = 1/8$ is a better choice. These two equations can be combined to express the non-flux-limited SHASTA prediction as follows:

$$c_j^{n+1} = \left(\frac{-\epsilon^2}{16} + \frac{\epsilon}{16} - \frac{1}{64}\right)c_{j+2}^n + \left(\frac{3}{4}\epsilon^2 - \frac{5}{8}\epsilon + \frac{1}{16}\right)c_{j+1}^n$$

$$+ \left(\frac{29}{32} - \frac{11}{8}\epsilon^2\right)c_j^n + \left(\frac{3}{4}\epsilon^2 + \frac{5}{8}\epsilon + \frac{1}{16}\right)c_{j-1}^n$$

$$+ \left(\frac{-\epsilon^2}{16} - \frac{\epsilon}{16} - \frac{1}{64}\right)c_{j-2}^n \qquad (23)$$

for the case in which η is equal to 1/8.

4. Standard Explicit (Flux-Limited) SHASTA

In both the original version of SHASTA and its later refinements, Boris and Book incorporated an additional device known as flux limiting. The antidiffusion stage could be written in the form

$$c_j^{n+1} = c_j^* + \mathrm{FLUX}_{j-\frac{1}{2}} - \mathrm{FLUX}_{j+\frac{1}{2}} \quad , \qquad (24)$$

where

$$\mathrm{FLUX}_{j\pm\frac{1}{2}} = \pm\eta\left(c_{j\pm1}^* - c_j^*\right) \quad .$$

According to Boris and Book, the flux-limiting procedure modifies these fluxes so that "the antidiffusion stage should generate no new maxima or minima in the solution, nor should it accentuate already existing extrema" (Boris and Book, 1973). This prescription is quantified by defining corrected fluxes $\mathrm{FLUX}_{j\pm\frac{1}{2}}^c$ as

$$\mathrm{FLUX}^{c}_{j+\frac{1}{2}} = \mathrm{sgn}\,\Delta_{j+\frac{1}{2}} \max\left[0, \min\left(\Delta_{j-\frac{1}{2}}\,\mathrm{sgn}\,\Delta_{j+\frac{1}{2}},\right.\right. \tag{25}$$

$$\left.\left.\eta\left|\Delta_{j+\frac{1}{2}}\right|, \Delta_{j+\frac{3}{2}}\,\mathrm{sgn}\,\Delta_{j+\frac{1}{2}}\right)\right] \quad ,$$

where $\Delta_{j+\frac{1}{2}} = \overset{*}{c}_{j+1} - \overset{*}{c}_{j}$,

$$\eta = \text{Antidiffusion Coefficient} = 1/8 \quad .$$

Given a solution at the end of the transport stage that appears as shown in Figure 3, the antidiffusion stage would, if not flux-limited, tend to alter c_j and c_{j+1} in the directions indicated by the arrows. This could result in an undershoot-overshoot situation and possible dispersive ripples; flux limiting prevents such an occurrence. If the initial concentrations are all nonnegative, flux limiting will prevent the occurrence of negative concentrations (provided that $u\Delta t/\Delta x < 1/2$ in the transport stage). Although flux limiting produces an aesthetically pleasing solution, it does not necessarily improve the accuracy of the solution: Neither the average nor the maximum absolute errors need decrease.

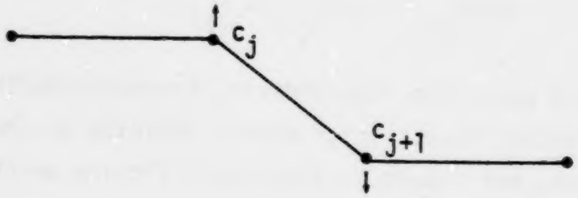

FIGURE 3. INFLUENCE OF THE FLUX-LIMITATION STEP

5. Phoenical SHASTA

If the velocity field is zero, then from the analytic solution to Eq. (2) we should find that

$$c_j^{n+1} = c_j^n \quad . \tag{26}$$

Neither of the previous two versions of SHASTA produce such a result. Phoenical SHASTA is designed to eliminate this problem. It is formulated as follows:

$$c_j^{*} = c_j^n + \frac{\varepsilon}{2}\left(c_{j-1}^n - c_{j+1}^n\right) + \frac{\varepsilon^2}{2}\left(c_{j+1}^n - 2c_j^n + c_{j-1}^n\right) \quad ,$$

$$c_j^{**} = c_j^n + \frac{\varepsilon}{2}\left(c_{j-1}^n - c_{j+1}^n\right) + \left(\frac{1}{8} + \frac{\varepsilon^2}{2}\right)\left(c_{j+1}^n - 2c_j^n + c_{j-1}^n\right) \quad ,$$

$$\mathrm{FLUX}_{j+\frac{1}{2}}^{c} = \mathrm{sgn}\,\Delta_{j+\frac{1}{2}} \max\Big[0, \min\Big(\Delta_{j-\frac{1}{2}}\,\mathrm{sgn}\,\Delta_{j+\frac{1}{2}},\ \eta\left|\Delta_{j+\frac{1}{2}}\right|,$$

$$\Delta_{j+3/2}\,\mathrm{sgn}\,\Delta_{j+\frac{1}{2}}\Big)\Big] \quad ,$$

$$\Delta_{j+\frac{1}{2}} = c_{j+1}^{*} - c_j^{*} \quad , \qquad \eta = \text{Antidiffusion Coefficient} = 1/8 \quad ,$$

$$c_j^{n+1} = c_j^{**} + \mathrm{FLUX}_{j-\frac{1}{2}}^{c} - \mathrm{FLUX}_{j+\frac{1}{2}}^{c} \quad . \tag{27}$$

For the case in which the velocity field is zero, the original solution is recovered.

6. Non-Flux-Limited, Non-Mass-Conservative SHASTA

The non-flux-limited, non-mass-conservative version of SHASTA is formulated as follows:

$$c_j^{*} = c_j^n + \frac{\varepsilon}{2}\left(c_{j-1}^n - c_{j+1}^n\right) + \left(\frac{1}{8} + \frac{\varepsilon^2}{2}\right)\left(c_{j+1}^n - 2c_j^n + c_{j-1}^n\right) \quad ,$$

$$c_j^{**} = c_j^{*} - \frac{1}{8}\left(c_{j+1}^{*} - 2c_j^{*} + c_{j-1}^{*}\right) \quad ,$$

$$c_j^{n+1} = \max\left(c^B, c_j^{**}\right) \quad , \tag{28}$$

where c^B = background concentration. This technique prevents negative concentrations, but in light of the refinements just discussed it probably appears a bit simplistic.

7. The Method of Egan and Mahoney

A novel method of solving advection problems in the urban environment was developed by Egan and Mahoney at Harvard in 1970. In this method, the movement of various air parcels is tracked as they are advected across a three-dimensional grid system and then their first, second, and third moments are followed with respect to the various coordinate axes. In general, the method can be adapted to problems involving any number of dimensions, but such applications usually entail large storage requirements, particularly if several species are simulated.

Preliminary results indicate that this technique minimizes the introduction of numerical diffusion into the prediction, since it does not rely on any type of finite differencing scheme to produce a result. The rules used to establish the algorithm are complex, and the reader is referred to the original articles for their presentation (Egan and Mahoney, 1971, 1972).

B. TEST RESULTS

A major problem in evaluating alternative numerical methods is the selection of test problems that realistically parallel actual simulation conditions yet have either analytic solutions or solutions obtainable from highly accurate approximation techniques. Our approach has been to progress in the analysis from simple one-dimensional problems without reactions to multidimensional reactive comparisons. Taken individually, each problem may appear limiting insofar as it incorporates only a few aspects of an actual simulation in its analysis. Taken collectively, however, the total work covers the spectrum of problems that could occur in a realistic treatment.

1. One-Dimensional Advection

As a starting point, a simple one-dimensional advection problem was treated:

$$\frac{\partial c}{\partial t} + \frac{\partial uc}{\partial x} = 0 \quad . \tag{29}$$

In this problem, the wind field was allowed to vary spatially according to the expression

$$u(x) = 50\left[1 + \sin\left(\frac{\pi x}{57600}\right)\right] + 20\cos\left(\frac{\pi x}{7200}\right) \quad , \tag{30}$$

and the following initial conditions were chosen:

$$c(0,t) = 15 \quad ,$$

$$c(x,0) = 15 \quad .$$

This form of the wind field was selected because its variations are representative of those that could be expected to occur in an urban airshed.

The results of this analysis for a time step of 5 minutes and a grid spacing of 1200 meters are presented in Figure 4 at the end of 100 minutes of simulation time. For both the SHASTA and Egan-Mahoney methods, excellent

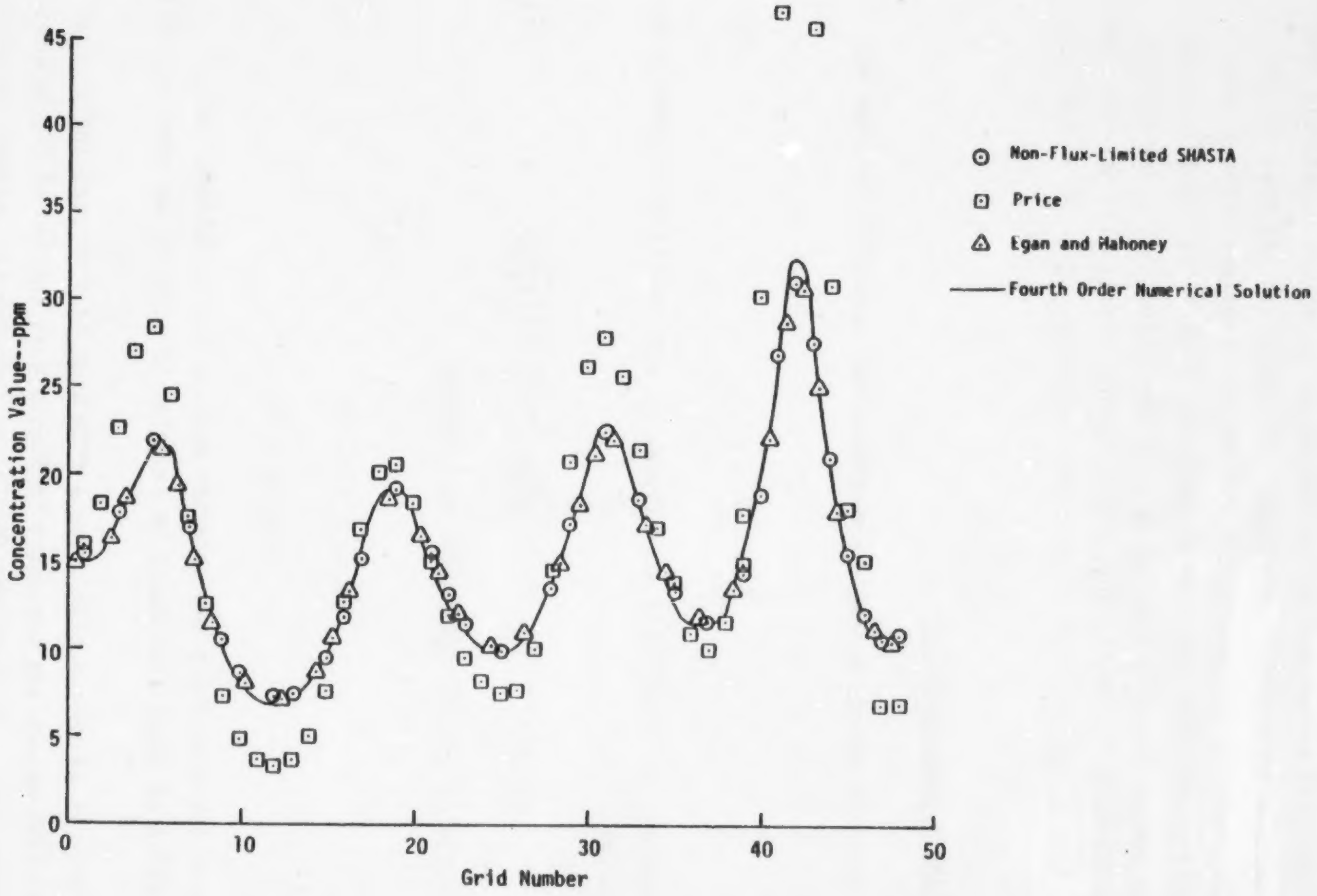

FIGURE 4. ONE-DIMENSIONAL COMPARISON OF THE PRICE, EGAN-MAHONEY, AND SHASTA ALGORITHMS

agreement occurs with a very accurate solution obtained using a fourth-order method developed by Kriess and Oliger (1973). The tests were run using the non-flux-corrected, non-mass-conservative variation of the SHASTA algorithm for reasons presented in the following sections.

2. Two-Dimensional Advection in a Nonreactive System

Classically, two-dimensional transport analysis is used to assess the errors associated with horizontal advection; these errors are known to constitute a major fraction of the numerical errors incurred in airshed simulations. In essence, this procedure entails the specification of both an initial concentration distribution c(x,y,0) and a constant wind field and then the tracking of the concentration profile in space as the problem evolves in time. Since the wind field is constant, the solution to the advection equation

$$\frac{\partial c}{\partial t} + u \frac{\partial c}{\partial x} + v \frac{\partial c}{\partial y} = 0 \qquad (31)$$

is given by

$$c(x,y,t) = c(x-ut,y-vt,0) \qquad (32)$$

where u and v are both equal to a constant. In our study, the initial distribution was chosen as

$$c(x,y,0) = \begin{cases} 10 \cos\frac{\pi\rho}{12000} \text{ for } \rho^2 = (x - 12000)^2 + (y - 12000)^2 , \\ \qquad\qquad 0 \geq \rho \geq 12000 \\ 0 \text{ elsewhere} , \end{cases} \qquad (33)$$

and the velocity profile was selected as u = v = 120 meters per minute. Care was taken to select a concentration profile that had gradients comparable to those encountered in the urban environment.

In the analysis, the grid spacing was set at 1200-meter intervals, and the time step was allowed to vary from one to five minutes. In this way, the parameter ε,

$$\varepsilon = \frac{u\Delta t}{\Delta x} = \frac{v\Delta t}{\Delta y} \quad , \tag{34}$$

could vary from 0.1 to 0.5.

For each of the different integration methods, a series of parametric studies were executed for different values of the parameter ε. The results of these analyses after 100 minutes of simulation time are given in Table 1 and Figures 5 through 8.

The average absolute error and maximum error are defined by the relationships

$$\bar{\psi} = \sum_{j}^{N} \frac{\left| c_j^{\mathrm{EXACT}} - c_j^{\mathrm{NUMERICAL}} \right|}{N} \qquad \text{(Average Absolute Error)}$$

and

$$\psi_{\max} = \operatorname*{Max}_{j} \left| c_j^{\mathrm{EXACT}} - c_j^{\mathrm{NUMERICAL}} \right| \qquad \text{(Maximum Absolute Error)} \quad ,$$

where N is the number of points on the grid. Also included in Table 1 are the CDC 7600 execution time (expressed in seconds) and the product of the average absolute error and the execution time.

From a computational point of view, Figures 5 through 7 indicate that the non-flux-limited SHASTA algorithm is superior to both the flux-limited and phoenical variations in terms of both accuracy and computational speed for all values of the parameter ε. Although it can be argued that the arbitrary specification of setting any negative prediction to background value makes the system non-mass-conservative, the results of our study indicate that this option accounted for an error of no more than 0.5 percent. Of greater significance in these results is the reduction in

Table 1

RESULTS OF THE PARAMETRIC ANALYSIS

(a) Egan and Mahoney Method

ε	$\bar{\psi}$	ψ_{max}	Time	$\bar{\psi}\cdot$Time
0.1	0.0358	0.3955	11.791	0.4221
0.2	0.0323	0.2793	5.751	0.1858
0.3	0.0319	0.2393	3.796	0.1211
0.4	0.0329	0.2473	2.876	0.0946
0.5	0.0331	0.2498	2.284	0.0756

(b) SHASTA Non-Flux-Corrected Method

ε	$\bar{\psi}$	ψ_{max}	Time	$\bar{\psi}\cdot$Time
0.1	0.0924	0.7408	2.734	0.2526
0.2	0.0648	0.7799	1.426	0.0924
0.3	0.0512	0.6739	0.806	0.0413
0.4	0.0400	0.5264	0.688	0.0275
0.5	0.0309	0.3507	0.560	0.0173

(c) Price Method

ε	$\bar{\psi}$	ψ_{max}	Time	$\bar{\psi}\cdot$Time
0.1	0.2566	1.8287	1.514	0.3885
0.2	0.3099	2.3771	0.757	0.2346
0.3	0.4203	3.3186	0.509	0.2139
0.4	0.5709	4.5322	0.375	0.2141
0.5	0.7870	9.0519	0.302	0.2377

(d) SHASTA Flux-Limited Method

ε	$\bar{\psi}$	ψ_{max}	Time	$\bar{\psi}\cdot$Time
0.1	0.1150	2.1689	3.109	0.3575
0.2	0.0951	1.7540	1.544	0.1468
0.3	0.0710	1.3713	0.932	0.0662
0.4	0.0548	1.1529	0.769	0.0421
0.5	0.0536	1.2131	0.621	0.0332

(e) Phoenical SHASTA Method

ε	$\bar{\psi}$	ψ_{max}	Time	$\bar{\psi}\cdot$Time
0.1	0.1108	1.9102	3.440	0.3811
0.2	0.1007	1.6867	1.707	0.1719
0.3	0.0773	1.3252	1.070	0.0827
0.4	0.0575	1.1237	0.872	0.0501
0.5	0.0484	1.0828	0.692	0.0335

Note:

Δx = 1200 m
u = 120 m/min
v = 120 m/min
T = 100 min

The problem solved was the following:

$$\frac{\partial c}{\partial t} + 120\,\frac{\partial c}{\partial x} + 120\,\frac{\partial c}{\partial y} = 0 \quad . \qquad (35)$$

The initial conditions were:

$$c(0,x) = 10[1 + \cos(\pi\rho)] \quad , \qquad (36)$$

$$\rho = \frac{\sqrt{(x - 12{,}000)^2 + (y - 12{,}000)^2}}{12{,}000} \qquad (37)$$

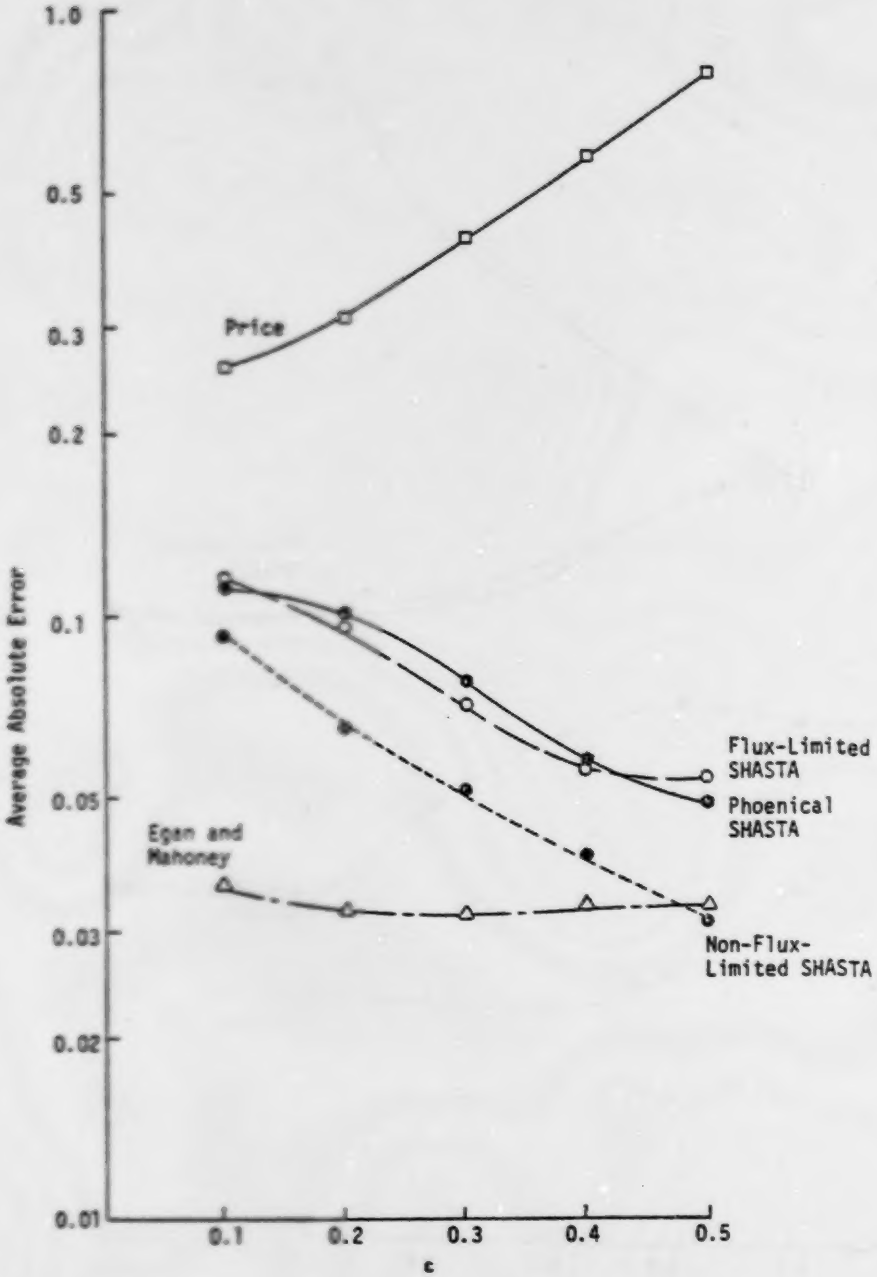

FIGURE 5. AVERAGE ABSOLUTE ERROR AS A FUNCTION OF ε

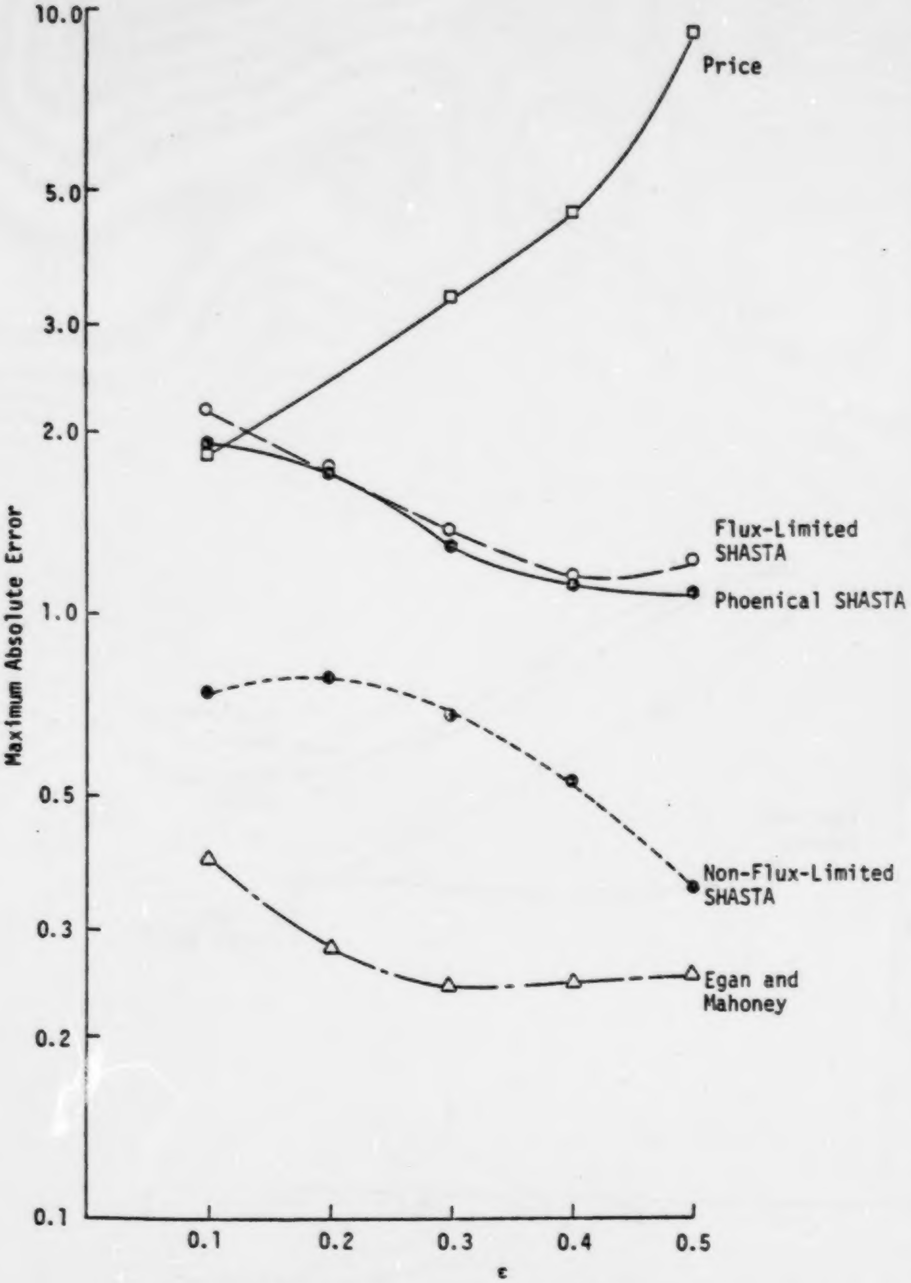

FIGURE 6. MAXIMUM ABSOLUTE ERROR AS A FUNCTION OF ε

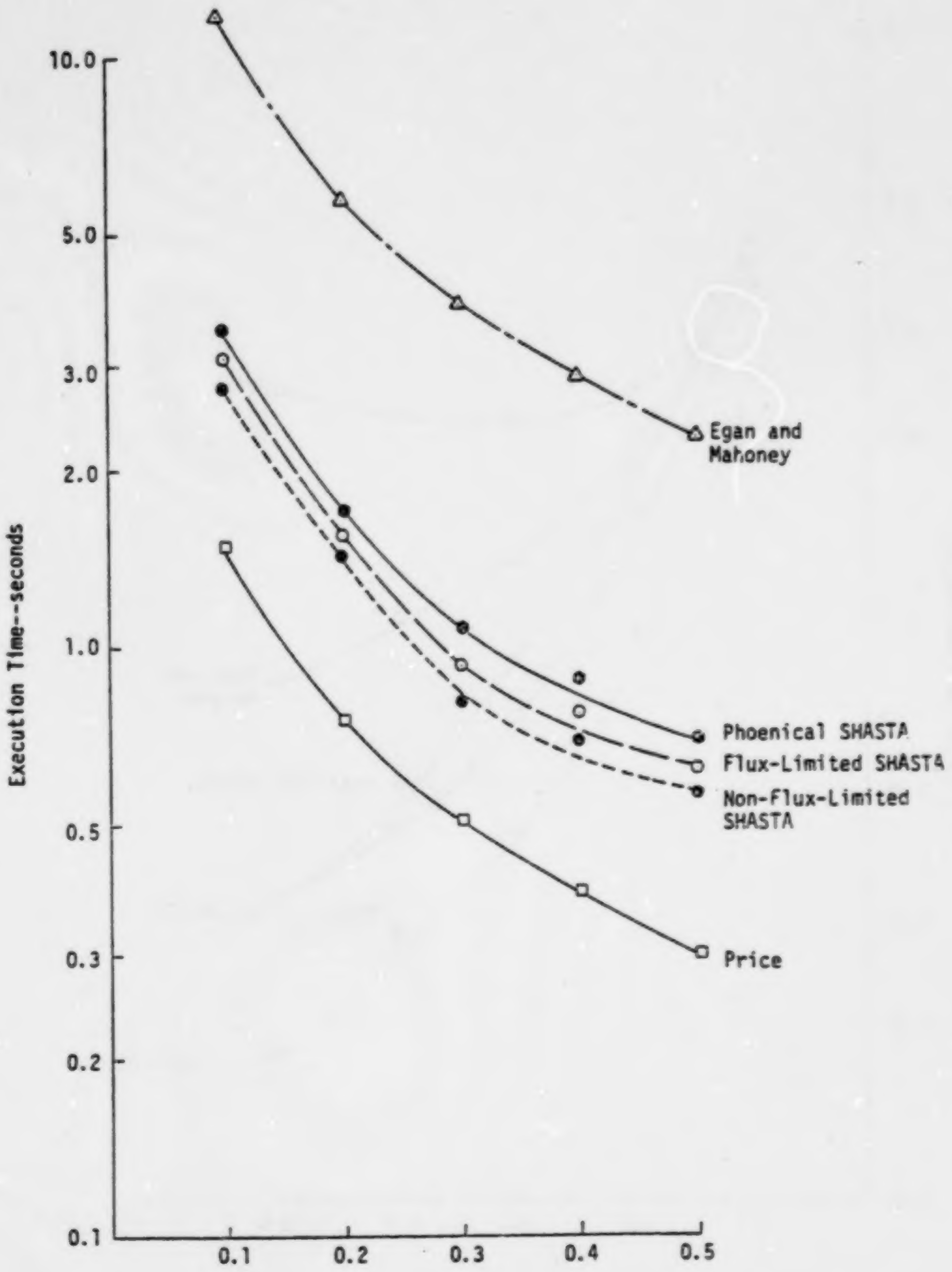

FIGURE 7. EXECUTION TIME AS A FUNCTION OF ε

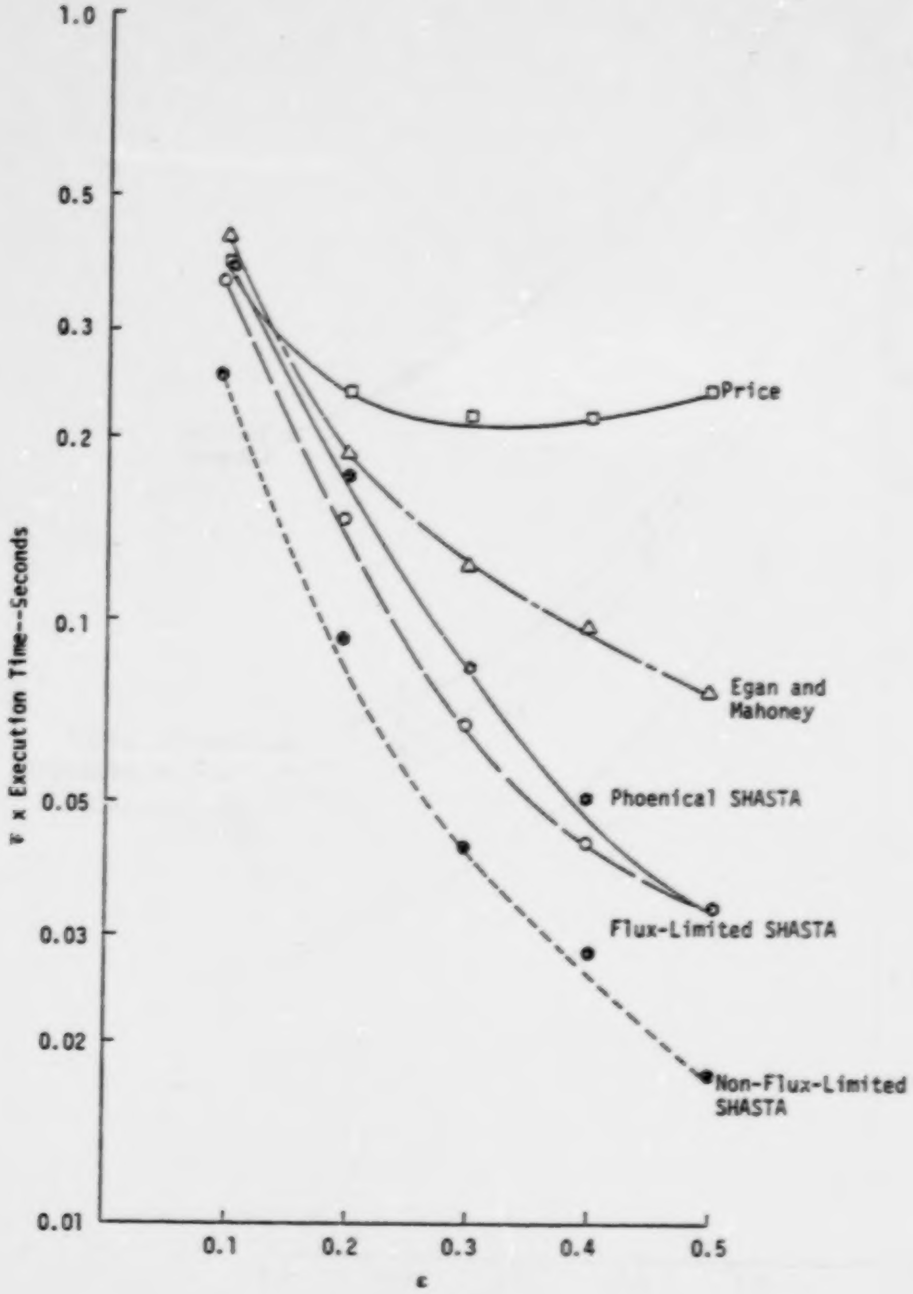

FIGURE 8. THE PRODUCT OF THE AVERAGE ABSOLUTE ERROR AND THE EXECUTION TIME AS A FUNCTION OF ϵ

computational error at increased values of the parameter ε. This is discussed further in Section C.

Clearly, from a computational point of view, the method of Egan and Mahoney is a superior integration method compared with the other methods in terms of both its average absolute error and maximum absolute error. Its main drawbacks are that it requires an extremely large amount of computational time to execute a time step and that it needs a large amount of core storage to accommodate the various moments associated with each of the coordinate axes. In this analysis, the method was written in an unfractionalized form that treated both directions of the horizontal advection simultaneously.

In every case, the Price integration method yielded results inferior to those produced by both the Egan-Mahoney and SHASTA algorithms. The accuracy of the Price method increased with decreasing values of ε, though it was never comparable to that of the other two methods independent of the time step chosen. In an actual airshed simulation, the parameter ε may vary from 0 to 0.5, depending on various combinations of wind speed, time step, and grid spacing. Hence, we might anticipate that considerable error could be introduced into the calculations if the Price method was used.

One interesting way of identifying an optimum value for the parameter ε is to plot values of the product of the average absolute error and the execution time for various values of ε while Δx and u are held fixed. Figure 8 shows that, as with most numerical methods designed to approximate hyperbolic problems, it is best to use the SHASTA and Egan and Mahoney algorithms with the largest value of ε for which the algorithm remains stable. In contrast, the accuracy of the Price method increases with decreasing ε (see Figure 5). Hence, as shown in Figure 8, the optimal value of ε lies at a trade-off point between high computation time and high accuracy.

In the rest of this chapter, only the non-flux-limited, non-mass-conservative SHASTA algorithm is considered for analysis. Its superior accuracy and reduced computational costs relative to the other two alternative forms of this algorithm warrant its selection for further scrutiny.

3. Two-Dimensional Advection with Chemical Reactions

Having identified the non-flux-limited, non-mass-conservative SHASTA algorithm as an optimal choice, we conducted a test to investigate the effects of introducing reactive chemistry into a system undergoing horizontal advection. The equations to be solved followed the governing expression

$$\frac{\partial c_i}{\partial t} + u \frac{\partial c_i}{\partial x} + v \frac{\partial c_i}{\partial y} = R_i \quad , \tag{38}$$

where the u and v were chosen to be 268.2 meters per minute.* The shapes of the initial concentration profiles were chosen to be identical to those used in the nonreactive analysis, except that the peak concentration values varied from component to component in a ratio similar to that found in the morning hours in an urban airshed. The parameter ε was set to 0.25 by specifying a grid spacing of 3218 meters† and a time increment of three minutes. This value is close to the optimum one for the Price method.

To establish an independent basis of comparison, we considered a trajectory-type simulation described by the following equation:

$$\frac{dc_i}{dt} = R_i \quad . \tag{39}$$

---

*268.2 meters per minute = 10 mph

†3218 meters = 2 miles

The initial conditions used were identical to those employed in the advection analysis, and we used the Gear method for integrating the ordinary differential equations. This technique has been shown to produce highly accurate results at reasonable computational costs. Two runs were executed in which the initial concentrations were chosen to be identical to those found at the peak and at the point of steepest gradient of the advected pattern. The full 31-step NO_x-hydrocarbon kinetic mechanism, as described in Volume II, Chapter II and incorporated in the SAI airshed model, was used in the simulation. To correlate the results of the two methods, we had to make the elapsed simulation time in the Gear method equal to the travel time in the advected problem. In the latter case, the travel time is equal to the distance traveled divided by the local wind speed. By carefully choosing the wind speed, grid spacing, and time step, one can generate results that are easy to compare on a point-by-point basis.

In the advection simulation, the non-flux-limited, non-mass-conservative SHASTA algorithm was executed as if it were solving an actual airshed problem. All three spatial dimensions were treated in the analysis, though no vertical movement of material occurred because all vertical planes had identical concentration profiles. Measured against the accurate trajectory solution, a comparison of the two sets of results provides some indication of the combined error associated with both numerical inaccuracies and the fractional step procedure. Figures 9 through 16 illustrate the results for the components NO, NO_2, O_3, and CO at both the peak and the point of steepest gradient locations after 100 minutes of simulation time.

An examination of the results of this comparison shows that the SHASTA algorithm is superior to the Price method at both peak and gradient locations. Not only does the SHASTA scheme almost identically follow the exact solution, but also it exhibits none of the divergence that occurs with the Price method.

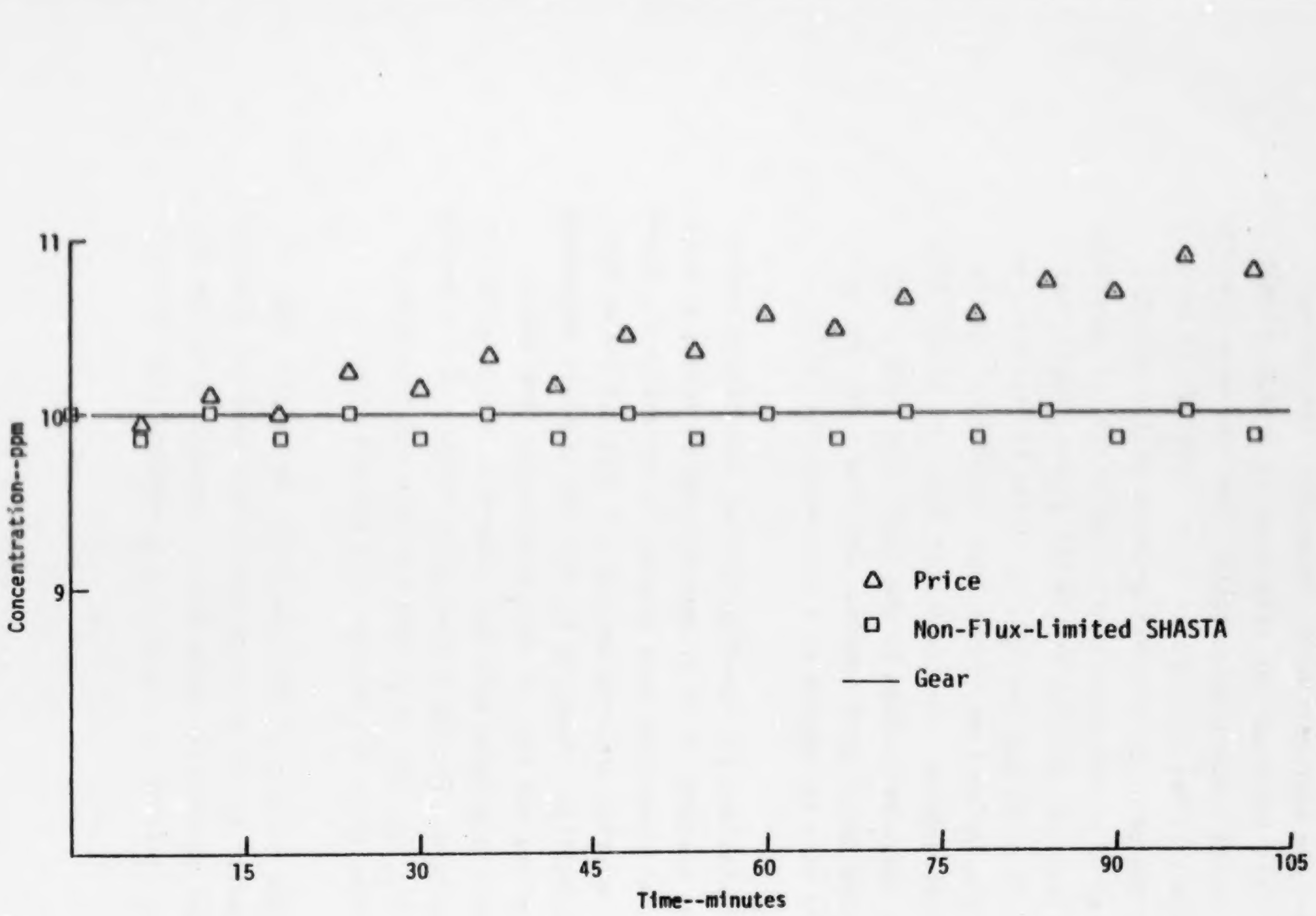

FIGURE 9. PEAK CONCENTRATION OF CO AS A FUNCTION OF TIME

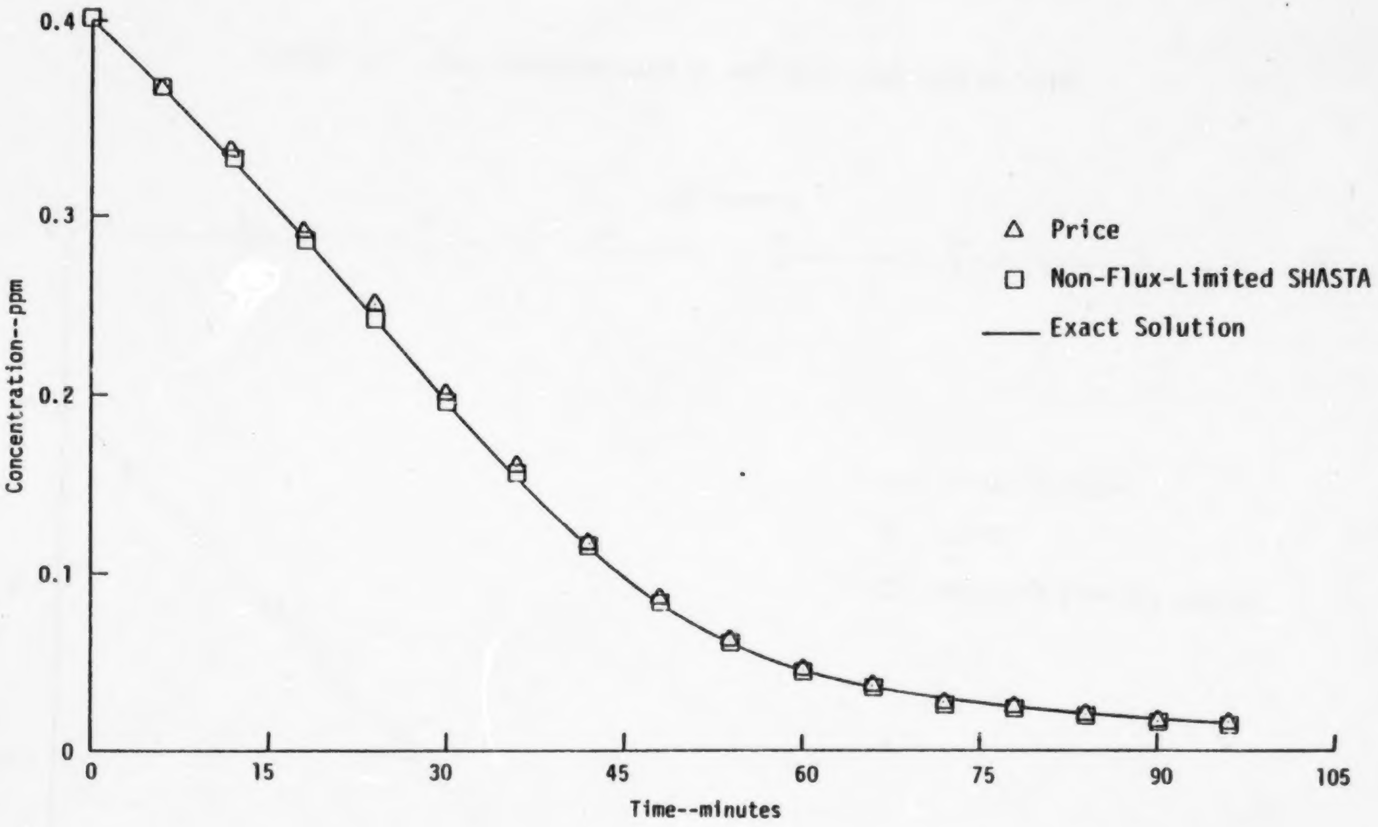

FIGURE 10. PEAK CONCENTRATION OF NO AS A FUNCTION OF TIME

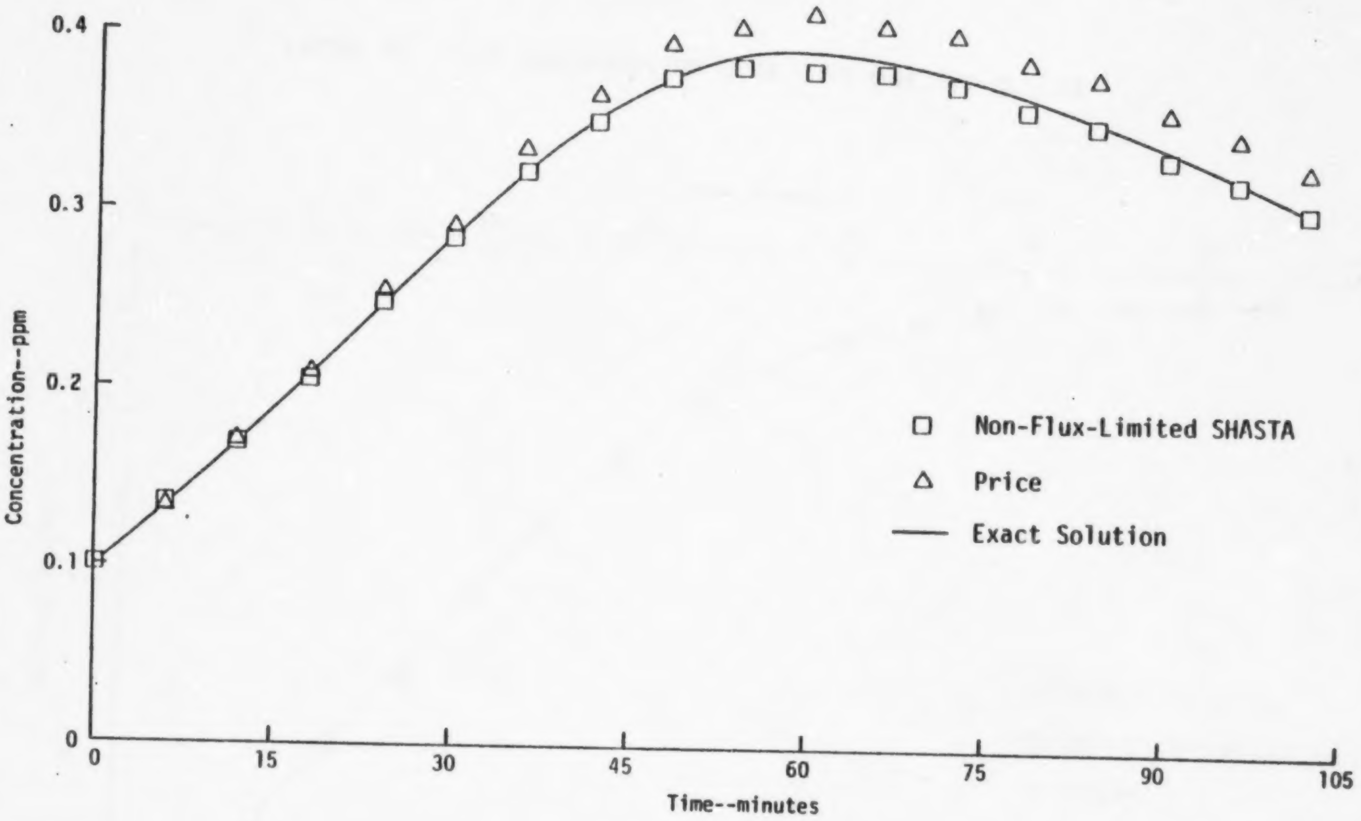

FIGURE 11. PEAK CONCENTRATION OF NO_2 AS A FUNCTION OF TIME

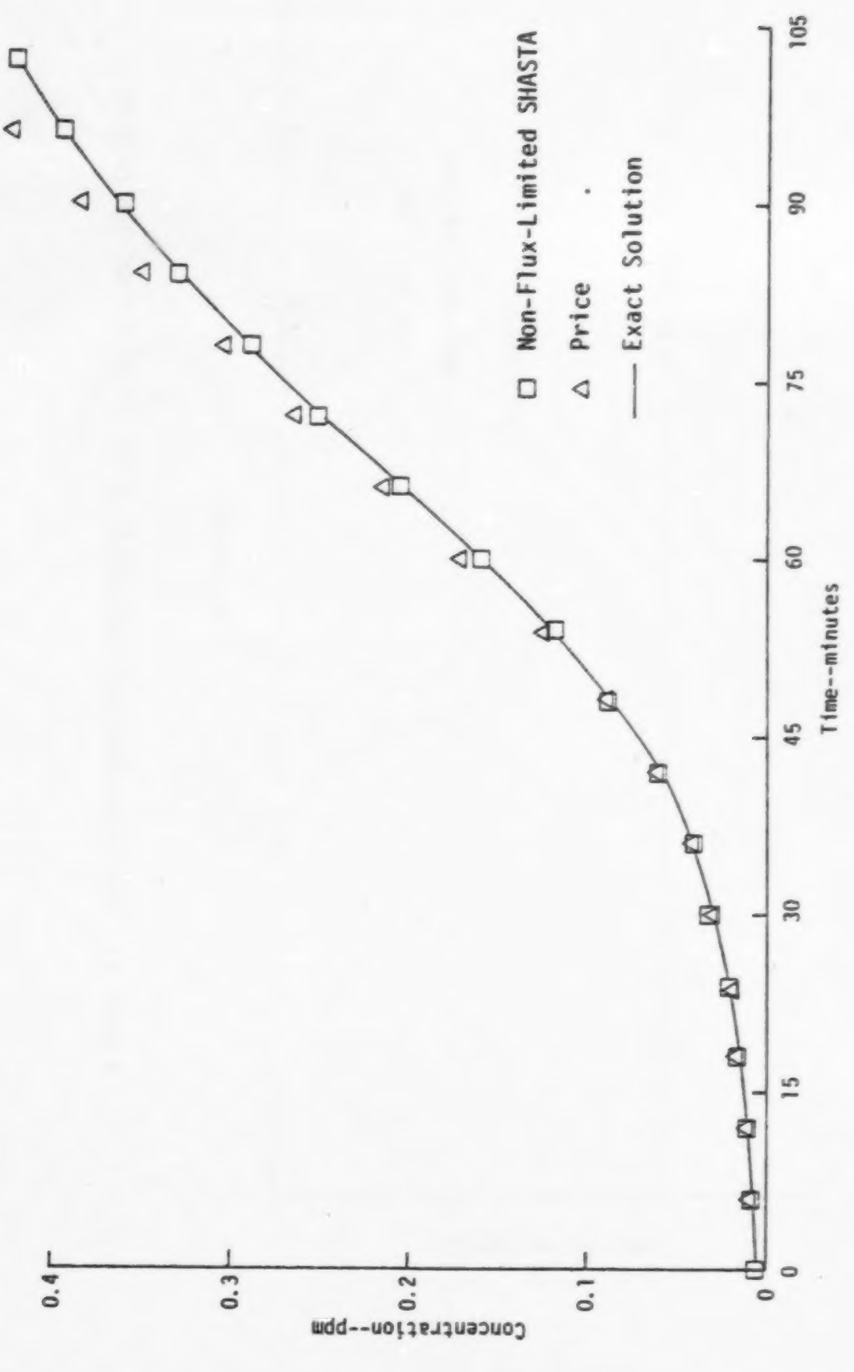

FIGURE 12. PEAK CONCENTRATION OF O_3 AS A FUNCTION OF TIME

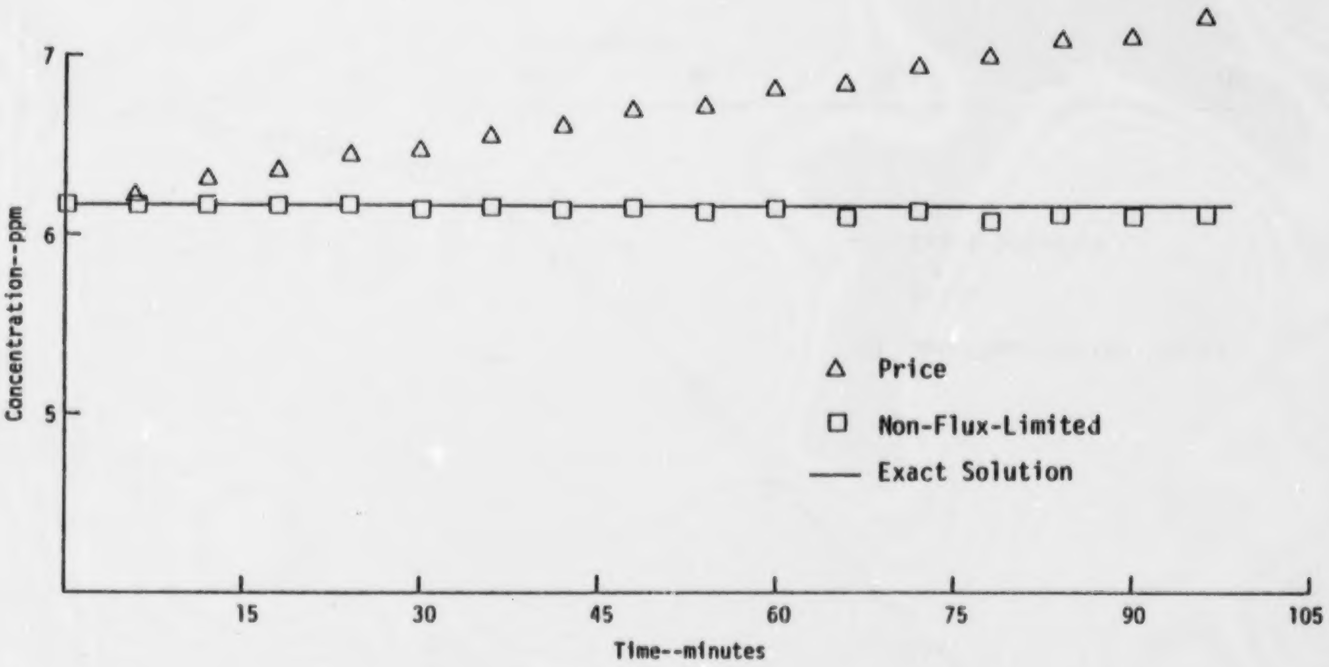

FIGURE 13. STEEPEST GRADIENT CONCENTRATION OF CO AS A FUNCTION OF TIME

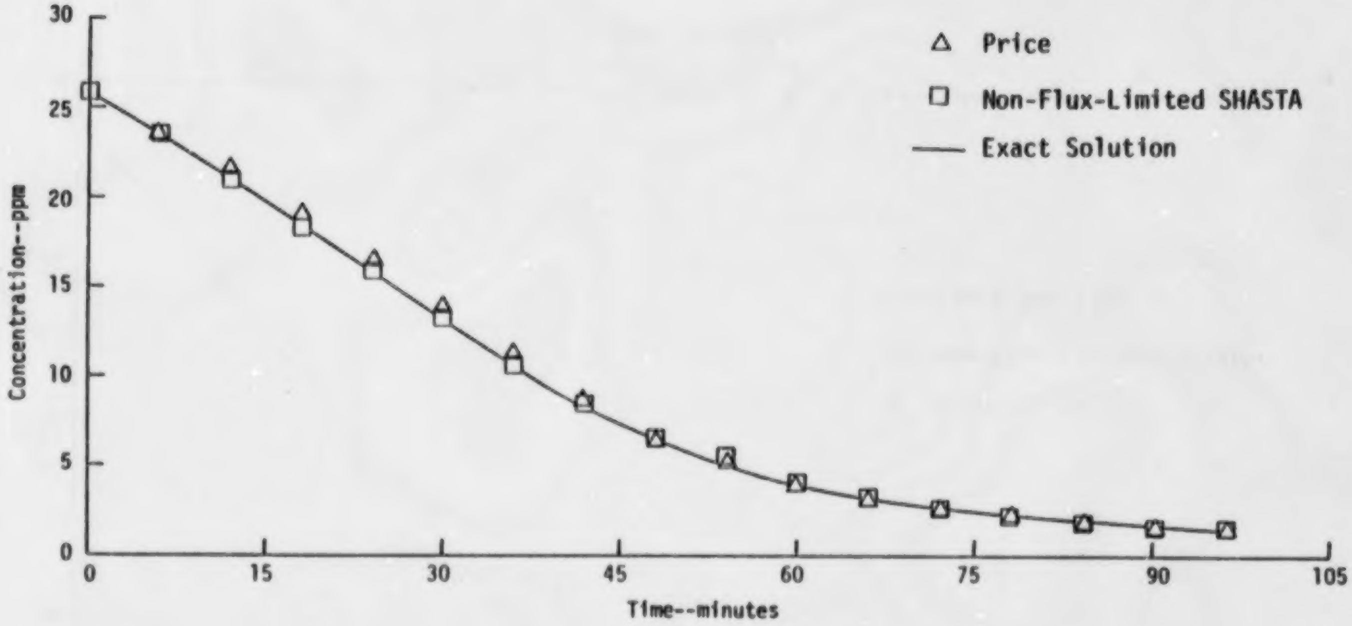

FIGURE 14. STEEPEST GRADIENT CONCENTRATION OF NO AS A FUNCTION OF TIME

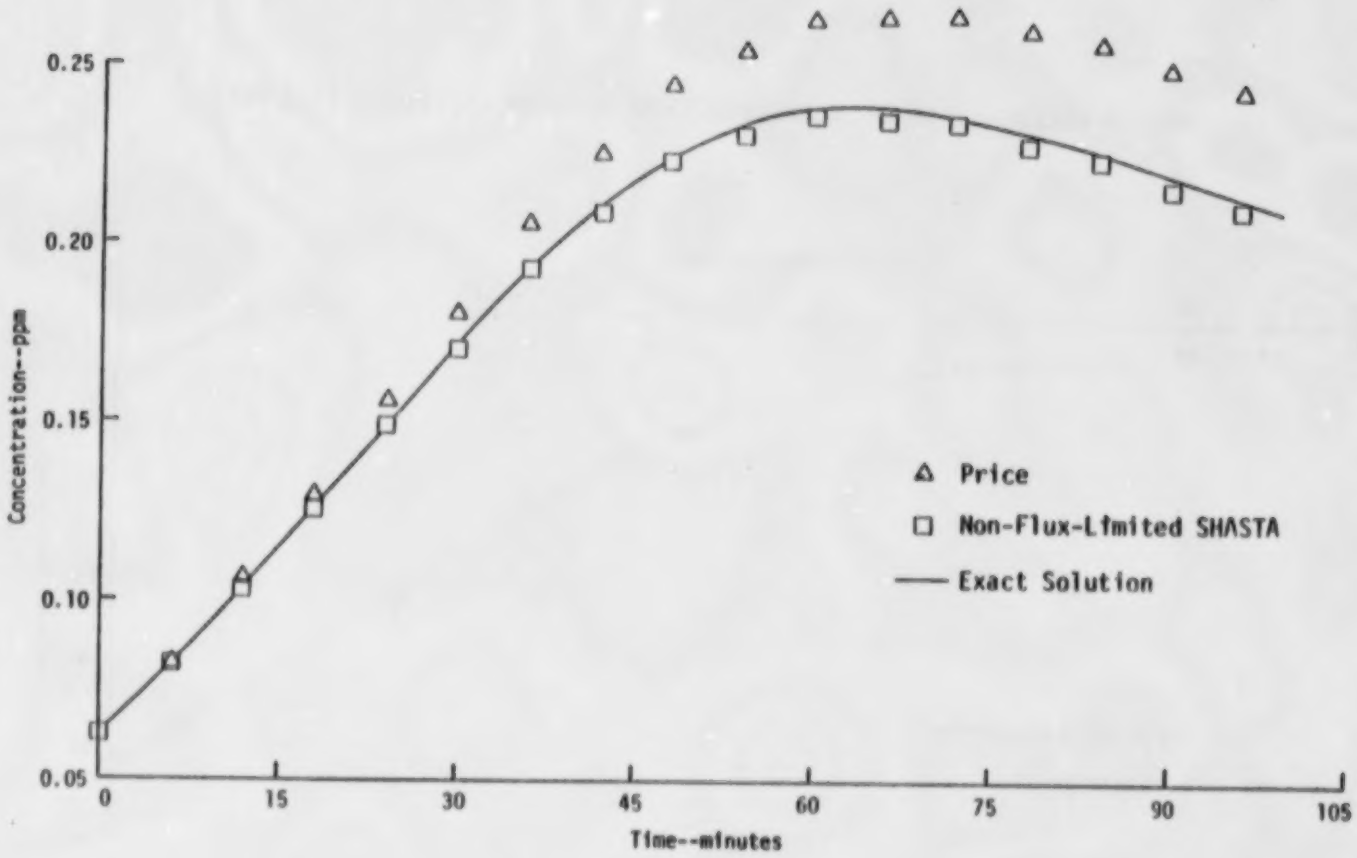

FIGURE 15. STEEPEST GRADIENT CONCENTRATION OF NO_2 AS A FUNCTION OF TIME

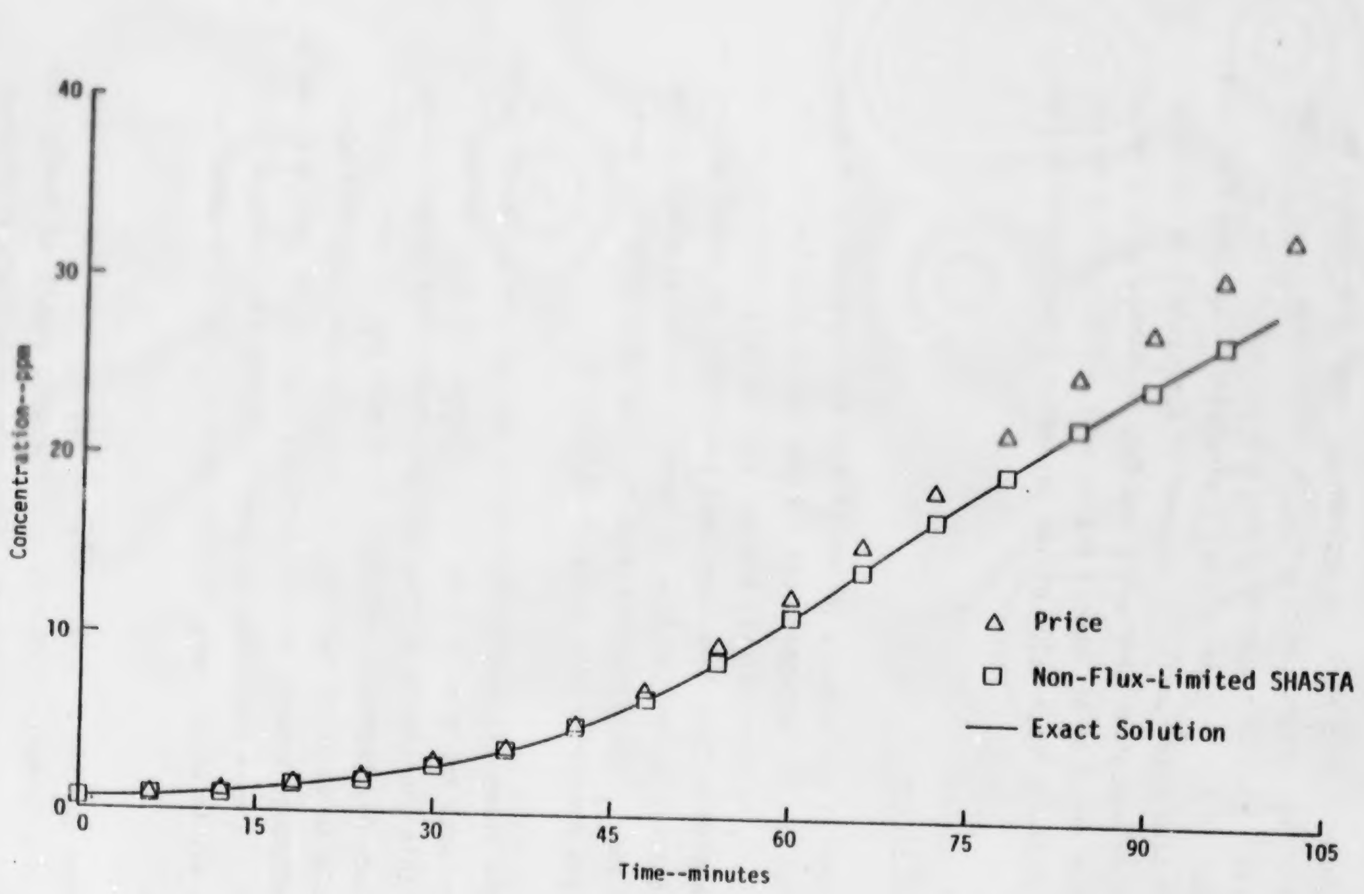

FIGURE 16. STEEPEST GRADIENT CONCENTRATION OF O_3 AS A FUNCTION OF TIME

In conjunction with this work, we decided to remove the kinetic mechanism from the vertical integration step and to incorporate it as an independent fourth step. With this modification, the execution time was reduced by a factor of 2. This means that a simulation employing the Price method that would have been run in 100 seconds of execution time could be run in 90 seconds of execution time using the SHASTA method, with a reduction in the average error of at least a factor of 3 and possibly a factor of 6, depending on the average value of the parameter ε that characterizes the flow field.

4. Airshed Simulations

As a final set of analyses, a series of runs was executed in an actual airshed simulation for 29 September 1969 for the Los Angeles basin. The necessary emissions, meteorological, and air quality data required for this simulation, assembled by SAI, have been used previously for model validation. For several test sites in the Los Angeles basin, a series of plots giving ground-level CO and O_3 concentrations as a function of time of day were prepared; they are presented in Figures 17 through 28.

Although the Price and SHASTA integration methods are dramatically different, their outputs are similar. At first glance, the most obvious explanation of this phenomenon is that the test cases used in evaluating the two techniques may represent extremes in meteorological conditions that are unlikely to occur in reality. In fact, however, the test conditions chosen, although severe, are not entirely atypical of possible simulation conditions. A more plausible explanation of the similarity of their outputs is the way in which averaging over grid cells affects emissions distributions.

To implement the SAI airshed model, one must average the emissions contributions of a variety of sources within a grid square uniformly over an area of several square kilometers. This step effectively eliminates

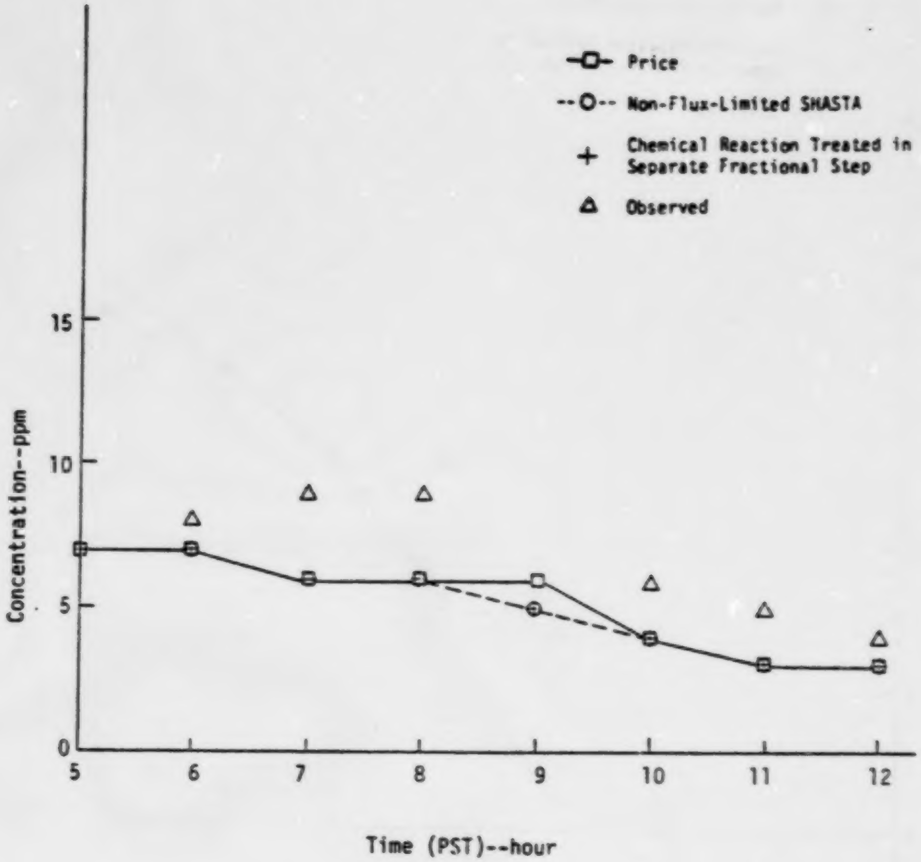

FIGURE 17. CO CONCENTRATION AT POMONA ON 29 SEPTEMBER 1969 AS A FUNCTION OF TIME

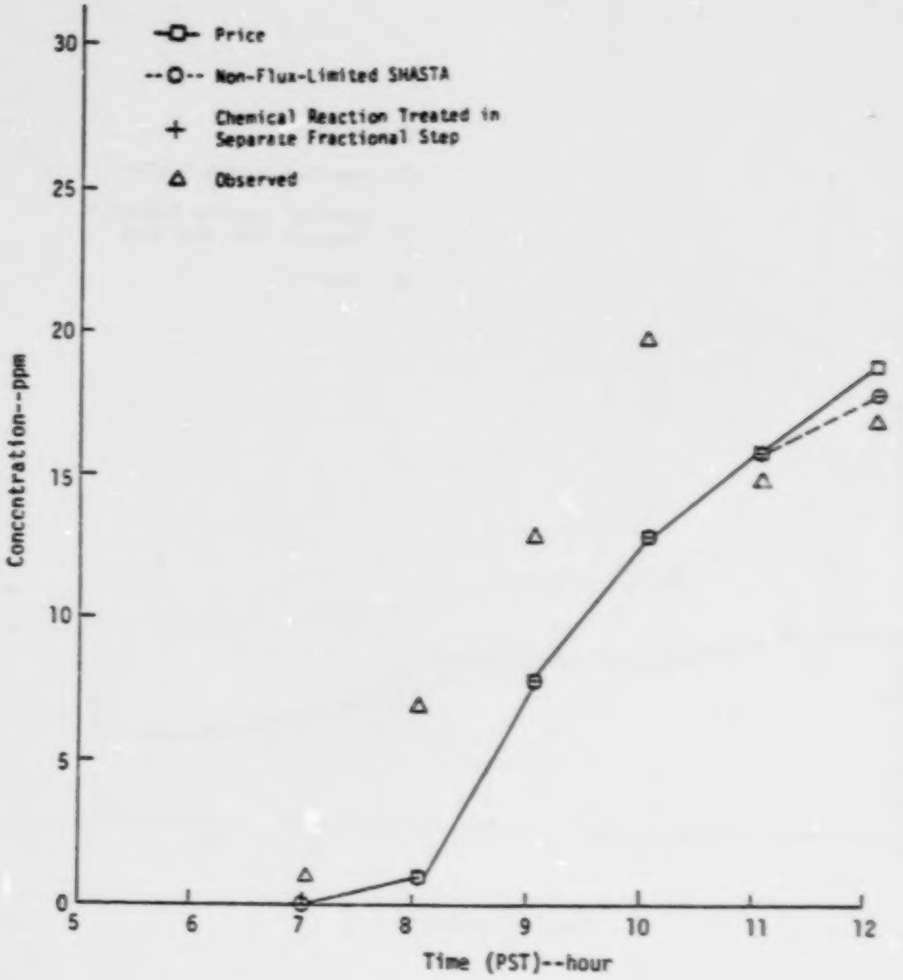

FIGURE 18. OZONE CONCENTRATION AT POMONA ON 29 SEPTEMBER 1969 AS A FUNCTION OF TIME

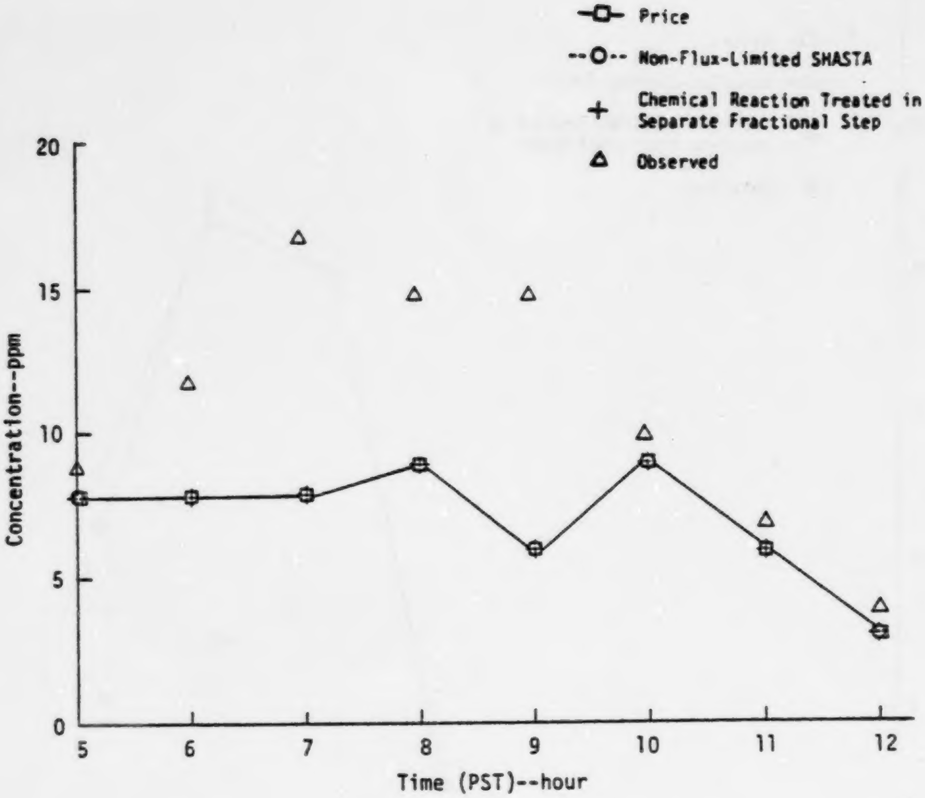

FIGURE 19. CO CONCENTRATION AT COMMERCE ON 29 SEPTEMBER 1969 AS A FUNCTION OF TIME

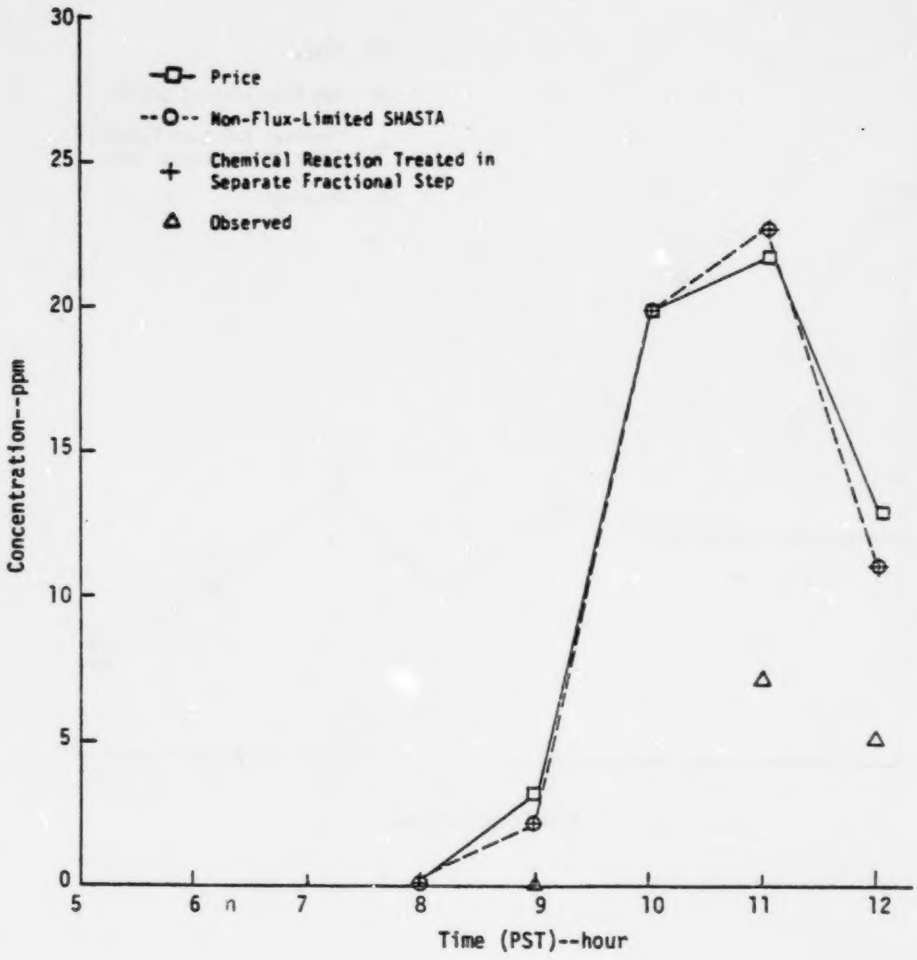

FIGURE 20. OZONE CONCENTRATION AT COMMERCE ON 29 SEPTEMBER 1969 AS A FUNCTION OF TIME

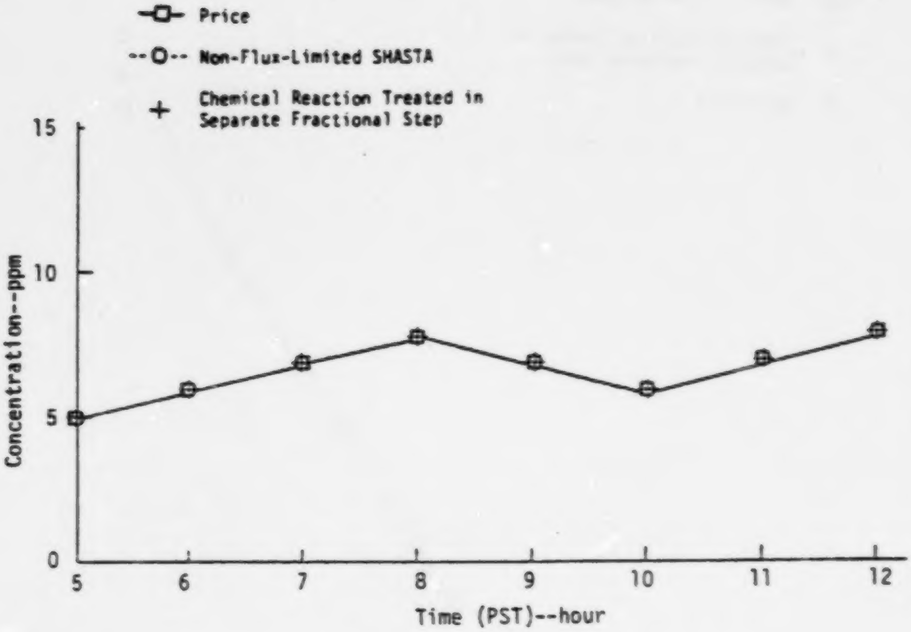

FIGURE 21. CO CONCENTRATION AT ANAHEIM ON 29 SEPTEMBER 1969 AS A FUNCTION OF TIME

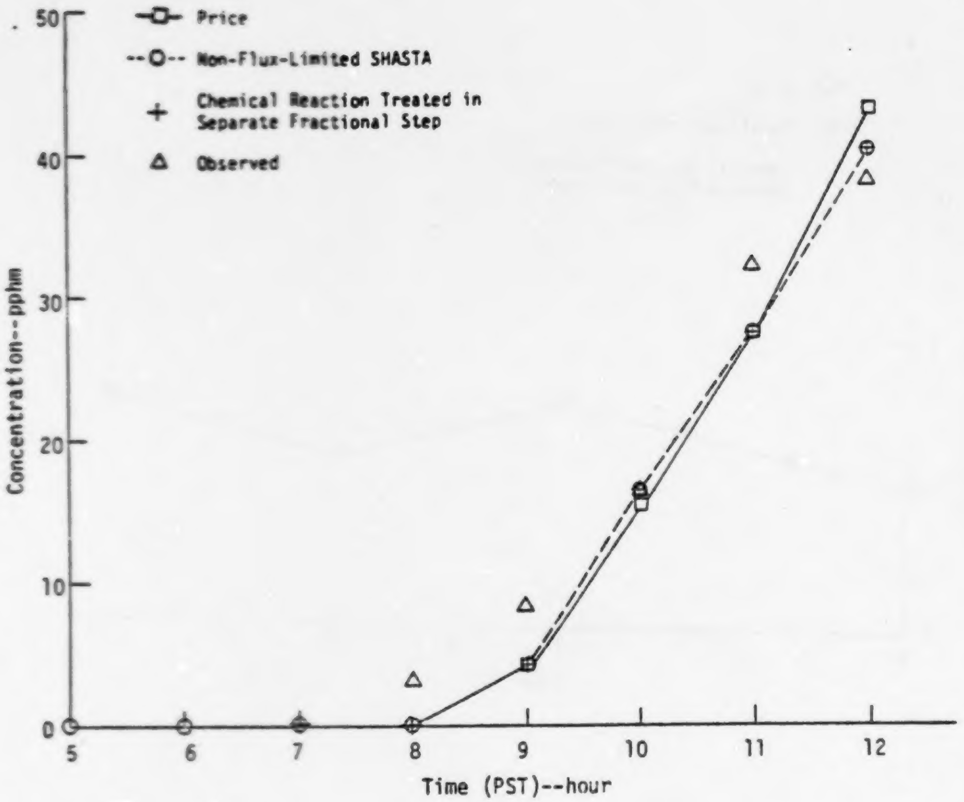

FIGURE 22. OZONE CONCENTRATION AT ANAHEIM ON 29 SEPTEMBER 1969 AS A FUNCTION OF TIME

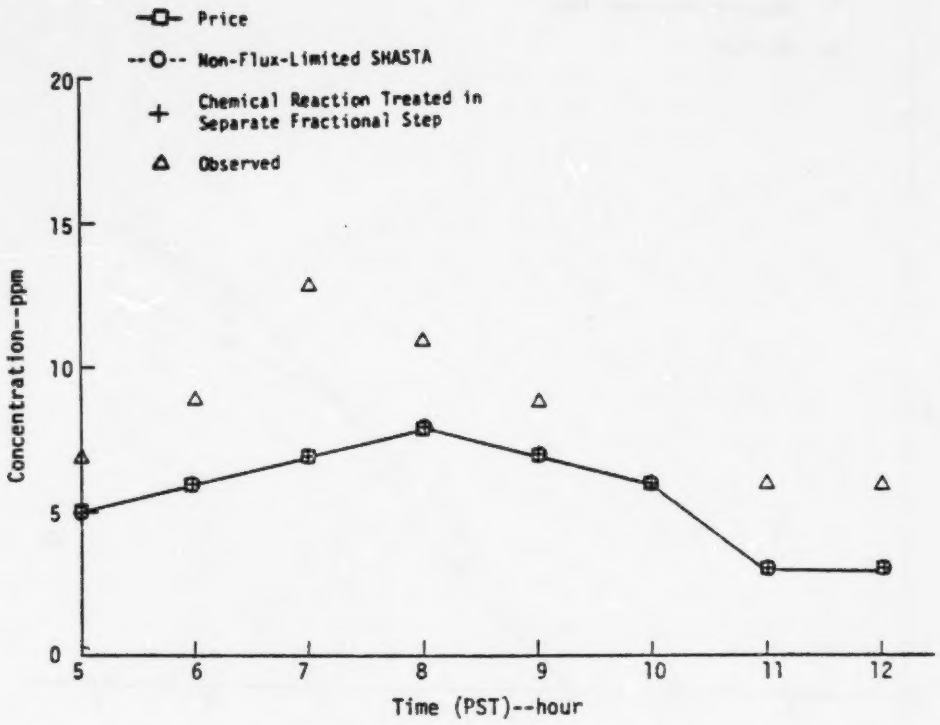

FIGURE 23. CO CONCENTRATION AT LONG BEACH ON 29 SEPTEMBER 1969 AS A FUNCTION OF TIME

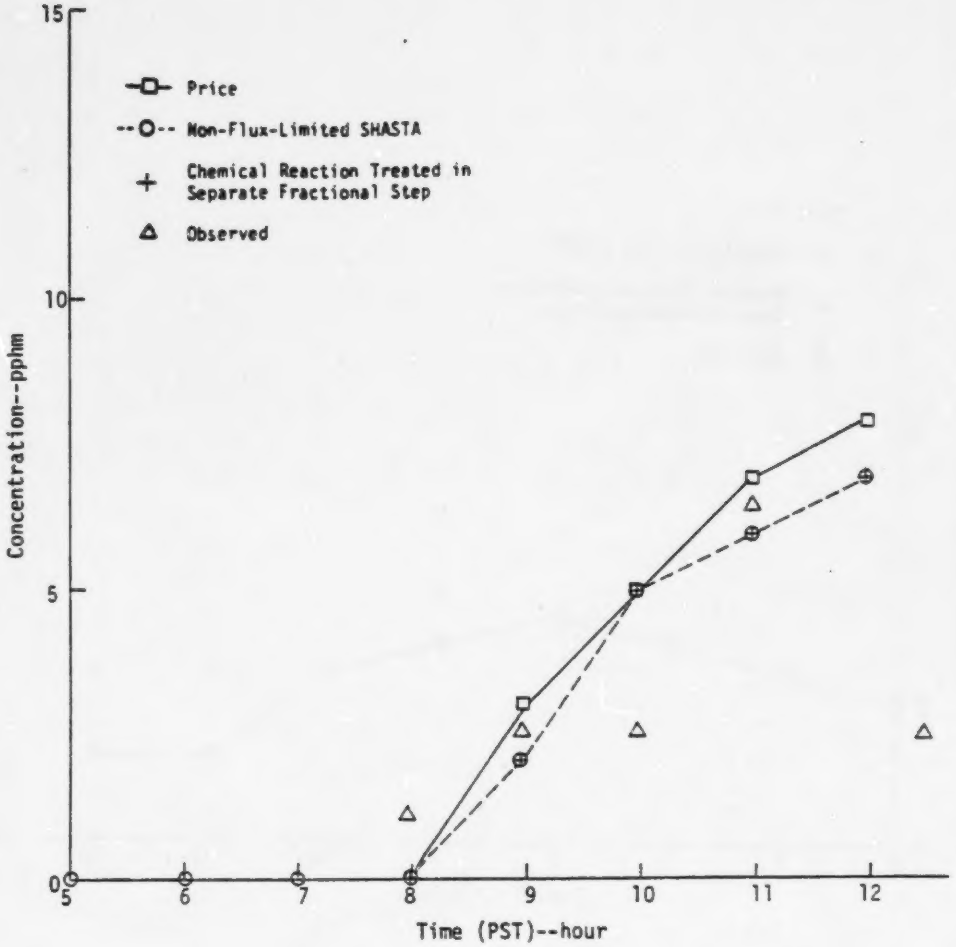

FIGURE 24. OZONE CONCENTRATION AT LONG BEACH ON 29 SEPTEMBER 1969 AS A FUNCTION OF TIME

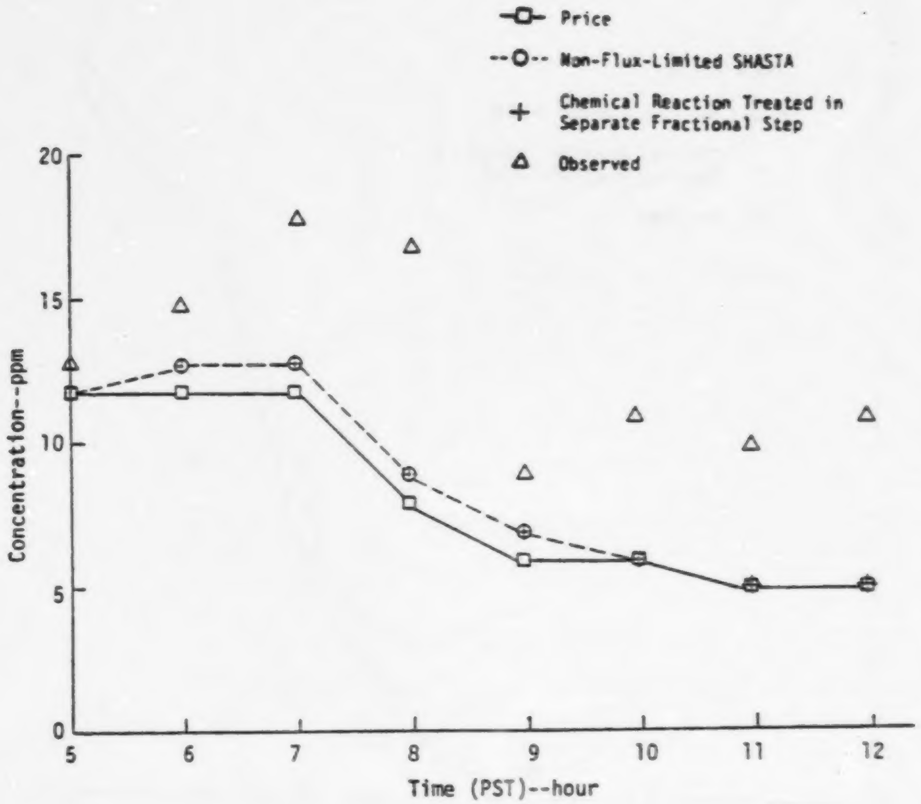

FIGURE 25. CO CONCENTRATION AT BURBANK ON 29 SEPTEMBER 1969 AS A FUNCTION OF TIME

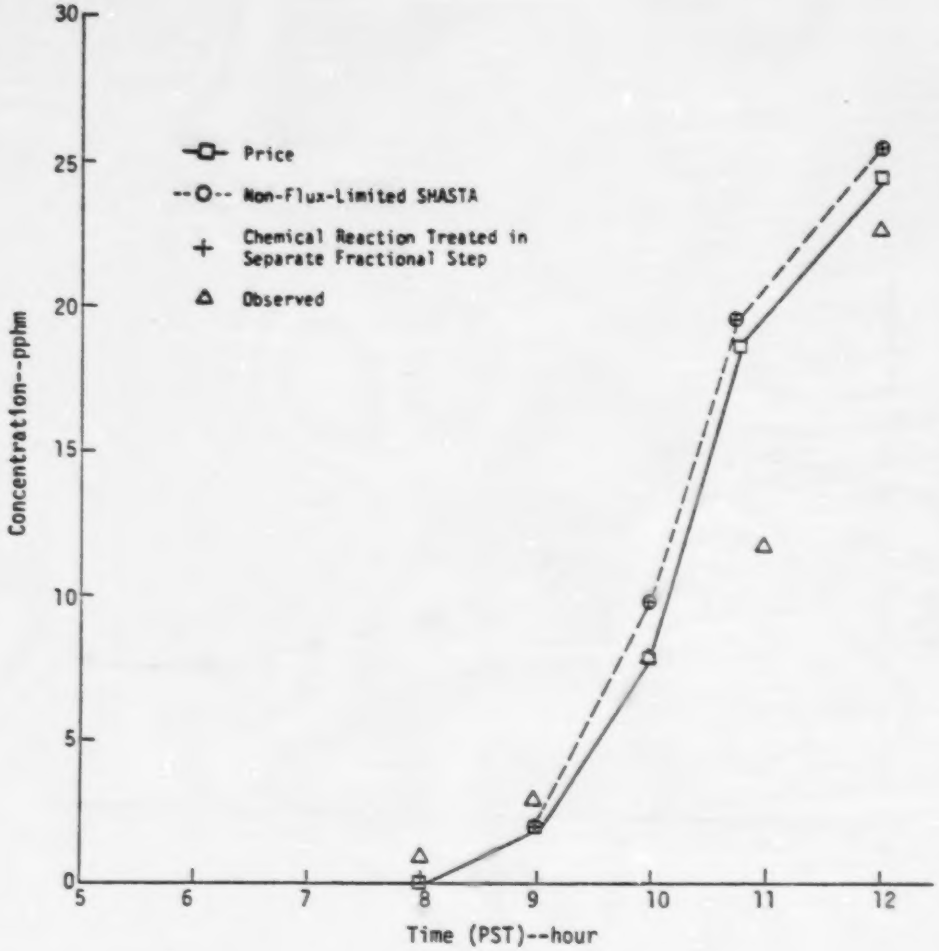

FIGURE 26. OZONE CONCENTRATION AT BURBANK ON 29 SEPTEMBER 1969 AS A FUNCTION OF TIME

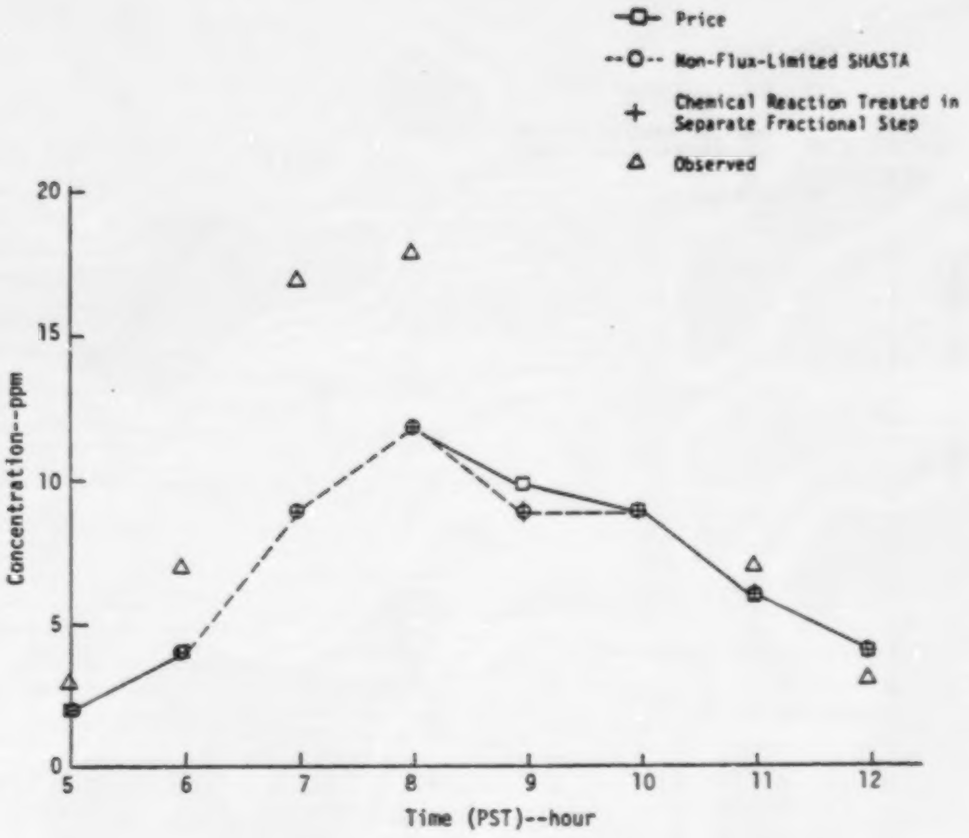

FIGURE 27. CO CONCENTRATION IN DOWNTOWN LOS ANGELES ON 29 SEPTEMBER 1969 AS A FUNCTION OF TIME

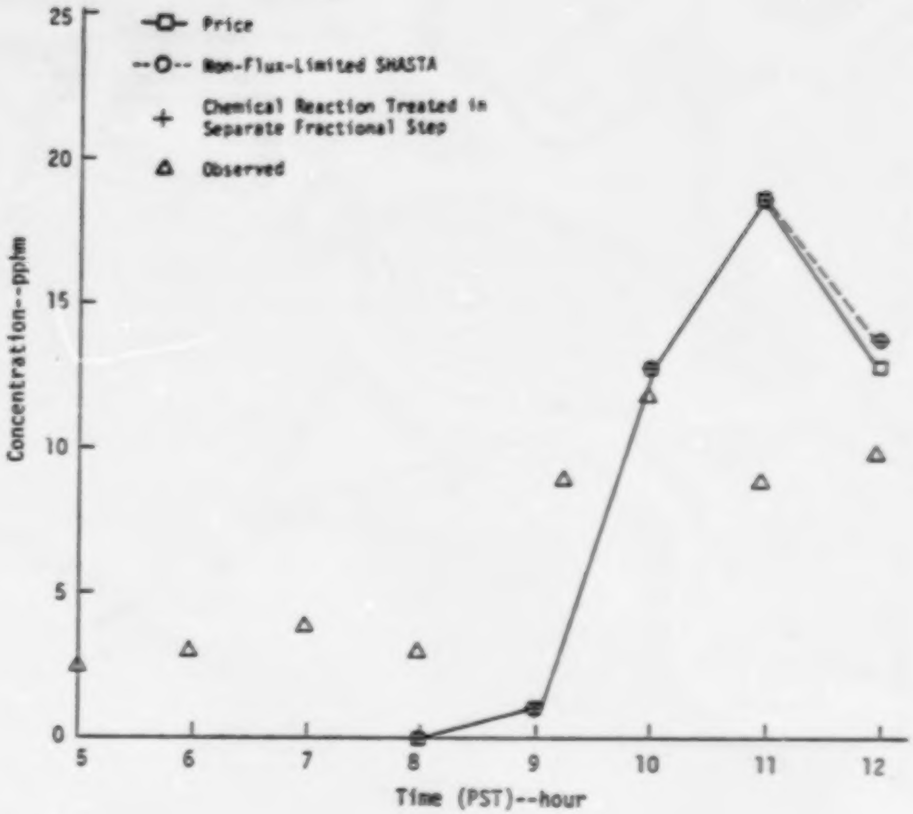

FIGURE 28. OZONE CONCENTRATION IN DOWNTOWN LOS ANGELES ON 29 SEPTEMBER 1969 AS A FUNCTION OF TIME

naturally occurring concentration gradients due to the influence of roadways and large point sources. Consequently, the enhanced resolution gained by implementing a more accurate numerical integration method is somewhat offset by the reduction in concentration gradients due to area-wide averaging. Evidence supporting this conclusion is given in Figures 29 and 30, which show the distributions of carbon monoxide and ozone over the Los Angeles basin on 29 September 1969 at 10:00 and 12:00 a.m., respectively. Although large regional differences in predicted concentrations occur in any single simulation when considered over a scale of 5 to 6 grid squares, local concentration differences on a scale of 1 to 2 squares are seldom larger than a factor of 2. If finer resolution in the spatial dimensions had been used, more distinctive differences between the two techniques would most likely have been detected.

In addition to investigating the accuracy of the alternative integration methods, we performed an independent test to determine the decrease in execution time and the corresponding influence on the results of incorporating the reaction sequence into an independent fractional step. The results of this test indicate that for a typical seven-hour airshed simulation the execution time for the SHASTA method would be reduced from 861.5 to 479.2 seconds if this change were made. This 44 percent decrease had little or no effect on the predicted results. Obviously, this change is highly desirable from a computing cost point of view. The execution time of 479.2 seconds is roughly 55 percent of the 877.7 seconds needed for the execution of the Price method for the same problem.

C. NUMERICAL ANALYSIS

Many of the results obtained in the previous section can be explained in terms of the numerical properties associated with the various difference methods. The simplest and perhaps the only case that lends itself to analysis is the classical one in which the velocity field is constant. For this condition, the Price algorithm can be put in the form

Reproduced from
best available copy.

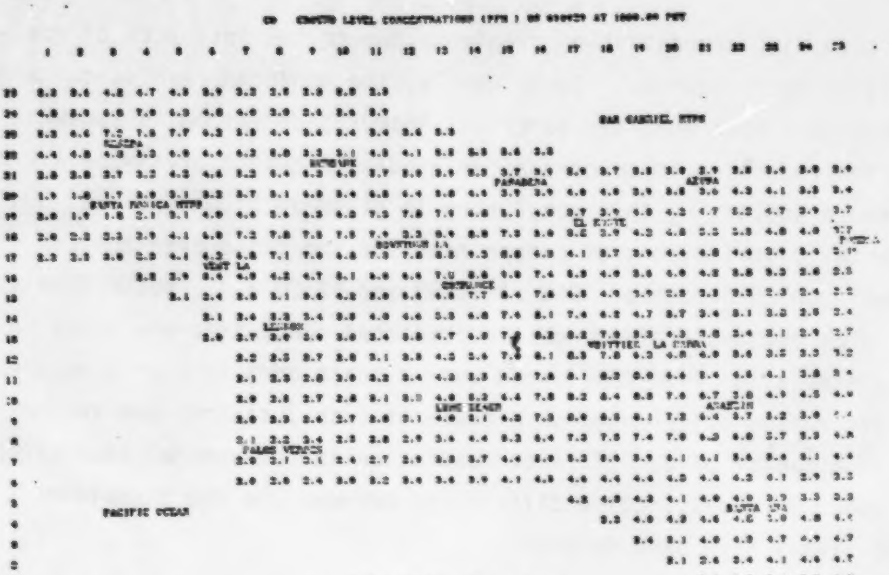
SAN GABRIEL MTNS
RESEDA
BURBANK
PASADENA
AZUSA
SANTA MONICA MTNS
EL MONTE
POMONA
DOWNTOWN LA
WEST LA
COMMERCE
LENNOX
WHITTIER
LA HABRA
LONG BEACH
ANAHEIM
PALOS VERDES
SANTA ANA
PACIFIC OCEAN

(a) Price Algorithm

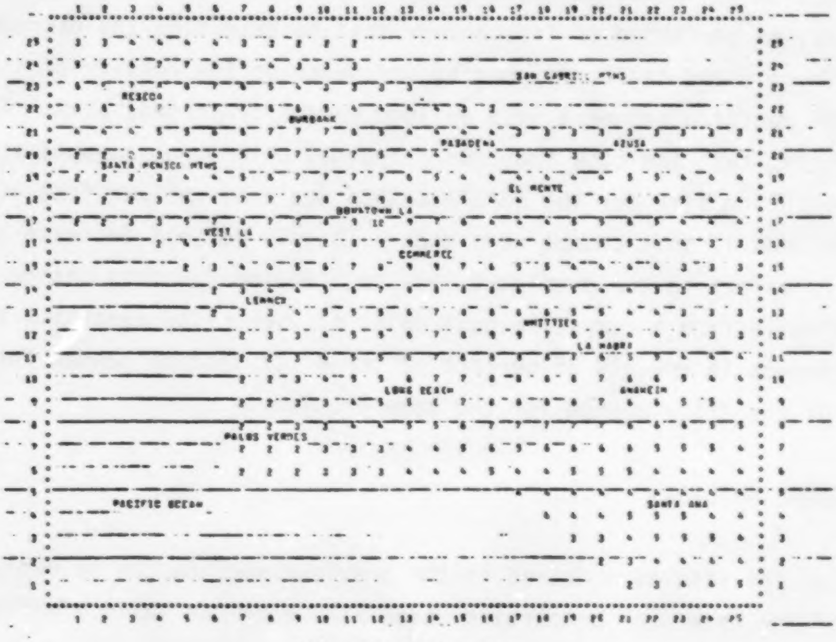
SAN GABRIEL MTNS
RESEDA
BURBANK
PASADENA
AZUSA
SANTA MONICA MTNS
EL MONTE
DOWNTOWN LA
WEST LA
COMMERCE
LENNOX
WHITTIER
LA HABRA
LONG BEACH
ANAHEIM
PALOS VERDES
PACIFIC OCEAN
SANTA ANA

(b) SHASTA Algorithm

FIGURE 29. CARBON MONOXIDE CONCENTRATION PROFILES IN THE LOS ANGELES BASIN AT 1000 PST ON 29 SEPTEMBER 1969

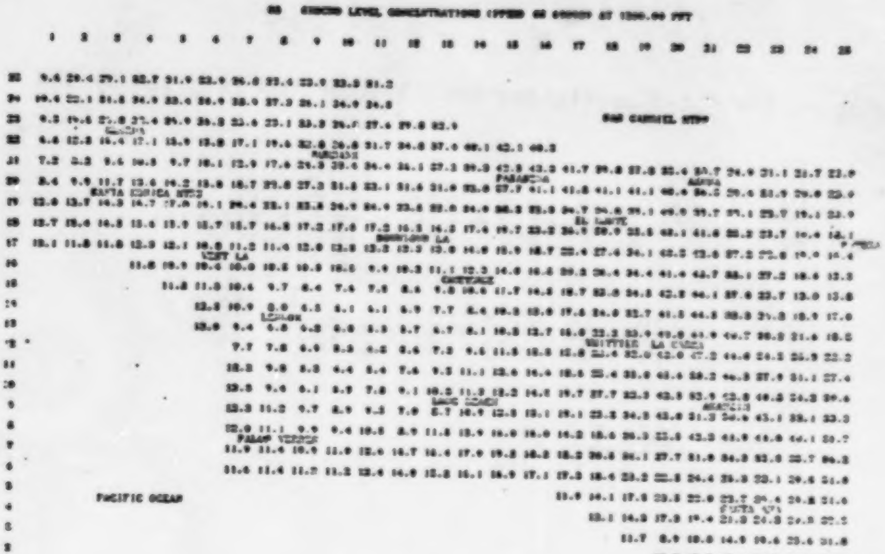
SAN GABRIEL MTNS
PASADENA
EL MONTE
BURBANK
WEST LA
COMMERCE
LENNOX
WHITTIER
LA HABRA
LONG BEACH
ANAHEIM
PALOS VERDES
SANTA ANA
PACIFIC OCEAN

(a) Price Algorithm

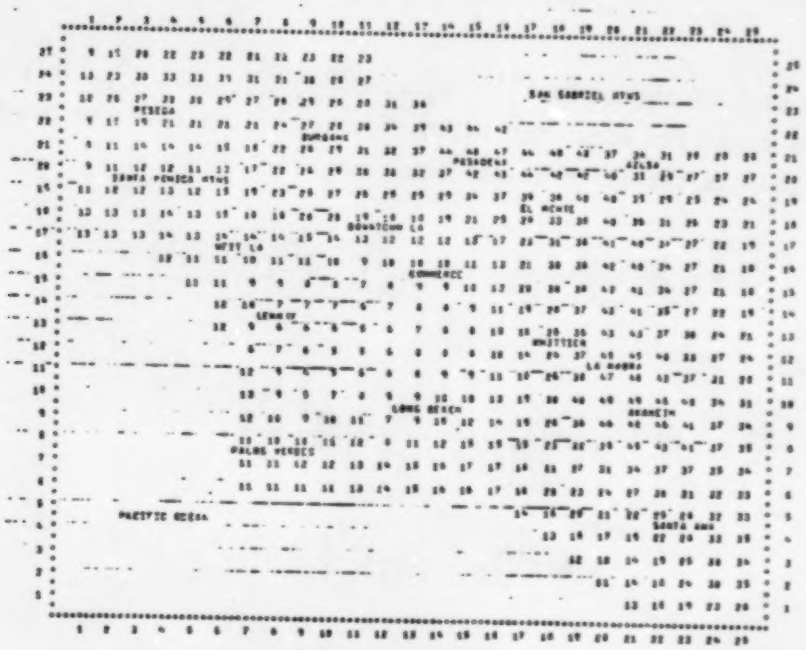
SAN GABRIEL MTNS
RESEDA
BURBANK
PASADENA
AZUSA
SANTA MONICA MTNS
EL MONTE
BURBANK LA
WEST LA
COMMERCE
LENNOX
WHITTIER
LA HABRA
LONG BEACH
ANAHEIM
PALOS VERDES
PACIFIC OCEAN
SANTA ANA

(b) SHASTA Algorithm

FIGURE 30. OZONE CONCENTRATION PROFILES IN THE LOS ANGELES BASIN AT 1200 PST ON 29 SEPTEMBER 1969

$$c_j^{n+1} = \left(1 - \frac{3}{2}\,\varepsilon\right) c_j^n + 2\varepsilon c_{j-1}^n - \frac{1}{2}\,\varepsilon c_{j-2}^n \quad . \tag{40}$$

Correspondingly, the non-flux-limited SHASTA algorithm is given by the expression

$$\begin{aligned} c_j^{n+1} = {} & -\left(\frac{2\varepsilon - 1}{8}\right)^2 c_{j+2}^n + \frac{3}{4}\left[\left(\varepsilon - \frac{5}{12}\right)^2 - \frac{13}{144}\right] c_{j+1}^n \\ & + \left(\frac{29}{32} - \frac{11}{8}\,\varepsilon^2\right) c_j^n + \frac{3}{4}\left[\left(\varepsilon + \frac{5}{12}\right)^2 - \frac{13}{144}\right] c_{j-1}^n \\ & -\left(\frac{2\varepsilon + 1}{8}\right)^2 c_{j-2}^n \quad , \end{aligned} \tag{41}$$

where

$$\varepsilon = \frac{u\Delta t}{\Delta x} \qquad (0 < \varepsilon < 1/2) \quad .$$

By expanding each of the terms c_j^{n+1}, c_{j-1}^n, c_{j-2}^n, c_{j+1}^n, and c_{j+2}^n in a Taylor series expansion about the point c_j^n, one can see that the two formulations approximate the differential equations

$$\frac{\partial c}{\partial t} + u\,\frac{\partial c}{\partial x} = \frac{\Delta t}{2}\,\frac{\partial^2 c}{\partial t^2} + u\Delta x^2\,\frac{\partial c^3}{\partial x^3} + 0\left(\Delta t^2 + \Delta x^3\right) \tag{42}$$

for Price and

$$\begin{aligned} \frac{\partial c}{\partial t} + u\,\frac{\partial c}{\partial x} = {} & u\Delta x^2\left(\frac{1}{24} - \frac{\varepsilon^2}{6}\right)\frac{\partial^3 c}{\partial x^3} + \frac{\Delta t^3}{24}\,\frac{\partial^4 c}{\partial t^4} \\ & - u\Delta x^3\left(\frac{\varepsilon}{48} - \frac{3}{172\varepsilon}\right)\frac{\partial^4 c}{\partial x^4} + 0\left(\Delta x^4 + \Delta t^4\right) \end{aligned} \tag{43}$$

for SHASTA.

If we fix the spatial resolution Δx but decrease the time step Δt (the velocity u is constant), the first term in Eq. (42) decreases; thus, we would expect a reduction in the error produced by the Price method. Figure 5 confirms this expectation. In contrast, the error produced by the SHASTA algorithm increases with each decrease in Δt because when $\varepsilon = 1/2$ the dominant term in the truncation error associated with SHASTA [the first term in Eq. (43)] cancels completely. Therefore, we would expect an optimal value of Δt to correspond with $\varepsilon = 1/2$. As the results show, smaller values of t do not cause this cancellation. (Larger values of Δt cannot be used because they make the scheme unstable.) SHASTA is thus the most accurate when it is most economical.

Since the error associated with the Price algorithm appears to increase as the time step is increased, it appears reasonable to examine the stability limits associated with that method. We begin with the finite difference equation

$$c_j^{n+1} = \left(1 - \frac{3}{2}\varepsilon\right)c_j^n + 2\varepsilon c_{j-1}^n - \frac{\varepsilon}{2}c_{j-2}^n \qquad (44)$$

and express the solution in terms of the Fourier series

$$c(j\Delta x,t) = \sum_{k=1}^{M} \psi_k(t)e^{ikj\Delta x} \qquad (45)$$

where

$i = \sqrt{-1}$,
k = wave number (meters^{-1}),
Δx = grid spacing (meters),
j = grid location,
$\psi_k(t)$ = Fourier coefficient for the k-th term.

Substituting Eq. (45) into Eq. (44), the amplification factor A is given by

$$A = \frac{\psi_k(t + \Delta t)}{\psi_k(t)} = 1 - \frac{3\varepsilon}{2} + 2\varepsilon\, e^{-ik\Delta x} - \frac{\varepsilon}{2} e^{-2ik\Delta x} \quad . \tag{46}$$

For stability, it is necessary that $|A| < 1$. Thus,

$$|A|^2 = \left[(1 - 2\varepsilon + 5\varepsilon^2) + (4\varepsilon - 8\varepsilon^2)\cos\theta + (3\varepsilon^2 - 2\varepsilon)\cos^2\theta\right] \leq 1 \tag{47}$$

where

$\theta = k\Delta x$.

Differentiating the previous expression with respect to $\cos\theta$ shows that it yields a maximum when

$$\cos\theta = \frac{2 - 4\varepsilon}{2 - 3\varepsilon} \tag{48}$$

provided that ε is in the interval (0, 4/7). Resubstituting this result into the original expression yields the maximum value of the modulus as

$$|A|^2_{max} = (1 - 2\varepsilon + 5\varepsilon^2) + \frac{\varepsilon(2 - 4\varepsilon)^2}{(2 - 3\varepsilon)} \quad . \tag{49}$$

For any value of ε greater than zero, this modulus will be larger than one, and the solution will be unstable and will diverge with increasing time. The rate of divergence, however, will be a strong function of the parameter ε and the initial value of the Fourier coefficient $\psi_m(0)$. Table 2 gives typical values of $|A|^2$ and $|A|^{200}$ for different values of ε. In an actual simulation, $|A|^{200}$ would represent the modulus after 100 time steps (one in the x and one in the y direction) which for a four-minute time step is over 6.5 hours.

The reader should keep in mind that a small amount of horizontal diffusion occurs in an actual simulation problem. The net effect of this diffusion is the addition of a certain amount of stability to the problem

Table 2

AMPLIFICATION FACTORS AS A FUNCTION OF STABILITY PARAMETER FOR THE PRICE METHOD

ε	$\|A\|^2$
0	1.00000000E+00
0.02	1.00000412E+00
0.04	1.00003404E+00
0.06	1.000 1868E+00
0.08	1.00029001E+00
0.10	1.00058324E+00
0.12	1.00105366E+00
0.14	1.00173671E+00
0.16	1.00269474E+00
0.18	1.00899452E+00
0.20	1.00571429E+00
0.22	1.00794627E+00
0.24	1.01080000E+00
0.26	1.01440656E+00
0.28	1.01892414E+00
0.30	1.02454545E+00
0.32	1.03150769E+00
0.34	1.04010612E+00
0.36	1.05071304E+00
0.38	1.06380465E+00
0.40	1.08000000E+00
0.42	1.10011892E+00
0.44	1.12527059E+00
0.46	1.15699355E+00
0.48	1.19748471E+00
0.50	1.25000000E+00

TABLE 2 (Concluded)

ε	$\lvert A\rvert^{200}$
0.1	1.06
0.2	1.76
0.3	11.25
0.4	2199.76

so that the solution remains stable over a limited range of ε values; hence, meaningful results can be predicted. In the absence of this stability, meaningful results can still be obtained if small values of ε are chosen during the simulation, so that the errors accrued at the end of the simulation remain small and can be attributed primarily to uncertainties in the model formulation and data inputs.

D. RECOMMENDATIONS AND CONCLUSIONS

In the past, one shortcoming of the SAI airshed simulation program has been the inability to assess the numerical errors associated with the solution of the governing species transport equation. In general, this is an extremely difficult task for all possible combinations of emissions, meteorology, and chemistry that can occur in a natural environment. Consequently, the approach that is frequently used to assess accuracy is to examine several limiting cases and to infer both qualitatively and quantitatively some general characteristics that one could expect in a more complex situation.

During the past two years, the EPA has supported our investigation of numerical methods appropriate for the solution of the species transport equation. In the initial phase of this study, the SHASTA, Egan-Mahoney, and Galerkin algorithms were identified as numerical integration methods offering greater accuracy than the existing Price algorithm. In addition, both the SHASTA and Egan-Mahoney techniques have shown promise of being as computationally efficient as the Price method. The following conclusions can be drawn on the basis of our examination of the SHASTA and Egan-Mahoney algorithms:

> Of all the variants of the SHASTA technique, the non-flux-limited, non-mass-conservative formulation appears to be the most accurate, as well as the most computationally efficient.

> The non-flux-limited, non-mass-conservative SHASTA algorithm is substantially more accurate than the Price integration method. In the two-dimensional reactive and nonreactive analyses, the predictions of the SHASTA algorithm were superior to those of the Price algorithm at both peak and gradient locations for all species observed.

> The SHASTA algorithm, unlike the Price method, is stable for all values of the parameter ε less than 1/2. Hence, simulations over long time intervals do not exhibit the instability observed when the Price algorithm is used.

> Although more accurate, the Egan-Mahoney method requires considerably more computational time and substantially more computer storage than the SHASTA method. For a nonreactive species, such as CO alone, this technique could most probably be optimized to produce superior results at reasonable computing costs for a three-dimensional problem. In cases involving many species, however, the computational costs and storage requirements for the necessary generating moments would be exorbitant.

> In the future, efforts should be devoted to optimizing the computer codes and simulation scheme so as to increase program efficiency and to reduce execution time. Searching for an optimal time step, putting the kinetic mechanism into an individual step, and computing the reaction rates of every other time interval are some of the possible ways in which this objective could be achieved. In addition efforts should be made to keep abreast of the latest developments in the literature concerning integration

of partial differential equations and changes in computer technology to permit implementation of methods that are currently unattractive with the existing technology.

III SURFACE SINKS

by James P. Killus and Terry N. Jerskey

A. OVERVIEW

Pollutant gases in the lower troposphere are removed from the atmosphere by chemical reaction, rainout or washout, adsorption, condensation, or reaction on suspended particulates, and deposition on surfaces. In this chapter we focus on surface deposition processes, or surface sinks. Our purpose is to determine which sinks of photochemical pollutants are important, and to develop means of treating them in urban air quality models. We begin by discussing the measure most often used in studying the magnitudes of surface sinks, the deposition velocity. We then review measurements of deposition velocities for pollutants of interest, estimate the importance of surface sinks for various species, and incorporate the important sinks in the SAI Urban Airshed Model. The effects on model predictions of sinks and of averaging surface uptake rates over grid squares are analyzed.

We wish to point out that surface sinks are complex and infrequently studied. In many cases we were forced to estimate surface uptake rates, which produces a considerable uncertainty in our results. This uncertainty can be reduced only by further measurements.

B. THE DEPOSITION VELOCITY

Surface removal of pollutants is described mathematically through the ground-level boundary condition. The flux (F) of a gas to a surface can be represented by the expression

$$F = v_d\, c(0) \quad , \qquad (50)$$

where $c(0)$ is the ground-level concentration, and v_d has the units of velocity and is commonly referred to as the deposition velocity. Although in this equation the deposition velocity appears as a proportionality constant, in reality it is not a constant. For example, Hill (1971) observed that the adsorption of ozone by leaves does not vary linearly with concentration at high concentration levels. In general, however, the regions of linearity are quite broad.

Bolin et al. (1974) noted that for a perfect sink of a particular gas, in which all molecules of that gas reaching the surface are absorbed, the ground-level concentration is zero and the deposition velocity is infinite. In such a case the flux is diffusion-limited:

$$F = K \frac{dc}{dz} \quad , \qquad (51)$$

where K is the diffusion coefficient. Even if the ground-level concentration is nonzero, the flux is diffusion-limited when the deposition velocity is high. However, few sinks are perfect. For most surfaces, removal of gases from the atmosphere occurs by one of the following processes:

- The formation of a solution on the surface.
- The chemical reaction of the gas with the surface.
- The adhesion of the gas to the surface.
- The uptake of the gas by plants, which involves one or more of the above processes.

In the first process the gas will be present above the surface in a concentration such that the gas in the solution is in equilibrium with the gas in the atmosphere. When chemical reaction occurs, the rate may be slower than the rate of transfer of the gas to the surface, resulting in a nonzero concentration of the gas at the surface. When adhesion controls the rate of surface uptake, the ground-level concentration depends upon the efficiency with which gas molecules adhere to the surface.

Because few sinks are perfect, specifying the proper ground-level boundary condition is often difficult. This difficulty is compounded by the virtual impossibility of directly measuring a ground-level concentration. Therefore, the formulation of the deposition velocity is often extended heuristically to a level z_0 at which the concentration is measurable. Then the deposition velocity is defined:

$$v_d \equiv \frac{F}{c(z_0)} \quad . \tag{52}$$

and it represents a bulk transfer coefficient between the level z_0 and the ground. Basically two experimental methods are used to determine the deposition velocity, the flux and the gradient methods. The flux method, commonly used in the laboratory, is based on the determination of the surface flux below an atmosphere of known composition. The flux is determined indirectly. For example, Hill (1971) determined the influx required to keep a constant pollutant concentration over an alfalfa canopy in a closed reactor, while Heichel (1973) measured the amount of CO removed from a stream of gas of known composition after it was passed over a soil bed. Owers and Powell (1974) released SO_2 labeled with the isotope ^{35}S and determined the surface flux by measuring the $^{35}SO_2$ that had accumulated. $v_d(z_0)$ was then determined from this flux and a measurement of $\left[^{35}SO_2\right]$ at z_0.

The gradient method is better suited to in situ determination of v_d. It requires measurements of pollutant concentration at two or more elevations. These concentrations, combined with a similarity hypothesis (and wind and temperature measurements as required by the hypothesis), are used to estimate the flux of pollutant from a given height (z_0) to the surface. The deposition velocity $v_d(z_0)$ is then calculated from Eq. (52) using the estimated flux (F) and concentration at z_0. For example, Dannevik et al. (1974) measured wind, temperature, and SO_2 concentrations at one, three, and seven meters above ground level in order to calculate SO_2 deposition to a variety of agricultural surfaces.

These and other measurements of deposition velocities are discussed at length in Section D of this chapter, but first we discuss some practical and theoretical limitations to the concept of the deposition velocity.

Because of the complexity of gas transfer processes, no theoretical expressions have been derived for the mass transfer coefficients of gases removed from the atmosphere by surfaces. The only readily available information on the rate of transfer of gases to surfaces is provided by measurements of surface fluxes and deposition velocities. These measurements have been made for a variety of surfaces under different meteorological conditions, but unfortunately the magnitude of the deposition velocity depends upon numerous variables that change with weather conditions and surface characteristics. For sinks involving only surface absorption, the deposition velocity depends upon both surface composition and effective surface area. For sinks affected by diffusion rates, the effects of the bulk diffusivity, which depends upon wind speed, surface roughness, and lapse rate, must be included. Consequently, the extrapolation of measured deposition velocities to other weather and surface conditions requires a number of assumptions.

The complexity of the physical process underlying the concept of a deposition velocity is illustrated by a model of the process of transfer of gases to a surface presented by Sehmel et al. (1973). In this model the transfer of gases from the atmosphere to a surface is considered to occur in three stages:

> The gases are transported to a layer just above the surface (or the vegetation canopy) by turbulent diffusion and advection.
> The gases are transported through the layer just above the surface by transport processes that are influenced by the shape of the surface and the vegetation.
> The gases interact by adsorption or reaction with the surface. In this stage the chemical interaction of the gases and the vegetation is very important.

This breakdown illustrates that the magnitude of surface flux of a pollutant, or the sink strength, depends on both chemical and meteorological variables.

Clearly, the first stage depends only on meteorological variables and the last stage depends only on the pollutant and the surface characteristics. The first stage of the transfer process could be adequately treated in air quality models by existing theories for the transport of mass through the planetary boundary layer. The last stage could conceivably be treated if laboratory data were available on the interaction of pollutants with the various surfaces. Alternatively, models now only in very early stages of development could be used to simulate the interaction of gases with surfaces (see Section C). There is far less promise of being able to adequately treat the second stage of the transfer process, which depends on meteorological variables, the surface, and the pollutant being transferred.

Mathematically, the conceptual model above has been treated in terms of the resistance to transfer of matter, in analogy with the treatment of electrical circuits (Bolin et al., 1974; Chamberlain, 1966). The resistance for transfer of matter from the free atmosphere (at a height z_1) to a natural surface may be considered to be the sum of three resistances:

(1) The resistance to transfer down to the level z_2 (the level at which surface-induced turbulence becomes important), which is equal to the resistance to momentum transfer to the surface.

(2) The resistance to the transfer of matter from the level z_2 to the surface in the case where the surface is a perfect sink.

(3) The surface resistance, which expresses the accommodation of the compound on the surface. For a perfect sink the surface resistance approaches zero.

To understand the concept of a resistance to mass transfer, consider that the transport velocity between two heights z_i and z_j is defined by

$$v(z_i, z_j) = \frac{F}{c(z_i) - c(z_j)} \quad , \tag{53}$$

where F is the flux and c(z) is the concentration of the pollutant of interest at height z above the surface. If the flux of the pollutant in each stage of transfer is assumed to be constant, then we can write

$$\begin{aligned} F &= v_a\left[c(z_1) - c(z_2)\right], \\ F &= v_{a,s}\left[c(z_2) - c(z_3)\right], \\ F &= v_s\left[c(z_3) - c(z_s)\right], \end{aligned} \tag{54}$$

where v_a is the transport velocity through the layer in which atmospheric diffusion affects the transport rate, $v_{a,s}$ is the transport velocity through the layer in which both the surface and atmospheric diffusion affect the transport rate, and v_s is the transport velocity that depends only on surface characteristics. In Eq. (54), $c(z_3)$ and $c(z_s)$ are the concentrations of the pollutant directly above the surface and on the surface, respectively. When a reaction occurs on the surface to remove the pollutant, $c(z_s) = 0$. If we define the resistance, R, to be the reciprocal of the transport velocity, then the difference between the concentrations at z_1 and z_s is

$$c(z_1) - c(z_s) = F(R_a + R_{a,s} + R_s) \quad . \tag{55}$$

The deposition velocity, v_d, is defined by

$$F = v_d c(z_1) = c(z_1)/R_d \quad , \tag{56}$$

and if $c(z_1) \gg c(z_s)$ then

$$R_d = R_a + R_{a,s} + R_s \quad . \tag{57}$$

The objective of expressing the deposition resistance in this way is to obtain from the measured deposition velocities empirical estimates of the strengths of various surfaces for removing pollutants. As noted above, estimates of R_s can be obtained empirically. R_a can be approximated from existing theories for turbulent transfer through the atmospheric boundary layer. If some expression could be derived for $R_{a,s}$, then the empirically obtained deposition velocities could be used to calculate the flux of pollutants to surfaces under any set of meteorological conditions. However, no methodology has been developed for calculating $R_{a,s}$. In the remainder of this analysis we include $R_{a,s}$ as part of the atmospheric transport, so that the total diffusional resistance becomes

$$R_m = R_a + R_{a,s} \quad , \tag{58}$$

and

$$R_d = R_m + R_s \quad . \tag{59}$$

In order to estimate R_s from the empirically determined R_d it is first necessary to decide how R_m will be treated theoretically. Chamberlain (1966) assumed that mass and momentum are transferred through the turbulent boundary layer in the same manner and at the same rate. Momentum resistance within the friction layer is given by the momentum divided by the shearing stress (Chamberlain, 1966):

$$R_m\ (\text{momentum}) = u(z)/u_*^2 \quad , \tag{60}$$

since $u_*^2 = \tau/\rho$ by definition. In Eq. (60), $u(z)$ is the wind speed at height z, τ represents the shearing stress, and ρ is the density of air.

Attempts have been made to correct Eq. (60) for the difference between the rate of diffusion of momentum and the rate of diffusion of mass through the planetary boundary layer. Owen and Thomson (1963) accounted for the difference between momentum and mass transfer by adding an empirically determined correction term to the resistance to momentum transfer; they expressed the diffusional resistance as

$$R_m = R_m(\text{momentum}) + R_b \quad , \tag{61}$$

where

$$R_b = B^{-1}u_*^{-1} \quad , \tag{62}$$

$$B^{-1} = 2.2u_*^{-1/3} \quad . \tag{63}$$

We have included R_b in our calculations. In cases where the atmospheric resistance is large, we found R_b to be typically 30 percent of R_m. Garland et al. (1974) found that R_b was typically 40 percent of R_m.

The form of Eq. (59) provides a means for determining the strength of pollutant uptake by a surface if deposition fluxes are measured for a range of meteorological variables. As the rate of turbulent mixing becomes high, the transport to the surface is rapid, the resistance for transport through the boundary layer approaches zero, and the resistance for deposition is limited by the surface resistance. Unfortunately, very limited data are available to apply even this simplified scheme for determining surface uptake rates. Very few studies of pollutant uptake by surfaces have considered either a wide range of meteorological variables or surface types under controlled conditions. Perhaps the most comprehensive study was reported by Hill (1971), who measured pollutant uptake as a function of light intensity, wind speed, canopy height, and pollutant concentration for eight pollutants, including CO, NO, NO_2, O_3, and SO_2. Plant pollutant uptake rates were measured in chambers that were designed specifically for gaseous exchange studies. In all of these measurements alfalfa canopies of various heights were the only vegetation.

Hill (1971) observed that ozone uptake rates over a 40.6 cm (16 inch) alfalfa canopy increased rapidly with increasing wind speed at wind speeds below 3.2 kph (2 mph). Above a wind speed of 4.8 kph (3 mph) the ozone uptake rate was nearly independent of wind speed. These results suggest that turbulent transport increases with wind speed, and that the rate of diffusion to the surface at wind speeds above 4 kph is sufficiently rapid that the surface uptake rate is limited by the surface resistance. Assuming that the surface resistance, R_s, is equivalent to the deposition resistance, R_d, measured at wind speeds above 4.8 kph, we calculated the surface resistance of a 40.6 cm alfalfa canopy from data obtained by Hill (1971) at wind speeds of 6.4 to 8 kph. These results are listed in Table 3. The surface resistance in parenthesis for ozone was calculated from data for wind speeds of 4.8 kph. Other data presented by Hill indicate that at wind speeds above 4.8 kph the surface flux becomes constant at between 60 and 70 $\mu l\ min^{-1} m^{-2}$ at ozone concentrations of 0.05 ppm. However, the data from which the surface resistance of 0.6 sec cm^{-1} for ozone was calculated indicate a flux of only 50 $\mu l\ min^{-1} m^{-2}$ at the same concentration and wind speeds of 6.4 to 8 kph.

TABLE 3. SURFACE RESISTANCE OF AN ALFALFA CANOPY

Pollutant	Surface Resistance (sec cm^{-1})
NO	10
NO_2	0.5
O_3	0.6(0.4)
SO_2	0.3

As a test of the validity of our approach for calculating the surface resistance, we calculated the deposition resistance, R_d, for the conditions used by Hill (1971). The diffusional transport resistance was calculated for a given wind speed from Eqs. (60) through (63) and the following expression for the friction velocity (Myrup and Ranzieri, 1975):

$$u_* = 0.35\, u(z_a) \Big/ \left[\ln(z_a/z_r) + (2/L)(z_a - z_r) \right] \quad , (64)$$

where z_a denotes the anemometric height, z_r denotes the surface roughness length scale, and L is the Monin-Obukhov length scale (a measure of the atmospheric stability).

To calculate the friction velocity from Eq. (64) one must assume values for z_r and L since these are not given by Hill. Typically, the roughness length scale is one-tenth of the maximum height of structures or vegetation in the area of interest (Lettau, 1970). Since the alfalfa canopy was 40.6 cm high, the roughness length was assumed to be 4.06 cm. No information on the stability of the air in the chamber is provided by Hill (1971), but he did report that the light intensity in the chamber was high and the wind speed was less than 4.8 kph ($\sim$ 1.3 m sec^{-1}). According to Table 4, these conditions approximate Pasquill Stability Class A. According to the stability

TABLE 4. KEY TO PASQUILL STABILITY CATEGORIES

Surface Wind Speed (at 10 m), (m sec^{-1})	Daytime Incoming Solar Radiation			Nighttime Cloud Cover	
	Strong	Moderate	Slight	Thinly Overcast or ≥4/8 Low Cloud	<3/8 Cloud
<2	A	A-B	B		
2-3	A-B	B	C	E	F
3-5	B	B-C	C	D	E
5-6	C	C-D	D	D	D
>6	C	D	D	D	D

The neutral class, D, should be assumed for overcast conditions during day or night.

Source: Turner (1969).

classification scheme proposed by Golder (1972), at a surface roughness height of 4 cm (∿ 1.6 inches), the reciprocal of the Monin-Obukhov length is less than $-0.11\ m^{-1}$ ($\sim -2.8 \times 10^{-3} in^{-1}$) (see Figure 31). The friction velocity can then be approximated by

$$u_* = 0.154\ u(z_a) \quad . \qquad (65)$$

The results of these calculations are shown in Figures 32, 33, and 34 for surface resistances of 0.3, 0.4, and 0.6 sec cm^{-1}, respectively. In neither case do the calculated results compare well with the data when $u_* = 0.15\ u$. Because the friction velocity is very sensitive to the surface roughness, we recalculated the surface uptake rate with $u_* = 0.35\ u$ and $u_* = 0.28\ u$ (the former corresponds to a surface roughness of about 23 cm, or 9 inches). At these higher friction velocities the calculated flux approximates the data much better.

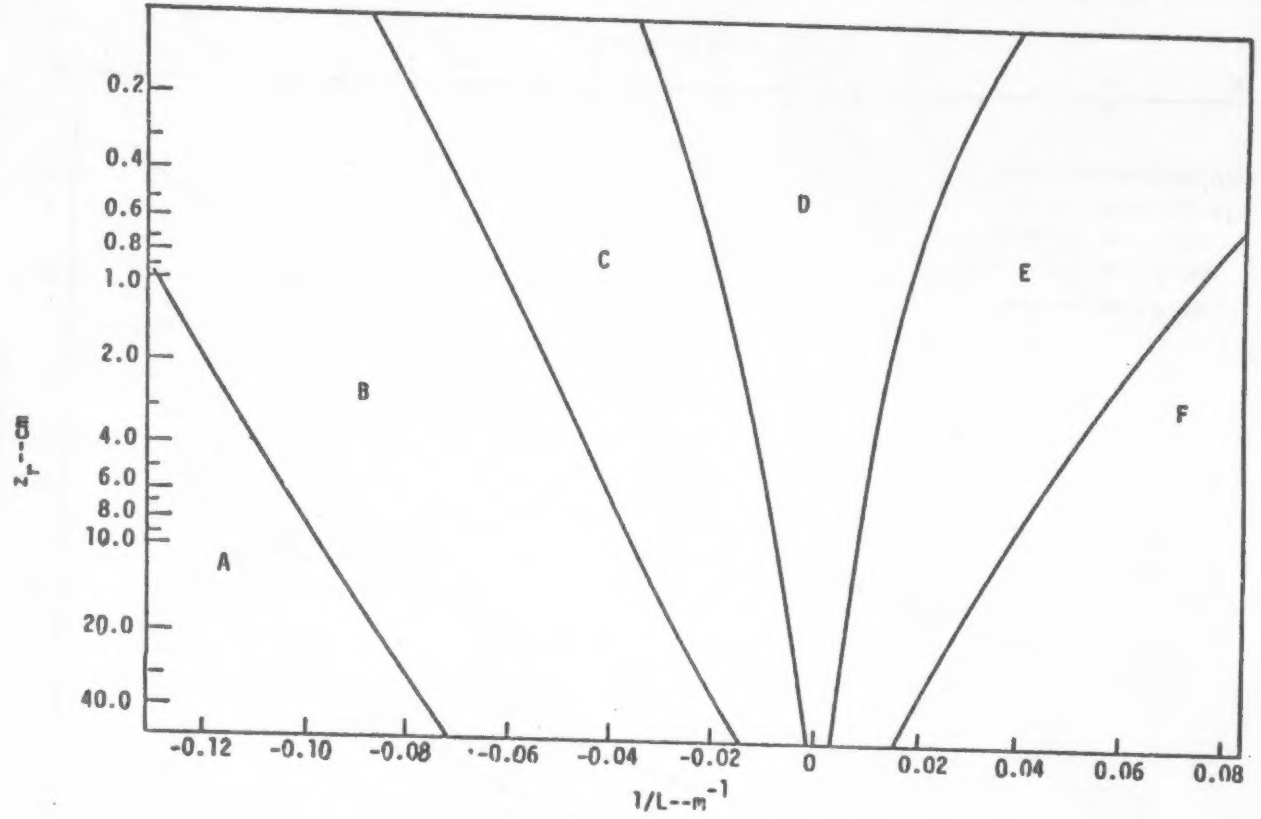

Source: Golder (1972).

FIGURE 31. 1/L AS A FUNCTION OF PASQUILL CLASSES AND z_r

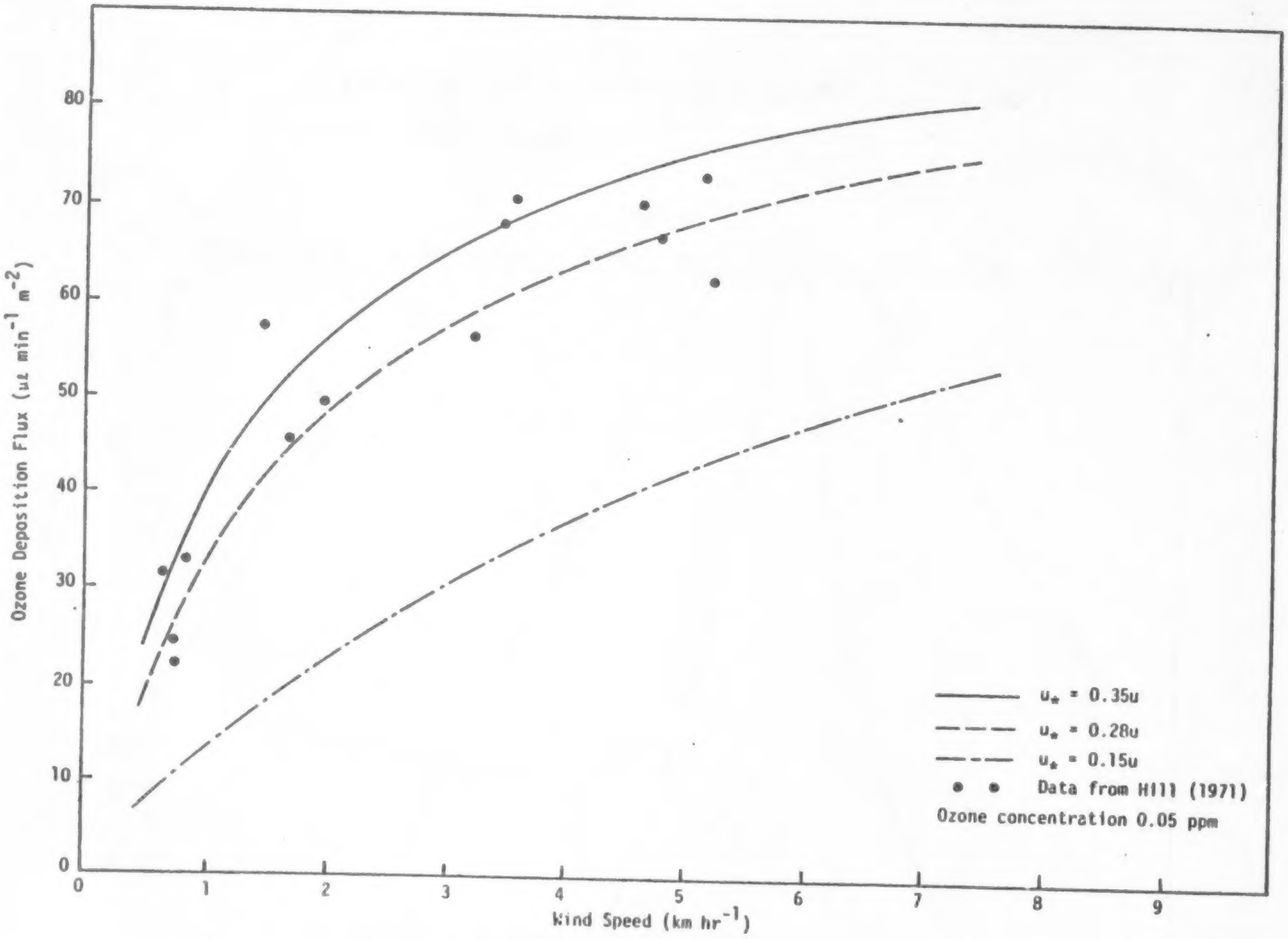

FIGURE 32. OZONE FLUXES MEASURED AND CALCULATED ASSUMING A SURFACE RESISTANCE OF 0.3 SEC/CM

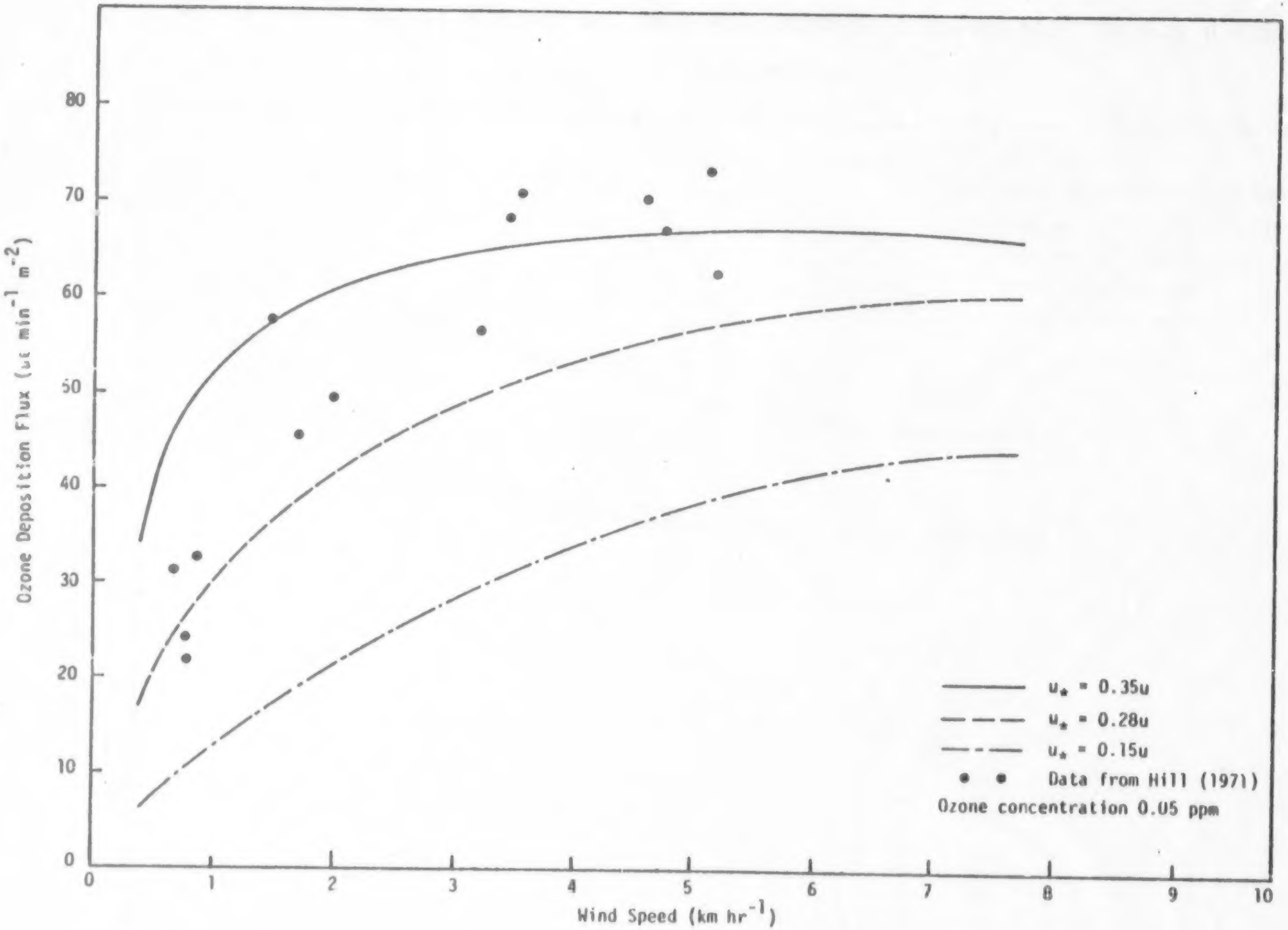

FIGURE 33. OZONE FLUXES MEASURED AND CALCULATED ASSUMING A SURFACE RESISTANCE OF 0.4 SEC/CM

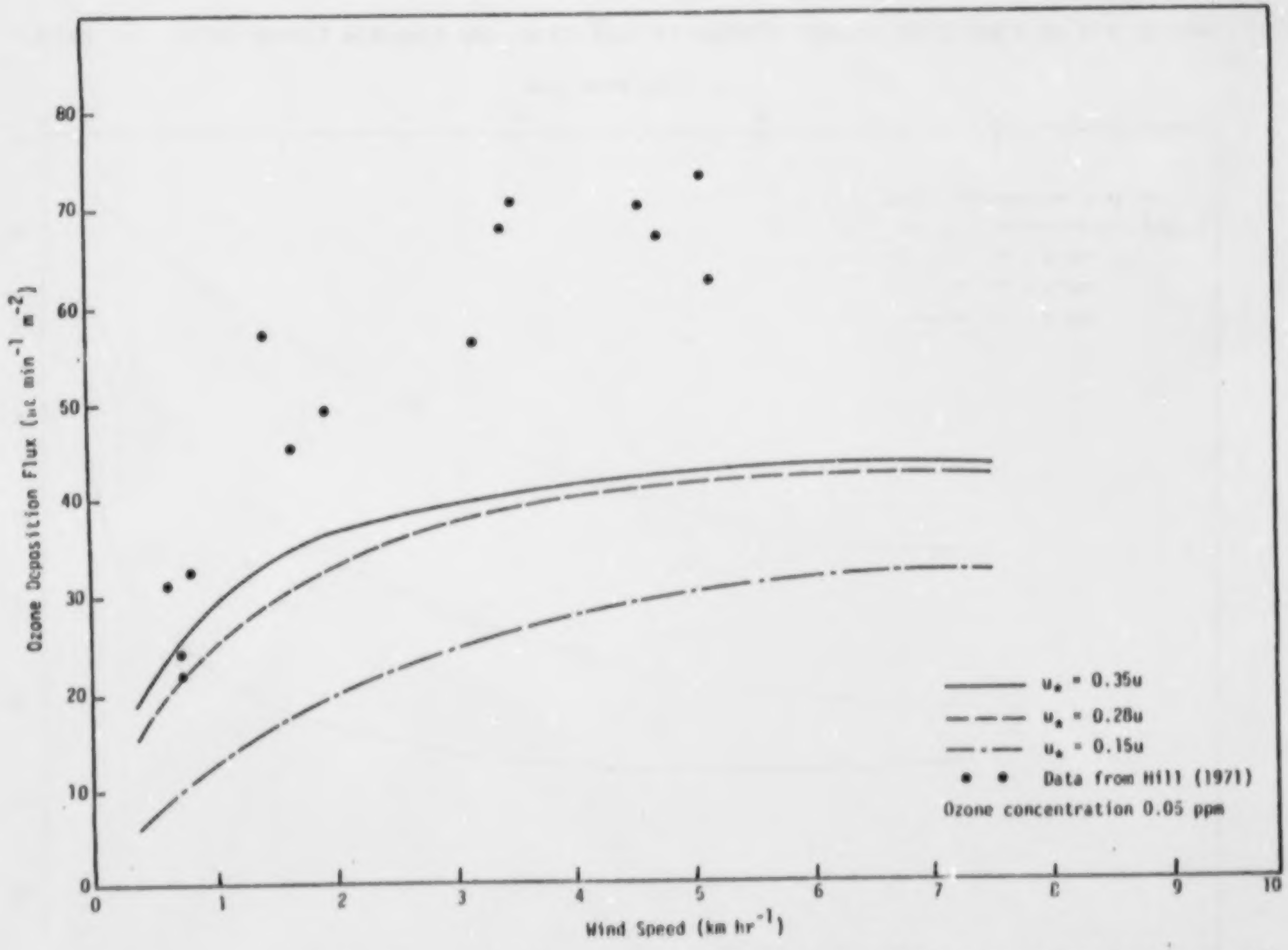

FIGURE 34. OZONE FLUXES MEASURED AND CALCULATED ASSUMING A SURFACE RESISTANCE OF 0.6 SEC/CM

If we assume that the measurements made by Hill at 4.8 kph and at between 6.4 and 8 kph are not limited by surface uptake (that is, the turbulence levels are not sufficiently high to make this assumption) then it may be that the actual surface resistance is less than 0.4 sec cm^{-1}. For this case, the lower friction velocity again gives a poor fit to the data, but the higher friction velocities fit the data much better than when the surface resistance was assumed to be as high as 0.4 sec cm^{-1}. In order for the surface resistance to be as low as 0.3 sec cm^{-1}, the surface flux must be 100 μl $min^{-1}m^{-2}$ at an ozone concentration of 0.05 ppm when the resistance to transport to the surface is negligible. Considering that Hill (1971) measured surface uptake rates greater than 70 μl $min^{-1}m^{-2}$ at wind speeds below 4.8 kph, it is conceivable that the surface resistance may be as low as 0.30 sec cm^{-1}.

In summary, our analysis of Hill's data indicates that the surface resistance for ozone uptake by an alfalfa canopy is probably in the range of 0.3 sec cm^{-1} to 0.6 sec cm^{-1}. The uncertainty is attributable in part to the scatter in Hill's data and in part to the uncertainty of both the atmospheric stability in the chamber and the surface roughness. Hill's data for other pollutants are insufficient to do a similar analysis, but there is no reason to expect less scatter in data for these pollutants.

C. OTHER MODELS FOR TREATING SURFACE SINKS

Any methodology for treating surface sinks in numerical models must take into account the three stages of transfer as described above. The deposition velocity is a mass transfer coefficient, and it depends upon meteorological conditions, surface conditions, and pollutant type. As noted above, the first stage of transfer does not depend on the surface characteristics and only weakly depends on the pollutant type. The other two stages do depend on both the pollutant type and the surface characteristics.

We are not aware of any attempt to model the second stage of transfer, although there has been an attempt to model the process of pollutant uptake by leaves. Bennett, Hill, and Gates (1973) patterned a model after an electrical analogue simulator, designing it to emphasize the effects of pollutant and leaf properties on the process of pollutant uptake by plants. The model development considers the relative significance to pollutant uptake of factors affecting gas transfer, sorption of pollutants by leaf surfaces, and pollutant solubility and fate. The model provides a relationship between the internal pollutant solute concentration and external concentration, leaf and boundary layer diffusion resistance, surface sorption, and pollutant solubility. A model of this type could be used if an inventory of surface vegetation data was also available to determine the sink strength.

D. MEASUREMENTS OF DEPOSITION VELOCITIES

Only limited data are available on the surface uptake rates of pollutants. Here we present a review of surface flux measurements for the pollutants SO_2, O_3, NO, NO_2, hydrocarbons, and CO. A more extensive discussion is presented in Rasmussen, Taheri, and Kabel (1974).

1. Surface Deposition of SO_2

Using the gradient method, Whelpdale and Shaw (1974) estimated deposition velocities for SO_2. They made concentration measurements at 8 and 2 meters and used a bulk transfer coefficient to approximate the surface flux. The deposition velocity at 2 m determined by this method was defined as:

$$v_d = C_{SO_2} \overline{U}_{10} \frac{\Delta\left[SO_2\right]_0^{10}}{\Delta\left[SO_2\right]_0^{2}} \quad , \qquad (66)$$

where C_{SO_2} is the bulk transfer coefficient for SO_2, $\overline{U}_{10}$ is the mean wind speed at 10 m, and $\Delta\left[SO_2\right]_a^b$ represents the difference between SO_2 concentrations at heights b and a. The bulk transfer coefficient for SO_2 was assumed to be equal to the bulk transfer coefficient for water vapor. The SO_2 concentrations at 10 meters and at the ground level were extrapolated from the measurements at 8 m and 2 m. The resulting deposition velocities over grass, snow and water are listed in Table 5, along with calculated SO_2 fluxes. The stability classes are based on a bulk Richardson number (Ri):

Lapse = $Ri < -.02$
Neutral = $-.02 < Ri < .02$
Stable = $Ri > .02$

TABLE 5. AVERAGE VALUES OF FLUX AND DEPOSITION VELOCITY FOR THE THREE SURFACES UNDER THREE STABILITY CLASSES

Surface	Stability	No. of Cases	SO_2 Flux ($g\ m^{-2}\ s^{-1}$)	Deposition Velocity* ($cm\ s^{-1}$)
Grass	Lapse	10	0.84	2.4
	Neutral	3	0.29	2.6
	Stable	2	0.015	0.5
Snow	Lapse	1	0.17	1.6
	Neutral	3	0.051	0.52
	Stable	8	0.005	0.05
Water	Lapse	7	0.59	4.0
	Neutral	7	0.27	2.2
	Stable	4	0.05	0.16

---

*at 2 m

Source: Whelpdale and Shaw (1974)

Shepherd (1974) also used a gradient method, though his approach was more sophisticated than that of Whelpdale and Shaw. Both wind velocity and SO_2 concentration measurements were made at four heights between 2 and 0.25 m. Surface fluxes were calculated from similarity theory as a function of computed friction velocities (u_*), stability (Monin-Obukhov) lengths (L), and concentration differences (Δc). Deposition velocities at 0.2 m were then calculated and are presented in Table 6 along with atmospheric and surface characteristics. In an attempt to separate sink efficiency from the efficiency of atmospheric transport, Shepherd calculated a diffusion velocity (v^*) that represents the theoretical deposition velocity over a perfect sink. With the exception of sequence J it can be seen, from Table 6, that surface effects are rate limiting ($v_d < v^*$). The results of case J were thought to be the least accurate of those presented.

TABLE 6. DEPOSITION OF SO_2 ONTO GRASS

	Value of Datum in Sequence				
Datum	E	F	J	K	I
No. of profiles	2	4	2	6	5
Date (all 1972)	29 June	5 July	12 July	18 July	18 Oct.
Temp. (°C)	17	16	21	24	10
Relative humidity (%)	50	60	60	50	70
Cloud (eighths)	3 Cu, 6 Ci	5 Cu, 4 Ci	4 Cu	1 Cu	8 Sc
Wind speed (m s^{-1}) at 2 m	2.8	3.3	2.6	5.0	4.0
SO_2 max. ($\mu g\ m^{-3}$) at 2 m	135	50	115	110	135
SO_2 min. ($\mu g\ m^{-3}$) at 2 m	30	15	55	55	90
Frict. vel. u_* (m s^{-1})	0.24	0.25	0.23	0.43	0.32
Depn. vel. v_d(m s^{-1})†	3.9 ± 2.3	7.5 ± 1.9	15.1 ± 7.0	8.7 ± 1.6	2.7 ± 1.0
Diff. vel. v^* (m s^{-1})†	19	20	16	34	28
Stability length L (m)	21	41	6.5	39	-
Height above datum and state of grass	200 mm damp	200 mm dry	50 mm dry	80 mm dry, recently mown	120 mm dry
State of soil	Damp	Wet	Sl. damp	Dry	Damp

Source: Shepherd (1974)

†Referred to lowest level possible, 0.2 meters.

It is worthy of note that although the deposition velocity is always less than the diffusion velocity, this difference is less than an order of magnitude. The test surface, grass, is a sufficiently efficient sink that it is influenced by atmospheric diffusion rates.

Results obtained over water (salinity about 20 parts per thousand; pH = 7.5) indicate that it is an almost perfect sink. Shepherd found deposition velocities over water to be proportional to the strength of atmospheric diffusion, as indicated by the friction velocity. He presented the following correlation for deposition onto water:

$$v_d\ (.2\text{m}) = (.024 \pm .004)u_* \quad . \tag{67}$$

A gradient technique incorporating K-theory to represent turbulent transport was used by Garland et al. (1974). By using regression analysis to fit smooth curves for wind speed, SO_2 concentration, and potential temperature, they estimated concentration gradients and eddy diffusivities (K_M) at 1 meter heights (Table 7). In this way, the surface flux (K_M dc/dz) for SO_2 was determined. After comparing deposition velocities with diffusion velocities, Garland et al. concluded that grassland was not a perfect sink for SO_2.

In another study, Dannevik et al. (1974) observed deposition velocities that were considerably higher than those previously measured for vegetation (Table 7). To explain this disparity, they concluded that their grass samples had larger leaf areas than those used previously and that the increased uptake was caused by this increase in effective surface area.

Table 8 summarizes the dry deposition fluxes and net bulk deposition velocities obtained by Dannevik et al. (1974). The fluxes were computed for the 1.0 meter level, and the deposition velocities were computed using the SO_2 concentration at the lowest measurement point in the profile.

TABLE 7. MEASUREMENTS OF THE DEPOSITION VELOCITY OF SO_2 ON SHORT GRASSES AT CARDINGTON, ENGLAND

Date	Time	Concentration $\chi(1)$ ($\mu g\ m^{-3}$)	z_0 (m)	u_* (ms^{-1})	$u(1)$ (ms^{-1})	Ri	K_m ($m^2 s^{-1}$)	v_g (ms^{-1})	State of grass	Weather
7 March 1972	11.09-11.49	90	0·005	0·11	1·50	−0·17	0·051	0·0014	Wet	Thinning fog, 6°C
	12.10-13.17	63·5	0·003	0·07	0·94.	−0·72	0·043	0·0026	Wet	Sunny 10°C
	13.38-14.26	34	0·009	0·154	1·94	−0.11	0·066	0·0039	Drying	Sunny 13·3°C
13 April 1972	13.22-14.22	36	0·004	0·111	1·66	−0·13	0·052	0·0024	Dry	Overcast 12·7°C
	15.00-15.45	77	0·003	0·123	1·67	−0·07	0·048	0·0023	Dry	4/8 cloud 12·8°C
	16.07-17.07	30·4	0·005	0·156	2·37	0·01	0·051	0·005	Dry	2/8 cloud 13·0°C
25 April 1972	16.12-17.32	16·6	0·009	0·314	4·05	−0·02	0·112	0·0145	Dry	2/8 cloud 11·4°C
	22.23-00.23	9·4	0·003	0·038	0·67	0·06	0·010	0·0027	Slight dew	
26 April 1972	01:13-03.13	8·8	0·003	0·038	0·67	0·06	0·010	0·002	Slight dew	
6 June 1972	15.15-16.15	3·3	0·003	0·282	4·70	−0·01	0·092	0·0120	Dry	17·7°C
7 June 1972	10.02-11.02	7·8	0·004	0·331	5·23	0·00	0·116	0·0206	Dry	7/8 cloud 14°C
22 June 1972	13.35-14:35	61·3	0·0003	0·253	5·76	−0·01	0·076	0·0029	Dry	7/8 cloud 14·9°C
	15.05-16.05	60·5	0·0004	0·235	5·19	−0·02	0·073	0·0010	Dry	6/8 cloud 15·9°C
23 June 1972	10.40-11.40	19	0·0004	0·286	6·24	−0·02	0·090	0·0035	Dry	7/8 cloud 14·7°C

Source: Garland et al. (1974).

TABLE 8. ESTIMATED SURFACE FLUXES AND NET BULK DEPOSITION VELOCITIES

Vegetation	Surface Flux (ppm cm sec^{-1})	Net Deposition Velocity (cm sec^{-1})
10 cm grass	0.46	5.9
70 cm field weed	0.23	26.1
30 cm soybean	0.06	11.7
30 cm field weed	0.35	7.1

Source: Dannevik et al. (1974)

Owers and Powell (1974) released $^{35}SO_2$ in a rural grassland environment and determined the surface fluxes from tracer studies of the surface concentration and exposure time. They reported surface and atmospheric diffusion resistances as well as deposition velocities (see Table 9). Resistances could not be calculated for Experiment 4, although water may be assumed to be a perfect sink and its lower deposition velocities attributed to reduced surface roughness.

While all of the tabular results are for grassland, the presence of a hedge in Experiment 3 allowed estimates of the hedge's removal efficiency. A mean deposition velocity of 4.0 cm sec^{-1} indicated a higher sink efficiency for SO_2 removal by hedge than by grassland, which corroborates the findings of Dannevik et al.

TABLE 9. SUMMARY OF DEPOSITION VELOCITY MEASUREMENTS[*] (AND CALCULATED RESISTANCES)

Measurement or Observation	Value in Experiment			
	1 and 2	3	4 (grassland)	4 (water)
Pasquill Stability Class	B	B	D	D
Weather	Sunny	Dull-no rain	Dull-no rain	Dull-no rain
Wind speed (m $\sec^{-1}$)	2.6	5.2	1.8	1.8
Relative humidity (%)	65	77	80	80
v_d (cm $\sec^{-1}$)	0.7 ± 0.1	2.6 ± 0.3	0.7 ± 0.1	0.5 ± 0.1
R_m (sec cm^{-1})	0.65	0.38	0.70	see text
R_s (sec cm^{-1})	0.75	0.01	0.73	see text

---

[*] These measurements refer to the air-sampling heights above the vegetation or water surface (viz. 20 cm for Experiments 1 and 2, and 5 cm for Experiments 3 and 4). All wind speeds were measured 2 m above the ground.

Source: Owers and Powell (1974)

2. Surface Deposition of O_3, NO, and NO_2

As an example of ozone deposition velocity data we present decomposition rates on various surfaces measured by Sabersky et al. (1971) in Table 10. Their experiments were performed in a lucite chamber; deposition velocities were determined from the slope of log c/c_0 plotted versus time. Although for a given experiment their results indicate first-order decay, it was found that an "aging" process causes the deposition velocity to decrease from one experiment to the next.

In a similar analysis, Aldaz (1969) measured sink fluxes of ozone by observing the decay of ozone injected into a Mylar box covering the surface of interest. His results, converted to deposition velocities, are reported in Figure 35.

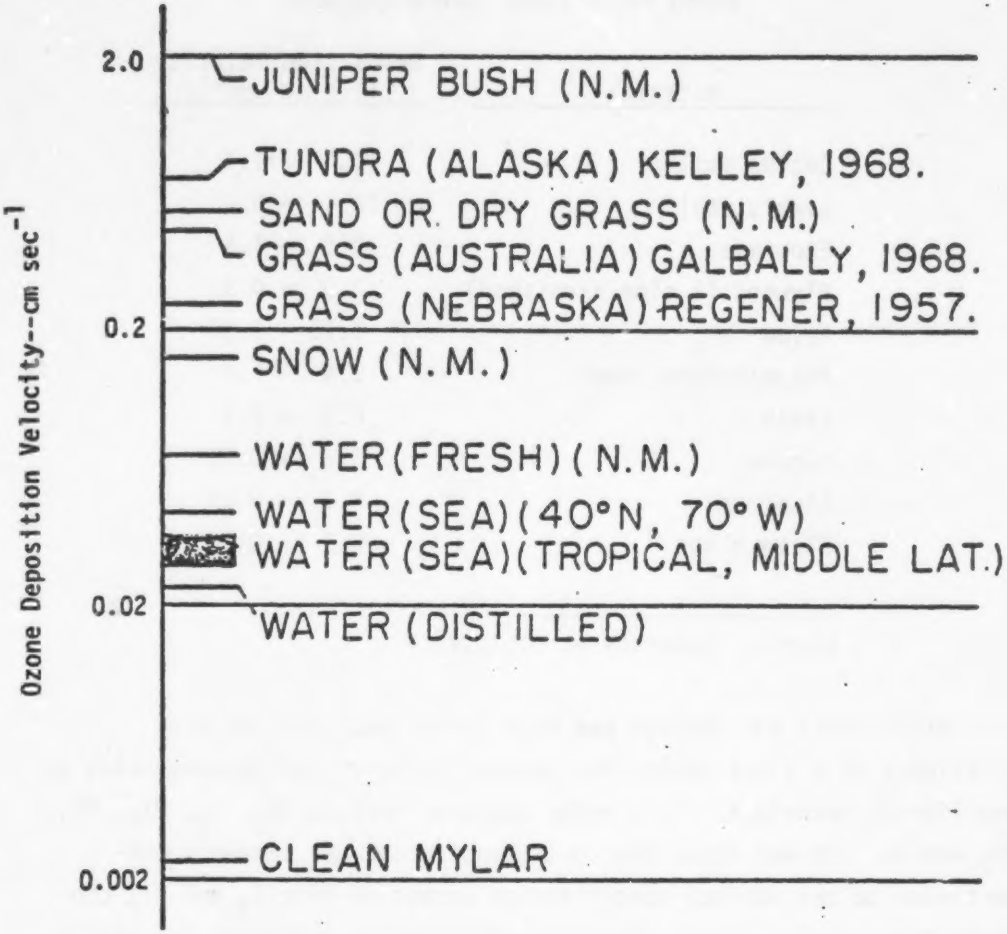

Source: Aldaz (1969).

FIGURE 35. OZONE DEPOSITION VELOCITIES OVER DIFFERENT SURFACES ASSUMING A PARTIAL OZONE DENSITY OF 40 $\mu g/m^3$

TABLE 10. MEASURED VALUES OF OZONE DECOMPOSITION RATES FOR SEVERAL COMMON SURFACES

Material	Deposition Velocity (10^{-2} cm sec^{-1})
Cotton muslin	10.7 → 1.4
Lamb's wool	10.4 → 0.4
Neoprene	9.5 → 1.5
Plywood (1 side varnished)	3.0 → 0.5
Nylon	3.15 → 0.05
Polyethylene sheet	2.4 → 1.0
Linen	0.9 → 0.5
Lucite	0.6 → 0.05
Aluminum	0.1 → 0.05
Plate glass	0.1 → 0.05

Source: Sabersky et al. (1971)

Hill (1971) and Bennett and Hill (1973) measured the sink efficiency of a plant canopy for several different pollutants using an equilibrium technique. Pollutants measured include SO_2, O_3, Cl_2, NO, NO_2 and CO. It was found that pollutant uptake was linearly proportional to the ambient concentration except at high O_3 and Cl_2 concentration levels. Light intensity was shown to influence the uptake of O_3 and NO_2. (Full sunlight tripled the NO_2 uptake rate.) Table 11 presents their deposition velocities measured under the following conditions: ambient concentrations of 5 pphm; wind speed 6.4-8 kph; light intensity 40-45 klux; canopy height 36-46 cm; temperature 24-25°C, and relative humidity 45-50%.

TABLE 11. DEPOSITION VELOCITIES OF SELECTED POLLUTANTS

Pollutant	Deposition Velocity (in m sec^{-1})
CO	0
NO	10^{-3}
O_3	1.7×10^{-2}
NO_2	1.8×10^{-2}
SO_2	2.8×10^{-2}

Source: Hill (1971) and Bennett and Hill (1973)

An interesting result of Hill's NO_2 deposition experiments was the production of NO and its subsequent buildup within the chamber. To overcome this, he placed sheets of fiberglass impregnated with H_2SO_4 and Na_2CrO_4 in the chamber to oxidize the NO to NO_2. Thus, the reported NO_2 deposition values represent a net deposition.

At high NO_2 concentrations, vegetation would then be a sink for NO_2 and a source of NO. Both factors would tend to depress ozone levels. Unfortunately, Hill gives no data concerning the magnitude of NO production. However, if the heterogeneous reaction

$$3NO_2 + H_2O \rightarrow 2HNO_3 + NO \qquad (68)$$

is responsible for both NO_2 deposition and NO emission, then the actual sink strength for NO_2 is 50 percent greater than the net value reported. In this case, vegetation would be a source of NO, yielding 1 NO molecule for every 3 NO_2 molecules deposited.

3. Surface Deposition of Hydrocarbons

Very little data are available on surface removal rates for hydrocarbons from the atmosphere. Hydrocarbons are generally not water soluble (Rasmussen, Taheri, and Kabel, 1974) and therefore surface moisture is not expected to have a significant effect on the removal of these gases by soil and vegetation. Smith et al. (1973) investigated the capacity of soils to absorb ethylene and acetylene. They concluded, as did Abeles et al. (1971) in an experiment on ethylene uptake by soil, that the sorption of both ethylene and acetylene is due to microbial activity in the soil. Rasmussen, Hutton, and Garner (1968) and Robinson and Robbins (1968) have also suggested that the volatile organic components of the atmosphere are removed by bacteriological processes and vegetation. Smith et al. found that the soils they tested remove ethylene at average rates ranging from 0.14 to 0.97×10^{-9} moles per gram of soil per day (moles/g·d) and acetylene from 0.24 to 3.12×10^{-9} moles/g·d.

Using the greatest removal rate found by Smith et al. for acetylene, we can calculate what is probably the upper limit for removal of gaseous hydrocarbons from the atmosphere by absorption and reaction in soils. We assume that the hydrocarbons react with a one centimeter depth of soil of density of 1.3 gram per cubic centimeter, and that the hydrocarbon gases are uniformly mixed throughout a 500 meter depth of the atmosphere. In the absence of advection we calculate a loss of hydrocarbon gas of 8×10^{-14} moles per cubic centimeter per day. This corresponds to a loss rate of approximately 1.5 ppb per day. This is a very low loss rate and is probably overshadowed in many areas by natural emissions of hydrocarbons. Based on this limited data we conclude that surface removal of hydrocarbons need not be included in photochemical smog simulation models.

4. Surface Deposition of HNO_2, H_2O_2, and Aldehydes

Aldehydes, HNO_2, and H_2O_2 play an important role in the radical formation and exchange processes in photochemical smog. Because radical chemistry lies at the heart of the smog generating mechanism, it is conceivable that surface sinks of these compounds might have an effect on smog formation. However, there is no direct information on the strength of surface sinks for these compounds. In a later section of this chapter we estimate upper limits for surface sinks of these compounds and perform sensitivity studies.

5. Surface Deposition of CO

While vegetation does not seem to remove atmospheric CO, certain soil fungi and bacteria are sinks. Ingersoll et al. (1974) conducted a series of experiments in closed chambers constructed in fields around soil plots. In addition, they studied the influence of environmental factors via laboratory experiments. Table 12 reports the deposition velocities calculated from their field data obtained with CO concentrations of 100 ppm. The data in Table 12 were obtained along U.S. Highway 101 near Menlo Park, California. The unusually high deposition velocities were ascribed to constant exposure of the soil to CO. A similar result was obtained by Heichel (1973). He found that CO uptake increased almost exponentially with concentration (see Fig. 36). Heichel attributed this behavior to activation, by CO, of enzymes present in the soil.

The nonlinear dependence of CO uptake rate on concentration is not as important as it might seem. Because surface removal processes for CO are quite slow, and because concentrations of CO rarely reach the extremes examined by Heichel, it is possible to estimate representative average deposition rates. Thus, if it becomes appropriate to include deposition of CO in air quality models, we should be able to adequately characterize CO surface uptake through an appropriate deposition velocity.

TABLE 12a. COMPARISON OF THE CO UPTAKE CAPACITY OF SOILS UNDER CULTIVATION AND SOILS UNDER NATURAL VEGETATION

	Soils under Natural Vegetation		Soils under Cultivation	
Test Site	Vegetation Type	Deposition Velocity (in 10^{-5}m sec^{-1})	Type	Deposition Velocity (in 10^{-5}m sec^{-1})
Grouard, Alb.	Boreal forest	0.9	Plowed field	0.2
Athens, Ohio	Mixed deciduous forest	4.5	Plowed field	0.7
Ft. McMurray, Alb.	Boreal forest	1.4	Plowed field	0.5
Chenango, N. Y.	Deciduous forest	5.3	Plowed field	0.4
Wichita Falls, Tex.	Grassland	2.5	Wheat stubble	1.6
Regina, Sask.	Grassland	0.6	Plowed field	0.3
Van Meter, Mo.	Oak-hickory forest	2.1	Newly planted milo field	0.6
Shrevesport, La.	Flood plain forest	5.3	Plowed field	0.9
Sabetha, Kans.	Grassland	0.8	Milo stubble	0.6
Grants Pass, Ore.	Coastal forest	3.0	Plowed field	0.5
Cincinnati, Ohio	Oak-hickory forest	4.5	Fallow field	0.7
Prairie View, Kans.	Bluestem prairie	0.5	Plowed field	0.2

Source: Ingersoll et al. (1974)

TABLE 12b. SOIL ACTIVITY AT SITES ALONGSIDE A 20-MILE STRETCH OF THE BAYSHORE FREEWAY (U.S. 101) PRESELECTED ON THE BASIS OF REPRESENTATIVE VEGETATION OR GROUND COVER

Test Site	Vegetation	Deposition Velocity (in 10^{-5}m sec^{-1})	Avg. Temp. (F°)*	Soil pH	Soil Moisture (%)†
Embarcadero Road interchange	Iceplant	14.5	65	7.6	19.6
San Antonio Road interchange	Iceplant	9.6	85	7.8	5.7
Mathilda Avenue interchange	Ivy	11.0	66	8.2	3.9
W. Bayshore Road§	Ivy	9.0	60	8.3	19.2
Frontage Road§	Grass	13.3	69	7.8	10.0
Dirt road§	Barley	6.9	81	7.6	2.5
San Tomas Expressway interchange	Grass	7.7	80	7.4	5.1
Trimble Road interchange	Grass	3.7	76	8.0	7.3
U.S. 85 interchange	Bare	4.7	95	7.7	6.1
Mathilda Avenue off-ramp	Bare	3.4	82	7.7	3.7
W. Bayshore Road§	Plowed	4.9	77	7.0	4.2
W. Bayshore Road§	Plowed	3.2	71	8.7	3.5

* Soil temperature inside test chamber.

† Percent moisture of surface soil.

§ Site off freeway right-of-way, but within 100 feet of freeway

Source: Ingersoll et al. (1974)

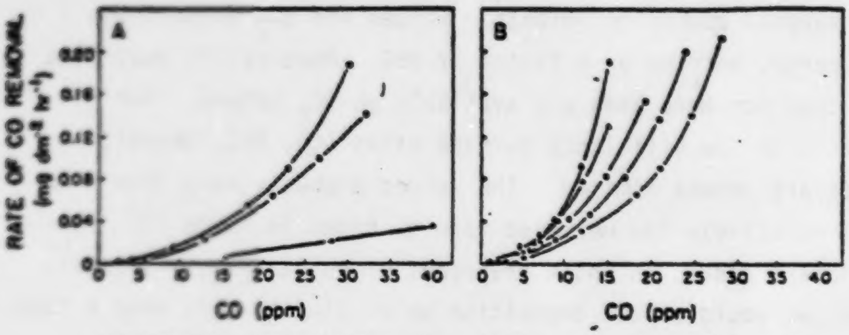

•–• smooth, water-slaked soil surface with the profile having a uniform 17% (w/w) H_2O content.

•–• smooth, air-dry, crusted surface with the soil profile having 2.7% (w/w) H_2O content in the upper 2.5 cm and 6.1% (w/w) H_2O content in the lower 4.0 cm.

•–• smooth, air-dry, crusted surface with the soil profile having 1.7% (w/w) H_2O content in the upper 2.5 cm and 2.3% (w/w) H_2O content in the lower 4.0 cm.

All surfaces are rough and water-slaked.

•–• profile having a uniform 117% (w/w) H_2O content.

•–• profile having a uniform 101% (w/w) H_2O content.

•–• profile having 35.8% (w/w) H_2O content in the upper 2.5 cm and 65.6% (w/w) H_2O content in the lower 4.0 cm.

•–• profile having 26.2% (w/w) H_2O content in the upper 2.5 cm and 45.4% (w/w) H_2O content in the lower 4.0 cm.

•–• profile having 11.4% (w/w) H_2O content in the upper 2.5 cm and 32.1% (w/w) H_2O content in the lower 4.0 cm.

Source: Heichel (1973).

FIGURE 36. RESPONSE OF CO REMOVAL TO CO CONCENTRATION IN FIELD AND FOREST SOILS. A--CHESHIRE FINE SANDY LOAM (FIELD SOIL) AND B--CHARLTON FINE SANDY LOAM (FOREST SOIL).

6. Summary of Results

Table 13 summarizes the range of reported deposition velocities for several common pollutants. Values for SO_2 exhibit the greatest range, varying by a factor of 260. However, it must also be noted that far more data are available on SO_2 uptake. For pollutants with low efficiency surface sinks (CO, NO), deposition velocities are uptake limited. The values probably vary from zero up to the relatively low measured figures cited in Table 13. For more efficient sinks, in which transport processes play a significant role, we would expect deposition velocities to vary over a much greater range, as exhibited by those for SO_2.

TABLE 13. RANGE OF DEPOSITION VELOCITIES FOR VARIOUS POLLUTANTS

Pollutant	Deposition Velocity ($cm\ sec^{-1}$)
CO	0 - 0.03
NO	0.1
NO_2	0.6 - 1.8
O_3	0.2 - 2.0
SO_2	0.1 - 26
HNO_2	N.A.
H_2O_2	N.A.
Aldehydes	N.A.
Hydrocarbons	very low

N.A. No data available.

E. ESTIMATION OF THE IMPORTANCE OF VARIOUS SURFACE SINKS

Including a particular surface sink in an airshed model is necessary only if the effects of that sink are significant. In order to determine which of the sinks described in Section D are significant, we conducted sensitivity studies. We have already indicated that surface sinks of hydrocarbons are not likely to be important in modeling short time periods. The effects of the other sinks are discussed in the following sections.

1. Sinks of CO

The major sink for CO seems to be the biological activity of certain soil fungi and other microorganisms (Ingersoll et al., 1974). The CO removal rate is nonlinear; apparently it is substantially increased by exposing the soil to elevated levels of CO. Ingersoll et al. noted that soils near roadways had the highest uptakes of CO. These soils had CO removal rates that were ten times greater than those of typical grassland or forest soils.

However, even the highest CO removal rates reported are far below the level at which it would be necessary to include this sink in an urban airshed model. Ingersoll et al. reported that the highest flux rate obtained was 115 mg $hr^{-1}m^{-2}$, for exposure to air containing 114 mg m^{-3} of CO (100 ppm). This gives a deposition velocity of 2.8×10^{-2} cm sec^{-1}. At this deposition velocity, a ground level concentration of 10 ppm CO would produce a surface flux of 0.28 ppm cm sec^{-1} or 0.55 ppm ft min^{-1}. Emissions of CO in the Los Angeles Basin are commonly an order of magnitude greater than this loss rate. Since typical deposition velocities of CO are one-tenth of the values cited above, surface deposition of CO should account for only about 1 percent of the mass balance in an urban airshed. Thus, we conclude that we may safely ignore surface sinks of CO within urban areas.

2. Sinks of SO_2

The rate of removal of sulfur dioxide from the atmosphere depends on the combined rates of surface removal and atmospheric oxidation. Measurements by Urone et al. (1968) indicate that rates of SO_2 oxidation in a photochemically active atmosphere may be on the order of 10 to 20 percent per hour, compared to rates on the order of 1 percent per hour in nonphotochemically active atmospheres. Furthermore, deposition velocities for SO_2 are among the highest measured for any pollutant. For example, the uptake of sulfur dioxide by ocean water appears to be limited primarily by atmospheric transport (Shepherd, 1974).

In order to determine the relative importance of surface sinks, we examined a series of photochemical model predictions with various SO_2 deposition velocities for the Los Angeles Basin. Deposition velocities of 4 cm sec^{-1} over water and 1 cm sec^{-1} over land produced a ground-cell concentration loss of 25 percent over Long Beach and 70 percent over the ocean in only one hour (see Figures 37 through 39. With deposition velocities reduced to one-fourth of the above values (Figure 40), the reductions in SO_2 concentrations in the same time period were 10 and 25 percent, respectively. Figures 41 and 42 illustrate the SO_2 concentrations with the lower and higher deposition rates. The deposition velocities that we have used are well within the range of reported values. Clearly, surface sinks for SO_2 should be considered in air quality models.

3. Sinks of Photochemical Pollutants

If one accepts the concept of a deposition velocity, there are two limitations in its successful implementation in the airshed model. The first limitation is a lack of data for surfaces that are typically found in urban areas. The second limitation is the difficulty in

```
     1    2    3    4    5    6    7    8    9   10   11   12   13   14   15   16   17   18   19   20   21   22   23   24   25

15  3.0  3.0  3.0  3.0  3.0  3.0  3.0  2.0  3.0  3.0  3.0  3.0  3.0  3.0  3.0  3.0  2.0  2.0  2.0  2.0  2.0  1.0  1.0  1.0  1.0
14  3.0  3.0  3.0  3.0  3.0  3.0  4.0  4.0  3.0  3.0  3.0  3.0  3.0  3.0  3.0  3.0  2.0  2.0  2.0  2.0  2.0  2.0  1.0  1.0  1.0
                                       LENNOX
13  3.0  3.0  3.0  3.0  3.0  4.0  4.0  4.0  4.0  3.0  3.0  3.0  3.0  3.0  3.0  3.0  2.0  2.0  2.0  1.0  1.0  2.0  1.0  1.0  1.0
                                                                                       WHITTIER  LA HABRA
12  3.0  3.0  3.0  3.0  3.0  3.0  4.0  4.0  3.0  3.0  3.0  3.0  3.0  3.0  3.0  3.0  2.0  2.0  2.0  2.0  2.0  2.0  2.0  1.0  1.0
11  3.0  3.0  3.0  3.0  3.0  3.0  3.0  3.0  3.0  3.0  3.0  3.0  3.0  3.0  3.0  3.0  2.0  2.0  2.0  2.0  2.0  2.0  2.0  1.0  1.0
10  3.0  3.0  3.0  3.0  3.0  3.0  3.0  3.0  3.0  3.0  3.0  4.0  4.0  4.0  3.0  3.0  2.0  2.0  2.0  2.0  1.0  1.0  2.0  1.0  1.0
                                                                LONG BEACH                                ANAHEIM
 9  3.0  3.0  3.0  3.0  3.0  3.0  3.0  3.0  3.0  4.0  4.0  4.0  5.0  4.0  3.0  2.0  2.0  2.0  2.0  2.0  1.0  1.0  2.0  1.0  1.0

 8  3.0  3.0  3.0  3.0  3.0  3.0  3.0  3.0  4.0  3.0  4.0  4.0  4.0  3.0  3.0  2.0  2.0  2.0  2.0  2.0  2.0  2.0  2.0  1.0  1.0
                                   PALOS VERDES
 7  3.0  3.0  3.0  3.0  3.0  3.0  3.0  3.0  4.0  4.0  4.0  3.0  3.0  3.0  3.0  2.0  2.0  2.0  2.0  2.0  2.0  2.0  2.0  1.0  1.0
 6  3.0  3.0  3.0  3.0  3.0  3.0  3.0  3.0  3.0  3.0  4.0  3.0  3.0  3.0  3.0  2.0  2.0  2.0  2.0  2.0  2.0  2.0  1.0  1.0  1.0
 5  3.0  3.0  3.0  3.0  3.0  3.0  3.0  3.0  3.0  3.0  3.0  3.0  3.0  3.0  3.0  3.0  3.0  2.0  2.0  2.0  2.0  2.0  2.0  2.0  1.0
              PACIFIC OCEAN                                                                                  SANTA ANA
 4  3.0  3.0  3.0  3.0  3.0  3.0  3.0  3.0  3.0  3.0  3.0  3.0  3.0  3.0  3.0  3.0  2.0  2.0  2.0  2.0  2.0  2.0  2.0  1.0  2.0

 3  3.0  3.0  3.0  3.0  3.0  3.0  3.0  3.0  3.0  3.0  3.0  3.0  3.0  3.0  3.0  3.0  3.0  2.0  2.0  2.0  2.0  2.0  2.0  2.0  2.0
 2  3.0  3.0  3.0  3.0  3.0  3.0  3.0  3.0  3.0  3.0  3.0  3.0  3.0  3.0  3.0  3.0  3.0  2.0  2.0  2.0  2.0  2.0  2.0  2.0  2.0
 1  3.0  3.0  3.0  3.0  3.0  3.0  3.0  3.0  3.0  3.0  3.0  3.0  3.0  3.0  3.0  3.0  3.0  2.0  2.0  2.0  2.0  2.0  2.0  2.0  2.0
```

Reproduced from
best available copy.

FIGURE 37. GROUND-LEVEL SO_2 CONCENTRATIONS IN PPHM AT START OF SIMULATIONS (12:00 A.M.)

```
      1    2    3    4    5    6    7    8    9   10   11   12   13   14   15   16   17   18   19   20   21   22   23   24   25

15  2.3  2.7  2.7  2.7  2.8  3.2  2.7  2.6  2.0  2.1  2.0  1.9  1.7  1.8  1.8  1.6  1.4  1.4  1.4  1.4  1.4  1.1  1.0  1.0  1.0
14  2.7  3.2  3.1  3.1  3.1  3.0  4.6  4.2  3.8  3.1  3.0  2.9  2.7  2.8  2.8  2.6  2.2  1.9  1.9  1.9  1.9  1.8  1.1  1.0  1.0
                                      LENNOX

13  2.6  3.1  3.1  3.0  3.1  3.7 13.4  7.9  4.2  3.4  3.4  3.4  3.3  3.3  3.4  3.4  5.1  3.0  2.3  1.0  1.7  1.8  1.2  1.0  1.0
                                                                                   WHITTIER  LA HABRA
12  2.8  3.1  3.0  3.0  3.0  3.2 10.8  9.1  4.3  3.2  3.3  3.4  3.4  3.5  3.5  3.5 11.5  4.1  2.2  1.9  1.9  2.2  1.7  1.1  1.0
11  2.8  3.1  3.0  3.0  3.0  3.0  8.8  7.0  8.4  3.7  3.3  3.2  3.3  3.3  3.4  3.4  6.3  3.4  2.3  2.2  2.0  2.4  2.2  1.8  1.3
10  2.8  3.1  3.0  3.0  3.0  3.0  3.1  9.4 14.0  8.8  3.7  3.0  3.8  3.6  3.4  3.3  3.1  2.8  2.3  2.4  2.0  1.8  2.2  1.6  1.3
                                                                LONG BEACH                             ANAHEIM
 9  2.8  3.1  3.0  3.0  3.0  3.0  3.0  3.3  3.7  4.4  3.9  3.8  4.2  4.2  3.6  3.0  2.2  2.2  2.0  2.3  1.6  1.4  2.1  1.8  1.3

 8  2.8  3.1  3.0  3.0  3.0  3.0  3.1  3.2  3.8  3.7  4.3 11.8  8.7  4.7  3.3  2.7  2.2  2.2  2.3  2.3  1.9  2.0  2.2  1.4  1.3
                                  PALOS VERDES
 7  2.8  3.1  3.0  3.0  3.0  3.0  3.1  3.2  3.7  4.7 12.9 11.6  7.1  3.7  3.0  2.8  2.2  2.3  2.3  2.3  2.3  2.3  2.1  1.8  1.3
 6  2.4  3.1  3.1  3.0  3.0  3.0  3.0  3.1  3.3  3.9  5.8  8.2  3.8  2.8  2.9  2.4  2.2  2.2  2.3  2.3  2.3  2.3  1.7  1.6  1.3
 5  2.4  3.1  3.1  3.0  3.0  3.0  3.0  3.0  3.0  3.0  3.1  2.8  2.8  2.9  3.0  2.7  2.2  2.2  2.3  2.3  3.0  2.3  2.3  1.8  1.7
             PACIFIC OCEAN                                                                            SANTA ANA

 4  2.4  3.1  3.1  3.0  3.0  3.0  3.0  3.0  3.0  3.0  2.9  2.9  3.0  3.0  3.0  2.9  2.2  2.1  2.2  2.3  2.3  2.3  2.2  2.0  2.1
 3  2.4  3.1  3.1  3.0  3.0  3.0  3.0  3.0  3.0  3.0  3.0  3.0  3.0  3.0  3.0  3.0  2.8  2.2  2.1  2.2  2.3  2.3  2.3  2.4  2.0
 2  2.8  3.1  3.1  3.0  3.0  3.0  3.0  3.0  3.0  3.0  3.0  3.0  3.0  3.0  3.0  3.0  2.9  2.2  2.0  2.1  2.1  2.1  2.1  2.1  1.9
 1  2.3  2.9  2.9  2.9  2.9  2.9  2.9  2.9  3.0  3.0  3.0  3.0  3.0  3.0  3.0  3.0  2.9  2.2  2.0  1.9  1.4  1.4  1.8  1.8  1.4
```

FIGURE 38. GROUND-LEVEL SO_2 CONCENTRATIONS IN PPHM AFTER 1 HOUR OF SIMULATION USING $v_d = 0$

	1	2	3	4	5	6	7	8	9	10	11	12	13	14	15	16	17	18	19	20	21	22	23	24	25
15	.7	.8	.8	.8	1.2	2.1	1.9	1.8	1.6	1.5	1.4	1.4	1.3	1.1	1.1	1.2	1.0	.8	.8	.8	.8	.6	.5	.5	.6
14	.8	.9	.9	.9	1.0	1.9	3.2	2.9	2.4	3.1	2.0	1.9	1.7	1.6	1.6	1.6	1.3	1.0	1.0	.9	.9	.7	.5	.4	.4
								LENNOX																	
13	.8	.9	.9	.9	.9	1.4	9.5	6.0	2.9	2.3	2.3	2.3	2.2	2.1	2.1	2.1	3.6	1.8	1.2	1.0	.9	.9	.6	.4	.4
																		WHITTIER		LA HABRA					
12	.8	.9	.9	.9	.9	1.0	9.6	6.6	3.0	2.1	2.2	2.0	2.0	2.3	2.3	2.2	6.7	2.6	1.3	1.1	1.2	1.2	.9	.5	.5
11	.8	.9	.9	.9	.9	.9	1.8	5.7	3.9	2.6	2.3	2.2	2.3	2.2	2.2	2.2	4.2	2.2	1.4	1.4	1.3	1.4	1.5	.8	.7
10	.8	.9	.9	.9	.9	.9	1.0	6.9	10.8	6.7	2.6	2.1	3.4	2.4	2.3	2.3	2.0	1.6	1.5	1.5	1.2	1.1	1.3	.9	.8
													LONG	BEACH							ANAHEIM				
9	.8	.9	.9	.9	.9	.9	1.8	3.1	2.6	3.1	2.7	2.6	2.9	2.9	2.4	2.1	1.4	1.4	1.5	1.5	1.0	.9	1.3	.9	.8
8	.8	.9	.9	.9	.9	.9	1.5	2.1	2.8	2.6	3.0	8.7	6.2	3.2	2.2	1.8	1.5	1.5	1.5	1.8	1.3	1.3	1.4	.9	.8
								PALOS VERDES																	
7	.8	.9	.9	.9	.9	.9	1.4	2.1	2.6	3.3	8.0	6.7	3.9	2.0	2.0	1.8	1.5	1.8	1.8	1.5	1.5	1.5	1.4	.9	.8
6	.8	.9	.9	.9	.9	.9	1.1	1.2	1.6	2.5	2.3	1.7	1.0	.9	1.0	1.2	1.5	1.5	1.5	1.5	1.5	1.5	1.1	1.0	.8
5	.8	.9	.9	.9	.9	.9	.9	.9	.9	.9	.9	.8	.8	.8	.8	.8	.9	1.5	1.5	1.5	1.5	1.5	1.5	1.2	1.1
			PACIFIC	OCEAN																		SANTA	ANA		
4	.8	.9	.9	.9	.9	.9	.9	.9	.8	.8	.8	.8	.8	.8	.8	.8	.6	.9	1.5	1.4	1.6	1.6	1.5	1.4	1.4
3	.8	.9	.9	.9	.9	.9	.9	.9	.8	.8	.8	.8	.8	.8	.8	.8	.8	.6	.9	1.4	1.6	1.6	1.6	1.6	1.4
2	.8	.9	.9	.9	.9	.9	.9	.9	.9	.8	.8	.8	.8	.8	.8	.9	.8	.6	.6	.7	1.2	1.5	1.4	1.5	1.5
1	.8	.8	.8	.8	.8	.8	.8	.9	.8	.8	.8	.8	.8	.8	.8	.9	.8	.6	.6	.4	.5	.7	.9	1.1	1.1

Reproduced from
best available copy.

FIGURE 39. GROUND-LEVEL SO_2 CONCENTRATIONS IN PPHM AFTER 1 HOUR OF SIMULATION USING v_d = 4 CM SEC^{-1} OVER WATER AND 1 CM SEC^{-1} OVER LAND

```
         1     2     3     4     5     6     7     8     9    10    11    12    13    14    15    16    17    18    19    20    21    22    23    24    25

  15   1.6   1.8   1.8   1.8   2.3   2.8   2.4   2.3   2.1   1.9   1.8   1.7   1.6   1.4   1.4   1.8   1.8   1.2   1.3   1.2   1.3    .9    .8    .8    .8
  14   1.8   3.1   2.1   2.0   3.1   3.0   4.1   3.7   3.1   3.7   3.7   3.6   3.4   2.2   2.3   2.3   1.9   1.6   1.4   1.6   1.8   1.2    .9    .7    .8
                                               LENNOX

  13   1.8   2.1   2.0   2.0   2.1   2.7  11.4   7.0   3.0   3.0   3.0   3.0   2.9   2.9   2.9   3.0   4.6   2.8   1.9   1.8   1.4   1.8   1.0    .8    .8
                                                                                                          WHITTIER  LA HABRA
  12   1.7   2.0   3.0   3.0   2.0   2.3  11.8   3.3   3.9   2.0   2.9   3.0   3.0   3.0   3.1   3.1  10.6   3.6   1.9   1.6   1.6   1.9   1.4    .9    .8
  11   1.7   2.1   2.0   2.0   2.0   2.0   2.8   7.1   4.9   3.0   3.9   3.9   2.9   2.9   3.0   3.0   3.6   3.0   2.0   1.9   1.9   2.0   1.9   1.3   1.1
  10   1.7   2.1   2.0   2.0   2.0   2.0   2.1   8.8  13.9   3.1   3.3   2.7   3.1   3.2   3.0   2.9   2.7   2.3   2.0   2.1   1.7   1.6   1.9   1.3   1.2
                                                                              LONG BEACH                                  ANAHEIM
   9   1.7   2.1   2.0   2.0   2.0   2.0   2.1   2.0   3.3   3.9   3.8   3.4   3.8   3.8   3.2   2.7   1.9   1.9   2.0   2.0   1.4   1.2   1.0   1.3   1.1

   8   1.7   2.1   2.0   2.0   2.0   2.0   2.4   2.8   3.2   3.3   3.8  10.5   7.8   4.1   2.9   2.4   1.9   2.0   2.0   2.0   1.7   1.7   1.9   1.2   1.1
                                          PALOS VERDES
   7   1.7   2.1   2.0   2.0   2.0   2.0   2.4   3.0   3.3   4.2  11.2   9.0   5.9   3.1   2.6   2.3   2.0   2.0   2.0   2.0   2.0   2.1   1.9   1.2   1.1
   6   1.7   2.0   2.0   2.0   2.0   2.0   2.0   2.1   2.3   2.7   4.3   3.7   2.8   2.0   2.0   2.0   1.9   2.0   2.0   2.0   2.0   2.0   1.8   1.4   1.1
   5   1.7   2.0   2.0   2.0   2.0   2.0   2.0   2.0   2.0   2.0   2.0   1.8   1.8   1.9   1.9   1.8   1.7   1.9   2.0   2.0   2.0   2.0   1.9   1.6   1.8
                  PACIFIC OCEAN                                                                                                 SANTA ANA

   4   1.7   2.0   2.0   2.0   2.0   2.0   2.0   2.0   2.0   2.0   1.9   2.0   2.0   2.0   2.0   1.9   1.8   1.6   2.0   2.0   2.0   2.0   2.0   1.8   1.8
   3   1.7   2.0   2.0   2.0   2.0   2.0   2.0   2.0   2.0   2.0   2.0   2.0   2.0   2.0   2.0   2.0   1.8   1.4   1.6   1.9   2.1   2.1   2.1   2.1   1.8
   2   1.7   2.1   2.1   2.0   2.0   2.0   2.0   2.0   2.0   2.0   2.0   2.0   2.0   2.0   2.0   2.0   2.0   1.8   1.8   1.8   1.7   1.8   1.8   1.9   1.7
   1   1.6   2.0   2.0   1.9   1.9   2.0   2.0   2.0   2.0   2.0   2.0   2.0   2.0   2.0   2.0   2.0   1.9   1.8   1.8   1.8   1.8   1.1   1.8   1.4   1.0
```

FIGURE 40. GROUND-LEVEL SO_2 CONCENTRATIONS IN PPHM AFTER 1 HOUR OF SIMULATION USING v_d = 1.0 CM SEC^{-1} OVER WATER AND 0.25 CM SEC^{-1} OVER LAND

```
         1     2     3     4     5     6     7     8     9    10    11    12    13    14    15    16    17    18    19    20    21    22    23    24    25

15     1.0   1.2   1.4   1.4   1.7   2.5   3.0   2.6   3.3   2.0   1.8   1.6   1.5   1.4   1.3   1.4   1.1   1.0    .9   1.0    .9    .8    .7    .7    .8
14     1.0   1.3   1.5   1.5   1.6   2.8   4.1   6.2   4.6   3.0   2.8   2.2   2.1   2.0   1.9   1.9   1.8   1.4   1.2   1.2   1.1    .9    .6    .6    .7
                                               LENNOX
13     1.0   1.3   1.5   1.5   1.5   1.9   7.2  13.9  11.1   5.4   2.4   3.2   2.6   2.6   2.6   2.6   5.6   3.2   1.9   1.4   1.3   1.2    .7    .6    .7
                                                                                                         WHITTIER  LA HABRA
12     1.0   1.2   1.5   1.6   1.5   1.6   7.0  10.5   9.4   5.8   3.9   3.0   3.6   2.9   3.0   3.0  10.4   6.7   2.3   1.6   1.7   1.5   1.1    .7    .8
11     1.0   1.3   1.5   1.6   1.5   1.5   1.5   5.0   9.6  11.5   6.7   3.9   3.3   2.8   3.0   3.0   5.5   5.0   2.3   1.8   1.9   2.0   1.5   1.3   1.2
10     1.0   1.3   1.5   1.6   1.6   1.4   1.6   4.0   8.3  11.2  10.0   6.5   5.3   3.4   2.9   2.9   8.4   5.1   2.2   2.0   1.9   1.8   1.9   1.5   1.3
                                                                            LONG BEACH                                 ANAHEIM

 9     1.0   1.2   1.5   1.6   1.6   1.6   1.7   2.8   2.8   3.5   4.3   7.0   9.4   5.2   3.1   2.8   2.3   2.0   2.0   2.0   1.7   1.8   1.8   1.8   1.8
 8     1.0   1.3   1.5   1.6   1.6   1.5   1.9   3.4   2.8   3.1   3.6   9.2  12.6   5.1   3.6   2.5   2.0   1.8   3.0   2.0   1.7   1.6   1.6   1.5   1.2
                                         PALOS VERDES
 7     1.0   1.2   1.5   1.6   1.5   1.5   2.0   3.2   2.6   3.9   5.1  12.8  11.1   6.9   3.5  10.7   5.5   2.3   1.9   2.0   2.0   2.0   1.9   1.4   1.2
 6     1.0   1.2   1.5   1.6   1.5   1.5   1.5   1.6   1.7   1.7   3.8   5.4   5.0   3.3   2.1   3.0   2.7   3.1   2.0   2.0   2.0   2.0   1.7   1.5   1.3
 5     1.0   1.2   1.3   1.6   1.5   1.5   1.6   1.8   1.5   1.5   1.5   1.4   1.4   1.3   1.4   1.4   1.5   1.8   2.0   2.0   2.0   2.3   1.9   1.8   1.5
                 PACIFIC OCEAN                                                                                            SANTA ANA

 4     1.0   1.2   1.5   1.6   1.5   1.5   1.5   1.5   1.5   1.5   1.4   1.4   1.4   1.4   1.4   1.4   1.5   1.4   1.8   2.0   2.0   2.1   2.0   2.0   1.9
 3     1.0   1.2   1.5   1.6   1.5   1.5   1.5   1.5   1.5   1.5   1.5   1.5   1.5   1.5   1.5   1.5   1.4   1.2   1.3   1.7   2.0   2.0   2.0   2.0   1.9
 2     1.0   1.2   1.5   1.6   1.5   1.5   1.5   1.5   1.5   1.5   1.5   1.5   1.5   1.5   1.5   1.5   1.5   1.3   1.1   1.1   1.5   1.6   1.7   1.7   1.7
 1      .9   1.1   1.3   1.4   1.4   1.4   1.4   1.4   1.4   1.4   1.4   1.5   1.5   1.5   1.5   1.5   1.5   1.3   1.1    .9    .8    .9   1.1   1.3   1.5
```

Reproduced from
best available copy.

FIGURE 41. GROUND-LEVEL SO_2 CONCENTRATIONS IN PPHM AFTER 2 HOURS OF SIMULATION USING v_d = 1 CM SEC^{-1} OVER WATER AND 0.25 CM SEC^{-1} OVER LAND

	1	2	3	4	5	6	7	8	9	10	11	12	13	14	15	16	17	18	19	20	21	22	23	24	25
15	.5	.3	.3	.3	.6	1.4	1.0	1.7	1.8	1.3	1.2	1.1	1.0	1.0	.9	.9	.7	.5	.8	.4	.4	.3	.2	.2	.5
14	.5	.3	.3	.4	.4	1.0	2.6	3.5	3.3	2.1	1.6	1.4	1.3	1.2	1.1	1.1	1.0	.7	.5	.5	.4	.3	.2	.2	.4
13	.5	.3	.3	.4	.4	.6	5.0	LENNOX 10.6	8.1	3.7	1.8	1.3	1.6	1.6	1.8	1.8	8.9	1.9	.9	.7	.6	.3	.2	.2	.4
12	.5	.3	.3	.4	.4	.4	5.5	7.8	6.7	3.9	2.0	1.4	1.6	1.8	1.8	1.8	10.1	WHITTIER 4.3	1.1	LA HABRA 1.0	1.0	.9	.8	.2	.4
11	.5	.3	.4	.4	.4	.4	.6	4.1	7.1	8.9	6.0	1.9	1.4	1.7	1.8	1.0	3.4	3.0	1.3	1.1	1.1	1.1	.9	.7	.6
10	.5	.3	.4	.4	.4	.5	.5	3.7	6.2	8.2	7.2	4.7	4.1 LONG BEACH	2.4	1.0	1.0	2.0	1.0	1.0	1.2	1.1	1.0 ANAHEIM	1.0	.8	.7
9	.5	.4	.4	.4	.4	.4	.6	1.3	1.0	2.4	2.9	5.7	7.7	3.8	2.0	1.7	1.4	1.2	1.2	1.2	1.0	.9	1.0	.9	.8
8	.5	.4	.4	.4	.4	.4	.8	1.4 PALOS VERDES	1.0	2.1	3.4	7.1	9.7	6.0	2.8	1.6	1.0	1.2	1.2	1.2	1.0	1.0	1.1	.9	.8
7	.5	.4	.4	.4	.4	.4	.8	1.0	1.7	2.0	5.0	7.9	6.2	3.5	2.0	11.9	7.4	1.5	1.8	1.0	1.2	1.3	1.2	.9	.7
6	.5	.4	.4	.4	.4	.6	.8	.6	.0	1.4	1.3	1.0	1.1	.9	.6	1.7	1.8	1.4	1.3	1.3	1.0	1.3	1.1	.9	.8
5	.5	.3	.4	.4 PACIFIC OCEAN	.4	.4	.4	.4	.4	.4	.4	.4	.4	.3	.8	.8	.6	1.1	1.0	1.3	1.3	1.3 SANTA ANA	1.2	1.1	1.0
4	.5	.3	.3	.4	.4	.6	.4	.4	.4	.3	.3	.0	.8	.8	.8	.0	.8	.5	1.1	1.3	1.4	1.4	1.3	1.3	1.2
3	.5	.5	.3	.4	.4	.4	.4	.4	.4	.4	.4	.3	.0	.0	.0	.0	.3	.0	.5	1.0	1.8	1.8	1.3	1.3	1.2
2	.5	.3	.3	.4	.4	.4	.4	.4	.4	.4	.3	.3	.3	.8	.3	.3	.3	.8	.0	.5	.7	1.0	1.0	1.1	1.1
1	.5	.4	.3	.4	.4	.4	.4	.4	.4	.4	.4	.4	.4	.4	.3	.3	.3	.3	.3	.2	.3	.4	.6	.9	1.0

FIGURE 42. GROUND-LEVEL SO_2 CONCENTRATIONS AFTER 2 HOURS OF SIMULATION USING v_d = 4 CM SEC^{-1} OVER WATER AND 1 CM SEC^{-1} OVER LAND

determining the grid-averaged surface characteristics that would be necessary to select an appropriate deposition velocity.

The limitations mentioned above were encountered when the SAI trajectory model was used to determine the sensitivity of predictions of surface concentrations of photochemical pollutants to surface sinks. Deposition velocities of approximately 1.5 cm sec^{-1} for NO_2 and O_3 have been reported by Hill (1971) over a 40.6 cm alfalfa canopy. Measured surface loss rates of NO (Hill, 1971) are at least an order of magnitude lower than those for NO_2 and O_3. Sabersky et al. (1971) measured a deposition velocity on the order of less than 0.01 cm sec^{-1} for ozone over lucite. Based on these values and the limited vegetation in the Los Angeles Basin, we have used deposition velocities of 0.5 cm sec^{-1} for ozone and nitrogen dioxide and 0.05 cm sec^{-1} for NO.

a. Results for NO_2 and O_3

The results of running a trajectory model both with and without surface losses are presented in Table 14 and shown graphically in Figure 43. The data used to exercise the trajectory model were collected in the Los Angeles Basin on 29 September 1969, which was a typical "smoggy" day that has been well characterized by Reynolds et al. (1973). The parcel trajectory began at 5 a.m. in the Los Angeles Basin between Pasadena and Burbank, and moved southeast at approximately 3 mph until 9 a.m. Then the parcel moved northeast, crossing El Monte at 11 a.m. The parcel continued on this path and passed out of the modeling region at 1 p.m. When ozone deposition was included in the model, the ozone concentration averaged over the column of grid cells decreased by 11 percent. In the ground cell ozone was reduced by 25 percent.

The predicted NO_2 concentrations were insensitive to the deposition of ozone. When NO_2 deposition was included, however, an NO_2 loss of 40

TABLE 14. DIFFERENCES IN PREDICTED CONCENTRATIONS AT 1300 HRS DUE TO INCLUSION OF DEPOSITION VELOCITIES

	Concentration--pphm*					
Model	O_3		NO_2		NO_x	
	Ground Cell	Column Average	Ground Cell	Column Average	Ground Cell	Column Average
Base Case	28	16.8	7.8	4.76	8.2	5.2
Including O_3 deposition	23	14.9	7.7	4.5	8.2	5.0
(v_d = 0.5 cm sec^{-1})	(18%)	(11%)	(1%)	(5%)	(0%)	(4%)
Including NO_2 deposition	25	14.7	4.7	3.5	4.9	3.9
(v_d = 0.5 cm sec^{-1})	(11%)	(11%)	(40%)	(25%)	(40%)	(25%)
Including NO_2 and O_3 deposition	21	14.8	4.7	3.6	5.1	4.0
(v_d = 0.5 cm sec^{-1})	(25%)	(11%)	(40%)	(25%)	(40%)	(23%)

---

[*] Numbers in parenthesis represent percentage reduction from base case .

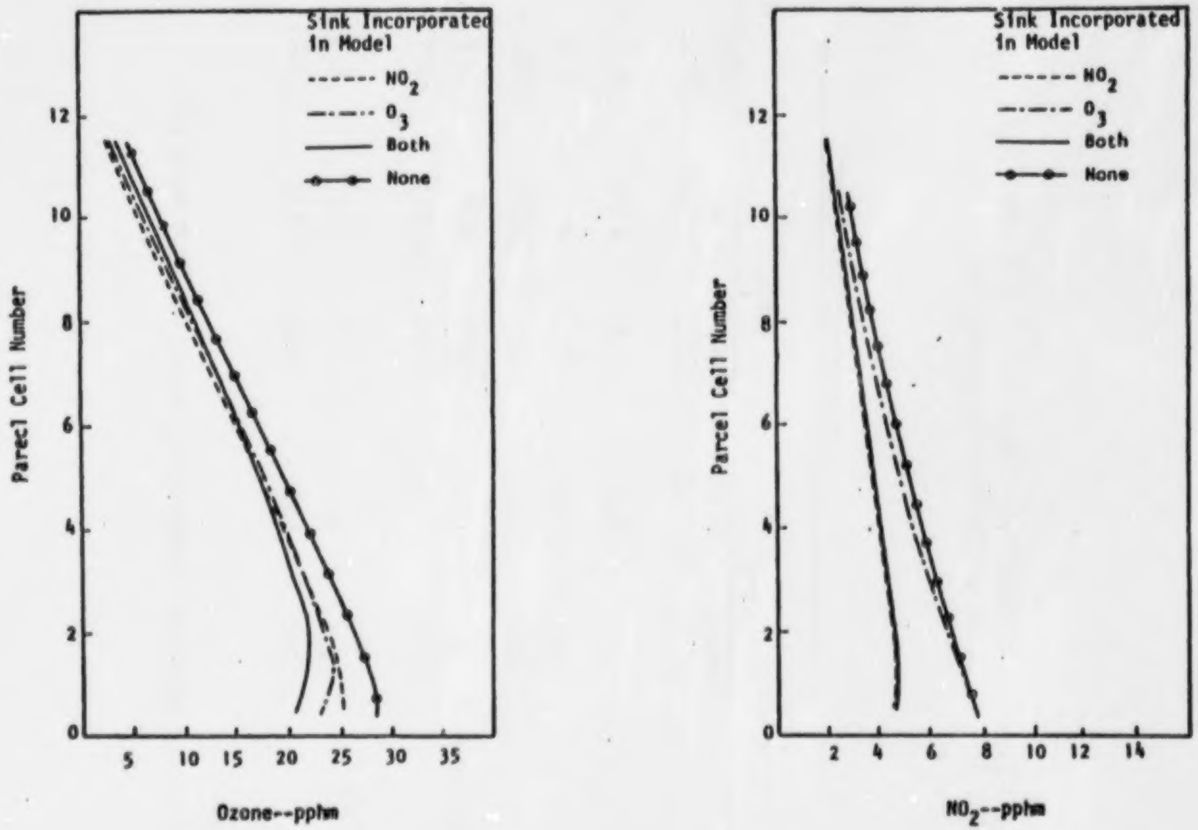

FIGURE 43. PREDICTED PROFILES OF POLLUTANT CONCENTRATIONS AT 1300 PST 29 SEPTEMBER 1969 FOR VARIOUS SINKS INCORPORATED IN THE TRAJECTORY MODEL

percent was found for the ground cell and 25 percent for the entire column.

Since ozone is produced by a process involving photolysis of NO_2, it is reasonable to presume that a loss of NO_2 would produce a loss of ozone. This did, in fact, occur. However, the total ozone in the column showed very much the same reduction regardless of whether the surface sink included was for O_3, NO_2, or both. Indeed, the upper cells in the column show similar ozone profiles for all combinations of values that we used for these sinks. The results differ primarily in the ground cell concentrations.

To some extent these results are reflective only of the particular point chosen along the trajectory for comparison. Inspection of other points along the trajectory, i.e., earlier in the day, indicates that ozone profiles do not always behave in this fashion. However, it is likely that, in any given case, ozone reduction for combined NO_2 and ozone deposition is much less than the sum of the reductions when each is taken separately.

There are two possible explanations for this. Because ozone is a product of the photochemical reactions, and thus is continually being created and destroyed, externally subtracting ozone does not result in an equivalent loss to the system.

Also, because nitric oxide is both a precursor and a destructor of ozone, the relationship between NO_x and O_3 concentrations is complicated. Results from smog chamber experiments suggest that in such environments addition or reduction of NO_x may not produce a corresponding change in ozone concentrations. In extremely hydrocarbon-poor environments, reducing NO_x might produce little change or even an increase in observed ozone levels. While the correspondence between the effect of reducing NO_x (primarily NO) in smog chambers and the effect of NO_2 sinks in airshed models is not exact, the chamber observations do indicate the complicated, nonlinear nature of the problem.

We also studied the persistence of the ozone reduction after the sink was removed from the model (Figure 44). When ozone is the only sink included, switching it off at 11 a.m. results in nearly a full recovery of ozone by 1 p.m. By contrast, ozone loss due to the NO_2 sink appears permanent.

b. Results for NO

As might have been expected, we did not observe significant effects on model predictions due to deposition of NO. Not only is the deposition velocity of NO much smaller than that of NO_2, but also the percentage of NO_x that exists as NO at any given time is often relatively small. In addition, during daylight hours any small loss of NO is immediately replaced by photolysis of NO_2.

In the immediate vicinity of roadways the percentage of NO_x in the form NO is higher. However, the effect of NO sinks is slight, as can be demonstrated with the simple box model. Taking 30 meters as the "immediate vicinity" of the roadway, the loss to the surface would be 1-exp (-.003t/30 meters), where t is the mean residence time of NO within the box. A conservative estimate of t of 20 minutes yields an NO_x loss of 10 percent. During the day, conversion of NO to NO_2 by ozone is rapid, and advection and diffusion also reduce the residence time.

Under nighttime conditions with zero wind speed and very stable atmospheric conditions (a ground-based inversion), NO_x loss due to NO deposition might produce losses of the magnitude of 10 percent.

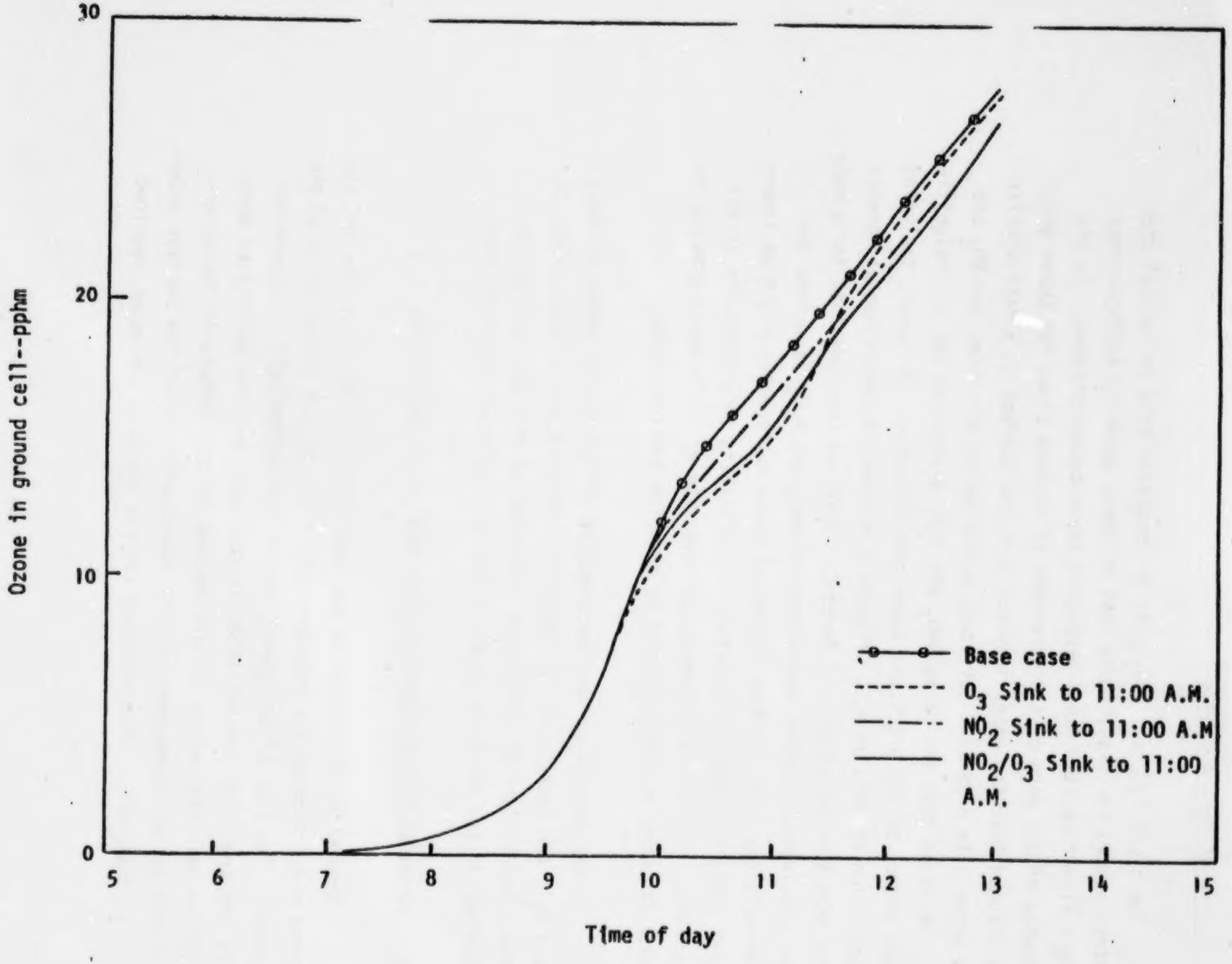

FIGURE 44. PERSISTENCE OF OXIDANT REDUCTION DUE TO SINKS

4. Sinks of H_2O_2 and HNO_2

The gases H_2O_2 and HNO_2 play an important role in radical chemistry; hence, any significant loss of these gases by surface sinks might significantly change predicted ozone concentrations. In the absence of any data on the strengths of surface sinks for these gases, we assumed that the gases interact with the surface at a rate similar to ozone. In a sensitivity study conducted as described for NO_2 and O_3, we found that including HNO_2 and H_2O_2 deposition has an insignificant effect on the predicted ozone concentration. Moreover, including deposition of HNO_2 or H_2O_2 produced a maximum concentration difference for that species of about 5 percent. Thus, we conclude that for single day simulations surface deposition of HNO_2 and H_2O_2 is unimportant. For multiday runs, surface losses of these two species might be important since both may be important in initiating smog chemistry in the morning. However, a ground-based inversion at night would greatly reduce atmospheric transport and so minimize surface losses.

In the absence of any measurements of deposition rates for HNO_2 and H_2O_2 and because of the apparent insensitivity of predictions to their deposition for single-day transport we did not incorporate surface losses of these gases in the air quality simulation models.

F. INCORPORATION OF SURFACE SINKS INTO THE AIRSHED MODEL

Removal of pollutants by surface sinks is treated in the SAI airshed model through the boundary conditions on the bottom cells of the model. The flux of pollutants out of the bottom cell is determined by the predicted concentration in that cell and the calculated deposition velocity, which in turn depends on the turbulence characteristics of the atmosphere and the characteristics of the surface underlying that cell. Incorporating surface sinks in the model required changes to

- Determine the diffusional resistance through the bottom cell.
- Determine the surface uptake characteristics of each grid square.
- Determine the NO released as a result of NO_2 uptake.

1. Determination of the Diffusional Resistance Through the Bottom Cell

In the airshed model, the flux to the surface is calculated by determining the deposition velocity from the diffusional resistance and the surface resistance. Section B presents a methodology for separating the dependence of the deposition velocity for a given pollutant on meteorology from its dependence on surface conditions. The surface resistance is discussed in the next subsection. The diffusional resistance is calculated from Equations (60) through (63) and the friction velocity, u_*, which is calculated as part of the diffusivity algorithm described in Volume 6 of this report.

2. Determination of the Surface Uptake Characteristics of Each Grid Square

As an aid to model users, we consider the preparation of sink inputs for the Los Angeles Basin. In this section we discuss the estimation of surface characteristics by grid square for that region. Note that many assumptions and approximations are required in this estimation because of the limited data available at present.

A large portion of the land surface of the Los Angeles Basin is composed of concrete and asphalt. The remaining soil and vegetation have been exposed to air pollutants for years. To determine the surface resistance, R_{sij}, for pollutant i in grid square j, we estimated the surface uptake velocity v_{sij} (= R_{sij}^{-1}) from

$$v_{sij} = \sum_k \alpha_{jk} \beta_k v_{si}^a \quad , \qquad (69)$$

where v_{si}^a is the surface uptake velocity for the 40.6 cm alfalfa canopy for species i (Hill, 1971), β_k is a factor that adjusts the surface uptake rate for alfalfa to the rate for land use k, and α_{jk} is the fraction of grid square j represented by land use k. Although alfalfa is not typical vegetation in the Los Angeles Basin, we used Hill's data for alfalfa because they are the most extensive data available. To obtain values for β_k we assumed that each land use type in the Los Angeles Basin was made up of different proportions of three surface types. The surface types used were trees, short grasses, and man-made surfaces such as concrete and asphalt. The value of β_k was calculated by relating the rate of surface uptake for a particular surface to rate measured by Hill for alfalfa, and then taking a weighted average of these rates based on the fraction of that surface type in a particular land use type.

For all pollutants, the rate of surface uptake by short grasses was taken initially to be one-half the rate for the alfalfa canopy. Shepherd (1974) measured SO_2 deposition to short grasses and found a surface resistance of 80 sec m^{-1}, roughly twice the resistance that Hill (1971) measured for alfalfa. However, it is unlikely that the same factor of one-half applies to all the pollutants considered in this study. Further measurements of the adsorption of these pollutants by different surfaces would permit more accurate estimates of the relative uptake rates.

For trees we assumed that the surface uptake rate is twice that of the alfalfa canopy. This choice is somewhat arbitrary, but is supported qualitatively by observed relationships between pollutant uptake rates and leaf area (Dannevik et al., 1974). Again, these surface uptake rates must be reconsidered when additional data become available.

The remaining surface area in the Los Angeles Basin was assumed to be composed of asphalt, concrete, and other man-made substances. Data on pollutant uptake rates by these surfaces are limited, but deposition velocities for ozone over man-made surfaces such as plywood, plate glass, aluminum, and lucite indicate extremely low uptake rates. Hence for dry asphalt and concrete surfaces we assumed negligible uptake rates for pollutant gases.

Land use maps were studied to determine the types of surfaces to be found in each grid square of the model. Three types of land use were considered: (1) central business district, (2) suburban residential areas, and (3) rural or agricultural areas. For central business districts we assumed that the land area was ten percent vegetation (primarily trees), so β_1 in Eq. (69) equals 0.2. For suburban residential areas the following breakdown of land usage was obtained from Myrup and Morgan (1972):

- 20 percent roads and sidewalks
- 30 percent lawns
- 20 percent tree cover
- 30 percent houses, driveways, etc.

Combining these factors, we obtained a value of 0.5 for β_2. Rural areas of the Los Angeles Basin are composed primarily of short and tall grasses and chapparal. To our knowledge, no data exist on pollutant uptake rates by chapparal. We assumed a value of 1 for β_3 based on our speculation that uptake rates by rural areas should be greater than those of short grasses and less than those of trees.

Many of the grid squares in the modeling region are over the Pacific Ocean. Intuitively, we expect that the surface uptake rate for a particular pollutant gas over water is related to its solubility in water. Ozone is relatively soluble in water (at 20°C the Henry's Law constant is approximately an order of magnitude less than that for molecular oxygen). Thus we might expect that water is a more efficient sink for ozone than are vegetative surfaces or soil. However, data presented by Aldaz (1969) indicate that ozone deposition velocities over water are about an order of magnitude less than deposition velocities measured over sand or dry grass. The uptake rate of SO_2 by sea water was found to be diffusion-limited (Shepherd, 1974). However, it must be noted that the solubility (as measured by the weight of pollutant dissolved per 100 weights of water at a given partial pressure of the pollutant) of SO_2 is about three orders of magnitude greater than the solubility of ozone (at 20° C; Chemical Engineer's Handbook, 1963). Because of the wide range of solubilities of pollutant gases in water, the assumption that β_k is independent of the pollutant is apparently not valid for water surfaces (and may in fact be a poor approximation for vegetation, which is largely composed of water). For the present study, we assumed a value of β equal to 4, based on the range of observed SO_2 deposition velocities. Clearly, more work is required to determine suitable uptake rates by water of pollutants other than SO_2.

Using the procedures described above, we calculated values of $\sum_k \alpha_{jk}\beta_k$ for each grid square in the Los Angeles Basin. These results are shown in Figure 45.

3. The Treatment of NO Release from NO_2 Uptake

In order to account for the previously mentioned conversion of NO_2 to NO by vegetation, which we hypothesize is due to the reaction

$$3NO_2 + H_2O \rightarrow 2HNO_3 + NO \quad , \qquad (70)$$

we added an NO source term equal to one-third the deposition flux

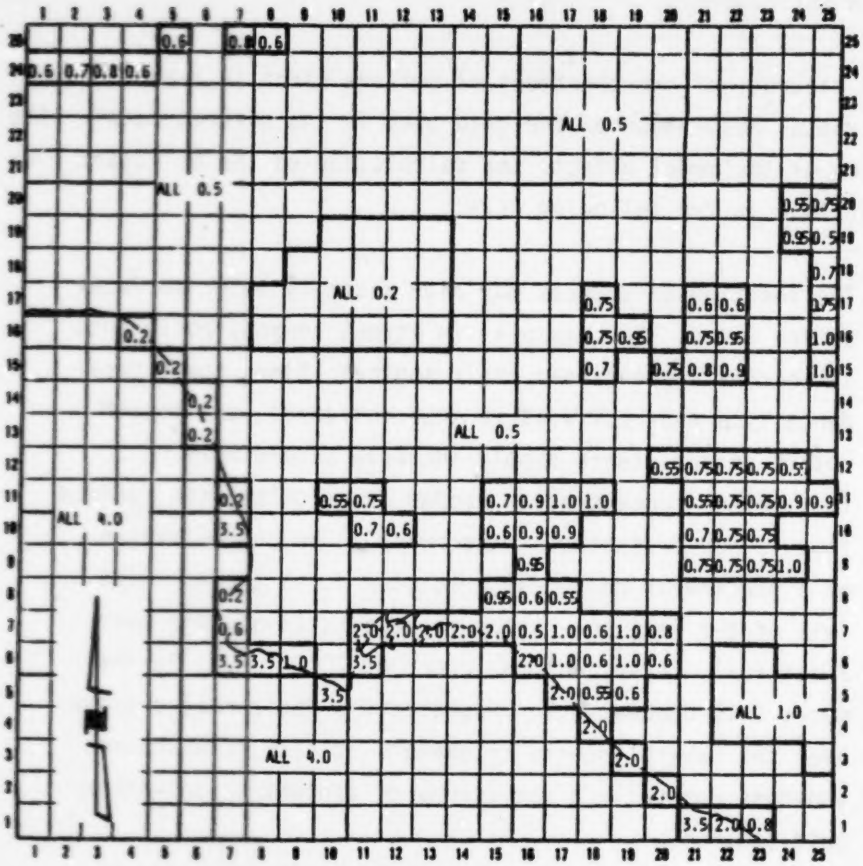
0.6
0.8
0.6
0.6
0.7
0.8
0.6
ALL 0.5
ALL 0.5
0.55
0.75
0.95
0.5
0.7
ALL 0.2
0.75
0.6
0.6
0.75
0.2
0.75
0.95
0.75
0.95
1.0
0.2
0.7
0.75
0.8
0.9
1.0
0.2
0.2
ALL 0.5
0.55
0.75
0.75
0.75
0.57
0.2
0.55
0.75
0.7
0.9
1.0
1.0
0.55
0.75
0.75
0.9
0.9
ALL 4.0
3.5
0.7
0.6
0.6
0.9
0.9
0.7
0.75
0.75
0.95
0.75
0.75
0.75
1.0
0.2
0.95
0.6
0.55
0.6
2.0
2.0
2.0
2.0
2.0
0.5
1.0
0.6
1.0
0.8
3.5
3.5
1.0
3.5
2.0
1.0
0.6
1.0
0.6
3.5
2.0
0.55
0.6
ALL 1.0
2.0
ALL 4.0
2.0
2.0
3.5
2.0
0.8

FIGURE 45. VALUES OF $\sum_k \alpha_{jk}\beta_k$ FOR GRID SQUARES IN THE LOS ANGELES BASIN

calculated for NO_2. An appropriate modification was made to the NO_2 surface deposition velocity to make this value conform to the net NO_2 flux observed by Hill (1971).

G. THE EFFECTS OF AVERAGING SURFACE UPTAKE RATES AND CONCENTRATIONS OVER GRID SQUARES

The accuracy of the treatment of surface sinks is restricted by the horizontal resolution of the grid used in the airshed model. The resolution of the model affects the calculation of the pollutant flux to the surface in the following ways:

- > The location of sources may significantly alter surface uptake rates. For example, in street canyons pollutants can become trapped near their source. Since their residence time near surfaces is thus increased, the total uptake of pollutants should increase accordingly.
- > The surface concentration needed to calculate the surface flux is not predicted by the model. The concentration of a particular pollutant predicted for a ground-level cell of the modeling region represents an average over a vertical distance on the order of 20 meters. Furthermore, this concentration represents a horizontal average over the several square kilometers of each grid square, and does not reflect variations of concentration within grid squares.
- > The surface characteristics, and hence the deposition velocity and surface uptake rates, may vary significantly within the grid squares. The surface flux of a pollutant is given by the product of its surface concentration and its deposition velocity. The actual average surface flux of a pollutant is not simply the product of its average concentration and its average deposition velocity over a grid square.

The first effect is treated in the microscale work which is reported in Volume VI of this report. We have not attempted to deal with this effect any further in this phase of the contract. We considered a methodology for extrapolating surface pollutant concentrations from predicted ground-cell concentrations. In this methodology, a boundary layer profile of pollutant concentrations is assumed and the near-surface concentration is calculated from the average concentration within the ground cell. However, the concentrations from which deposition velocities are calculated are generally measured within 2 meters of the surface. Because surface elevations often vary much more than this over the grid squares, extrapolation of the concentrations in this manner without taking into account variations in surface roughness within the ground-level grid cells would be inconsistent. Hence, we assumed that the concentrations in the ground cell are uniform, and calculated the surface flux on the basis of the predicted cell-averaged concentrations.

H. SUMMARY AND CONCLUSIONS

A simple model for the removal of gaseous pollutants by surface sinks has been incorporated into the SAI Urban Airshed Model. The surface sink model considers surface removal to occur in two phases--transport to the surface followed by adsorption on the surface. The resistance to surface uptake (the reciprocal of the deposition velocity) was determined from deposition velocities measured under atmospheric conditions that lead to rapid transport to the surface (that is, so that surface removal was limited by the surface uptake rate).

Deposition rates have been measured under the widest range of conditions for SO_2, but even for this pollutant few surface types have been studied. Because of this lack of data it is necessary to make crude estimates for deposition rates over surfaces found in the urban environment. The improvement of these estimates for the Los Angeles Basin awaits additional measurements of deposition velocities under a variety of meteorological conditions over surfaces common in the Basin. Sensitivity studies performed with our estimated deposition rates indicate that surface uptake of SO_2, NO_2, and ozone in the Basin can have a significant effect on the concentration of these pollutants.

IV OBJECTIVE CONSTRUCTION OF THREE-DIMENSIONAL WINDFIELDS

by Gerald E. Anderson

This chapter describes the windfield input needed by the SAI Urban Airshed Model, the data resources available, some analytical techniques for determining the windfield input, and the technique adopted. Because of the present interest in applying the model to air pollution problems in the St. Lcuis area using the Regional Air Pollution Study (RAPS) data base, the windfield algorithm described herein is intended to be particularly applicable to the climatology, topography, and urban development pattern of that area. The analytical approach suggests rather straightforward extensions of the algorithm for application to areas with more complex characteristics. Background discussions of principles and practices presented here substantiate the view that no single objective technique is applicable to all problems. The validity of the technique presented for application to St. Louis cannot be fully assessed on the basis of the arguments of this report but must depend on careful review of application experience.

A. BACKGROUND

A basic element of any pollution analysis is to determine where the pollutants that reach a given receptor volume came from. The sources of the photochemical pollutants for each receptor volume are the chemical reactions within, and the emission and diffusion into, the bundle of streamlines that enter that receptor volume. All of the streamlines in the modeling region constitute the region's "windfield." Thus an accurate specification of the windfield is required for accurate modeling. The size of the grid cells in a model determines the resolution required in the windfield. The spatial and temporal resolution of pollutant concentrations obtainable from model predictions cannot be finer than the resolution of the emissions distribution. That is, if the location of an emissions source is not known to within 1000 meters, pollutant concentration patterns cannot be predicted with a resolution finer than 1000 meters, and therefore the windfield transporting the pollutants need not be known with a resolution finer than 1000 meters. The converse is also true; if streamlines cannot be resolved to within 1000 meters, the emission sources need not be known to within 1000 meters.

Consider the sketch below:

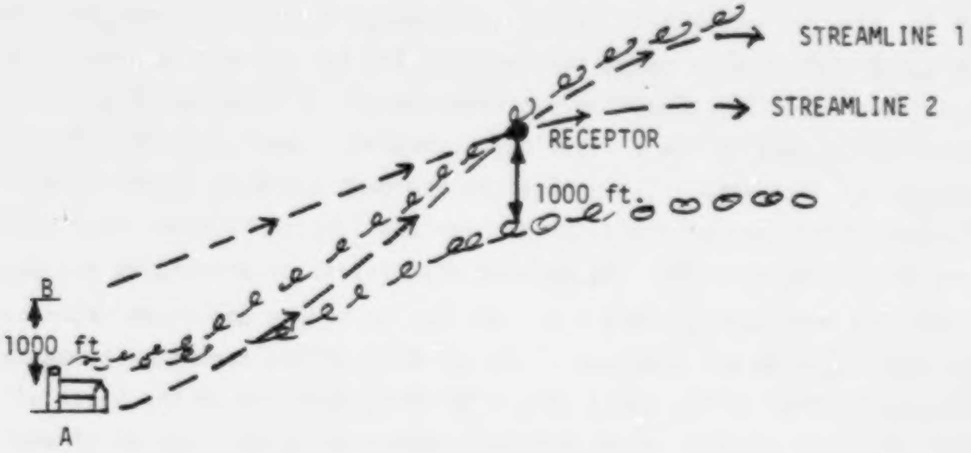

If it is uncertain whether the wind passing the receptor came along Streamline 1 or Streamline 2, then it is uncertain whether the smokestack shown at A would impact the receptor or a point 1000 feet to the side. Similarly it is uncertain whether the source would have impacted the receptor if it had been located on Streamline 2 at B. Thus, given the uncertainty in the streamlines, it is irrelevant whether the source is placed at A or B in the analysis of impacts at the receptor.

Given a situation in which observations of the wind are too sparse and/or too dependent on subgrid-scale disturbances, it may yet be possible to define wind patterns by using information about some physical determinor of the wind pattern. This approach may be possible if the factors that affect the wind pattern are themselves measurable.

Wind patterns may be determined by local factors or distant upwind (and possibly downwind) factors. If the factors are local (such as topography or surface temperature within the analysis region), the possibility exists that the patterns could be defined as functions of the local measurements of the influencing factors. If the factors are distant (such as eddy-producing upwind topography) or if they are not easily measured within the scope of a modeling application (such as thermal fields associated with air-mass boundaries), then they probably cannot be looked to as candidates for wind determining functions.

Wind variations on time or space scales larger than the grid cell size and time interval used in a model are treated simply as patterns on the grid. That is, they constitute features of the defined windfield. If the scale of the wind variability is large enough, the variations are not discernible over the modeling region and are considered as different boundary or driving conditions that may be encountered. Wind variations on scales smaller than the grid cell size must be assumed to have zero means when averaged over a grid cell, since they do not contribute to the mean motion. Expressed statistically, wind fluctuations about the mean constitute a nonzero variance in the wind. Since the variations are, by definition, not zero, they result in pollutant exchanges between grid cells; these subgrid-scale variations are interpreted as turbulence. Thus the definition of turbulent diffusion coefficients cannot be made independently of the size of the grid cell being used.

Though subgrid-scale wind variations must be assumed to have zero means when averaged over a grid cell, they also can have local biases in addition to variance; for example, they can have nonzero means when averaged over some smaller space or time domain.

Interpolation of wind measurements is based on the assumption that the differences between wind vectors at adjacent stations represent variations on the scale of the station separation. If large variations can exist at much smaller scales, the wind vectors give no clues at all to behavior at the larger scales. The situation is schematically shown in Figure 46. The wind vectors measured at A and B in this sketch are not sufficient to distinguish between the wind patterns a, b, and c or, indeed, between any patterns that are tangent to the given vectors at A and B.

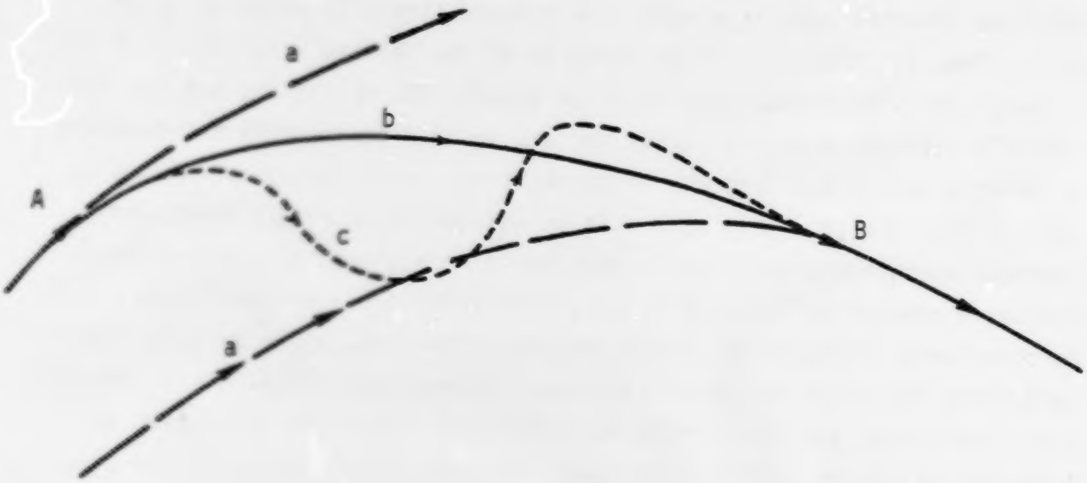

FIGURE 46. THREE WIND PATTERNS CONSISTENT WITH TWO MEASURED WIND VECTORS

This effect must be considered in judging the adequacy of direct wind measurements or measurements of related parameters. The potential danger of relying on instrumental measurements can be seen clearly in Figures 47 and 48. These figures show seasonal wind roses from five sites spaced roughly around a 3000-foot circle (the grid cells shown are 1000 feet) in a mostly wooded area of rolling hills in rural Connecticut. Sites A and B are at 2500 and 65 feet above ground level respectively, and C, D, and G are at 8 feet. The lack of correspondence between these wind roses, which must result from local biases, would leave indeterminancy (such as that shown in Figure 46) in grid-scale wind patterns. Thus these anemometers, though correct, are not providing measures of the wind that are useful for dispersion analyses. It is safe to rely on instrumental measurements only if the instrument measures a parameter of interest and defines that parameter on a time-and-space scale of interest.

The relationship between instrumental and analytical scales is described by Anderson (1971). An anemometer senses the state of motion of a volume of air not much larger than itself, perhaps a few feet in each direction. Average wind vectors for much larger volumes are commonly inferred by averaging anemometer readings over long times. The validity of this inference depends on the assumption, called the "Taylor hypothesis," that a windfield with statistically stationary, homogeneous, and isotropic variations is passing the anemometer. Because of the statistical uniformity, the anemometer cannot distinguish between the temporal variations that sweep by it and the spatial variations it would encounter if it traversed the volume. Thus the Taylor hypothesis allows the equating of spatial and temporal averages of wind velocities.

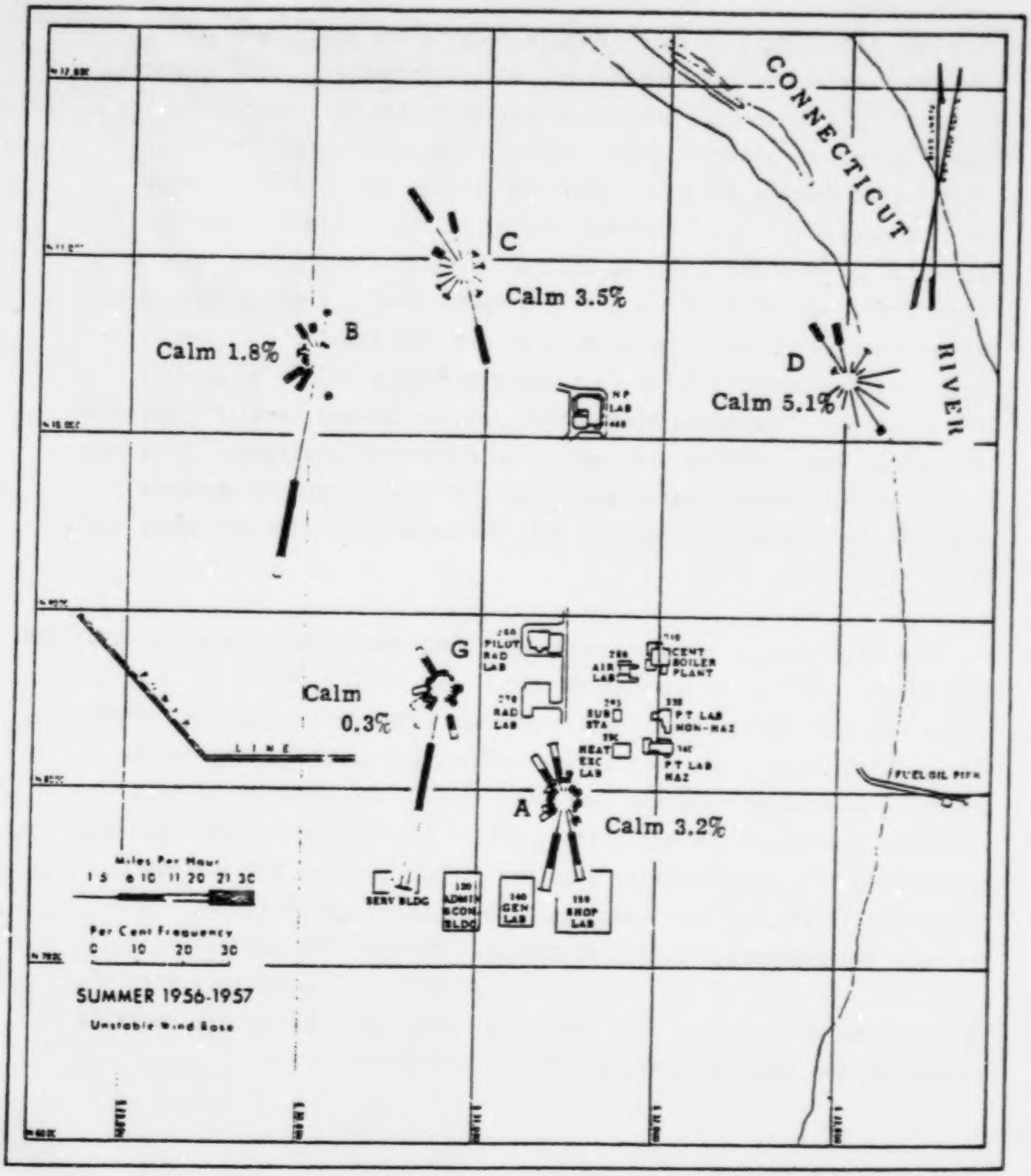
CONNECTICUT RIVER
C
Calm 3.5%
B
Calm 1.8%
D
Calm 5.1%
NP LAB
G
Calm 0.3%
PILUT RAD LAB
RAD LAB
AIR LAB
CENT BOILER PLANT
SUB STA
P T LAB NON-HAZ
HEAT EXC LAB
P T LAB HAZ
A
Calm 3.2%
LINE
FUEL OIL PIPE
SERV BLDG
ADMIN &CON. BLDG
GEN LAB
SHOP LAB
Miles Per Hour
1 5 6 10 11 20 21 30
Per Cent Frequency
0 10 20 30
SUMMER 1956-1957
Unstable Wind Rose

FIGURE 47. WIND ROSE VARIATIONS AT A CONNECTICUT SITE

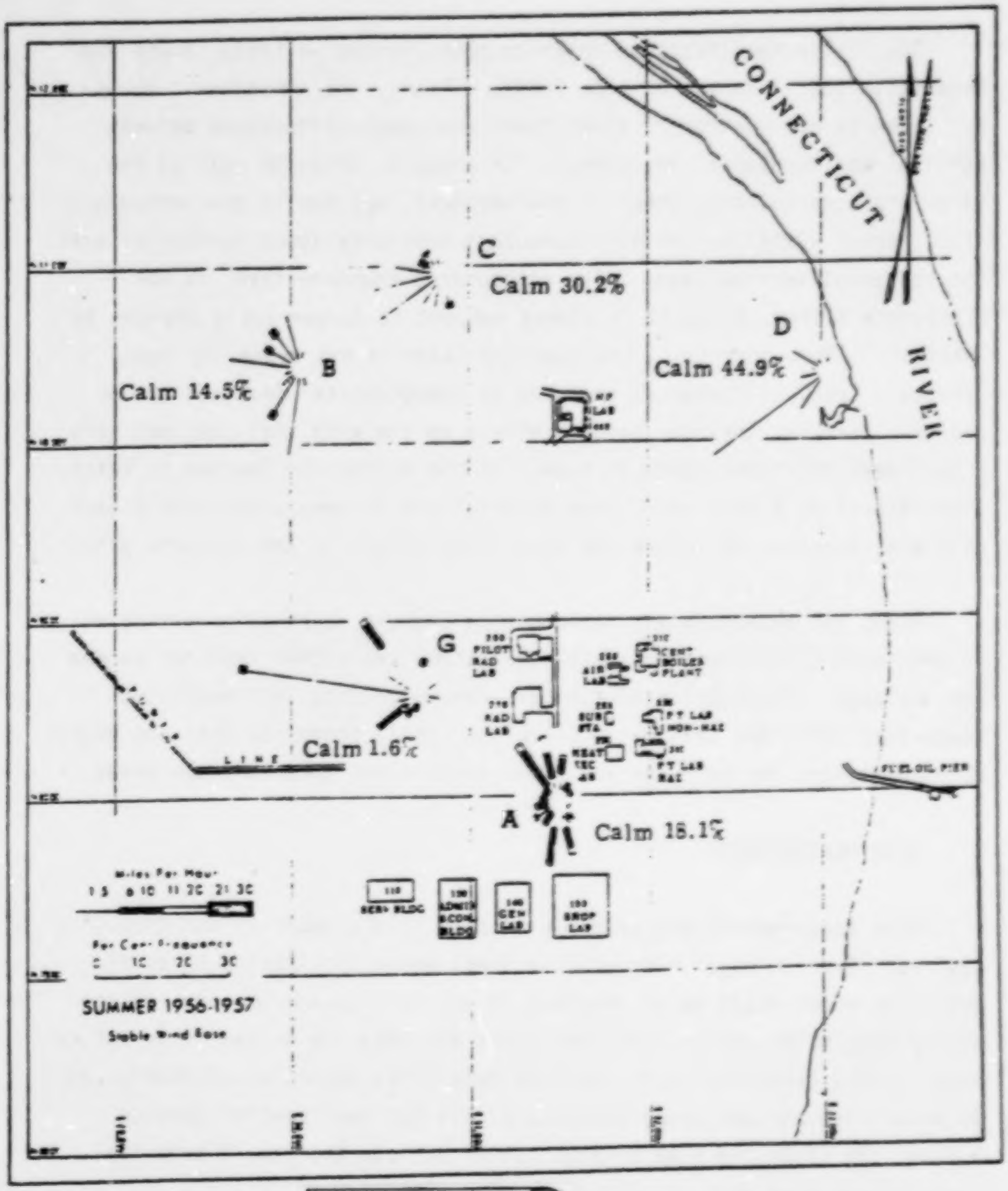
CONNECTICUT
RIVER
C
Calm 30.2%
B
Calm 14.5%
D
Calm 44.9%
HP
LAB
G
PILOT
RAD
LAB
RAD
LAB
AIR
LAB
CENT
BOILER
PLANT
SUB
STA
PT LAB
NON-RAD
REAT
TEC
AB
PT LAB
RAD
FUEL OIL PIER
LINE
Calm 1.6%
A
Calm 15.1%
SERV BLDG
ADMIN
& CONL
BLDG
GEN
LAB
SHOP
LAB
Miles Per Hour
1 5
6 10
11 20
21 30
Per Cent Frequency
0
10
20
30
SUMMER 1956-1957
Stable Wind Rose

Reproduced from
best available copy.

FIGURE 48. WIND ROSE VARIATIONS AT A CONNECTICUT SITE

The Taylor hypothesis is known to have limited validity (Bowne and Anderson, 1968; Anderson et al., 1969). Clearly the atmospheric boundary layer is not isotropic, since there are great differences between vertical and horizontal phenomena. For example, friction against the earth produces velocity shear in the vertical, but not in the horizontal. Also thermal stability inhibits turbulent vorticity about horizontal axes, but not about vertical axes. The atmospheric boundary layer is not stationary either, since it is always subject to larger-scale changes in "weather." More important, the boundary layer is not typically homogeneous. Local disturbances produced by topographical features can be biased. That is, they can have an effect on the wind that does not have a zero mean in either space or time. If the disturbing feature is small with respect to a grid cell, then observations at many sites within each cell are necessary to define the wind distribution on the analysis grid.

Winds can be accurately interpolated between observation points only if the local (i.e., subgrid-scale) variations are either small or random and unbiased. Examination of typical anemometer data in Connecticut (Anderson, 1971) and California (Anderson, 1973) indicates that the necessary conditions for wind interpolation are not well met in those areas.

B. WIND MEASUREMENTS

Wind measurements are seldom available in the quantity and frequency desired. Even in major metropolitan areas where application of an air pollution model might be of greatest value, surface anemometers are generally many miles apart; sometimes there are only one or two in an entire area. Sites contributing to the STAR data files record winds hourly, as do major airports and urban stations of the National Weather Service (often such sites are STAR sites). Other private and public organizations record wind data at different intervals.

The only routinely collected data on winds above ground level come from pibals (pilot balloons, free-rising balloons tracked by theodolites) and rawinsondes (radio wind sounders, free-rising balloons carrying transmitters that are tracked by radar). Rawinsondes are typically released twice a day (midnight and noon GMT) from NWS stations. Rawinsonde data are collected at irregular altitude intervals, ranging from a measurement every few tens of meters to every few hundreds of meters in the lower, boundary-layer portion of the atmosphere. The lowest rawinsonde wind observation is typically about 150 meters above the point of release.

Special study areas may have much more dense arrays of instruments. The St. Louis metropolitan region has one of the most extensive observational networks. The Metromex (Chagnon, 1975) and RAPS (Burton and Hidy, 1974) studies operated up to 25 anemometers read continuously. Two to four sites releasing four rawinsondes each per day were planned. It is understood that more may be added (Demerjian, 1976); these data are to be supplemented by frequent pibal soundings. The Regional Air Monitoring Systems (RAMS), a part of RAPS, is intended to provide input for local and regional air quality simulation models (Burton and Hidy, 1974). Research programs have been planned to study the three-dimensional structure of the planetary boundary layer, the variability of meteorology and pollutant concentrations, plume behavior, and other subjects.

C. OBJECTIVE ANALYSIS TECHNIQUES

Measurements cannot mathematically define dependent variables at a scale finer than the separation of measurement stations. The minimum definable scale of variability is that which contains two measurement stations; specification of variables on a finer scale through interpolation can only be "right" in the sense that the results are consistent with physical principles and possess the least information (i.e., second and higher derivatives are minimized) beyond that required to fit the data.

A wide variety of objective analysis techniques have been proposed and used to determine the values at grid points of variables measured at irregular points (Panofsky, 1949; Gilchrist and Cressman, 1954; Gandin, 1965; Dartt, 1972; Barnes, 1973; Liu and Goodin, 1975). Since the grid points are generally between measurement points, objective analysis is generally an interpolative process. As discussed in Section A, any interpolation or extrapolation of wind measurements is valid only if the measurements are substantially free of local biases and if the Taylor hypothesis holds, allowing the equating of spatial and temporal averages.

For application of the SAI Urban Airshed Model to the St. Louis area, an interpolative scheme must be used to define three-dimensional windfields consistent with data from a sparse network of measurement stations. The network is sparse in the sense that resolution is required at many more grid points than there are stations. The 25 RAMS anemometers are distributed irregularly within a 100 x 100 km region (Burton and Hidy, 1974). They are quite close together in the center of the region, but the total set is roughly contained in a square that is inscribed within the 100 km square and oriented diagonally to it. No anemometers are located within the grid corners, which contain roughly half of the region. Thus, objective analysis involves substantial extrapolation. Of the rawinsonde stations, one is at the center of the region and three others are 30 to 35 km from the center. Estimation of model inputs for the subregion outside of the diagonal (inscribed) square requires the use of extrapolation techniques.

The following four types of interpolative techniques have been used widely for deriving gridded fields from measurements:

> Statistical Fits--e.g., the "least squares" fits of the constants of a chosen functional form (often plane surfaces in two-dimensional problems).

> Influence Factor Fits--the value of the field at a given grid point is the sum of the "contribution" from each data point, where each contribution is the value at the

data point weighted by some function of the distance between the data point and the grid point.

> Spectral Fits--a family of functions of periodic form (sine and cosine waves for Fourier analysis) is spectrally weighted to provide a desired degree of approximation to the data points; spectral filtering is often used to limit the family "membership" and/or to specify the data fitting accuracy required.

> Boundary Value Fits--the value of the field at any grid point is the solution of a differential equation given the data points as boundary values.

Each of these techniques offers advantages for certain classes of problems. In the following sections we consider the strengths and weaknesses of each.

1. Statistical Fits

Statistical fits are most suited to problems where there are many more data points than there are acceptable degrees of freedom on the functions to be fit. This is not the case in deriving windfields for the St. Louis area. In St. Louis, significant wind variations can exist in the areas between measurement stations; thus, nearly as many empirical coefficients would be needed to derive a windfield as there are stations.

2. Influence Factor Fits

Influence factor fits (Cressman, 1959; Inman, 1970; Barnes, 1973; Adkins, 1974) seem appropriate when they represent a conceptual model; that is, the field at one point is seen to actually depend on the shape of the field beyond the nearest data point. For the St. Louis windfield, it is not clear why there should be such an influence past the nearest data point. It would seem more likely that influences closer than the nearest data point would be important.

As shown in this sketch,

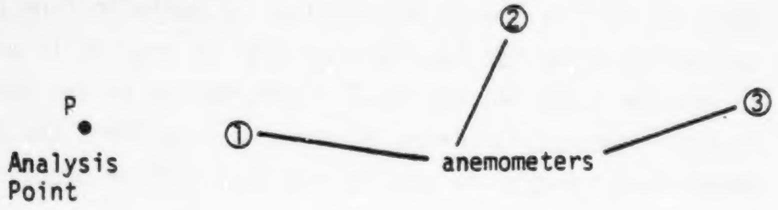

in an influence factor approach the wind at P depends strongly on the wind at 1, less on that at 2, and even less on the wind at 3. Why should the wind at P depend on 2 and 3? There is some doubt that it even correlates with the wind at 1. If an anemometer were placed at P, its reading might depend on the physical factors (e.g., obstacles) much nearer P than anemometer 1.

The advantage of influence factor fits is that only the nearest neighbors have any significant influence because of the weighting factors commonly used. The technique tends to minimize first and second derivatives of the functions near data points. Minimizing first derivatives seems undesirable, since eliminating slopes tends to leave "terraces" in the resulting field. Minimizing second derivatives seems desirable, but the system has little ability to reduce second derivatives in spaces between data observations.

This type of objective analysis was applied to the RAMS data and the RAPS region by Hovland et al. (1976). They concluded that:

> The program documented in this report, when properly applied to reliable data sets, should yield satisfactory analyses on the scale of RAPS. Error rejection can be accomplished whenever there are sufficient data to check on inter-station consistency. This cannot be done with the sparse network utilized to collect the upper air data for RAPS. Furthermore, even in the surface network, having reliable data at the outermost stations is crucial for a successful analysis of the entire field. This is due to the varying density of the observing network of the Regional Air Monitoring System. Special priority should be given to the proper functioning of these key stations.
>
> The results of this development effort strongly suggest that the RAPS upper air network is insufficient to adequately observe the three-dimensional structure of the meteorological

> fields. An intensive period of adequate upper air sampling would provide a basis for vertical continuity from the surface to upper levels which is not possible with available data.

The technique of Hovland et al. involves iteration from an initial-guess field to a final field consistent with the observations. At each iteration step, influence factor weighting is used on the differences between the data and the current iterative result.

Our review indicates that much of this computing effort is unnecessary because the result of any grid point depends only on direct, noniterative use of the weighting factor and on iteration at the measurement stations. Hovland et al. did not show that their technique is superior to a direct, noniterative use of influence factors. (See Exhibit IV-1.)

The results show a basic shortcoming of this type of analysis. In Figure 18 of Hovland et al. (1976), there is no way to say the resultant field is "right" or "wrong," but the curvature of the isopleths toward the corners of the region seems to be an artifact of the station arrangement rather than of the measurements at the stations. For example, the data seem to be consistent with an overall temperature gradient from NE to SW with an urban "heat island" superimposed in the central region. Nothing in the data seems to support the curvature of the 88°F isotherm toward the SW corner, or of the 82°F isotherm toward the NE corner, except the absence of data in those regions.

An infinite number of patterns may be fit through a finite number of points with equal mathematical validity, but prudence suggests that the pattern with the least detail required by the data (and additional information) would be the safest. For example, a single measurement should imply no more than a uniform field unless additional information requires a more complex field.

Writing Equation (1) as

$$(1)\qquad \chi(x,y,k) = \chi(x,y,o) + \sum_{k=1}^{K} \frac{\sum_{j=1}^{J} w(x,y,j)[D(j) - \chi(j,k-1)]}{\sum_{j=1}^{J} w(x,y,j)}$$

where $j \equiv x(j), y(j) \equiv$ coordinate sets for data stations affecting x,y

k = iteration count

Other symbols as in Hovland's Eq. 1.

Since $w(x,y,j)$ and $D(j)$ are independent of k,

$$(2)\quad \chi(x,y,k) = \chi(x,y,o) + K \sum_{j=1}^{J} w^*(x,y,j)\, D(j) - \sum_{j=1}^{J} w^*(x,y,j) \sum_{k=1}^{K} \chi(j,k-1)$$

where $w^* = \dfrac{w(x,y,j)}{\sum_{j=1}^{J} w(x,y,j)}$

If then

w^* is weighting function from conservative, Non-Iterative Scheme (NIS)

$$\chi(x,y,\mathrm{NIS}) \equiv \sum_{j=1}^{J} w^*(x,y,j) D(j) \quad .$$

$$(3)\quad \chi(x,y,k) = K\ \chi(x,y,\mathrm{NIS}) + \left\{ \chi(x,y,0) - \sum_{j=1}^{J} w^*(x,y,j) \sum_{k=1}^{K} \chi(j,k-1) \right\}$$

If further, $\chi(x,y,0) \equiv 0$.

$$(4)\quad \chi(x,y,k) = K\ \chi(x,y,\mathrm{NIS}) - \sum_{j=1}^{J} w^*(x,y,j) \sum_{k=1}^{K} \chi(j,k-1) \quad .$$

Note that in Equation (3) or (4), $\chi(x,y)$ does not really depend on iteration at (x,y) but only iteration at (j), the data stations themselves, and on the initial guess at (x,y).

EXHIBIT 1. OBSERVATIONS ON ITERATIVE METHOD OF HOVLAND, DARTT, AND GAGE (1976)

The second term in the adjustment bracket of Equation (3)

$$\sum_{j=1}^{J} w^*(x,y,j) \sum_{k=1}^{K} x(j,k-1)$$

depends only on a priori information

$$w^*(x,y,j)$$

and

$$x(j,0)$$

and upon the iteration at j, the data station. Since the iteration is at j alone, it should be possible to develop a recursion formula for this term.

At the data stations, at a given interation, k,

$$x(j,k) = kx(j,NIS) + x(j,0) - \sum_{i=1}^{I} [w^*(j,i) \sum_{\ell=1}^{k} x(i,\ell-1)] \quad .$$

For typical weighting functions

$$w^*(j,j) = 1 \quad ; \quad w^*(j,i) \approx 0 \quad .$$

Then

$$x(j,k) = kx(j,NIS) + x(j,0) - \sum_{\ell=1}^{k} x(j,\ell-1)$$

$$= x(j,NIS) + x(j,0) - x(j,0)$$

$$x(j,1) = x(j,NIS)$$

$$x(j,2) = 2x(j,NIS) + x(j,0) - x(j,0) - x(j,NIS) = x(j,NIS)$$

$$x(j,3) = 3x(j,NIS) + x(j,0) - x(j,0) - x(j,NIS) - x(j,NIS) = x(j,NIS)$$

That is,

$x(j,0)$ = initial guess
$x(j,1) = x(j,NIS)$
$x(j,2) = \cdot$
$\cdot \quad \cdot$
$\cdot \quad \cdot$
$\cdot \quad \cdot$

After the first iteration, the result is equal to the result from a non-iterative-scheme if the weighting function influence is small at typical data station separations.

EXHIBIT 1 (Concluded)

3. Spectral Fits

Spectral fits (Peterson and Truske, 1971; Jones, 1972) are generally used when there are not only many more data points than acceptable degrees of freedom, but there are also many realizations of each degree of freedom (i.e., many wavelengths) within the region. Spectral fits seem unsuitable for deriving windfields in St. Louis because of the sparsity of data.

4. Boundary Value Fits

Several facts and assumptions about the fields to be fit in the St. Louis region suggest that the boundary value fit is more appropriate than the techniques described above. Ideally this technique would involve solving the relevant conservation equations on the analysis grid. This has been done for RAPS by Vukovich et al. (1976), but the procedure seems excessive as a subroutine to an already complex air quality simulation model.

Specification of boundary values lends an arbitrariness to the technique, but is consistent with the view that no analytic scheme can be known to be correct in an area for which no data are available. Boundary values that simply preserve the essentials of the field in the interior of the region do less violence to our sensibilities than do the other methods, which are essentially extrapolative near boundaries. Viewed this way, the specification of boundary values does not add assumptions about the structure of the field, but rather assures adherence to no more than is defined within the field. The technique introduces no degrees of freedom not required by the data, and allows each data point to influence the field very strongly in its own neighborhood, but does not reduce the first derivatives of the data.

Boundary value fits do not directly obviate problems of interpreting noisy data. Turbulence constitutes observational noise in an anemometer signal, but time-averaging effectively filters the random components of this effect. Local biases of anemometers (due to topography, buildings, surface characteristics, and so on) introduce stationary small-scale modes, which are "noise" in the spatial distribution. Boundary value fits seem to have very desirable interpolative properties, but they do not resolve problems about the inherent interpolability of the data.

As an example of the use of this technique, consider the Poisson equation, a simple elliptic, second-order differential equation:

$$\nabla^2\phi = F(x,y) \qquad (71)$$

This equation is solved with ϕ held fixed at all known or assumed interior data points and at peripheral points. Specification at data points allows a perfect fit of the data, and the form of the equation and the specification of $F(x,y)$ assure that only enough degrees of freedom to fit the data are allowed.

That is, if it is assumed that $F(x,y) = 0$ (the Laplace equation), one obtains a surface of zero curvature that cannot be fit through the data points. The equation may be solved with the data points as well as the boundary points held fixed (i.e., with internal boundary points) but the surface curvature will then, in general, be finite at the data points. In fact, there will be quite unrealistic delta function discontinuities in curvature.

It is desired to define a forcing function, $F(x,y)$, that reduces the function curvature, $\nabla^2\phi$, as much as possible in the neighborhood of each data point while allowing "smooth" transitions between neighborhoods. That is, neighboring points should determine the intervening surface slopes, but surface curvature should be small everywhere. This can be accomplished by first solving the Laplace equation,

$$\nabla^2\phi = 0 \quad , \qquad (72)$$

where ϕ is specified at the data points and the periphery, and then computing the Laplacian at the data points (it is necessarily zero elsewhere). Repeated smoothing of the point values of $\nabla^2\phi$ is carried out by an operation that preserves total curvature. This then produces a distribution of surface curvature that, in the region about any data point, is proportional to the deviation of that data point from a mean surface. The smoothing algorithm used first defines the value at the center of each grid cell to be the average of the values at each corner of that cell. Next, the value at each grid intersection is taken to be the average of the values at the centers of the four adjacent cells. Each pass through this smoothing operation spreads the same total surface curvature to a region one grid square larger on each side. The smoothing is repeated for a number of times equal to the average spacing (in grid units) between data points. The smoothed curvature distribution is finally used as the forcing function, $F(x,y)$, in re-solving the Poisson equation.

Trials of this technique on Los Angeles surface temperature data by Anderson (1973) give temperature distributions that are qualitatively consistent with subjective analyses and have somewhat more detail, i.e., smaller scale content, in the patterns. A typical computed temperature field is shown in Figure 49.

D. CONSTRAINTS ON THE ST. LOUIS WINDFIELD

To make use of the desirable properties of boundary value fits and yet address the problems of local bias in the observational data and the need for extrapolation over most of the analysis region, we applied substantial constraints to the structure of the St. Louis windfield. To avoid excessive complexity, it was necessary to apply these constraints in an analysis considerably simpler than solution of the boundary layer equations.

Topographic and thermal constraints were studied and applied to the two-dimensional mixing layer for use with air quality simulation models for the Connecticut, Toronto, and Los Angeles areas (Anderson, 1971;

Reproduced from
best available copy.

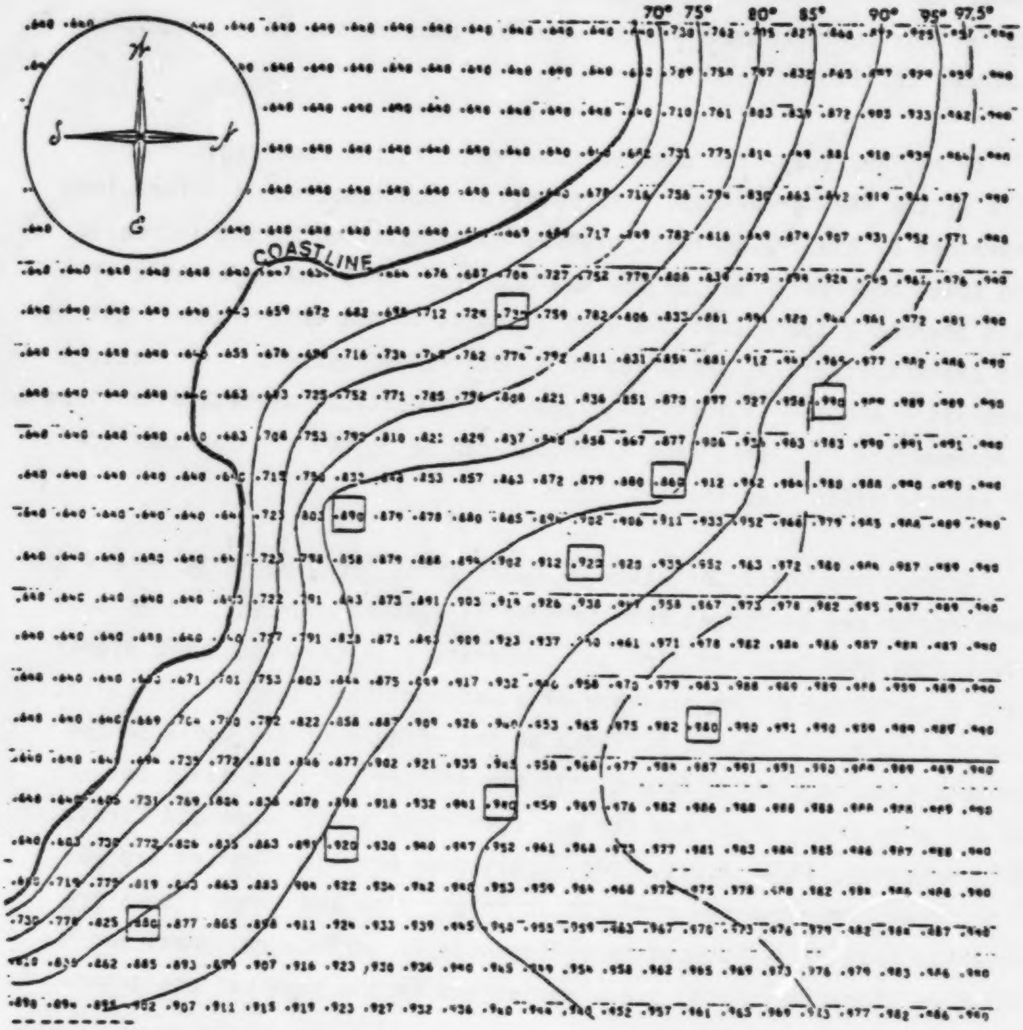
70°
75°
80°
85°
90°
95°
97.5°
COASTLINE

Source: Anderson (1973).

FIGURE 49. ISOTHERMS (°F x 10^{-2}) IN THE LOS ANGELES BASIN. Observed values are in the squares.

Anderson, 1973), urban areas (Fosberg et al., 1972), forest fire studies in complex terrain (Fosberg et al., 1976), and for the San Francisco Bay Region (MacCracken et al., 1974). Recent work at Lawrence Livermore Laboratory (LLL) involved a three-dimensional analysis in which topographic and other physical constraints were applied in an objective windfield analysis. In this technique the data were interpolated onto the grid by a numerical analysis without physical constraints, and then "minimally adjusted" to be "mass-consistent" with the constraints (e.g., topography) (Sherman, 1975).

In regions away from observations--say, in the upper corner grid cells of the RAPS grid--most interpolation techniques would infer winds determined by the ground-level observations amplified by the increased wind speed observed aloft by the rawinsondes. This characteristic affects Sherman's technique; the initial guess is not mass-inconsistent, so this characteristic is preserved in a "minimal adjustment." In fact, unrealistic and spurious circulations in the vertical plane are required to accommodate it. Thus that technique can be no better than the numerical interpolation used for its input.

Appropriate characteristics of constraints for windfields in the St. Louis region may be judged from several background sources. It is well established that both air flow and temperature distributions are significantly perturbed by the presence of a metropolitan region. The collection of studies in Project METROMEX on the effects of St. Louis on the atmosphere quite clearly demonstrate the differences that exist between the air over urban areas and the air over rural areas (Auer and Dirks, 1974; Ackerman, 1974; Moses, 1974). Although hard conclusions are yet to be drawn, the observed differences in air flow and temperatures are certainly heavily influenced by differences in surface roughness and radiative characteristics; i.e., variations in the physical characteristics of the boundary layer.

These effects are being studied through boundary layer analyses, such as those carried out by Vukovich et al. (1976) for the St. Louis area, Pandolfo et al. (1971) for Los Angeles, and others. A two-dimensional analysis (in a vertical plane along the wind streamline) by Bornstein (1975) gives a simplified view of results similar to those of Vukovich et al. (1976). Bornstein's figures clearly show the thermal circulation cell over a heated urban area, with a close correlation between regions of maximum temperature and wind speed anomaly (Figures 4 and 5) and vertical and horizontal wind speed anomaly (Figures 6 and 8, 9 and 11). These results are, in turn, qualitatively consistent with the streamline patterns computed by Vukovich et al. (1976) and the hypothetical sketch by Anderson (1971).

These results are the basis of the system of physical constraints used in this study. In the present model we assume that surface temperature measurements are available for each RAMS station at the time of each surface wind measurement. We also assume that surface temperature measurements exhibit less local bias than the corresponding wind measurements. [This assumption is supported by studies of Connecticut and Los Angeles by Anderson (1971, 1973)]. Surface isotherms are assumed to be well and linearly correlated with near-ground vertical velocity isopleths. Finally, it is assumed that vertical mixing is sufficient to assure that the winds at upper-level grid points correlate better with rawinsonde data at the same altitude than with surface measurements that may have been made closer in time or space.

E. THE WINDFIELD ALGORITHM DEVELOPED IN THIS STUDY

Wind vector components at each location of the three-dimensional grid are derived using an analysis that considers both the measurements and the constraints imposed by a simple model of the atmospheric boundary layer. This model applies to a region that includes an urban core surrounded by open, rural land. The model is based on the assumption that the major perturbation of the mean boundary layer is a thermal circulation induced by the urban-rural temperature difference. (Topographic effects for example, are not important.)

It is assumed that sufficient surface measurements of wind and temperature are available to define the convergence patterns produced by thermal effects in the lowest layer of the grid. The convergence distribution is determined by the surface temperatures; that is, the divergence of the velocity potential field ($\nabla\phi$)* is directly proportional to the local temperature anomaly. Since hot air rises, low altitude convergence must be present to replace the rising air:

$$\nabla^2\phi(x,y) = \alpha[T(x,y) - \bar{T}] \quad , \tag{73}$$

where

ϕ = velocity potential for two-dimensional, horizontal flow
T = temperature
$\bar{T}$ = regional mean temperature
α = a scaling parameter.

The scaling parameter, α, represents the flow convergence produced per unit of temperature differential. The value of α is determined as follows.

In this approach the pattern of horizontal winds near the ground is determined by the ground-level temperature pattern, but the magnitude of the wind velocity depends on measured surface winds. It seems appropriate that α be chosen so as to assure that the averages of measured and computed winds are equal. Using the measured temperature, $T(i)$ to determine the computed wind

$$\vec{V}_{comp}(i) = \alpha\,\nabla[\phi(i)/\alpha] \quad ,$$

where i is a measured station index and setting the computed wind equal to the measured wind

$$\vec{V}_{meas}(i) = \alpha\,\nabla[\phi(i)/\alpha] \quad .$$

---

* In the atmosphere the wind velocity is often determined by pressures alone (i.e., not by friction). In such a case the velocity is represented by the gradient, ∇, of a potential function, ϕ.

Then,

$$\alpha(i) = \frac{\vec{V}_{meas}(i)}{\nabla[\phi(i)/\alpha]} \quad .$$

Taking the scalar product of the gradient operator with the numerator and denominator assures that $\alpha(i)$ is the best scale factor relating the vector components of the measured and computed winds. Averaging over all anemometers gives

$$\alpha = \frac{\sum_i \left\{ u(i)\,\frac{\partial[\phi(i)/\alpha]}{\partial x} + v(i)\,\frac{\partial[\phi(i)/\alpha]}{\partial y} \right\}}{\sum_i \left[\left| \frac{\partial[\phi(i)/\alpha]}{\partial x} \right|^2 + \left| \frac{\partial[\phi(i)/\alpha]}{\partial y} \right|^2 \right]} \quad , \tag{74}$$

where u, v = deviations of measured wind components from their means.

The three-dimensional nature of the thermal circulation patterns is approximated by multiplying $\nabla^2\phi$ by an algebraic function of altitude that has unit value at $z = 0$, is zero at some altitude, goes negative above that height, and returns asymptotically to zero. Its integral from $z = 0$ to $z = \infty$ is zero, and it is scaled by Pasquill's dispersion parameter, ∂_z. The parameter ∂_z is a function of x, the distance downwind from the source. In this case x is set equal to Δx where Δx is the cell size in the analysis grid. At larger x's, the wind variations are explicitly accounted for and are not properly included in the variance, ∂_z. The function used for expressing the vertical variation of the wind pattern is

$$\zeta(z) = (1 - z^{*2})\exp(-\tfrac{1}{2}\, z^{*2}) \quad , \tag{75}$$

where

$$z^* = z/\sigma_z(x = \Delta x).$$

The function crosses zero at $z = \sigma_z$, and is again very close to zero at $z = 3\sigma_z$. It is further assumed that boundary layer soundings define the mean boundary layer profile, but are too few to define any horizontal variability of the boundary layer.

If the rawinsondes are insufficient to clearly define horizontal variation in the boundary layer profiles [i.e., U(z), V(z)], the rawinsonde data are simply averaged:

$$U(z),V(z) = \frac{1}{N}\sum_{n=1}^{N} [u(n,z),v(n,z)] \quad , \qquad (76)$$

where

n = rawinsonde station index,
N = number of rawinsondes.

If the soundings clearly define some of the horizontal variability, but are insufficient for a grid-scale objective analysis, they will be used to define a simple functional description of the horizontal variation. That is, if there are many stations taking soundings simultaneously, it would be desirable to use each sounding at its location and interpolate between them to develop U(x,y,z), V(x,y,z), for every grid point just as is done with surface winds. If there are fewer stations, soundings might be interpolated by a very simple, perhaps linear, formula. If the number of stations is very small, soundings should probably be averaged as in Equation (76). The final output of the analysis, which is input to the SAI Urban Airshed Model, is

$$u(x,y,z) = \alpha\zeta(z) \frac{\partial(\phi/\alpha)}{\partial x} + U(z) \quad , \qquad (77)$$

$$v(x,y,z) = \alpha\zeta(z) \frac{\partial(\phi/\alpha)}{\partial y} + V(z) \quad , \qquad (78)$$

$$w(x,y,z) = \alpha[T(x,y) - \bar{T}] \int_0^z \zeta(z)dz \quad . \qquad (79)$$

In this development we have said the wind vector consists of a mean boundary layer profile, U(z),V(z), which is independent of x and contains the rotational part of the windfield. Added to this mean profile is an irrotational disturbance produced by surface temperature patterns. At the surface the disturbance components are:

$$\alpha \frac{\partial\phi/\alpha}{\partial x} , \quad \alpha \frac{\partial\phi/\alpha}{\partial y} \quad .$$

Above the surface there is a nondivergent layer (analogous to the nondivergent layer at approximately 500 mb in synoptic flow). Above the nondivergent layer the sign of the divergence pattern is opposite that at the surface. The vertical variation of the divergence pattern is $\zeta(z)$. The three-dimensional pertubation is

$$\alpha\zeta(z)\frac{\partial\phi/\alpha}{\partial x} , \quad \alpha\zeta(z)\frac{\partial\phi/\alpha}{\partial z} \quad .$$

The total resultant horizontal wind vector is the sum of the perturbation and the mean as shown in Eqs. (77), (78). Equation (79) follows from continuity of mass.

F. COMPUTER SOLUTION

In solving the algorithm described above, a mean temperature gradient is allowed in $\bar{T}$, the regional temperature. Since the 100 km grid is large enough to "see" some synoptic-scale events, the purely local thermal cell is assumed to be due to deviations from a temperature "plane" defined by the three RAMS stations nearest the edges of the region. Thus a simple gradient is allowed for the regional temperature. The regional temperature may then be described by evenly spaced, straight, parallel isotherms.

Temperature boundary values are determined from this plane. In general, the appropriate boundary condition is that deviation from the mean temperature goes to zero at the perimeter. Deviation from measured values goes to zero at each data station.

Equation (73) is solved holding the boundary values and all temperatures constant. Solution is by the Gauss-Seidel relaxation technique, with specified or default values of the relaxation coefficient, the convergence criterion, and the maximum allowable number of iterations. Choice of the relaxation coefficient will depend on the spatial array of data stations. The remaining equations, (74) through (79), are then evaluated algebraically.

G. SUMMARY

It must be emphasized that the algorithm described above was chosen and implemented on the basis of general principles and prior experience, without access to data for the St. Louis area.

We anticipate that this algorithm will miss some significant windfield features, such as the bending of the thermal cell in the boundary layer shear zone (Vukovich et al., 1976; Bornstein, 1975) and the effect of surface friction variations (Anderson, 1971; Fosberg et al., 1976). However, we also anticipate that the analysis will reproduce the most important phenomena known to influence the urban boundary layer and will, in particular, avoid introducing the large spurious features that might be expected from any algorithm that depends on influence factors or other unconstrained interpolation techniques.

The computed velocity is not irrotational unless soundings show it to be so. The rotationality is in U(z), V(z), and their rotationality is determined by the soundings. The velocity is irrotational about a vertical axis. This is, of course, not perfectly true in nature, but in most cases the dominant perturbations to the mean flow are irrotational. In this case the only perturbance addressed is the heat island effect, which is a potential flow disturbance except to the extent that it couples to the mean shear profile. Since the momentum and energy equations were not used, these second order effects could not be addressed.

We recommend that subgrid-scale bias be investigated for a typical St. Louis site by collecting and statistically analyzing wind records from several (say 5 to 10) surface anemometers placed within the same grid cell.

We draw the reader's attention to the appropriateness of other wind algorithms for other applications. Examples are the Los Angeles algorithm (Anderson, 1973) which necessarily includes account of the severe topographic and land-sea thermal disturbances known to affect the winds in the Los Angeles basin and the Denver algorithm (Anderson et al., 1977) which was based solely on influence factor interpolation because of the dominance of disturbances (the Rocky Mountains) from outside the modeling region.

V IMPROVED TREATMENT OF ATMOSPHERIC CHEMISTRY

by Gary Z. Whitten, Terry N. Jerskey, and James P. Killus

A. INTRODUCTION

The mechanism describing the chemical transformations that take place in the atmosphere is one of the most important components of a photochemical model. In this study, we endeavored to incorporate into the SAI Urban Airshed Model an improved mechanism for hydrocarbon/NO_x/O_3 reactions that was developed at SAI by Whitten and Hogo (1976). In that mechanism the reactions of a hydrocarbon molecule are characterized by the bond structure of each carbon atom in the molecule, so it is termed the carbon-bond mechanism. In addition, we included reactions to describe the oxidation of SO_2 and the formation of secondary organic, nitrate, and sulfate aerosol products. The reactions in the SAI Urban Airshed Model are listed in Tables 15a-c.

B. HYDROCARBON NO_x/O_3 CHEMISTRY

1. Overview

Because of the association of reactions and reactivities with carbon bonds, the range of reactions and the range of rate constants in a kinetic mechanism can be narrowed considerably when each carbon atom is treated according to its bond type. This concept is the basis for the carbon-bond mechanism listed in Tables 15a and 15b. In this mechanism, hydrocarbons are divided into four groups: single-bonded carbon atoms, fast double bonds (i.e., relatively reactive double bonds), slow double bonds, and carbonyl bonds. Single-bonded carbon includes not only paraffin molecules, but also the single-bonded carbon atoms of olefin, aromatic, and aldehyde molecules. Double bonds are treated in pairs of carbon atoms. An activated aromatic ring is considered as three double bonds in the present formulation of the mechanism, and because of a

TABLE 15. CHEMICAL REACTIONS IN THE SAI URBAN AIRSHED MODEL

(a) The Carbon-Bond Mechanism--Reactions

No.	Reaction
1	$NO_2 + h\nu \rightarrow NO + O$
2	$O + O_2\ (+M) \rightarrow O_3\ (+M)$
3	$O_3 + NO \rightarrow NO_2 + O_2$
4	$O + NO_2 \rightarrow NO + O_2$
5	$O_3 + NO_2 \rightarrow NO_3 + O_2$
6	$NO_3 + NO \rightarrow NO_2 + NO_2$
7	$NO_3 + NO_2 + H_2O \rightarrow 2HNO_3$
8	$HO_2^{\cdot} + NO_2 \rightarrow HNO_2$
9	$NO_2 + OH\cdot \rightarrow HNO_3$
10	$HNO_2 + h\nu \rightarrow NO + OH\cdot$
11	$NO + OH\cdot \rightarrow HNO_2$
12	$CO + OH\cdot \xrightarrow{O_2} CO_2 + HO_2^{\cdot}$
13	$HO_2^{\cdot} + NO \rightarrow OH\cdot + NO_2$
14	$HO_2^{\cdot} + HO_2^{\cdot} \rightarrow H_2O_2 + O_2$
15	$PAN \rightarrow HC(O)O_2^{\cdot} + NO_2$
16	$H_2O_2 + h\nu \rightarrow OH\cdot + OH\cdot$
17	$OLE + OH\cdot \xrightarrow{O_2} HCHO + CH_3O_2^{\cdot}$
18	$OLE + O \xrightarrow{2O_2} HC(O)O_2^{\cdot} + CH_3O_2^{\cdot}$
19	$OLE + O_3 \xrightarrow{O_2} HC(O)O_2^{\cdot} + HCHO + OH\cdot$
20	$PAR + OH\cdot \xrightarrow{O_2} CH_3O_2 + H_2O$
21	$PAR + O \xrightarrow{O_2} CH_3O_2^{\cdot} + OH\cdot$
22	$HCHO + OH\cdot \xrightarrow{O_2} HC(O)O_2^{\cdot} + H_2O$
23	$HCHO + h\nu \xrightarrow{2O_2} \alpha HC(O)O_2^{\cdot} + \alpha HO_2^{\cdot}$
24	$ARO + OH\cdot \xrightarrow{O_2} HCHO + CH_3O_2^{\cdot}$
25	$ARO + O \xrightarrow{2O_2} HC(O)O_2^{\cdot} + CH_3O_2^{\cdot}$
26	$ARO + O_3 \xrightarrow{O_2} HC(O)O_2^{\cdot} + HCHO + OH\cdot$
27	$ARO + NO_3 \rightarrow$ Products
28	$CH_3O_2^{\cdot} + NO \rightarrow NO_2 + HCHO + HO_2^{\cdot}$
29	$HC(O)O_2^{\cdot} + NO \rightarrow NO_2 + CO_2 + HO_2^{\cdot}$
30	$HC(O)O_2^{\cdot} + NO_2 \rightarrow PAN$
31	$CH_3O_2^{\cdot} + HO_2^{\cdot} \rightarrow CH_3OOH + O_2$
32	$HC(O)O_2^{\cdot} + HO_2^{\cdot} \rightarrow HC(O)OOH + O_2$

TABLE 15. CHEMICAL REACTIONS IN THE SAI URBAN AIRSHED MODEL

(b) The Carbon-Bond Mechanism--Rate Constants*

Reaction Number	Rate Constant	Reaction Number	Rate Constant	Reaction Number	Rate Constant
1	k_1[†]	14	4.0×10^3	28	2.0×10^3
2	2.08×10^{-5}	15	2.0×10^{-2}	29	2.0×10^3
3	2.52×10^1	16	$7.0 \times 10^{-4} k_1$	30	1.5×10^2
4	1.34×10^4	17	3.8×10^4	31	4.0×10^3
5	5×10^{-2}	18	5.3×10^3	32	4.0×10^3
6	1.3×10^4	19	1.5×10^{-2}		
7	2.0×10^{-3}	20	1.3×10^3		
8	3.0×10^1	21	2.0×10^1		
9	9.0×10^3	22	2.0×10^4		
10	$1.9 \times 10^{-1} k_1$	23	$6.0 \times 10^{-3} k_1$		
11	9.0×10^3	24	8.0×10^3		
12	2.06×10^2	25	3.7×10^1		
13	2.0×10^3	26	2.0×10^{-3}		
		27	5.0×10^1		

---

[*] In units of $ppm^{-1}min^{-1}$ except for photolysis reactions and Reaction 15 (units of min^{-1}) and Reaction 7 (units of $ppm^{-2}min^{-1}$). These rate constants are tentative; they will be changed as dictated by future experimental studies.

[†] The rate constant for NO_2 photolysis, k_1, depends on the UV intensity. In the model k_1 is determined by the Multi-Layer Light-Scattering Model, which accounts for the variation of UV intensity with solar zenith angle and aerosol scattering (see Chapter VI).

TABLE 15. CHEMICAL REACTIONS IN THE SAI URBAN AIRSHED MODEL

(c) Sulfate and Aerosol Reactions

Sulfate Reactions			Aerosol Reactions		
No.	Reaction	Rate Constant $(ppm^{-1}min^{-1})$	No.	Reaction	Notes
33	$SO_2 + OH\cdot \xrightarrow{O_2} HSO_5\cdot$	9.0×10^2	39	$H_2SO_4 \rightarrow AERO(S)$	Assumed to be instantaneous
34	$HSO_5\cdot + NO \rightarrow NO_2 + HSO_4\cdot$	8.0×10^2	40	$\eta\ HNO_3 \rightarrow AERO(N)$	$\eta = 0.1$
35	$HSO_4\cdot + HO_2\cdot \rightarrow H_2SO_4 + O_2$	9.0×10^3	41	β Olefin Oxidation $\rightarrow$ AERO(O)	$\beta = 0.48$*
36	$SO_2 + HO_2\cdot \xrightarrow{H_2O} H_2SO_4 + OH\cdot$	1.3	42	γ Aromatic Oxidation $\rightarrow$ AERO(O)	$\gamma = 1.0$*
37	$CH_3O_2\cdot + SO_2 \xrightarrow{H_2O} H_2SO_4 + HCHO + HO_2\cdot$	1.5			
38	$HSO_4\cdot + NO_2 \xrightarrow{H_2O} H_2SO_4 + HNO_3$	1.0×10^4			

---

* β and γ represent the fractions of the carbon atoms associated with olefinic or aromatic bonds that eventually become aerosol if the bonds are oxidized. The initial oxidation step is either Reaction 17 or Reaction 24 in Table 15a. However, the conversion to aerosol is assumed to take place late in the reaction pathway, in order not to perturb the functioning of the kinetic mechanism. Aerosol may thus be taken to represent an alternative end product to CO or CO_2 in the oxidation process described in the carbon-bond mechanism. (See Section D-1.)

similarity in reactivities, aromatics are lumped with the slow (ethylene) double bonds rather than with the fast double bonds.

One of the goals in the development of the carbon-bond mechanism has been a mechanism responsive to the range of analytical detail in field measurements. At one end of the range, the only hydrocarbon data available might be the total ppmC of hydrocarbons at one time. At the other extreme, the time dependence of all types of hydrocarbons may be known. The carbon-bond mechanism will accept these data and any other information on the concentrations of double bonds, carbonyl groups, and aromatic rings. These data might be available through either spectral analysis or gas chromatography. Thus, the carbon-bond mechanism is directly responsive to the most basic measurement (non-methane hydrocarbon), yet will accept data at any level of sophistication. Of course, using the new mechanism with minimum data requires making an assumption as to the percentages of single, double, and carbonyl bonds.

The carbon-bond mechanism is an important improvement over the Hecht, Seinfeld, and Dodge (1974) lumped kinetic mechanism, which was previously used in the Urban Airshed Model. The central difference between the mechanisms is that the HSD mechanism accounts for molecules, but the carbon-bond mechanism accounts for atoms. The carbon-bond mechanism should provide equally accurate simulations with less input data than the HSD mechanism. For example, consider a source emitting 100 kg of hydrocarbons per hour. To use this measurement in the HSD mechanism, one must convert it into some number of molecules by estimating or determining an average molecular weight for the hydrocarbons. The molecular weights of hydrocarbons span a wide range, and the composition of the molecules may change with time as they react in the atmosphere. Thus the calculated average molecular weight can have a large uncertainty, which can produce a correspondingly large uncertainty in the predictions of the HSD mechanism. To use this measurement in the carbon-bond mechanism, one must estimate or determine the weight percentage of carbon in the hydrocarbons. But the weight percentage spans a relatively narrow range, from roughly 75 percent (for methane) to 92 percent (for benzene or C_nH_n). Thus the range of error in the calculated weight percentage is relatively small, which produces a correspondingly small uncertainty in the predictions of the carbon-bond mechanism.

The present formulation and parameterization of the carbon-bond mechanism is based on explicit mechanisms developed to simulate smog chamber experiments that were initiated with only one hydrocarbon species present. An explicit mechanism accounts for the fundamental or elementary reactions of all species in the smog chamber. For example, the explicit mechanism for propylene contains over seventy reactions representing thirty-five species. With the exception of the aromatic chemistry (for which no adequate explicit mechanism exists), the reactions in the carbon-bond mechanism represent the essential features of explicit mechanisms. The types and concentrations of radicals in the carbon-bond and explicit mechanisms are similar. The concentrations of carbon atoms by bond type are also similar. If a propylene/NO_x smog chamber experiment were to be simulated with both the explicit mechanism for propylene and the carbon-bond mechanism, the concentrations of NO, NO_2, O_3, OH·, and HO_2 in the two simulations would be very similar, because both mechanisms treat these species explicitly. The total concentration of all alkylperoxy radicals (RO_2) in the propylene system would be similar to the concentration of the lumped species CH_3O_2 in the carbon-bond mechanism. The concentration of double bonds (the original propylene) would be represented by OLE in the carbon-bond mechanism. The total concentration of all carbonyl compounds in the explicit simulation, such as acetaldehyde and formaldehyde, would be similar to the concentration of the carbonyl representative, HCHO, in the carbon-bond mechanism. For simulating smog chamber experiments at the University of California at Riverside (UCR) using propylene, butane, or toluene as the only hydrocarbon, the present formulation of the carbon-bond mechanism performs better than the HSD mechanism.

UCR experiments using mixtures of hydrocarbons are only now being studied. Thus the carbon-bond mechanism has not been validated for mixtures and the techniques for averaging rate constants are now being developed. Furthermore, the validation of this mechanism with atmospheric data has not been attempted, although such an effort seems appropriate.

2. Rate Constants for Hydrocarbon Classes

To perform computer simulations with the carbon-bond mechanism, one must select rate constants for the oxidation of the different hydrocarbon classes. This section describes the rate constants currently used for each class of hydrocarbons.

a. Single-Bonded Carbon Atoms

The carbon-bond mechanism presently uses hydrogen atom abstraction by hydroxyl radicals as the dominant reaction for single-bonded carbon atoms. The single-bond chemistry is derived from the chemistry of paraffins. Paraffins apparently undergo the following oxidation reactions:

$$\mathrm{PAR} + \mathrm{OH}\cdot \rightarrow \mathrm{RO}_2^{\cdot} + \mathrm{H_2O} \quad , \tag{80}$$

$$\mathrm{RO}_2^{\cdot} + \mathrm{NO} \rightarrow \mathrm{HO}_2^{\cdot} + \mathrm{ALD} + \mathrm{NO_2} \quad , \tag{81}$$

$$\mathrm{HO}_2^{\cdot} + \mathrm{NO} \rightarrow \mathrm{OH}\cdot + \mathrm{NO_2} \quad . \tag{82}$$

In this set of reactions, one hydroxyl radical reacts and is regenerated while two nitric oxide molecules are converted to nitrogen dioxide and the paraffin is converted into an aldehyde.

According to Greiner's (1970) formula for calculating alkane-OH· rate constants, primary carbon atoms at 300°K have a reactivity of 290 $\mathrm{ppm^{-1}min^{-1}}$; secondary carbon atoms of alkanes have a reactivity of 1600 ppm^{-1}min^{-1}; and tertiary carbons have a reactivity of 4200 ppm^{-1}min^{-1}. The creation of a side chain converts two secondary carbons into one primary carbon and one tertiary carbon, for an average reactivity of 2240 ppm^{-1}min^{-1}. Table 16 lists the reactivity per carbon atom for several common alkanes. Many of the alkanes--except propane and those containing the tertiary-butyl group--have reactivities within about 35 percent of 1300 ppmC^{-1}min^{-1}. The compounds

TABLE 16. REACTIVITIES TOWARDS OH· OF SEVERAL ALKANES

Alkane	Reactivity per Carbon Atom (ppm^{-1}min^{-1})
Propane	730
n-Butane	950
i-Butane	1250
n-Pentane	1060
neo-Pentane	232
i-Pentane	1340
n-Hexane	1170
i-Hexane	1380
2,3-Dimethyl-butane	1590
2,2-Dimethyl-butane	460
n-Heptane	1220
i-Heptane	1410
2,3-Dimethylpentane	1590
n-Octane	1280
i-Octane	1440
2,3,4-Trimethylpentane	1760
n-Nonane	1310
i-Nonane	1460

with tert-butyl groups may be present in low concentrations in typical atmospheric mixes. They were reported by Calvert (1976) to be less than 8 percent of the alkanes in observations made during the Los Angeles Reactive Pollutant Program (LARPP). Furthermore, recent experiments at UCR with 2,3-dimethylbutane show that its overall reactivity is similar to that of butane even though their rate constants for reaction with OH· are quite different.

b. Fast Double Bonds

Olefin or double-bond chemistry is represented by the following reactions:

$$\mathrm{OLE} + \mathrm{O} \rightarrow \mathrm{HCO_3} + \mathrm{CH_3O_2} \quad , \qquad (83)$$

$$\mathrm{OLE} + \mathrm{OH\cdot} \rightarrow \mathrm{HCHO} + \mathrm{CH_3O_2} \quad . \qquad (84)$$

$$\mathrm{OLE} + \mathrm{O_3} \rightarrow \mathrm{HCHO} + \mathrm{HCO_3} + \mathrm{OH\cdot} \quad . \qquad (85)$$

Olefins have a wider range of reactivity with hydroxyl radicals than paraffins. The rate constant for OH· oxidation differs greatly between ethylene and the longer chain olefins, especially the internal olefins. The mechanism is further complicated because olefins react with ozone to a significant extent, again with a wide range of rate constants.

Per double bond, the reaction rates of olefins with OH· jump from 8000 $\mathrm{ppm^{-1}min^{-1}}$ for ethylene to 38,000 $\mathrm{ppm^{-1}min^{-1}}$ for propylene (Davis, 1976) and vary only within a factor of 3 for longer olefins. The reactivity increases for 1-butene (to 4.3×10^4 $\mathrm{ppm^{-1}min^{-1}}$) and for internal olefins, such as cis-2-butene (6.3×10^4 $\mathrm{ppm^{-1}min^{-1}}$). Table 17 lists rate constants in $\mathrm{ppm^{-1}min^{-1}}$ for five olefins. Because of the low variation in rate constants of olefins (except ethylene), all olefins except ethylene are treated as one lumped species in the carbon-bond mechanism.

TABLE 17. RATE CONSTANTS PER DOUBLE BOND FOR THE REACTIONS OF SOME OLEFINS WITH OH· AT 300°K

Olefin	Rate Constant ($ppm^{-1}min^{-1}$)
Ethylene	7.9×10^3
Propylene	3.8×10^4
1-Butene	4.3×10^4
cis-2-Butene	6.3×10^4
Tetramethylethylene	8.4×10^4

The olefin-O_3 reactions are much more diverse in reactivity than the olefin-OH· reactions. Table 18 shows rate constants for some olefin reactions. The propylene reaction with ozone is roughly seven times faster than the ethylene reaction, and nonterminal olefins, such as cis-2-butene, react even faster. (Terminal olefins, such as isobutene, have reaction rate constants comparable to that of propylene.) Substituted internal olefins, such as 2,3-dimethyl-2-butene, react with ozone roughly 10^3 times faster than does ethylene. Thus, lumping parameters must be devised that can span a 10^3 difference in rate constants. This task has not yet been performed; it seems possible only if the slower O_3-olefin reactions are neglected. In future work, the reaction of fast olefins with NO_3 may be included in the carbon-bond mechanism. The rate of this reaction is slow for terminal olefins (ethylene, propylene, and 1-butene), but is fast for internal olefins (Japar and Niki, 1975). The reaction has not been included in the carbon-bond mechanism because little is known about its products.

TABLE 18. COMPARISON OF THE REACTIVITIES OF $O(^3P)$ ATOMS, OZONE, AND NO_3 TOWARD OLEFINS

Olefin	Rate Constant ($ppm^{-1}min^{-1}$)		
	$k_{O(^3P)}$*	k_{O_3}†	k_{NO_3}
Ethylene	9.2×10^2	2.8×10^{-3}	1.37 ± 0.15
Propylene	5.3×10^3	1.9×10^{-2}	7.82 ± 0.44
Propylene-d_6	--	2.2×10^{-2}	8.71 ± 0.59
1-Butene	5.3×10^3	1.8×10^{-2}	4.5 ± 1.2
Isobutene	2.2×10^4	2.1×10^{-2}	162 ± 14.8
trans-2-Butene	2.7×10^4	3.8×10^{-1}	207 ± 14.8
cis-2-Butene	2.2×10^4	2.4×10^{-1}	266 ± 29.5
2-Methyl-2-butene	7.4×10^4	7.2×10^{-1}	8120 ± 738
2,3-Dimethyl-2-butene	9.6×10^4	2.2	54600 ± 7380

---

*Based on $k(O+C_3H_6) = 5.3 \times 10^3$ $ppm^{-1}min^{-1}$, Stuhl and Niki (1971), and the relative reactivities of Cvetanovic (1963).

†Japar and Niki (1975).

Source: Japar and Niki (1975).

c. Slow Double Bonds

In the carbon-bond mechanism, the aromatic oxidation reactions are assumed to produce the same products as the olefin oxidation reactions:

$$ARO + O \rightarrow HCO_3 + CH_3O_2 \quad , \qquad (86)$$

$$ARO + OH\cdot \rightarrow HCHO + CH_3O_2 \quad , \qquad (87)$$

$$ARO + O_3 \rightarrow HCHO + HCO_3 + OH\cdot \quad . \qquad (88)$$

In these equations, ARO represents one slow double bond; thus, one toluene molecule equals three AROs (plus one single bond, PAR). We have found that an aromatic ring activated by the addition of an alkyl group, such as toluene, can be treated by the carbon-bond mechanism as three ethylenic double bonds (olefins). Thus, we treat ethylene and the aromatics together as one lumped species. This lumping is used primarily because the oxidation rate of ethylene by OH· is closer to that of aromatics than to the other olefins. In addition, ethylene typically makes up to 50 percent of atmospheric olefins, compared with only 10 to 20 percent of the aromatics (on the basis of total double bonds).

Whether ozone-aromatic reactions similar to ozone-olefin reactions should be included in the mechanism is a difficult question. As the aromatic ring decomposes, it surely must lead to some internal olefin species, which, of course, would react with ozone. We have tentatively included ozone-olefin reactions for slow double bonds for two reasons:

> The rate constant for the reaction of ethylene with ozone is very slow. It may be similar to the rate constant for the ozone-aromatic reaction, which has not been measured accurately but is known to be slow (Finlayson and Pitts, 1976).

> We wanted to maintain the treatment of aromatic bonds and ethylene together as one lumped species.

The choice of rate constant for the reaction of slow double bonds with oxygen atoms is more difficult because the rate constants for the reactions with oxygen atoms of aromatics and ethylene differ greatly. A procedure for estimating a rate constant in accordance with the relative amounts of aromatics and ethylene present in the system is being developed. However, the reactions of slow double bonds with oxygen atoms are not usually important. The mechanism includes a reaction between NO_3 and aromatics to account for the internal olefins that are formed as the aromatic rings open. A rate constant of 50 $ppm^{-1}min^{-1}$ for the reaction leads to simulations that fit most of the smog chamber runs with toluene studied to date. It is faster than that measured for the reaction of NO_3 with ethylene (1.4 $ppm^{-1}min^{-1}$) by Japar and Niki (1975), but far slower than their value for the reaction with substituted internal olefins (5×10^4 $ppm^{-1}min^{-1}$). The inclusion of the reaction of NO_3 with aromatics is partially justified by the observation that no NO_3 is formed in smog chamber simulations until some toluene has reacted.

As mentioned above, the aromatic ring is represented by three double bonds (ethylene groups) in the carbon-bond mechanism. Therefore, observed aromatic concentrations in ppm are multiplied by three to give input data for the mechanism. Any alkyl groups or carbonyl groups on the aromatics are considered separately. For toluene, three times the measured toluene concentration of slow double bonds and the toluene concentration of single-bonded carbon atoms are input to the mechanism.

d. Carbonyl Bonds

The carbon-bond mechanism treats carbon-oxygen double bonds, whether in ketones or aldehydes, as a single group. We are currently using a value of 1×10^4 $ppm^{-1}min^{-1}$ for the aldehyde-OH· reaction rate.

This compares with an estimate of 9.8×10^3 $ppm^{-1}min^{-1}$ as the lower limit of the reaction rate (Herron and Penzhorn, 1969). The present value falls midway between the value of 2.1×10^4 $ppm^{-1}min^{-1}$ measured by Morris and Niki (1971) and the Volman and Gorse (1972) estimate of 5.6×10^3 $ppm^{-1}min^{-1}$ for the reaction of propionaldehyde-OH·. Data on the rate constants of longer aldehydes are sketchy, but seem to be in accord with our choice of rate constant.

3. Sources of Radicals in the Carbon-Bond Mechanism

In computer simulations of smog chamber experiments, the initial concentration of hydroxyl radicals is typically produced by photolysis of nitrous acid:

$$HNO_2 + h\nu \rightarrow OH\cdot + NO \quad . \qquad (89)$$

The amounts of HNO_2 that give the best fits between predictions and smog chamber measurements are generally about one-third of the equilibrium concentration of HNO_2 from the reactions

$$H_2O + NO + NO_2 \rightleftharpoons 2HNO_2 \quad . \qquad (90)$$

HNO_2 is only an initial radical source in smog chambers because its half-life due to photolysis is about 15 minutes.

Some radicals can also come from oxygen atom attack on hydrocarbons:

$$O + PAR \rightarrow RO_2 + OH\cdot \quad , \qquad (91)$$

$$O + OLE \rightarrow RO_2 + RCO_3 \quad . \qquad (92)$$

This reaction is slower for paraffins, particularly for butane, than it is for olefins (Hampson and Garvin, 1975). Both of these radical sources are used in the carbon-bond mechanism.

The third source of radicals in the mechanism is the photolysis of carbonyls:

$$RR'CO + h\nu \rightarrow RO_2^{\cdot} + R'CO_3^{\cdot} \quad . \tag{93}$$

Maintaining the total concentration of radicals in the mechanism by carbonyl photolysis is necessary because of the numerous temporary and permanent radical sinks. For example, both nitrous acid and hydrogen peroxide are temporary radical sinks because they are formed rapidly via reactions that consume radicals:

$$OH\cdot + NO \rightarrow HNO_2 \quad , \tag{94}$$

$$HO_2^{\cdot} + HO_2^{\cdot} \rightarrow H_2O_2 \quad . \tag{95}$$

However, both species can reproduce radicals at a later time by photolysis. The most important permanent radical sink in the University of California Riverside (UCR) smog chamber experiments on butane/NO_x systems also appears to be the most important sink of oxides of nitrogen:

$$OH\cdot + NO_2 \rightarrow HONO_2 \quad . \tag{96}$$

Carbonyl photolysis is very important in maintaining the radical concentration, but it is also the most complex to treat in the mechanism. The complexity arises from the three reaction pathways of carbonyls--photolysis that produces radicals [Reaction (97)], photolysis that does not produce radicals [Reaction (98)], and reaction with hydroxyl radicals [Reactions (99) and (100)], which leads to oxidation of the carbonyl without net production of radicals:

$$RR'CO + h \rightarrow RO_2^{\cdot} + R'CO_3^{\cdot} \quad , \tag{97}$$

$$RR'CO + h\nu \rightarrow RR' + CO \quad , \tag{98}$$

$$RCHO + OH\cdot \rightarrow H_2O + RCO_3^{\cdot} \quad , \tag{99}$$

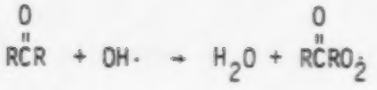

$$R\overset{\overset{O}{\|}}{C}R + OH\cdot \rightarrow H_2O + R\overset{\overset{O}{\|}}{C}RO_2\cdot \quad . \qquad (100)$$

For the carbon-bond mechanism shown in Table 15 the photolysis of carbonyl compounds is handled via a surrogate species (HCHO, which is not necessarily formaldehyde). The split between pathways to either radicals or unreactive products is handled by parameter α, a number between zero and one; most often a value of 0.5 has been used for applications of this mechanism. The magnitude of radical production from carbonyl photolysis is a function of the carbonyl concentration and the photolysis constant. Whitten and Hogo (1976) found that the principal carbonyl compound in the UCR butane/NO_x smog chamber experiments was MEK, but an important source of radicals was the photolysis of biacetyl (which presumably has a large photolysis constant). In the UCR data, the actual light spectrum was uncertain, as was the total carbonyl concentration because of a considerable mass recovery problem. Even if the kinetic mechanism and the light spectrum were known completely and the mass recovery were perfect, the photolysis constants would still be uncertain, primarily because of the uncertainties in the quantum yield data.

The relative importance of HNO_2 and carbonyl photolysis as sources of radicals in the atmosphere has yet to be determined. In the cleanest air of the troposphere it can be shown that ozone and water vapor lead to hydroxyl radical production via excited oxygen atoms:

$$O_3 + h\nu \rightarrow O(^1D) + O_2 \quad , \qquad (101)$$

$$O(^1D) + H_2O \rightarrow OH\cdot + OH\cdot \quad . \qquad (102)$$

In a polluted atmosphere in the morning, however, there is neither very much O_3 (due to reaction with NO emissions) nor much of the short wavelength light necessary to produce excited oxygen atoms (due to the angle of the sun and the ozone in the stratosphere). Available data--ambient concentrations of the species, solar spectral data, quantum yields--are insufficient to allow anything but the crudest estimates. The selection of initial conditions and photolysis rates for the initiation of the smog formation process in computer simulations is arbitrary.

C. CONSIDERATIONS IN THE TREATMENT OF HYDROCARBON EMISSIONS

As stated above, the HSD mechanism accounts for molecules, and the carbon-bond mechanism accounts for atoms. Thus, introduction of the carbon-bond mechanism in the SAI Urban Airshed Model necessitates a reexamination and reformulation of the existing emissions inputs, which were originally compiled for use with the HSD mechanism. In this section we discuss the preparation of appropriate emissions inputs for the Los Angeles Basin. Similar techniques may be used to prepare emission inputs for other urban areas.

In this effort we made use of an extensive study of hydrocarbon emissions in the Los Angeles Basin by Trijonis and Arledge (1975). They separated hydrocarbons into chemical types and reported both mole fraction and average molecular weight for each type for each source. Using their molecular weights to estimate average carbon numbers, we regrouped the Trijonis and Arledge hydrocarbon categories into the categories used in the carbon-bond mechanism. The regrouping involves multiplying mole fraction by molecular weight (with a minor correction for the oxygen content of alcohols, aldehydes and ketones) to obtain weights of species emitted, and then separating the species into new categories by bond type. The weight fractions and bond fractions obtained from this regrouping are given in Tables 19 and 20, respectively. An example of the use of these fractions is instructive. Consider the hydrocarbon emissions from petroleum refining. According to Table 19, 13 percent of the 50 tons of hydrocarbons emitted per day in petroleum refining are olefins other than ethylene, or 6.5 tons of olefins per day. From Table 20, 33 percent by weight of these olefin emissions, or 2.2 tons, are fast double bonds. (The remaining 67 percent are treated as single-bonded carbon atoms.) 2.2 tons equal 2×10^6 grams, which may be divided by the "molecular weight" of a fast double bond (26 g mole^{-1}, from Table 21), to yield 7×10^4 moles of fast double bonds emitted per day in the Los Angeles Basin from petroleum refining. This number is input to the carbon-bond mechanism.

TABLE 19. HYDROCARBON EMISSIONS IN THE LOS ANGELES BASIN BY SOURCE CATEGORY, WEIGHT, AND WEIGHT FRACTION

Source Category	Emissions (Tons/Day)	Percentage of Total Hydrocarbon Emissions	Weight Fraction*					
			Olefins	Paraffins	Aromatics	Ethylene	Carbonyls	Unreactive Hydrocarbons
Stationary Sources: Organic Fuels and Combustion								
Petroleum Production and Refining								
Petroleum Production	62	2.4	-	0.4	-	-	-	0.6
Petroleum Refining	50	1.9	0.13	0.72	0.10	-	-	0.05
Gasoline Marketing								
Underground Service Station Tanks	48	1.8	0.24	0.68	-	-	-	0.08
Auto Tank Filling	104	4.0	0.16	0.66	0.14	-	-	0.03
Fuel Combustion	23	0.9	0.08	0.10	0.05	-	0.103	0.67
Waste Burning and Fires	41	1.6	0.02	0.18	0.04	0.12	0.14	0.5
Stationary Sources: Organic Chemicals								
Surface Coating								
Heat Treated	14	0.5	0.01	0.25	0.67	-	-	0.07
Air Dried	129	5.0	-	0.72	0.22	-	0.08	0.03
Dry Cleaning								
Petroleum Based Solvent	16	0.6	-	0.94	0.06	-	-	-
Synthetic Solvent (PCE)	25	1.0	-	-	-	-	-	1.00
Degreasing								
TCE Solvent	11	0.4	-	-	-	0.27	-	0.73
1,1,1-T Solvent	95	3.6	-	-	-	-	-	1.00
Printing								
Rotogravure	31	1.2	-	0.80	0.14	-	-	0.06
Flexigraphic	15	0.6	-	0.70	-	-	0.12	0.18
Industrial Process Sources								
Rubber and Plastic Manufacturing	42	1.6	0.08	0.556	0.007	0.064	0.14	0.15
Pharmaceutical Manufacturing	16	0.6	-	0.66	-	-	0.12	0.13
Miscellaneous Operations	83	3.2	0.02	0.438	0.087	-	0.153	0.307
Mobile Sources: Gasoline-Powered								
Light Duty Vehicles								
Exhaust Emissions	780	30.0	0.068	0.42	0.346	0.048	0.146	0.116
Evaporative Emissions	481	18.5	0.117	0.56	0.283	-	-	0.04
Heavy Duty Vehicles								
Exhaust Emissions	285	10.9	0.068	0.42	0.346	0.048	0.146	0.116
Evaporative Emissions	67	2.6	0.117	0.56	0.283	-	-	0.04
Other Gasoline-Powered Equipment								
Exhaust Emissions	110	4.2	0.068	0.42	0.346	0.048	0.146	0.116
Evaporative Emissions	22	0.3	0.117	0.56	0.283	-	-	0.04
Mobile Sources: Diesel-Powered	12	0.5	0.064	0.53	0.12	0.06	0.2.	0.03
Aircraft								
Jet	20	0.8	0.18	0.43	0.25	-	0.11	0.03
Piston	22	0.8	0.145	0.40	0.22	0.075	0.22	0.15
TOTAL	2604	100						

---

* Carbonyl weight fractions are assumed in some cases, so the sum of the weight fractions for a given source category may be greater than 1.

Source: Derived from Trijonis and Arledge (1975)

Reproduced from best available copy.

TABLE 20. HYDROCARBON EMISSIONS IN THE LOS ANGELES BASIN BY SOURCE CATEGORY AND BOND FRACTION

Source Category	Bond Fraction					
	Fast Double Bonds	Single-Bonded Carbon Atoms	Slow Double Bonds (Aromatic)	Slow Double Bonds (Ethylene)	Carbonyl Bonds	Unreactive Hydrocarbons
Stationary Sources: Organic Fuels and Combustion						
Petroleum Production and Refining						
Petroleum Production	-	1.0	-	1.0	-	1.0
Petroleum Refining	0.32	1.0	0.70	1.0	-	1.0
Gasoline Marketing						
Underground Service Station Tanks	0.43	1.0	-	1.0	-	1.0
Auto Tank Filling	0.39	1.0	0.76	1.0	-	1.0
Fuel Combustion	0.4	1.0	0.61	1.0	0.33	1.0
Waste Burning and Fires	0.4	1.0	0.7	1.0	0.34	1.0
Stationary Sources: Organic Chemicals						
Surface Coating						
Heat Treated	0.5	1.0	0.55	1.0	-	1.0
Air Dried	-	1.0	0.7	1.0	0.35	1.0
Dry Cleaning						
Petroleum Based Solvent	-	1.0	0.67	1.0	-	1.0
Synthetic Solvent (PCE)	-	1.0	-	1.0	-	1.0
Degreasing						
TCE Solvent	-	1.0	-	1.0	-	1.0
1,1,1-T Solvent	-	1.0	-	1.0	-	1.0
Printing						
Rotogravure	-	1.0	0.71	1.0	-	1.0
Flexigraphic	-	1.0	-	1.0	0.39	1.0
Industrial Process Sources						
Rubber and Plastic Manufacturing	0.33	1.0	0.67	1.0	0.38	1.0
Pharmaceutical Manufacturing	-	1.0	-	1.0	0.35	1.0
Miscellaneous Operations	0.29	1.0	0.7	1.0	0.35	1.0
Mobile Sources: Gasoline-Powered						
Light Duty Vehicles						
Exhaust Emissions	0.41	1.0	0.72	1.0	0.65	1.0
Evaporative Emissions	0.34	1.0	0.73	1.0	-	1.0
Heavy Duty Vehicles						
Exhaust Emissions	0.41	1.0	0.72	1.0	0.65	1.0
Evaporative Emissions	0.34	1.0	0.73	1.0	-	1.0
Other Gasoline-Powered Equipment						
Exhaust Emissions	0.41	1.0	0.72	1.0	0.65	1.0
Evaporative Emissions	0.34	1.0	0.73	1.0	-	1.0
Mobile Sources: Diesel-Powered	0.38	1.0	0.43	1.0	0.83	1.0
Aircraft						
Jet	0.25	1.0	0.64	1.0	0.22	1.0
Piston	0.70	1.0	0.75	1.0	0.82	1.0

Source: Derived from Trijonis and Arledge (1975)

TABLE 21. ASSUMED WEIGHTS OF HYDROCARBON GROUPS IN THE CARBON-BOND MECHANISM

Group	Weight (grams mole^{-1})
Single-Bonded Carbon Atoms	14
Fast Double Bonds	26
Slow Double Bonds	26
Carbonyl Bonds	26

The hydrocarbon emissions inventory for the carbon-bond mechanism contains six groups: unreactive hydrocarbons, paraffins, ethylene, other olefins, aromatics, and carbonyls. The mechanism itself accepts as input emissions (in moles) of single-bonded carbon atoms, fast double bonds, slow double bonds, and carbonyl bonds. At present, ethylene and aromatics are treated together as slow double bonds. They are not treated together in the emissions inventory, however, because of the possibility that the aromatic reactions in the mechanism will be changed.

Because the new mechanism treats ethylene separately from the other olefins, it was necessary to estimate the fraction of ethylene in the olefin data given by Trijonis and Arledge. An examination of several gas chromatographic analyses of air in highway tunnels suggested that ethylene made up close to 60 percent of the olefin molecules in automobile exhaust. Assuming that emissions of diolefins are insignificant, 60 percent of automotive emissions of olefins are input as ethylene (or slow double-bonds) to the carbon-bond mechanism. We assumed that olefin emissions from noncombustion sources contain no ethylene except for plastics manufacture, for which we assumed that ethylene made up 50 percent of the olefins. Ethylene is not normally found in gasoline or in solvents. The data of Trijonis and Arledge also contain measurements of acetates and alcohols. With appropriate molecular weight adjustments to account for the oxygen atoms, these were grouped with single-bonded carbon atoms because of their low reactivity.

The automotive data presented by Trijonis and Arledge are based upon samplings of the ambient air in two heavily traveled highway tunnels, presumably by gas chromatography. While this is a good method for determining the emissions splits for an aggregate of vehicles, it commonly fails to detect aldehydes, which were not reported by Trijonis and Arledge. In another study (Scott Research Laboratories, 1970) gas chromatography and aldehyde measurements were performed at the same measuring station. An examination of data taken before nine o'clock on several days (i.e., before the onset of significant photochemical reaction) suggests that aldehydes are emitted on a molar basis at roughly the same rate as olefins. This suggestion is supported by data from at least two other combustion processes--fuel combustion and waste burning--reported by Trijonis and Arledge. As previously noted, this results in a higher weight fraction of aldehydes due to the added oxygen atoms.

The final emissions splits, regrouped into the categories used by the Emissions Data Preparation Program (EDPP) in the Airshed Model, are given in Table 22.

D. AEROSOL CHEMISTRY

The aerosol in the atmospheres of most cities is composed of both primary and secondary material. The secondary material forms from conversion of gaseous material to the particulate phase. As part of the aerosol work undertaken during this contract period, simple chemical kinetics were incorporated in the Urban Airshed Model to account for the three principal components of the secondary aerosol mass--organic, sulfate, and nitrate aerosols. These kinetics assume that all of the condensable material formed in the atmosphere is accommodated on existing particles. Furthermore, Jerskey and Seinfeld (1976) showed that for typical urban aerosol distributions over 90 percent of the material condensing on existing particles condenses on the submicron fraction. The following subsections describe the forms of the rate expressions

TABLE 22. HYDROCARBON EMISSIONS IN THE LOS ANGELES BASIN BY WEIGHT FRACTION IN CATEGORIES USED IN THE SAI URBAN AIRSHED MODEL

Source Category	Percentage of Total Hydrocarbon Emissions	Weight Fraction					
		Olefins*	Paraffins	Ethylene	Aromatics	Carbonyls	Unreactive Hydrocarbons
Land Motor Vehicles†	67.5	0.032	0.64	0.032	0.235	0.064	0.091
Aircraft	1.6	0.073	0.64	0.038	0.163	0.102	0.09
Refineries	1.9	0.04	0.84	0.0	0.17	0.0	0.05
Other	29.0	0.026	0.565	0.016	0.066	0.02	0.326
Total Hydrocarbons from All Sources	-	0.029	0.60	0.027	0.182	0.05	0.158

---

* Olefins excluding ethylene.

† Carbonyl emissions are assumed (because they would not have been detected by the measurement method used), so the sum of the weight fractions in this row is greater than 1.

assumed for each of the condensing species. In all cases the rates of formation of condensable material are expressed in $\mu g\ m^{-3} min^{-1}$ and concentrations of gases are expressed in ppm.

1. Organic Aerosol

For the organic aerosol, we wish to identify the major aerosol-forming hydrocarbons, the relevant reactions, and their rates. We further wish to apply the constraint that aerosol formation not be an additional hydrocarbon or radical sink. This constraint ensures that the ozone predictions of the Urban Airshed Model are unaffected by the addition of organic aerosol chemistry.

The mass concentration of secondary organic aerosol seems to be highly correlated with the ozone concentration at a ratio of roughly 1 carbon atom in the aerosol to 10 molecules of ozone (Appel et al., 1976). Since the ozone concentration is closely associated with the rate of reaction of OH radicals and hydrocarbons, we assume that OH·- hydrocarbon reactions are the rate-limiting step in the formation of organic aerosol.

Hydrocarbons known to be converted into aerosols include diolefins, cyclic olefins (specifically, cyclohexene), and, to a lesser extent, aromatics (O'Brien et al., 1975). The quantity of diolefins in the urban atmosphere is negligible. The greater aerosol-forming potential of cyclohexene relative to aromatics is partially offset by its lower abundance and much shorter residence time. Grosjean and Friedlander (1975) estimated that 3 percent of the organic gases in the Los Angeles Basin are converted to particulate matter, with a maximum conversion rate of 2 percent per hour. Cyclohexene constitutes less than 2 per cent of the organic gases in the Los Angeles Basin (Calvert, 1976), and less than 1 percent of gasoline (Maynard and Sanders, 1969). Thus, the cyclohexene in the Los Angeles atmosphere is insufficient to account for all secondary organic aerosol.

The rate expression for the formation of organic aerosol is assumed to have the form

$$\frac{d[\mathrm{AER(O)}]}{dt} = k_i\,[\mathrm{OLEF}][\mathrm{OH}\cdot] + k_j\,[\mathrm{ARO}][\mathrm{OH}\cdot] \quad , \qquad (103)$$

where k_i and k_j account for reaction rates, percentages of reactions that lead to aerosol, and other factors. In a measured sample of air over Los Angeles, Calvert (1976) estimated that the rate of the OH$\cdot$-cyclohexene reaction is 0.08 of the rate of the OH$\cdot$-olefin reaction. Since one ppm slow double bonds as cyclohexene represents six ppmC, and the rate constant for the OH$\cdot$-olefin reaction is 3.8×10^4 ppm^{-1}min^{-1} (Table 15b),

$$k_i = \frac{3.8 \times 10^4}{\mathrm{ppm\ min}} \cdot 0.08 \cdot \frac{6\ \mathrm{ppmC}}{1\ \mathrm{ppm\ cyclohexene}}$$

$$\cdot \frac{1000\,\ell}{\mathrm{m}^3} \cdot \frac{14\ \mathrm{g}}{\mathrm{mole}\ \text{-}\mathrm{CH_2}\text{-}} \cdot \frac{\mathrm{mole}}{22.4\,\ell} \cdot \frac{10^6\,\mu\mathrm{g}}{\mathrm{g}} \cdot \frac{1}{10^6\,\mathrm{ppm}}$$

$$= 1.14 \times 10^7\ \mu\mathrm{g\ m^{-3}ppm^{-2}min^{-1}} \quad . \qquad (104)$$

For k_j we assume a maximum aerosol formation of 1 carbon atom per reaction of an aromatic double bond with OH$\cdot$. This corresponds to the conversion of an aromatic carbon atom into organic aerosol at some point in the radical decay chain after all the important oxidation steps. That is, the decay chain terminates with aerosol carbon instead of CO_2. Since the rate constant for the OH$\cdot$-aromatic reaction is 8×10^3 (Table 15b),

$$k_j = \frac{8 \times 10^3}{\mathrm{ppm\ min}} \cdot \frac{14\ \mathrm{g}}{\mathrm{mole}\ \text{-}\mathrm{CH_2}\text{-}} \cdot \frac{\mathrm{mole}}{22.4\ \ell} \cdot \frac{10^3\,\ell}{\mathrm{m}^3} \cdot \frac{10^6\,\mu\mathrm{g}}{\mathrm{g}} \cdot \frac{1}{10^6\,\mathrm{ppm}}$$

$$= 5 \times 10^6\ \mu\mathrm{g\ m^{-3}ppm^{-2}min^{-1}} \quad . \qquad (105)$$

Assuming the relative emissions of 3 percent olefins and 21 percent aromatics presented in Table 22 and a typical OH· concentration of 10^{-7} ppm, one can calculate the change in the total hydrocarbon concentration leading to aerosol formation. This loss of hydrocarbons by aerosol formation is a fraction of the hydrocarbon loss by oxidation that occurs in the mechanism. Therefore, the rate of hydrocarbon loss in the mechanism is not affected by the organic aerosol chemistry; when this chemistry is added to the model, some fraction of the hydrocarbon oxidation and loss is assumed to form organic aerosol rather than CO_2 and H_2O. The rate of formation of organic aerosol is given by:

$$\begin{aligned}\frac{d[\text{Hydrocarbons}]}{dt} &= -\ 0.33\ \%\ \text{(due to olefins)} \\ &\quad -\ 0.96\ \%\ \text{(due to aromatics)} \\ &= -\ 1.3\ \%\ \text{per hour} \quad , \qquad (106)\end{aligned}$$

$$\frac{d[\text{AERO(O)}]}{dt} = \frac{8\ \mu g}{m^3\,\text{ppmC hydrocarbons}} \quad . \qquad (107)$$

As intended, this treatment of organic aerosols is consistent with the formation rate results of Grosjean and Friedlander (1975) discussed above. We also note that past experience with the carbon-bond mechanism and urban mixes has shown that roughly 3 molecules of ozone can be produced by any given OH·-hydrocarbon reaction, and one-third of the oxidizing radicals come from aromatics. This is consistent with the 10 to 1 ratio found by Appel et al. (1976). Furthermore, the assumption that the conversion to aerosol occurs far down the oxidation chain eliminates any influence of organic aerosol chemistry on predicted ozone concentrations. Thus this mechanism for organic aerosol formation stikes a balance between the empiricism necessary at the current stage of aerosol modeling and the demands of chemical kinetic modeling.

2. Nitrate Aerosol

The modes of formation of nitrate aerosol are the least well understood of the three components of the photochemical aerosol. Nitrate levels in the Los Angeles Basin are observed to peak sharply in the morning and then to increase slowly in air masses as they move over the eastern portions of the Basin. The rapid NO_3^- morning buildup appears to be unrelated to the gradual increase in NO_3^- eastward across the Basin later in the day. In the ACHEX study (Hidy et al., 1975), no systematic, useful relation could be established between NO_3^- levels and those of O_3, NO, NO_2, $SO_4^=$, relative humidity, or noncarbonate carbon.

There is virtually no quantitative information available on the rates of conversion of NO_x to NO_3^- in the atmosphere. A rapid transient conversion exists in conjunction with the morning influx of NO_x, perhaps associated with the high relative humidity in the morning hours. The second NO_3^- formation process is slower than that in the morning and is roughly comparable in rate to the oxidation of SO_2 to $SO_4^=$.

Nitrate aerosol can be formed by both heterogeneous and homogeneous pathways. Figure 50 summarizes many of these pathways. The low vapor pressure of sulfuric acid leads to rapid homogeneous nucleation at H_2SO_4 partial pressures in the range of 10^{-8} to 10^{-10} torr. The hydration of sulfuric acid droplets is thermodynamically favored over a wide range of relative humidities. Thus sulfuric acid formed in the gas phase can be expected to become rapidly incorporated into the particulate phase. Although nitric acid can be formed in the gas phase in several ways, the vapor pressure of nitric acid is relatively high and homogeneous nucleation of HNO_3 in humid atmospheres is not expected to take place under normal atmospheric conditions (Kiang et al., 1973). Nitric acid does form stable complexes in sulfuric acid solutions (Gillespie et al., 1958). Castleman (1974) suggested that HNO_3 may become incorporated in sulfuric

Reproduced from best available copy.

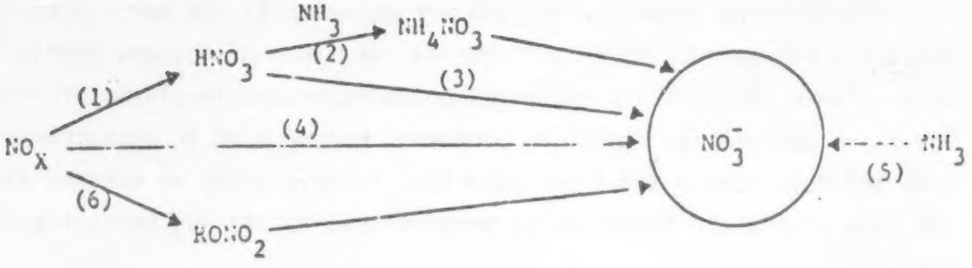

1. Gas-phase formation of HNO_3 from NO_x
2. Gas-phase formation of NH_4NO_3 followed by condensation of NH_4NO_3 on existing droplets
3. Absorption of HNO_3 in droplet
4. Direct absorption of NO_2 in droplet
5. Direct absorption of NH_3 in droplet
6. Formation of organic nitrates in the gas phase followed by condensation of the organic nitrates.

FIGURE 50. PATHWAYS FOR FORMATION OF NITRATE AEROSOLS

acid droplets.* It appears that the production of aerosol nitrate must involve the formation of a condensable species such as NH_4NO_3 in the gas phase followed by chemical stabilization.

The morning nitrate mechanism, generally associated with particles of diameter greater than 0.5 μm, probably involves absorption of NO_x species into droplets followed by chemical reaction. The afternoon mechanism, generally associated with particles of diameters less than 0.5 μm, probably involves the gas-phase oxidation of NO_x in photochemical smog reactions followed by condensation of products such as NH_4NO_3.

---

*To assess the importance of this pathway for removal of HNO_3 from the gas phase, Castleman (1974) suggested measurement of HNO_3 vapor pressures over H_2SO_4-H_2O-HNO_3 solutions.

The reaction paths for nitrate accumulation in the particulate phase via homogeneous steps all involve reactions of gaseous nitric acid. Table 23 lists six major gas-phase reactions involving nitrates. The major homogeneous reactions producing nitric acid in photochemical smog are Reactions 3 and 4 in Table 23. In this study we assumed that the rate of nitrate formation is proportional to the NO_2 concentration, that is

$$\frac{d[NO_3^-]}{dt} = \gamma k_3 [NO_2] \quad , \tag{108a}$$

where $k_3 = 4.1 \times 10^{-4}\ min^{-1}$ and $\gamma = 0.1$. In ACHEX the molecular weights of the nitrates in aerosols were found to be approximately 1.3 times the molecular weight of NO_3^-, or 66 g mole^{-1}. Using this value gives a rate of production of nitrate aerosol

$$\frac{d[AERO(N)]}{dt} = 0.11[NO_2]\ \mu g\ m^{-3} min^{-1} \quad . \tag{108b}$$

TABLE 23. MAJOR HOMOGENEOUS REACTIONS INVOLVING NITRATES IN PHOTOCHEMICAL SMOG

No.	Reaction	Rate Constant at 25°C, ppm^{-1}min^{-1}	Reference
1	$NO_3 + NO_2 \rightarrow N_2O_5$	5.6×10^3	Hampson and Garvin (1975)
2	$N_2O_5 \rightarrow NO_3 + NO_2$	30 min^{-1}	Hampson and Garvin (1975)
3	$N_2O_5 + H_2O \rightarrow 2HNO_3$	5×10^{-6}	Hampson and Garvin (1975)
4	$OH\cdot + NO_2 \rightarrow HNO_3$	10^4	Hampson and Garvin (1975)
5	$OH\cdot + HNO_3 \rightarrow H_2O + NO_3$	190	Hampson and Garvin (1975)
6	$HO_2^{\cdot} + NO_3 \rightarrow HNO_3 + O_2$	2.5×10^3	Demerjian et al. (1974)

3. Sulfate Aerosol and SO_2 Chemistry

The chemistry of the homogeneous, or gas-phase, oxidation of SO_2 to sulfate is represented in the carbon-bond mechanism by Reactions 33 to 38 in Table 15c, which are reproduced below. Computer simulations of some smog chamber experiments with SO_2, propylene, and NO_x performed at Battelle show that significant rates of SO_2 oxidation can be achieved in the apparent absence of heterogeneous oxidation paths. The addition of SO_2 to the propylene/NO_x system did not observably affect its behavior.

$$SO_2 + OH\cdot \xrightarrow{2O_2} HSO_5\cdot \qquad k = 900\ ppm^{-1}min^{-1} \qquad (109)$$

$$HSO_5\cdot + NO \rightarrow HSO_4\cdot + NO_2 \qquad k = 800\ ppm^{-1}min^{-1} \qquad (110)$$

$$HSO_4\cdot + HO_2\cdot \rightarrow H_2SO_4 + O_2 \qquad k = 9000\ ppm^{-1}min^{-1} \qquad (111)$$

$$SO_2 + HO_2\cdot \xrightarrow{H_2O} H_2SO_4 + OH\cdot \qquad k = 1.3\ ppm^{-1}min^{-1} \qquad (112)$$

$$SO_2 + CH_3O_2\cdot \xrightarrow{H_2O, O_2} H_2SO_4 + HCHO + HO_2\cdot \qquad k = 1.5\ ppm^{-1}min^{-1} \qquad (113)$$

$$HSO_4\cdot + NO_2 \xrightarrow{H_2O} H_2SO_4 + HNO_3 \qquad k = 1.0 \times 10^4\ ppm^{-1}min^{-1} \qquad (114)$$

Past smog chamber studies of irradiated SO_2-NO_x-hydrocarbon and SO_2-O_3-olefin mixtures have resulted in a variety of qualitative and quantitative observations, many of which are inconclusive or even contradictory. Of particular significance is an uncertainty about the effect of SO_2 on the yields of carbonyl products (see the reviews by Leighton, 1961; Wilson and Levy, 1970) and ozone (Wilson and Levy, 1970; Altshuller et al., 1968). Wilson and Levy (1970) showed that the overall reaction is strongly dependent on relative humidity. Undoubtedly, chamber effects also play a role in causing these inconsistencies. There is agreement, however, on the observation that the addition of SO_2 to the hydrocarbon-NO_x-air system results in increased aerosol production. It has also been generally observed that the addition of propylene to an irradiated SO_2-NO_x mixture increases SO_2 consumption and aerosol production. The aerosol is thought to be chiefly sulfuric acid and water, though it may contain small concentrations of organic and nitrite-type material (Filby and Penzhorn, 1974; Bufalini, 1971). Using the propylene-NO_x-SO_2 system, Smith and Urone (1974) found that the rate of SO_2 oxidation slowed when the NO_2 concentration was increased relative to the propylene concentration. They also found that the propylene disappeared faster than the SO_2.

A free radical mechanism for SO_2 oxidation is in accord with these observations. Because added hydrocarbon increases aerosol production, the radicals that oxidize SO_2 are probably the same as those oxidizing NO. These radicals must be either organic or of organic origin. The low reactivity of SO_2 accounts for the smallness of its effect on both hydrocarbon oxidation and ozone production. Sulfuric acid is probably the main oxidation product of SO_2.

Recent investigators of atmospheric SO_2 chemistry (e.g., Davis et al., 1974; Calvert and McQuigg, 1975; Castleman et al., 1974) suggested that the oxidation of SO_2 by $OH\cdot$, $HO_2^{\cdot}$, and $RO_2^{\cdot}$ is the primary means of SO_2 removal in the gas phase. Several recent measurements of the

SO_2-$OH\cdot$ rate constant are presented in Table 24. Although these measurements cover a wide range, a value of 900 ppm^{-1} min^{-1} encompasses the range with a 50 percent uncertainty.

As shown in Table 24, Davis (1974) measured a rate constant $k = 1.3\ ppm^{-1} min^{-1}$ for

$$HO_2\cdot + SO_2 \rightarrow OH\cdot + SO_3 \quad . \qquad (115)$$

Since the analogous peroxyalkyl radical reactions are about 8 kcal $mole^{-1}$ more exothermic than Reaction (115), they could in theory be somewhat faster:

$$RO_2\cdot + SO_2 \xrightarrow{O_2} R'CHO + HO_2\cdot + SO_3 \qquad (116)$$

Indeed, some very recent work by Whitbeck et al. (1976) suggests a rate constant for $CH_3O_2\cdot$ with SO_2 of $\leq 5\ ppm^{-1} min^{-1}$.

In some recent computer simulation studies at SAI, the peroxyacyl radical reactions were also considered:

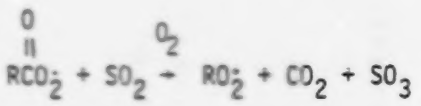

$$R\overset{\overset{O}{\|}}{C}O_2\cdot + SO_2 \xrightarrow{O_2} RO_2\cdot + CO_2 + SO_3 \quad . \qquad (117)$$

However, the results of these studies showed that the $HO_2\cdot$ and $RO_2\cdot$ radicals were sufficient to explain the rate of disappearance of SO_2 and of appearance of aerosol (presumably from the rapid reaction of SO_3 with H_2O). Furthermore, the inclusion of the peroxyacyl radical reactions produced too much SO_2 conversion too late in the simulation compared with the experimental observations in the Battelle smog chamber. The peroxyacyl radicals form later in the smog formation simulations because their major source is hydroxyl attack on the aldehydes, which are intermediate oxidation products from the original hydrocarbons.

TABLE 24. RATE CONSTANTS FOR SO_2 OXIDATION
($ppm^{-1}min^{-1}$)

Reaction	Davis (1974)	Calvert and McQuigg (1975)	Castleman et al. (1974)	Others	Values Used in Recent SAI Studies
$SO_2 + OH \rightarrow HSO_3^{\cdot}$	1350 ± 130		590	860 ± 120 (Cox, 1974)	900
$SO_2 + O \xrightarrow{M} SO_3$	$(7.6 \pm 0.9) \exp(-2240/RT)$				
$SO_2 + NO_3 \rightarrow SO_3 + NO_2$	< 14.7	< 10^{-5}			
$SO_2 + HO_2^{\cdot} \rightarrow SO_3 + OH\cdot$	1.35 ± 0.2	$10^{-4}k(OH\cdot + SO_2)$• if $HSO_4^{\cdot}$ is a product			1.3
$SO_2 + RC(O)O_2^{\cdot} \rightarrow R + CO + SO_3$		≳ $HO_2^{\cdot} + SO_2$			1.5
$SO_2 + RO_2^{\cdot} \rightarrow RO\cdot + SO_3$					
$SO_2 + h\nu \rightarrow SO_2^*$				~ 10^{-4} min^{-1} (Leighton, 1961)†	
$SO_2 + N_2O_5 \rightarrow 2NO_2 + SO_3$	≤ 1.2 10^{-8}	< 6.2 10^{-8}			
$SO_2 + O_3 \rightarrow SO_3 + O_2$	3×10^{-7}	< 1.2 10^{-10}			
$SO_3 + H_2O \xrightarrow{M} H_2SO_4$			740		Immediate
$RO_2^{\cdot} + SO_2 \rightarrow ROSO_3$		$10^{-4}k(OH\cdot + SO_2)$			
$HSO_3^{\cdot} + O_2 \rightarrow HSO_5^{\cdot} \rightarrow SO_3 + HO_2^{\cdot}$					800
$HSO_5^{\cdot} + NO \rightarrow HSO_4^{\cdot} + NO_2$					9000
$HSO_4^{\cdot} + HO_2^{\cdot} \rightarrow H_2SO_4 + O_2$					1×10^4
$HSO_4^{\cdot} + NO_2 \xrightarrow{H_2O} H_2SO_4 + HNO_3$					

---

† Quantum yields for SO_3 production (ϕ_{SO_3}) measured in an SO_2 atmosphere vary from 3×10^{-4} (Cox, 1972) to 0.1 (Chung et al., 1975). Chung et al. (1975) explained this discrepancy by considering secondary reactions. Extrapolation of these results to atmospheric condition is not possible at present because ϕ_{SO_3} varies with atmospheric pressure and type of diluent.

Reactions of NO_3 and N_2O_5 with SO_2 were postulated by Wilson and Levy (1969) to explain a rapid reaction observed between NO_2, O_3, and SO_2. As shown in Table 24, this could not be explained by direct reaction of SO_2 with O_3. Thus, the following sequence was suggested:

$$NO_2 + O_3 \rightarrow NO_3 \underset{M}{\overset{NO_2}{\rightleftharpoons}} N_2O_5 \quad , \qquad (118)$$

$$NO_3 + SO_2 \rightarrow SO_3 + NO_2 \quad , \qquad (119)$$

$$N_2O_5 + SO_2 \rightarrow SO_3 + 2NO_2 \quad . \qquad (120)$$

The upper limits of the $N_2O_5 + SO_2$ reaction rate (Table 24) indicate its insignificance. In contrast, the upper limits recorded for k_{119} are in severe disagreement.

Cox and Penkett (1972) found that SO_2 added to the olefin-O_3 system produced sulfate aerosol, which was presumed to be sulfuric acid. They also found that, when the ozone-olefin consumption ratio in the absence of SO_2 was greater than 1, the addition of SO_2 reduced this ratio. The addition of SO_2 also enhanced carbonyl product yields. From these and other results, Cox and Penkett inferred that a short-lived intermediate of the ozone-olefin reaction, which they speculated might be a zwitterion, was responsible for SO_2 oxidation. However, the observations made by Cox and Penkett can be accounted for in terms of reactions of SO_2 with hydroxyl, hydroperoxyl, and peroxyalkyl radicals rather than zwitterions (O'Neal and Blumstein, 1973).

The final mode of SO_2 oxidation included in Table 24 is direct oxidation by oxygen atoms. This can be ruled out, because the maximum oxygen concentration is only about 10^{-9} ppm. With SO_2 in ppm concentrations, this gives rates $\lesssim$ 0.01 percent per hour.

Direct reaction between the excited triplet state of SO_2 ($^3SO_2$) and hydrocarbons has been reported at high reactant pressures (Sidebottom et al., 1971; Filby and Penzhorn, 1974). However, at low concentrations, Demerjian et al. (1974) found that the primary result of the interaction of $^3SO_2$ with 2-butene was the interconversion of cis and trans isomers. Thus, a direct chemical reaction between $^3SO_2$ and olefins under atmospheric conditions can also be ruled out.

As shown in Table 24, SO_3 is produced by the reactions of $OH\cdot$, $HO_2\cdot$, and $RO_2\cdot$ with SO_2. Castleman et al. (1974) found that SO_3 rapidly combines with water to form H_2SO_4. Presumably, H_2SO_4 then nucleates and adds more water to form aerosol droplets ($H_2SO_4 \cdot nH_2O$). The studies carried out by Cox and Penkett (1972) and the more recent mass spectrometric measurements made by Schulten and Schurath (1975) indicate that H_2SO_4 is the major sulfur-containing product of the olefin-O_3-SO_2 reactions. Bufalini (1971) reported that the aerosol produced as a result of irradiation of 3 ppm of lower olefins in the presence of 1 ppm NO_2 and 0.5 ppm SO_2 at 50 percent relative humidity was primarily composed of sulfuric acid. Accordingly, no other products have been accounted for in the present mechanism. Furthermore, it has been assumed that SO_3 is rapidly converted to H_2SO_4 as long as the reaction mixture contains water vapor.

Davis et al. (1974) and Calvert and McQuigg (1975) have speculated on the formation of compounds containing S, O, H, and N when NO_x is present. Presumably, the formation of these nitrogen-containing species results from radical-radical reactions with oxidation products of the $OH\cdot$-SO_2 adduct. For example, $HSO_4\cdot$, formed as shown in Table 24, could combine with NO_2 to form HSO_4NO_2. Subsequent hydrolysis at the wall would produce nitric and sulfuric acid:

$$HSO_4\cdot + NO_2 \xrightarrow[\text{surface}]{H_2O} H_2SO_4 + HNO_3 \quad . \qquad (121)$$

This represents one possible fate of the $HSO_4^{\cdot}$ radical produced in the following series:

$$OH\cdot + SO_2 \rightarrow HSO_3^{\cdot} \xrightarrow{O_2} HSO_5^{\cdot} \quad , \qquad (122)^*$$

$$HSO_5^{\cdot} + NO \rightarrow HSO_4^{\cdot} + NO_2 \quad . \qquad (123)$$

Other possible reactions of $HSO_4^{\cdot}$ (and $HSO_5^{\cdot}$) assembled by Calvert and McQuigg (1975) include hydrogen abstractions from alkanes and $HO_2^{\cdot}$, and addition to olefinic double bonds. Davis et al. (1974) proposed that $HSO_6^{\cdot}$ could be produced by the addition of O_2 to $HSO_4^{\cdot}$. $HSO_6^{\cdot}$ could then oxidize two NO molecules to reform $HSO_4^{\cdot}$, which would then repeat the process:

$$HSO_4^{\cdot} + O_2 \rightarrow HSO_6^{\cdot} \xrightarrow{2NO} HSO_4^{\cdot} + 2NO_2 \quad . \qquad (124)$$

This mechanism was developed to explain an ozone bulge found by Davis et al. (1974) in the plume downwind of the Potomac Electric Power Company's power plant at Morgantown. However, laboratory studies have shown that the addition of SO_2 to the hydrocarbon-NO_x system (which, it can be argued, is not the system Davis et al. observed) actually causes either little change or a reduction in O_3 production (Wilson and Levy, 1970). As mentioned earlier, it is assumed in the present mechanism formulation that SO_2 has only minor effects on O_3 yield; thus, the suggestion made by Davis et al. has not been incorporated. In addition to Reaction (123) a simple termination reaction,

$$HO_2^{\cdot} + HSO_4^{\cdot} \rightarrow H_2SO_4 + O_2 \quad , \qquad (125)$$

which was suggested by Davis et al. (1974), has been included.

---

* An alternative to the last step in Reaction (122), $HSO_3^{\cdot} + O_2 \rightarrow HO_2^{\cdot} + SO_3$, seems implausible thermodynamically. ΔH is approximately 0 to 20 kcal mole^{-1} for this step, compared with ΔH ∿ -50 kcal mole^{-1} for the last step in Reaction (122).

Thus our formulation of a photochemical mechanism for conversion of SO_2 to sulfate aerosol consists of Reactions (115), (116), (121), (122), (123), and (125) plus the carbon-bond mechanism. We have tested this combination by modeling the Battelle experiments mentioned above. Basically, these experiments consisted of irradiations of propylene (about 1 ppm), NO_x (about 0.5 ppm), and SO_2 (about 0.5 ppm) that generated about 0.5 ppm of ozone after three hours. Such an oxidant level would constitute a very severe smog episode.

Table 25 presents the rates of SO_2 oxidation of various oxidants, as computed using the SAI model. As this table shows, $RO_2^{\cdot}$ and $HO_2^{\cdot}$ appear to be the most important oxidants. Nevertheless, the overall oxidation rate averages about 8 percent per hour. Because of the severity of the ozone formation, this value probably represents an upper limit for the homogeneous oxidation of SO_2.

TABLE 25. RATES OF SO_2 OXIDATION BY VARIOUS OXIDANTS FOR THE BATTELLE SIMULATION

Time (hour)	Oxidant	Rate (percent per hour)
1	$OH\cdot$	1.4%
	$RO_2^\cdot$	3.0
	$HO_2^\cdot$	2.7
	Total	7.1
2	$OH\cdot$	1.2
	$RO_2^\cdot$	4.6
	$HO_2^\cdot$	3.4
	Total	9.2
3	$OH\cdot$	0.8
	$RO_2^\cdot$	4.7
	$HO_2^\cdot$	2.9
	Total	8.4
4	$OH\cdot$	0.7
	$RO_2^\cdot$	4.8
	$HO_2^\cdot$	2.3
	Total	7.8

VI THE ESTIMATION OF PHOTOLYSIS RATE CONSTANTS

by James P. Killus

A. INTRODUCTION

Rate constants for photochemical smog models have for the most part been based upon theoretical calculations by Leighton (1961) that correlate k_1 with solar zenith angle by means of a model atmosphere. Because this model neglects attenuation within the polluted layer, and also because of inaccuracies in the solar spectrum used in the calculations, the calculated UV fluxes are too high. Fortunately for previous modeling efforts, Leighton's estimates of quantum yields for NO_2 are too low (Peterson and Flowers, 1976), and the two effects tend to cancel.

In this chapter we attempt to reformulate the procedures for calculating rate constants for the SAI Urban Airshed Model. In addition, we examine the optical characteristics of the polluted layer and their probable effects on photolysis.

The starting point for estimating the amount of solar radiation transmitted through the atmosphere is the Beers-Lambert Law,

$$I_t(\lambda) = I_0(\lambda)e^{-\alpha(\lambda)} \quad , \qquad (126)$$

where $I_0(\lambda)$ and $I_t(\lambda)$ are the incident and transmitted intensities and α is the attenuation coefficient at wavelength λ. The attenuation coefficient α is often called the optical thickness of the attenuation layer because

$$\alpha = \varepsilon(\lambda)m \qquad (127)$$

where $\sigma(\lambda)$ is the attenuation per unit mass at wavelength λ and m can be related to the amount of the absorbing gas. For aerosols σ is expressed in units of mass^{-1}, and for gases it is often expressed in units of the inverse of the partial pressure of the gas.

Attenuation of a beam of light occurs by absorption and scattering. Absorption converts light energy into heat or chemical energy. Scattering may cause the light to take a longer path through the polluted layer, which increases its probability of being absorbed.

Scattering itself occurs mainly in two ways. One is molecular or Rayleigh scattering, which is almost symmetric, that is, it occurs about equally in all directions. The amount of Rayleigh scattering depends on the inverse fourth power of the wavelength. Thus blue light is scattered 16 times more than red, which causes the blue color of the sky.

Mie or aerosol scattering is caused by aerosols with diameters on the order of one wavelength of visible light or larger. Unlike Rayleigh scattering, Mie scattering has a strong angular dependence. Mie scattering is more complex than Rayleigh scattering because it depends on both wavelength and particle diameter. Fortunately, when Mie scattering is averaged over a large number of particles with a common size distribution, this complexity diminishes. For example, the aerosol may have a power law size distribution

$$\frac{dN}{dr} = cr^{-v} \quad , \qquad (128)$$

where N is particle number density as a function of the particle radius, r, c is a constant that depends on the total number of particles, and v is the slope of the size distribution. In this case, the aerosol light extinction coefficient is related to the wavelength of light by

$$b_{scat}(\lambda) = k\lambda^{-\beta} \quad , \qquad (129)$$

(Van de Hulst, 1957), where β, called the Angstrom exponent, is the power dependence of light scattering on wavelength. This dependence of scattering on wavelength has been observed to hold in a variety of circumstances. In the absence of aerosol, $\beta = 4$, that is, Rayleigh scattering applies. In the lower atmosphere, β has been observed to vary from 0.5 for highly polluted air to 2.8 for very clean air (Thielke et al., 1972; Charlson et al., 1972; Butcher and Charlson, 1972). In high pollution conditions, Mie scattering is more important than Rayleigh scattering and β varies from 0.5 to 2.0, with 1.5 being a typical value.

Scattering is important for two reasons. First, it reduces the light intensity because some light is backscattered and escapes the atmosphere. Second, the diffuse radiation caused by scattering has geometric properties different from the direct radiation, so it must be treated differently. The light available for photolysis at any point is equal to

$$I_v = \int I_r \cdot dr \qquad (130)$$

where dr is the differential element of a sphere surrounding the point and I_r is the flux through that element. I_v is referred to as the volumetric flux. I_v is factored into three components, direct irradiance (I_d), sky irradiance (I_s), and backscattered irradiance (I_b). Sky irradiance is directed downward, and backscattered irradiance upward. UV is commonly measured as the flux through a horizontal surface. The direct radiation as measured by a horizontal plane is then

$$I_{d_{plane}} = I_d \cos(z) \quad , \qquad (131)$$

where I_d is the intensity measured normal to the direct radiation and z is the angle of the sun from the zenith, or the solar zenith angle.

Sky irradiance is more complex because it is the integral of a function over the entire sky. If we assume that sky irradiance is uniform, i.e., that I_s can be represented by a uniformly bright hemisphere, then for a horizontal plane near the earth's surface,

$$I_{s_{plane}} = \int_0^{\pi/2} \cos(z)\, dI_s \quad , \tag{132}$$

where dI_s is a set of annular rings at angle dz. Thus

$$dI_s = I_s \sin(z)\, dz \quad . \tag{133}$$

From Eqs. (132) and (133), sky irradiance becomes

$$I_{s_{plane}} = \int_0^{\pi/2} I_s \cos(z) \sin(z)\, dz$$

$$= 1/2\, I_s \quad . \tag{134}$$

Upward-directed or backscattered irradiance does not reach the top of a horizontal plane, so the intensity measured on a horizontal plane is

$$I_{plane} = I_{d_{plane}} + I_{s_{plane}} = I_d \cos(z) + \frac{1}{2} I_s \quad . \tag{135}$$

This relationship can be approached in a somewhat different manner with the same result (see Leighton, 1961, p. 27).

For a surface layer of height h containing a gas x at concentration c, by the Beers-Lambert Law,

$$I_{a\lambda} = \frac{I_{d\lambda}\left\{1-\exp[-\alpha(\lambda)\ ch \sec(z)]\right\} + I_{s\lambda}\left\{1-\exp[-\alpha(\lambda)\ cih]\right\}}{h} \quad , \tag{136}$$

where $I_{a\lambda}$ is the average light absorbed per unit volume at wavelength λ, $\alpha(\lambda)$ is the absorption coefficient of gas x at wavelength λ, and i is the optical path length (through the atmosphere) of sky irradiance at wavelength λ.

For weak absorption, such as by an infinitesimally thin layer, Eq. (136) becomes

$$I_a = \alpha(\lambda)\, c(I_{d\lambda_{plane}} \sec(z) + I_{s\lambda} \cdot i) \quad . \qquad (137)$$

When multiplied by the photolytic quantum yield, Eq. (137) becomes the formula for the photolysis rate.

Leighton further demonstrates that for the evenly lit hemisphere i = 2, thus obtaining

$$I_{volumetric} = I_{d_{plane}} \sec(z) + 2I_s \quad .$$

B. THE MULTI-LAYER LIGHT-SCATTERING MODEL

In 1973, the California Air Resources Board contracted Meteorology Research, Inc. (MRI) to use instrumented aircraft to obtain vertical profiles of b_{scat}, NO_x, ozone, and other pollutants in the Los Angeles Basin (Smith et al., 1976). We chose for examination two flights, both made at Riverside, California. The first was at 17:48 on 25 July 1973, a typical high pollutant day. The second was at 16:58 on 28 September 1973, a day with much cleaner air, as evidenced by a b_{scat} of 15 percent of the first flight (see Tables 26 and 27).

We prepared a Multi-Layer Light-Scattering Model that would accept the MRI data as input. The model divides the polluted layer (ground* to 1460 meters) into N sublayers and N+1 boundaries (including the ground).

---

*Riverside is 275 meters above sea level.

TABLE 26. MRI DATA FROM FLIGHT ENDING AT 17:48 ON 25 JULY 1973 AT RIVERSIDE, CALIFORNIA

Altitude (feet)	Integrations				
	b_{scat}	Condensation Nuclei ($\times 10^9$ m^{-2})	Carbon Monoxide ($g\ m^{-2}$)	Ozone ($mg\ m^{-2}$)	NO_x ($mg\ m^{-2}$ as NO_2)
900.	0.024	1296.	0.05	17.30	2.04
1000.	0.053	2915.	0.11	38.92	6.38
1100.	0.083	4535.	0.17	60.55	9.92
1200.	0.113	6155.	0.23	82.17	13.47
1300.	0.142	7949.	0.29	101.65	16.98
1400.	0.170	9410.	0.36	127.41	20.39
1500.	0.196	10627.	0.46	150.03	23.70
1600.	0.220	11829.	0.58	172.66	26.96
1700.	0.242	12869.	0.65	195.79	29.91
1800.	0.265	14018.	0.77	220.87	33.33
1900.	0.291	15016.	0.91	247.47	37.47
2000.	0.318	16444.	1.03	274.54	41.26
2100.	0.344	17785.	1.15	298.09	45.27
2200.	0.371	19138.	1.28	320.02	49.66
2300.	0.397	20269.	1.43	343.71	52.72
2400.	0.419	20951.	1.58	361.77	55.42
2500.	0.442	21842.	1.71	374.00	57.46
2600.	0.456	22082.	1.70	386.74	58.10
2700.	0.462	22082.	1.71	392.76	58.46
2800.	0.465	22082.	1.72	398.28	58.79
2900.	0.467	22082.	1.72	401.84	59.12
3000.	0.469	22090.	1.76	410.69	59.66
3100.	0.471	22099.	1.79	416.18	60.24
3200.	0.474	22099.	1.83	421.00	60.89
3300.	0.476	22107.	1.88	427.98	61.60
3400.	0.479	22109.	1.94	431.03	62.33
3500.	0.482	22111.	2.01	443.08	63.05
3600.	0.485	22121.	2.08	445.17	63.73
3700.	0.488	22128.	2.15	452.35	64.41
3800.	0.491	22128.	2.22	458.57	65.22
3900.	0.494	22136.	2.27	465.01	66.08
4000.	0.497	22150.	2.32	471.73	66.84
4100.	0.499	22151.	2.37	478.72	67.65
4200.	0.502	22151.	2.42	486.51	68.47
4300.	0.506	22182.	2.48	491.81	69.30
4400.	0.510	22335.	2.58	503.45	70.17
4500.	0.514	22478.	2.64	511.92	71.12
4600.	0.519	22593.	2.72	520.10	72.01
4700.	0.523	22664.	2.76	529.24	72.84
4800.	0.528	22733.	2.79	536.25	73.69
4900.	0.532	22816.	2.83	541.60	74.58
5000.	0.536	22926.	2.91	551.59	75.48

Note: Data extrapolated below 1100 feet. 1 foot = 0.3048 meters.

Reproduced from best available copy.

Source: Smith et al. (1976).

TABLE 27. MRI DATA FROM FLIGHT ENDING AT 16:58 ON 28 SEPTEMBER 1973 AT RIVERSIDE, CALIFORNIA

Altitude (feet)	Integrations				
	b_{scat}	Condensation Nuclei ($\times 10^9$ m^{-2})	Carbon Monoxide (g m^{-2})	Ozone (mg m^{-2})	NO_x (mg m^{-2} as NO_2)
900.	0.002	1337.	0.00	5.39	1.62
1000.	0.005	2626.	0.00	10.78	3.26
1100.	0.007	3680.	0.00	16.12	4.95
1200.	0.009	4795.	0.00	21.59	6.55
1300.	0.012	6137.	0.00	26.93	8.43
1400.	0.014	7058.	0.00	32.32	10.11
1500.	0.016	7971.	0.00	37.94	11.87
1600.	0.018	9106.	0.00	43.47	13.74
1700.	0.020	10041.	0.00	49.05	15.53
1800.	0.022	10746.	0.00	54.70	16.97
1900.	0.024	11435.	0.00	60.10	18.53
2000.	0.025	11880.	0.00	65.15	19.60
2100.	0.027	12193.	0.00	70.49	20.79
2200.	0.028	12660.	0.00	75.87	22.21
2300.	0.029	12990.	0.00	81.70	23.37
2400.	0.031	13360.	0.00	87.57	24.54
2500.	0.033	13754	0.00	91.02	25.72
2600.	0.035	14231.	0.00	100.71	27.07
2700.	0.037	14614.	0.00	108.01	28.41
2800.	0.039	15017.	0.00	115.11	29.75
2900.	0.041	15260.	0.00	122.32	30.94
3000.	0.043	15464.	0.00	127.41	32.09
3100.	0.045	15676.	0.00	134.61	33.23
3200.	0.047	15904.	0.00	141.56	34.38
3300.	0.049	16292.	0.00	150.57	35.60
3400.	0.051	16631.	0.00	157.50	36.84
3500.	0.053	16954.	0.00	164.51	38.11
3600.	0.055	17302.	0.00	171.54	39.24
3700.	0.057	17646.	0.00	178.46	40.43
3800.	0.059	18059.	0.00	185.34	41.60
3900.	0.061	18497.	0.00	192.67	42.96
4000.	0.064	18922.	0.00	200.00	44.33
4100.	0.066	19316.	0.00	207.31	45.52
4200.	0.068	19684.	0.00	214.49	46.91
4300.	0.070	19967.	0.00	221.79	48.05
4400.	0.071	20314.	0.00	228.34	49.35
4500.	0.072	20657.	0.00	234.17	50.62
4600.	0.074	20967.	0.00	239.81	51.89
4700.	0.075	21283.	0.00	245.41	53.10
4800.	0.076	21587.	0.00	250.90	54.29
4900.	0.077	21894.	0.00	256.24	55.47
5000.	0.079	22248.	0.00	261.28	56.78

Reproduced from best available copy.

Note: Data extrapolated below 1100 feet. 1 foot = 0.3048 meters.

Source: Smith et al. (1976).

The light at any boundary is taken to be equal to the downward-directed light at the boundary above, corrected for scattering and absorption, plus the upward-directed light at the boundary below, also corrected.

It is then possible to write a series of equations for the light in the i-th layer:

$$I_{d_i} = I_{d_{i-1}} \left[10^{-\alpha_{i-1} \sec(z)}\right] \left[10^{-b_{scat_{i-1}} \sec(z)}\right] , \qquad (138)$$

$$\begin{aligned} I_{s_i} = {} & (1 - C_2) \left[1 - 10^{-b_{scat_{i-1}} \sec(z)}\right] \left[I_{d_{i-1}} \, 10^{-\alpha_{i-1} \sec(z)}\right] \\ & + I_{s_{i-1}} \, 10^{-2(\alpha_{i-1})} \\ & - C_2 \, I_{s_{i-1}} \left(1 - 10^{-2b_{scat_{i-1}}}\right) \\ & + C_2 \, I_{b_i} \left(10^{-2\alpha_{i-1}}\right) \left(1 - 10^{-2b_{scat_{i-1}}}\right) , \end{aligned} \qquad (139)$$

$$\begin{aligned} I_{b_i} = {} & C_1 \left[1 - 10^{-b_{scat_i} \sec(z)}\right] \left[10^{-\alpha_i \sec(z)}\right] \\ & + I_{b_{i+1}} \, 10^{-2\alpha_i} \\ & - C_2 \, I_{b_{i-1}} \, 10^{-2\alpha_i} \\ & + C_2 \, I_{s_i} \, 10^{-2\alpha_i} \left(1 - 10^{-2b_{scat_i}}\right) , \end{aligned} \qquad (140)$$

where

I_d, I_s, I_b = the intensities of direct, sky, and backscattered irradiance,

C_1 = fraction of backscatter to total scatter for direct light*,

C_2 = fraction of backscatter to total scatter for diffuse light*,

b_{scat} = optical thickness of Mie scattering,

α = optical thickness of absorbers $[= \alpha(O_3) + \alpha(NO_2) + \alpha(b)]$,

$\alpha(O_3)$ = absorption due to ozone,

$\alpha(NO_2)$ = absorption due to NO_2, assuming that 70 percent of the measured NO_x is NO_2,

$\alpha(b)$ = absorption due to aerosols; assumed to be equal to a constant fraction of b_{scat}.

and the subscript i refers to the i-th layer in the model. The factors of 2 and sec (z) in the exponents account for the path lengths of sky and direct irradiance through the polluted layer. The derivation of the Multi-Layer Light-Scattering Model assumes that:

- > I_b at the ground equals the albedo times the sum of the sky and direct irradiance.
- > Solar irradiance can be divided into direct and diffuse irradiances. Direct irradiance is defined as the irradiance within 10° of the center of the sun.

---

*C_1 and C_2 are evaluated from Elterman (1968) by integrating over the angular dependence of the scattering function. C_2 is a constant for any given scattering function and was evaluated as 0.25. C_1 is dependent on zenith angle and varies from 0.08 at z = 0 to nearly 0.5 at z = 80°.

> Diffuse irradiance can be divided into downward-directed (sky) and upward-directed (backscattered) hemispheric radiation.
> Hemispheric radiation is uniform over the hemisphere.
> The dependence of scattering on wavelength follows a power law.
> Light absorption by aerosols is a constant proportion of light scattering by aerosols regardless of wavelength. In this study a value of 0.05 was used for this proportion.
> The albedo of the ground is independent of wavelength and angle.
> Polarization effects can be neglected.

Elterman (1968) tabulated Rayleigh and Mie scattering coefficients as a function of height. Using these values, we extended the model for 20 additional layers; with the final boundary at 20 km and the final layer containing all optical parameters above 20 km. With this extension, we can start with the extraterrestrial solar spectrum (Ackerman, 1971) and follow the scattering and absorption processes through the atmosphere.

Because of the importance of Rayleigh scattering above the bottom layer of the troposphere, and because Rayleigh scattering has properties significantly different from Mie scattering, the backscattering parameters were modified by taking a weighted average for the relevant Mie scattering parameter and 0.5 for the upward-directed fraction of Rayleigh scattering.

C. APPLICATION OF THE MODEL

The Multi-Layer Light-Scattering Model was exercised with the MRI data described in Tables 26 and 27 and the parameters in Table 28. These predictions were compared with both measurements of volumetric UV flux (Stair and Nader, 1965; Nader and White, 1969), and the predictions of a

TABLE 28. PARAMETERS USED IN MODEL CALCULATIONS

Parameter	Values Used		
Albedo of ground	0.15	0.25	
Ratio of absorption to scattering for aerosols	0.05	0.10	0.15
Ratio of backscatter to total scatter for direct radiation (at solar zenith angle 0°)		0.11	
Ratio of backscatter to total scattering for hemispheric radiation		0.25	
Power-law exponent for scattering (for MRI data)[*]	1.5		2.5
Zenith angle of sun	0° → 70°		
Ratio of NO_2 to NO_x		0.7	
Path length of hemispheric irradiance		2	

---

[*] 1.5 for "polluted case," 2.5 for "unpolluted case." The power-law exponents for most normal urban conditions are probably within this range.

considerably more sophisticated model that employs a direct numerical solution of the radiative transfer equation (Dave and Halpern, 1975). Since the MRI data were taken under a variety of conditions at both Mt. Wilson and downtown Los Angeles. the model was used to predict UV fluxes for 1525 meters and 275 meters (ground level) under both low and high pollutant conditions. In the following discussion, "polluted case" and "unpolluted case" refer to values of 1.5 and 2.5 for the exponent in Eq. (129), the power-law dependence of scattering on wavelength. Note that because of time-averaging and because the zenith angle varies with time of day, the zenith angles reported with the measurements may be inaccurate by several degrees. In general we chose the data points closest to the zenith angle for which the models were exercised, and avoided interpolations.

As shown in Table 29, the predictions of both models are greater than the measured UV fluxes. At lower zenith angles our model overpredicts by about 30 percent, and the Dave and Halpern model overpredicts by nearly 100 percent.

The inaccuracy of the Dave and Halpern model in these comparisons does not actually bring their model into question. Although they used an optical thickness for Rayleigh scattering the same as that used in this study, Dave and Halpern used an aerosol scattering thickness that is much smaller, indeed one that corresponds to an altitude of 4 km according to the data of Elterman (1968). Since the Elterman data are corroborated by the MRI data, this must be taken as a shortcoming of Dave and Halpern's results and a partial explanation of the discrepancies between the predictions of the two models--at least at low zenith angles. These discrepancies are mirrored in the differences between the two models in the percentages of direct and sky irradiances. (See Table 30.)

Another difference between the two models is that light absorption by aerosols is assumed to be 13 to 20 percent of light scattering by aerosols (depending on wavelength) in the Dave and Halpern model, and a constant 5 percent in our model. However, sensitivity studies with the Multi-Layer Light-Scattering Model showed that increasing this parameter to 15 percent generally reduced the predictions by about 10 percent for the unpolluted case and about 20 percent for the polluted case. These variations are surprisingly independent of zenith angle, perhaps because most of the light in the lower layers (where most aerosols are) is modeled as angle-independent sky irradiance.

A 20 percent to 30 percent discrepancy between model predictions and data is not large in view of the uncertainties in both the data and the inputs to the models. Of greater concern from the standpoint of model validation is the increasing overestimation of irradiance at higher zenith

TABLE 29. CALCULATED AND MEASURED IRRADIANCES IN WATTS/M^2 AT 360 nm

				Predictions (values in parenthesis include upward-directed radiation)							
	Measurements*			Dave and Halpern Model					Multi-Layer Light Scattering Model †		
					Diffuse Irradiance		Sec (z)· Direct Irradiance + 2· Sky Irradiance†				
Zenith Angle (degrees)	Mt. Wilson	Down-town L.A.	Down-town L.A. (clear day)	Direct Irradi-ance	Albedo = 0	Albedo = 0.3	Albedo = 0	Albedo = 0.3	5000 feet	Ground level (clear day)	Ground level (pollut-ed day)
15	--	--	--	5.2	2.6	3.4	10.5	12.1 (15.7)	9.4 (11.79)†	8.45 (9.72)	5.6 (6.46)
30	--	--	--	4.3	2.4	3.1	9.4	10.8 (14.0)	9.13 (10.88)	8.1 (9.32)	5.27 (6.07)
40	5.9	4.0	4.9	3.4	2.3	2.9	9.1	10.3	8.8 (10.54)	7.7 (8.86)	4.92 (5.66)
45	5.6	3.8	4.7	--	--	--	--	--	8.5 (10.28)	7.4 (8.52)	4.67 (5.37)
60	3.8	2.6	3.2	1.4	1.8	2.2	6.5	7.2	7.42 (9.1)	6.2 (7.09)	3.8 (4.34)
70	2.3	2.0	2.4	0.53	1.4	1.5	3.18	3.6	5.79 (7.8)	5.12 (5.89)	3.17 (3.64)

---

* Source: Stair and Nader (1967).

† Volumetric (irradiance that would be measured on the surface of a sphere).

TABLE 30. RATIO OF SKY TO DIRECT IRRADIANCE AT 360 nm

		Diffuse/Direct Irradiances		
		Multi-Layer Light-Scattering Model		
Zenith Angle (degrees)	Dave and Halpern Model	Ground Level	1 Km	4 Km
15	0.473	1.36	0.787	0.44
30	0.49	1.6	0.899	0.50
40	0.513	1.95	1.05	0.58
60	0.64	4.34	2.0	1.0
70	0.89	11.6	4.1	1.4

angles. At a zenith angle of 60°, the predictions of the Multi-Layer Light Scattering Model are 25 percent lower than those at solar noon while the data are 40 percent lower (Figure 51). At 70° those percentages are 40 percent and 65 percent respectively. Since for this comparison the detailed model of Dave and Halpern is close to the observations, one of the simplifying assumptions in our model must become invalid at higher zenith angles. Most probably, the assumption of uniform sky irradiance is in error to different amounts at different zenith angles, and the average path length varies from less than 2 at the lower zenith angles to greater than 2 at higher angles. Our results suggest that multiple scattering and boundary effects may cause the average path length to exceed 2 even at zenith angles below 60°.

The variation of the path length with zenith angle for sky irradiance is significant. Specifically, at some angle the path length for direct irradiance and the average path length for sky irradiance are equal. Below this angle, scattered light is more likely to be absorbed

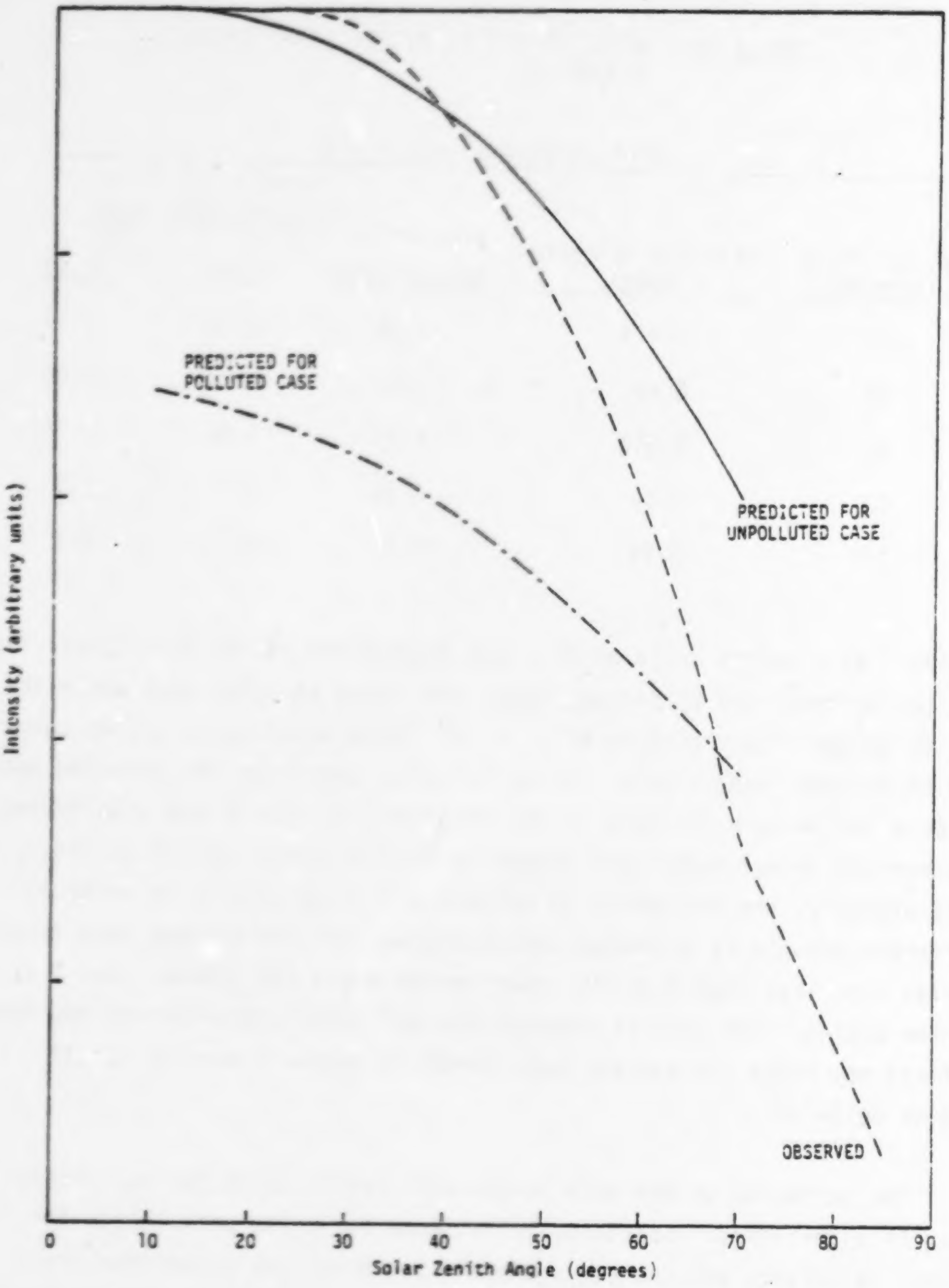

FIGURE 51. PREDICTED AND OBSERVED VOLUMETRIC UV INTENSITY AS A FUNCTION OF SOLAR ZENITH ANGLE

than is direct light. Above this angle, the opposite is true. It is assumed in our model that the path length of diffuse irradiance is constant. In reality, it is not constant, although it does not vary as much as does the path length of direct irradiance. Thus, photolysis rates are not a simple function of the secant of the zenith angle.

For the polluted case, calculated volumetric UV radiation declines about 10 percent between 1525 meters and 762 meters (the approximate inversion height) and 45 percent between there and the ground. The attenuation is linear within the polluted layer and b_{scat} is constant. (See Figure 52).

The intensity of upward-directed light increases with height because polluted air scatters more light than the ground reflects. Hence, the attenuation one would observe with upper hemisphere detectors (such as an Eppley detector) is less than the volumetric decrease, being about 40 percent at 30°. Peterson and Flowers (1976) have observed typical differences of 30 to 40 percent between Eppley measurements taken at Mt. Disappointment (15 miles northeast of downtown Los Angeles and approximately 1830 meters high) and downtown Los Angeles. Peterson and Flowers mention that attenuation increases with zenith angle. which of course, is hardly surprising. The attenuation also increases with decreasing wavelength (Stair and Nader, 1965).

Stair and Nader (1965) measured upward-directed radiation via an Eppley detector attached to the underside of an airplane wing. They observed that the outgoing radiation increased with height and also with greater overcast, haze, and smog. These results, though qualitative and general, are consistent with the model of smog as a turbid medium.

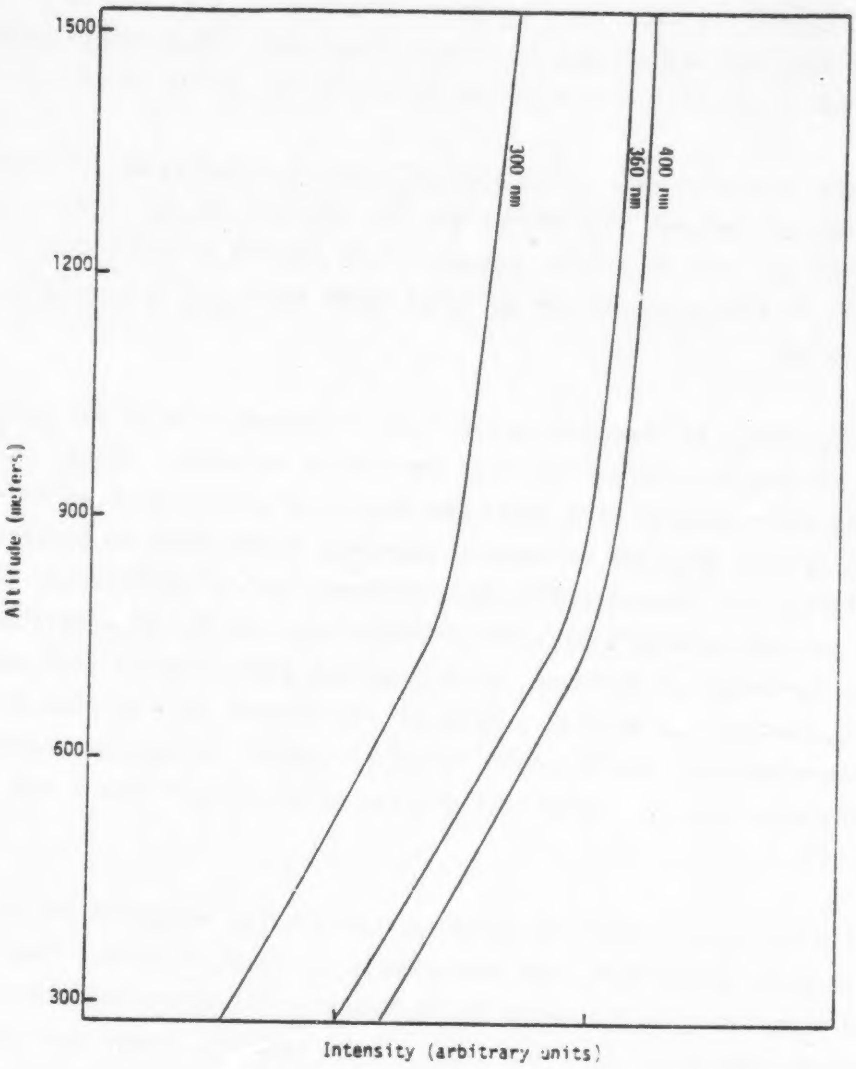

FIGURE 52. ATTENUATION OF UV IN THE POLLUTED LAYER AS A FUNCTION OF HEIGHT. Solar zenith angle = 35°.

D. PREDICTION OF PHOTOLYSIS RATE CONSTANTS

Jeffries, Fox, and Kamens (1974) measured k_1 with a one-liter quartz flask operating as a continuous stirred flow reactor and exposed to full volumetric solar irradiance. The UV transmission of the quartz flask was not reported. For 19 September 1974 they reported a maximum k_1 (maximum solar zenith ≅ 35°) of 0.4 min^{-1}. The Multi-Layer Light-Scattering Model predicts 0.47 min^{-1} and 0.42 min^{-1} for aerosol absorption coefficients of 5 percent and 15 percent of scattering, respectively. Jeffries, Fox, and Kamens also reported that k_1 varies nearly exactly with total solar radiation received on a flat surface. However, the highest zenith angle at which they made measurements was less than 60°, so it is impossible to judge if this relation persists at higher angles. The direct k_1 measurements confirm that the Multi-Layer Light-Scattering Model is inapplicable beyond 50°, except in a relative sense (see Figure 53).

There is an unfortunate paucity of information concerning the variations of photolytic rate constants at high zenith angles. To our knowledge, for zenith angles greater than approximately 70° there are no accurate models and no direct measurements of k_1 in the literature. Qualitatively, it seems likely that at high zenith angles the intensity of long wavelength UV (which affects k_1) decreases more slowly with increasing zenith angle than does total sunlight. The percentage of the long wavelength UV in sunlight is greater in the early morning (Peterson, 1974). Thus k_1 is unlikely to follow total sunlight Eppley readings during the first hour or so of daylight.

On the other hand, reactions depending on short-wavelength UV are probably depressed in the early morning due to the increased amount of ozone in the light path. Since these reactions include aldehyde photolysis, which is a possible initiator of free radical chemistry, this depression might have some significance in photochemistry.

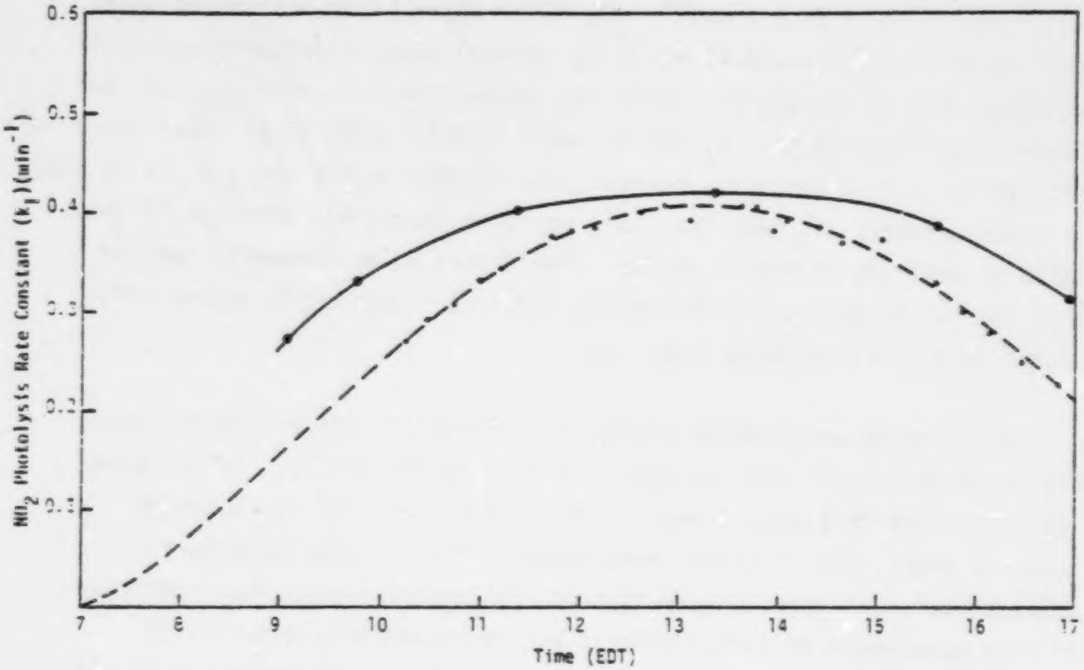

FIGURE 53. PREDICTED AND MEASURED NO_2 PHOTOLYSIS RATE CONSTANTS AS A FUNCTION OF TIME OF DAY. Asterisks indicate measurements by Eppley (1968), dots indicate predictions.

E. VARIATIONS IN PHOTOLYSIS RATE CONSTANTS WITH HEIGHT AND ATMOSPHERIC CONDITIONS

Calculated photolytic rate constants* are reported as functions of solar zenith angle in Figures 54, 55, and 56. Several points should be made with regard to these results. Although the predicted ground-level k_1 at 35° for the polluted case is 70 percent of that for the unpolluted case, the column-averaged k_1 declines by only 10 percent. Therefore, ground-level Eppley readings should probably not be used to modify k_1 estimates unless there is some knowledge concerning the nature of the reductions in sunlight. Is a decrease in Eppley readings due to cloud cover, fog, or smog? The answer markedly affects the average rate of NO_2 photolysis in the air column.

Aldehyde photolysis, as previously noted, is depressed at high zenith angles. This would tend to inhibit photochemical smog formation in the early morning. Also, this photolysis rate can vary by 10 percent simply through the normal daily and seasonal variance of the stratospheric ozone column. Thus, the common practice of specifying the aldehyde photolysis rate constant as a simple fraction of k_1 is almost certainly in error, although available information is insufficient to provide a more accurate specification.

In summary, UV fluxes were calculated for both clean and polluted urban atmospheres for several different elevations and solar zenith angles. These UV fluxes were used to calculate photolysis rate constants. These calculations are probably accurate to within 20 percent for zenith angles below 50° and less accurate (on the high side) for larger angles. The relative changes of rate constants through the polluted layer are probably more accurate than the absolute values, and they will be very useful in considering the effects of light scattering on photochemical smog.

---

* Photolysis rates were calculated with the method of Johnston and Whitten (1974) using cross-sections and quantum yields from Calvert and Pitts (1966), Johnston and Graham (1974), and Cox and Derwent (1976).

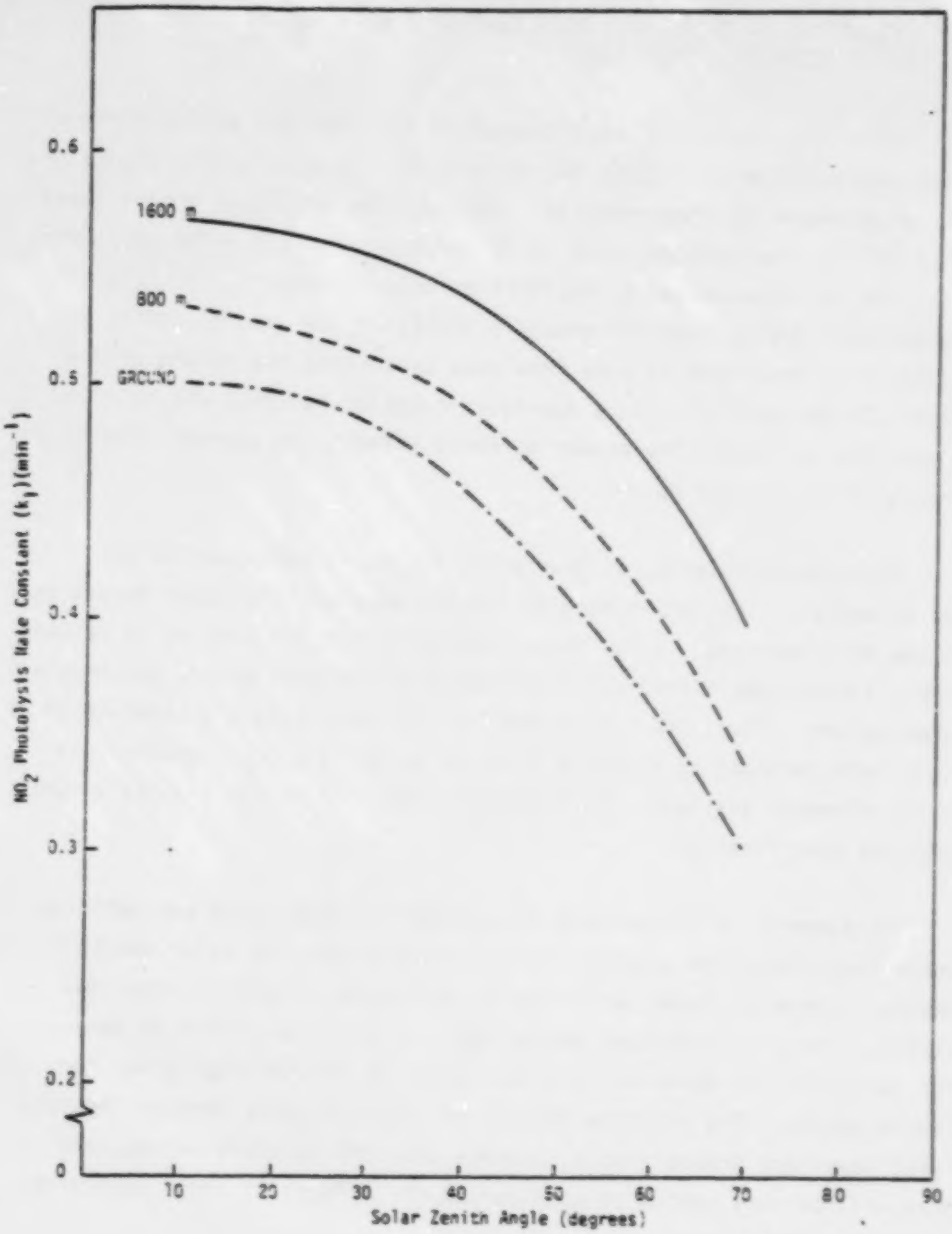

FIGURE 54. VARIATION OF NO_2 PHOTOLYSIS RATE CONSTANT WITH SOLAR ZENITH ANGLE--UNPOLLUTED CASE

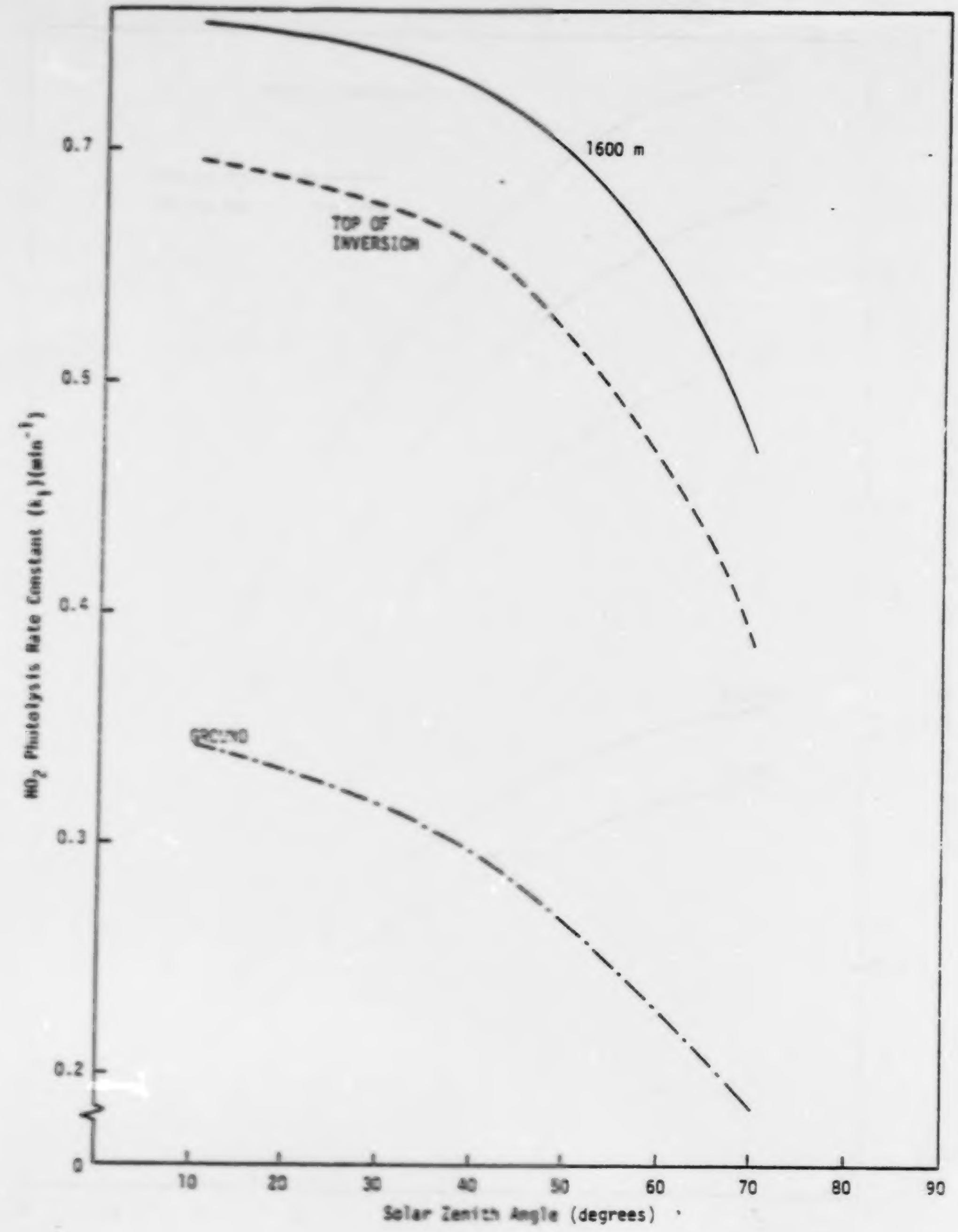

FIGURE 55. VARIATION OF NO$_2$ PHOTOLYSIS RATE CONSTANT WITH SOLAR ZENITH ANGLE--POLLUTED CASE

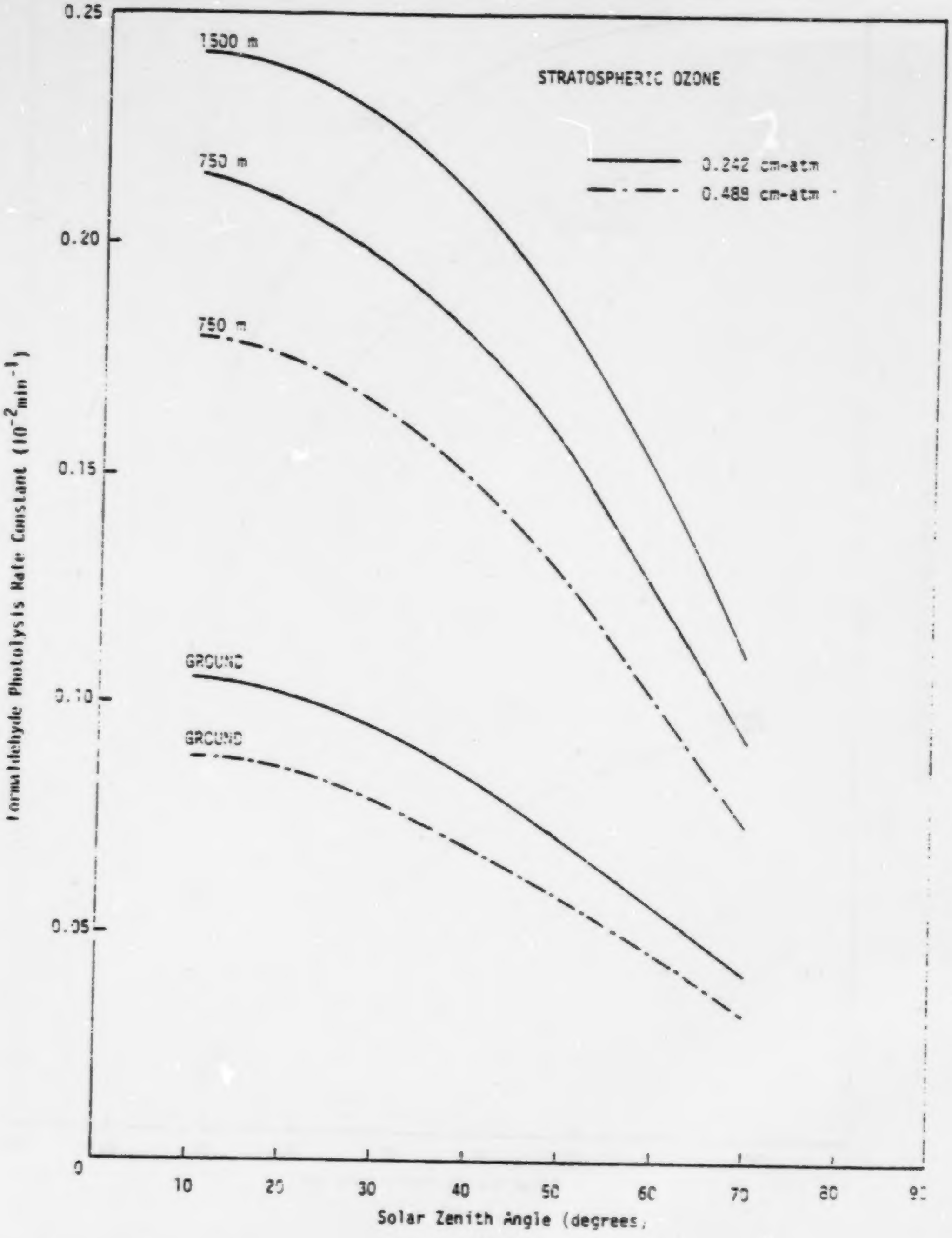

FIGURE 56. VARIATION OF FORMALDEHYDE PHOTOLYSIS RATE CONSTANT WITH SOLAR ZENITH ANGLE--POLLUTED CASE

The rate constant for NO_2 photolysis, k_1, varies through the mixed layer as a result of light scattering and absorption. Since this variation seems to be linear with height, and is a fairly simple function of the integrated b_{scat} within the air column, it should be possible to use an estimate of b_{scat} to obtain a vertical profile of k_1. The value of b_{scat} can be measured, estimated from visibility measurements, derived from some statistical algorithm relating it to other air pollutants, or obtained from an aerosol prediction model such as that described in Volume VII of this report (Jerskey et al., 1976).

F. PARAMETERIZATION OF THE EFFECTS OF LIGHT SCATTERING ON PHOTOLYSIS

Sufficient information now exists to estimate k_1 as a function of solar zenith angle, and thus, as a function of longitude, latitude, time of year, and time of day. Figure 57 contains our best estimates of k_1, based on various light models and the available data. The average k_1 in a mixing layer 760 meters thick would be (for the unpolluted case) 5 percent higher at the top than at ground level. For the polluted case, k_1 would differ by 50 percent between the top and bottom of the mixing layer, although the column average would be only 10 percent less than the values of Figure 57.

Since the attenuation of light through the polluted layer is essentially linear, parameterization involves merely finding algorithms appropriate for estimating the changes due to light scattering and absorption.

For a base case we use the unpolluted case described above, with a b_{scat} of 2×10^{-5} feet^{-1}. This value produced a decrease in k_1 of ≈ 8 percent between 762 meters and the ground (at 275 meters). Assuming that our input function for k_1 is the ground-level value, we therefore increase k_1 by 0.005 percent per foot. For polluted atmospheres, we expect that the changes in both ground-level k_1 and the k_1 at a height will be an exponential function of b_{scat}, due to the Beers-Lambert Law. Thus we assume the ground-level k_1 is a function of the form

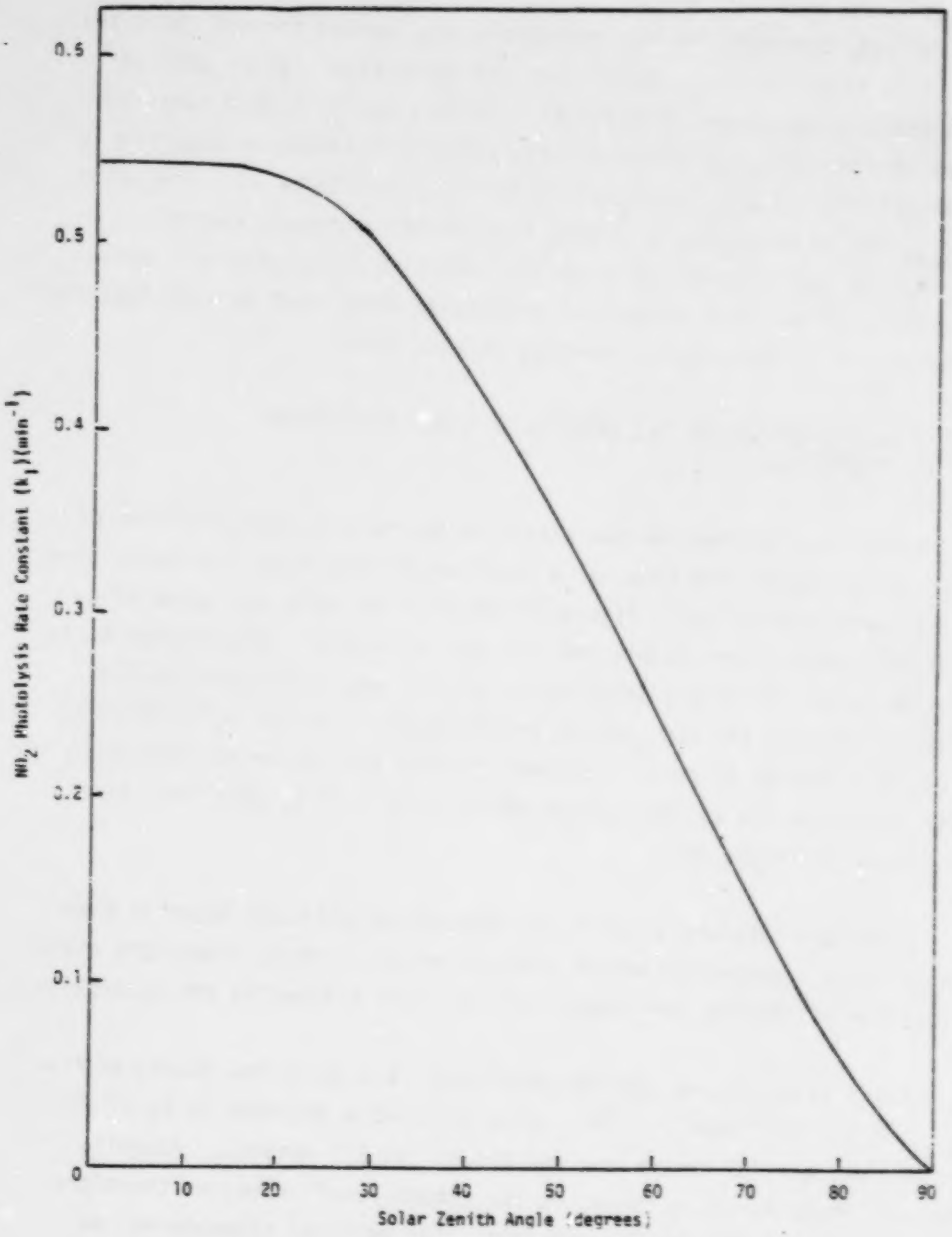

FIGURE 57. ESTIMATED GROUND-LEVEL NO_2 PHOTOLYSIS RATE CONSTANT AS A FUNCTION OF SOLAR ZENITH ANGLE FOR UNPOLLUTED CASE

$$k_1(\text{ground})_{new} = k_1(\text{ground})_{old} e^{-a(b_{scat})} \quad . \qquad (141)$$

For the polluted case, increasing the optical thickness 0.388 greater than the base case at a solar zenith angle of 40° lowered the ground-level value of k_1 from an estimated 0.45 to 0.3, so the constant a in the above equation equals 1.045.

The functional relationship between b_{scat} and the photolysis rate at some height should be of the form

$$k_{1_{new}} = k_{1_{old}} + \alpha_s \left(1 - e^{-c \cdot b_{scat}}\right) k_{1_{old}} \qquad (142)$$

where α_s is the ratio of scattered light to the sum of scattering plus absorption. Thus if the polluted layer did not absorb light α_s would equal 1. We assume α_s equals 0.9, in accord with the assumption that absorption is 10 percent of scattering. Assuming that k_1 equals 0.49 min^{-1} and 0.56 min^{-1} at the top of the modeling region for the unpolluted and polluted cases, respectively (which corresponds to a solar zenith angle of 40°), the value of the constant c in the above question is 0.445.

Our algorithm for the variation of k_1 with height is as follows. Subtract the assumed background b_{scat} of 6.6×10^{-5} meter^{-1} from the light scattering due to aerosols. Then calculate k_1 for the unpolluted case for the top of the modeling region. Then for the unpolluted case k_1 can be simply interpolated between the ground and the top of the modeling region. For the polluted atmosphere, recalculate photolysis rate constants as follows:

$$k_1(\text{ground})_{new} = k_1(\text{ground})_{old} e^{-1.045 \left(b_{scat} - \text{background } b_{scat}\right)} \qquad (143)$$

$$k_1(\text{top})_{new} = k_1(\text{top})_{old} + \left(0.9 - 0.9e^{-c \cdot b_{scat}}\right) k_1(\text{top})_{old} \quad . \qquad (144)$$

The aerosol concentration may be used to estimate b_{scat} as follows:

$$\text{aerosol } (\mu g/m^3) = 3.8 \times 10^5 \; b_{scat} \; m^{-1} \qquad (145)$$

(Charlson et al., 1972).

It would be relatively simple to include a treatment of the attenuating effects of fog and clouds in the Airshed Model, given the requisite data. These data would take the form of direct inputs of the b_{scat} due to fog and some specific information on attenuation due to clouds. Ideally, both of these factors would be supplied on both a temporal and spatial basis and both would necessitate the design of necessary input files and the inclusion of new data arrays in the model. Since we do not have a source of the requisite data, we did not make these programming changes.

It is possible, however, to give some consideration to temporal variations in cloud cover in the present model formulation. This is accomplished by merely varying the FACTRK sunlight input curve. Eppley readings might be used to effect this modification though care should be taken to ensure that the observed attenuation is due to clouds and not due to light variations within the polluted layer. These variations should be treated in the manner described in the previous section.

REFERENCES

Ackerman, B. (1974), "METROMEX: Airflow Analyses," Bull. Amer. Meteor. Soc., Vol. 55, pp. 93-95.

Ackerman, M. (1971), "Ultraviolet Solar Radiation Related to Mesospheric Processes," in Mesospheric Models and Related Experiments, N. Fiocco, ed. (D. Reidel Publishing Co., New York, New York).

Adkins, M. J. (1974), "The Objective Analysis of Relative Humidity," Tellus, Vol. 26, pp. 663-671.

Aldaz, L. (1969), "Flux Measurements of Atmospheric Ozone Over Land and Water," J. Geophys. Res., Vol. 74.

Altshuller, A. P., et al. (1968), Environ. Sci. Technol., Vol. 2, pp. 696-698.

Anderson, G. E. (1973), "A Mesoscale Windfield Analysis of the Los Angeles Basin," Final Report 4121-01-490C to EPA NERC Meteorology Laboratory, Research Triangle Park, North Carolina.

_________ (1971), "Mesoscale Influences on Windfields," J. Appl. Meteor., Vol. 10, pp. 377-386.

Anderson, G. E., R. R. Hippler, and G. D. Robinson (1969), "An Evaluation of Dispersion Formulas," Final Report 2005-370, The Travelers Research Corporation, Hartford, Connecticut.

Appel, B. R., P. Colodny, and J. J. Weselowski (1976), "Analysis of Carbonaceous Materials in Southern California Atmospheric Aerosols," Environ. Sci. Technol., Vol. 10, pp. 359-363.

Auer, A. H., Jr., and R. A. Dirks (1974), "Contributions to an Urban Meteorological Study: METROMEX," Bull. Amer. Meteor. Soc., Vol. 55, pp. 106-110.

Barnes, S. L. (1973), "Mesoscale Objective Map Analysis Using Weighted Time-Series Observations," NOAA Technical Memorandum ERL NSSL-62.

Bates, D. R., and A. E. Witherspoon (1952), "The Photochemistry of Some Minor Constituents of the Earth's Atmosphere," Mon. Notic. Roy. Astron. Soc., Vol. 112, pp. 101-124.

Bennett, J. H., and A. C. Hill (1973), "Absorption of Gaseous Air Pollutants by a Standardized Plant Canopy," J. Air Poll. Contr. Assoc., Vol. 23.

Bennett, J. H., A. C. Hill, and D. M. Gates (1973), "A Model for Gaseous Pollutant Sorption by Leaves," J. Air Poll. Contr. Assoc., Vol. 23, pp. 957-962.

Bolin, B., G. Aspling, and C. Persson (1974), "Residence Time of Atmospheric Pollutants as Dependent on Source Characteristics, Atmospheric Diffusion Processes, and Sink Mechanisms," Tellus, Vol. 26, pp. 185-195.

Boris, J. P., and D. L. Book (1975), "Minimizing Errors in Flux-Corrected Transport Algorithms," NRL Memorandum Report 3024, Naval Research Laboratory, Washington, D.C.

__________ (1973), "Flux-Corrected Transport: I. SHASTA, A Fluid Transport Algorithm That Works," J. Comp. Phys., Vol. II, pp. 38-69.

Boris, J. P., D. L. Book, and K. Hain (1975), "Generalizations of the Flux-Corrected Transport Technique," NRL Memorandum Report 3021, Naval Research Laboratory, Washington, D.C.

Bornstein, R. D. (1975), "The Two-Dimensional URBMET Urban Boundary Layer Model," J. Appl. Meteor., Vol. 14, pp. 1459-1477.

Bowne, N. E., and G. E. Anderson (1968), "Take-Off and Landing Critical Atmospheric Turbulence (TOLCAT) Analytical Investigation," Technical Report AFFDL-TR-68-23, The Travelers Research Center, Incorporated, Hartford, Connecticut.

Bowne, N. E., and R. R. Soller (1958), "A Meteorological Survey of the CANEL Site at Middletown, Conn.," Weather Bureau Office, Middletown, Connecticut, Office of Meteorological Research, U. S. Weather Bureau.

Bufalini, M. (1971), Environ. Sci. Technol., Vol. 8, pp. 685-700.

Burton, C. S., and G. M. Hidy (1974), "Regional Air Pollution Study Program Objectives and Plans," EPA-650/3-75-009, Environmental Protection Agency, Washington, D.C.

Butcher, S. S., and R. J. Charlson (1972), An Introduction to Air Chemistry, pp. 199-201 (Academic Press, New York, New York).

Calvert, J. G. (1976), "Hydrocarbon Involvement in Photochemical Smog Formation in Los Angeles Atmosphere," Environ. Sci. Technol., Vol. 10, pp. 256-262.

Calvert, J. G., and R. D. McQuigg (1975), The Computer Simulation of the Rates and Mechanisms of Photochemical Smog Formation," *Int. J. Chem. Kinet. Symposium No. 1*, pp. 113-154.

Calvert, J. G., and J. N. Pitts, Jr. (1967), *Photochemistry* (John Wiley & Sons, New York).

Castleman, A. W., Jr. (1974), "Nucleation Processes and Aerosol Chemistry," *Space Science Rev.*

Chagnon, S. A., Jr. (1975), "Operations of Mesoscale Networks, Illustrated by METROMEX," *Bull. Am. Meteor. Soc.*, Vol. 56, pp. 971-978.

Chamberlain, A. C. (1966), "Transport of Gases to and from Grass and Grass-like Surfaces," *Proc. Roy. Soc.*, Vol. A290, pp. 236-265.

Charlson, R. J., et al. (1972), "Multiwavelength Nephelometer Measurements in L. A. Smog Aerosol: Comparison to Light Extinction by NO_2," in *Aerosols and Atmospheric Chemistry*, G. M. Hidy, ed. (Academic Press, New York, New York).

__________(1969), "Monitoring of Atmospheric Aerosol Parameters With the Integrating Nephelometer," *J. Air Poll. Contr. Assoc.*, Vol. 19, p. 937.

Chung, K., J. G. Calvert, and J. W. Bottenheim (1975), *Int. J. Chem. Kinet.*, Vol. 7, pp. 161-182.

Cox, R. A. (1974), *J. Photochem.*, Vol. 3, pp. 291-304.

__________ (1972), *J. Phys. Chem.*, Vol. 76, p. 814.

Cox, R. A., and R. G. Derwent (1976), "The Ultra-Violet Absorption Spectrum of Gaseous Nitrous Acid," *J. Photochem.*, Vol. 6, pp. 23-34.

Cox, R. A., and S. A. Penkett (1972), *J. Chem. Soc., Faraday Trans. I*, Vol. 68, pp. 1736-1753.

Cressman, G. P. (1959), "An Operational Objective Analysis System," *Mon. Wea. Rev.*, Vol. 87, pp. 367-374.

Cvetanovic, R. J., (1963), *Adv. in Photochem.*, Vol. 1, p. 115.

Dannevik, W. P., S. Frisella, and J. Fishman (1974), "RAPS 1974 SO_2 Surface Flux Measurement Program," Environmental Quality Research, Incorporated, Clayton, Missouri.

Dartt, D. G. (1972), "Automated Streamline Analysis Using 'Optimum Interpolation'," *J. Appl. Meteor.*, Vol. 11, p. 901.

Dave, J. V., and P. Halpern (1975), "Effects of Changes in Ozone Amount on the Ultraviolet Radiation Received at Sea Level of a Model Atmosphere," Report 6320-3335, IBM Palo Alto Scientific Center, Palo Alto, California.

Davis, D. D. (1976), private communication with Dr. M. Dodge of EPA, Research Triangle Park, North Carolina.

———— (1974), "Absolute Rate Constants for Elementary Reactions of Atmospheric Importance: Results from the University of Maryland's Gas Kinetics Laboratory," Chemistry Department, University of Maryland, College Park, Maryland.

Davis, D. D., G. Smith, and G. Klauber (1974), Science, Vol. 179, p. 280.

Demerjian, K. L. (1976), private communication.

Demerjian, K. L., J. A. Kerr, and J. G. Calvert (1974), "The Mechanism of Photochemical Smog Formation," in Advances in Environmental Science Technology, J. N. Pitts and R. L. Metcalf, eds. (John Wiley & Sons, New York, New York).

Durbin, P. A., T. A. Hecht, and G. Z. Whitten (1975), "Mathematical Modeling of Simulated Photochemical Smog," EPA-650/4-75-026, Environmental Protection Agency, Research Triangle Park, North Carolina.

Egan, B., and J. R. Mahoney (1972), "Numberical Modeling of Advection and Diffusion of Urban Area Source Pollutants," J. Appl. Meteor., Vol. 11, pp. 312-322.

Elterman, L. (1968), "UV, Visible, and IR Attenuation for Altitudes to 50 Km," AFCRL-68-0153, Environmental Research Paper 285, Office of Aerospace Research, U.S. Air Force, Washington, D.C.

Filby, W. G., and R. D. Penzhorn (1974), "kinetics of the Photoreaction of SO_2 with Alkanes--The Diversion of Intermediate Radicals by Oxygen," in "Abstracts of Symposium on Chemical Data for the Lower and Upper Atmosphere," Warrenton, Virginia.

Finlayson, B. J., and J. N. Pitts, Jr. (1976), "Photochemistry of the Polluted Troposphere," Science, Vol. 192, pp. 111-119.

Fosberg, M. A., W. E. Marlatt, and L. Krupnak (1976), "Estimating Airflow Patterns Over Complex Terrain," RM-162, Rocky Mountain Forest and Range Experimental Station, U.S. Forest Service, Fort Collins, Colorado.

Fosberg, M. A., A. Rango, and W. E. Marlatt (1972), "Wind Computations from the Temperature Field in an Urban Area," Proceedings Conference on Urban Environment and 2nd Conference on Biometeorology, 31 October-2 November, Philadelphia, Pennsylvania.

Gandin, L. S. (1965), "Objective Analysis of Meteorological Fields (Obëktivngi analiz meterologicheskikh polei, 1963), Israel Program for Scientific Translations, Jerusalem, p. 242.

Garland, J. A., et al. (1974), "Deposition of Gaseous Sulphur Dioxide to the Ground," Atmos. Environ., Vol. 8, pp. 75-79.

Gilchrist, B., and G. P. Cressman (1954), "An Experiment in Objective Analysis", Tellus, Vol. 6, pp. 309-318.

Gillespie, J., et al. (1958), J. Chem. Soc., p. 2504.

Greiner, N. R. (1970, "Hydroxyl Radical Kinetics by Kinetic Spectroscopy: VI--Reactions with Alkanes in the Range 300 to 500K," J. Chem. Phys., Vol. 53, pp. 1070-1076.

Grosjean, Daniel, and S. K. Friedlander (1975), "Gas-Particle Distribution Factors for Organic and Other Pollutants in the Los Angeles Atmosphere," J. Air Poll. Contr. Assoc., Vol. 25, pp. 1038-1044.

Hampson, R. F., and D. Garvin (1975), "Chemical Kinetic and Photochemical Data for Modelling Atmospheric Chemistry," NBS Technical Note 866, National Bureau of Standards, Washington, D. C.

Hecht, T. A., J. H. Seinfeld, and M. C. Dodge (1974), "Further Development of a Generalized Kinetic Mechanism for Photochemical Smog," Environ. Sci. Technol., Vol. 8, pp. 327-339.

Heichel, G. H. (1973), "Removal of Carbon Monoxide by Field and Forest Soil," J. Environ. Qual., Vol. 2, pp. 419-423.

Herron, J. T., and R. D. Penzhorn (1969), "Mass Spectrometric Study of the Reactions of Atomic Oxygen with Ethylene and Formaldehyde," J. Phys. Chem., Vol. 73, pp. 191-196.

Hidy, G. M., et al. (1974), "Characterization of Aerosols in California (ACHEX)," ARB-358, State of California Air Resources Board, Sacramento, California.

Hill, A. C. (1971), "Vegetation: A Sink for Atmospheric Pollutants," J. Air Poll. Contr. Assoc., Vol. 21, pp. 341-346.

Hovland, D., D. Dartt, and K. Gage (1976), "Development of Objective Analysis Techniques for the Regional Air Pollution Study," Final Report, Part 1, to the Environmental Protection Agency under Contract 68-02-1827 by Control Data Corporation, Minneapolis, Minnesota.

Ingersoll, R. B., R. E. Inman, and W. R. Fisher (1974), "Soil's Potential as a Sink for Atmospheric Carbon Monoxide," Tellus, Vol. 26, pp. 151-159.

Inman, R. L. (1970), "Papers on Operational Objective Analysis Schemes at the National Severe Storms Forecast Center," NOAA Technical Memorandum ERLTM-NSSL 51.

Japar, S. M., and H. Niki (1975), "Gas-Phase Reactions of the Nitrate Radical with Olefins," J. Phys. Chem., Vol. 79, pp. 1629-1632.

Japar, S. M., C. H. Wu, and H. Niki (1974), "Rate Constants for the Reaction of Ozone with Olefins in the Gas Phase," J. Phys. Chem., Vol. 78, pp. 2318-2320.

Jeffries, H., D. Fox, and R. Kamens (1974), "Outdoor Smog Chambers," presented at EPA Smog Chamber Conference, Research Triangle Park, North Carolina (16-17 October).

Jerskey, T. N., et al. (1976), "Continued Research in Mesoscale Air Pollution Simulation Modeling: Vol. VII--Mathematical Modeling of Urban Aerosol Dynamics," Draft Report EF76-144 to the EPA by Systems Applications, Incorporated, San Rafael, California.

Jerskey, T. N., and J. H. Seinfeld (1976), "Continued Research in Mesoscale Air Pollution Simulation Modeling: Vol. IV--Examination of the Feasibility of Modeling Photochemical Aerosol Dynamics," EPA 600/4-76-016d, Environmental Protection Agency, Research Triangle Park, North Carolina.

Johnston, H. S., and R. Graham (1974), Canad. J. Chem., Vol. 52, pp. 1415-1423.

Johnston, H. S., and G. Whitten (1973), "Instantaneous Photochemical Rates in the Global Stratosphere," Pure Appl. Geogphys., Vols. 106-108, pp. 1468-1489.

Jones, R. H. (1972), "Aliasing with Unequally Spaced Observations," J. Appl. Meteor., Vol. 11, p. 245.

Kiang, C. S., et al. (1973), "Heteromolecular Nucleation Theory Applied to Gas-to-Particle Conversion," Atmos. Environ., Vol. 7, p. 1.

Kriess, H., and J. Oliger (1973), "Methods for the Approximate Solution of Time Dependent Problems," GARP Publications Series No. 10, Global Atmospheric Research Programme, pp. 79-80.

Leighton, P. A. (1961), Photochemistry of Air Pollution (Academic Press, New York, New York).

Lettau, H. H. (1970), "Physical and Meteorological Basis for Mathematical Models of Urban Diffusion Processes," Proceedings of Symposium on Multiple Source Urban Diffusion Models, Air Pollution Control Office Publication AP-86-2-1-2-26.

Liu, C. Y., and W. R. Goodin (1975), "An Iterative Algorithm for Objective Wind Field Analysis", Mon. Wea. Rev.

Lonneman, W. A., et al. (1974), "Hydrocarbon Composition of Urban Air Pollution," Environ. Sci. Technol., Vol. 8, pp. 229-236.

MacCracken, M. C., et al. (1974), "Development of an Air Pollution Model for the San Francisco Bay Area," UCRL-51537, Lawrence Livermore Laboratory, University of California, Livermore, California.

Maynard, J. B., and W. N. Sanders (1969), "Determination of the Detailed Hydrocarbon Composition and Potential Atmospheric Reactivity of Full-Range Motor Gasolines," J. Air Poll. Contr. Assoc., Vol. 19, pp. 505-510.

Miller, D. F., and C. W. Spicer (1975), "Measurement of Nitric Acid in Smog," J. Air Poll. Contr. Assoc., Vol. 25, pp. 940-942.

Morris, E. D., Jr., and H. Niki (1971), "Mass Spectrometric Study of the Reaction of Hydroxyl Radical with Formaldehyde," J. Chem. Phys., Vol. 55, pp. 1991-1992.

Moses, H. (1974), "Argonne Urban-Rural Airflow Program," Bull. Am. Meteor. Soc., Vol. 55, pp. 100-110.

Mueller, P. K., and M. Hitchcock (1969), "Air Quality Criteria--Toxicological Appraisal for Oxidants, Nitrogen Oxides, and Hydrocarbons," J. Air Poll. Contr. Assoc., Vol. 19, pp. 670-676.

Myrup, L. O., and D. L. Morgan (19__), "Numerical Model of the Urban Atmosphere, Vol. I. The City Surface Interface," Depts. of Agricultural Engineering and Water Science and Engineering, University of California, Davis, California.

Nader, J. S., and N. White (1969), "Volumetric Measurement of Ultraviolet Energy in an Urban Atmosphere," Environ. Sci. Technol., Vol. 3, pp. 848-853.

National Air Pollution Control Agency [NAPCA] (1970), "Air Quality Criteria for Photochemical Oxidants," AP-63, Cincinnati, Ohio.

O'Brien, R. J., et al. (1975), "Formation of Photochemical Aerosol from Hydrocarbons--Atmospheric Analysis," Environ. Sci. Technol., Vol. 9, pp. 577-582.

O'Brien, R. J., J. R. Holmes, and A. H. Bockian (1975), "Formation of Photochemical Aerosol from Hydrocarbons--Chemical Reactivity and Products," Environ. Sci. Technol., Vol. 9, pp. 568-576.

O'Neal, H. E., and C. Blumstein (1973), Int. J. Chem. Kinet., Vol. 6, pp. 397-413.

Owen, P. R., and W. R. Thompson (1963), "Heat Transfer Across Rough Surfaces," J. Fluid Mech., Vol. 15, pp. 321-334.

Owers, M. J., and R. Powell (1974), "Deposition Velocity of Sulphur Dioxide on Land and Water Surfaces Using a ^{35}S Tracer Method," Atmos. Environ., Vol. 8, pp. 63-69.

Pandolfo, J. P., M. A. Atwater, and G. E. Anderson (1971), "Prediction by Numerical Models of Transport and Diffusion in an Urban Boundary Layer," Vol. I, Final Report to the Environmental Protection Agency under Contract CPA-70-62 by The Center for the Environment and Man, Incorporated, Hartford, Connecticut.

Panofsky, H. A. (1969), "Objective Weather-Map Analysis," J. Meteorol., Vol. 6, pp. 386-392.

Peterson, D. P., and T. N. Truske (1971), "A Study of Data Processing Techniques for Satellite Meteorological Observations," EE-190(71)DC-185, Bureau of Engineering Research, University of New Mexico, Albuquerque, New Mexico.

Peterson, J. T. (1974), private communication.

Peterson, J. T., and E. C. Flowers (1976), "Urban-Rural Solar Radiation and Aerosol Measurements in St. Louis and Los Angeles," unpublished manuscript.

Price, H. S., R. S. Varga, and J. E. Warren (1966), "Applications of Oscillation Matrices to Diffusion and Convection Equations," J. Math. Phys., Vol. 45, pp. 301-311.

Rasmussen, K. H., M. Taheri, and R. L. Kabel (1974), "Sources and Natural Removal Processes for Some Atmospheric Pollutants," EPA-650/4-74-032, Environmental Protection Agency, Research Triangle Park, North Carolina.

Rasmussen, R. A., R. S. Hutton, and R. J. Garner (1968), "Factors in Establishing Microbial Populations on Biologically Inert Surfaces," Biodeterioration of Material, A. H. Walters and J. J. El Phick, eds., (Elsevier Publishing Company, Incorporated, London, England).

Rasmussen, R. A., and F. W. Went (1965), "Volatile Organic Material of Plant Origin in the Atmosphere," Proc. Nat. Acad. Sci., Vol. 53, pp. 215-220.

Reynolds, S. D., et al. (1976), "Model Development and Refinement," Final Report EF75-69, Systems Applications, Incorporated, San Rafael, California.

Reynolds, S. D., P. M. Roth, and J. H. Seinfeld (1973), "Mathematical Modeling of Photochemical Air Pollution--I. Formulation of the Model," Atmos. Environ., Vol. 7, pp. 1033-1061.

Rich, S. (1964), "Ozone Damage to Plants," Ann. Rev. Phytopathol., Vol. 2, pp. 253-266.

Ripperton, L. A., et al. (1975), "Urban Photochemistry and Rural Transport," Meeting of the Mid-Atlantic States Section, Air Pollution Control Association, 16 October 1975, Newark, New Jersey.

Ripperton, L. A., and J. J. B. Worth (1969), "Chemical and Environmental Factors Affecting Ozone Concentration in the Lower Troposphere," Department of Environment Science and Engineering Publication No. 234, National Science Foundation Grant No. GA-1022, University of North Carolina, Chapel Hill, North Carolina.

Ripperton, L. A., J.J.B. Worth, and L. Kornreich (1968), "NO_2 and NO in Nonurban Air," Paper 68-122, 61st Annual Meeting, Air Pollution Control Association.

Robinson, E., et al. (1973), "Interim Technical Report on Contribution of Natural Hydrocarbon Emissions to the Overall Hydrocarbon Burden," Washington State University, Pullman, Washington.

Robinson, E., and R. C. Robbins (1968), "Sources, Abundance and Fate of Gaseous Atmospheric Pollutants," Final Report, Project No. PR-6755, Stanford Research Institute, Menlo Park, California.

Roth, P. M., et al. (1974), "Mathematical Modeling of Photochemical Air Pollution--II. A Model and Inventory of Pollutant Emissions," Atmos. Environ., Vol. 8, pp. 97-130.

Sabersky, R. H., D. A. Sinema, and F. H. Shair (1973), "Concentrations, Decay Rates, and Removal of Ozone and Their Relation to Establishing Clean Indoor Air," Environ. Sci. Technol., Vol. 7, pp. 347-353.

Schuetzle, Dennis, et al. (1975), "Molecular Composition of Secondary Aerosol and Its Possible Origin," Environ. Sci. Technol., Vol. 9, pp. 838-845.

Schulten, H. R., and U. Schurath (1975), J. Phys. Chem., Vol. 79, pp. 51-57.

Schwartz, W. E., et al. (1974), "Chemical Characterizaiton of Model Aerosols," EPA-650/3-74-011, Environmental Protection Agency, Research Triangle Park, North Carolina (NTIS PB-238 557).

Scott Research Laboratories (1970), "1969 Atmospheric Reaction Studies in the Los Angeles Basin," Vol. III, "El Monte Ground Data," National Air Pollution Control Administration No. 70-6, Plumsteadville, Pennsylvania.

Sehmel, G. A., S. L. Sutter, and M. T. Dana (1973), "Dry Deposition Processes," BNWL-1751, Pt. 1, "Pacific Northwest Laboratory Annual Report for 1971, to the USAEC, Division of Biomedical and Environmental Research, Vol. II: Physical Sciences, Part 1, Atmospheric Science," Battelle Northwest Laboratories, Richland, Wash., pp. 150-153.

Shepherd, J. G. (1974), "Measurements of the Direct Deposition of Sulphur Dioxide Onto Grass and Water By the Profile Method," Atmos. Environ., Vol. 8, pp. 69-74.

Sherman, C. A. (1975), "A Mass-Consistent Model for Windfields Over Complex Terrain," First Conf. on Regional Mesoscale Modeling, Analysis, and Prediction, 6-9 May 1975, Las Vegas, Nevada.

Sidebottom, H. W., et al. (1971), J. Am. Chem. Soc., Vol. 93, pp. 3121-3128.

Smith, K. A., J. M. Bremner, and M. A. Tabatabai (1973), "Sorption of Gaseous Atmospheric Pollutants by Soils," Soil Sci., Vol. 116, pp. 313-319.

Smith, J. P., and P. Urone (1974), Environ. Sci. Technol., Vol. 8, pp. 742-746.

Smith, T. B., et al. (1976), "Analysis of the Data From the Three-Dimensional Gradient Study," MRI 75-FR-1395, Meteorology Research, Incorporated, Altadena, California.

Stair, Ralph, and J. S. Nader (1967), "Filter Phototube Measurements," in Pilot Study of UV Radiation in Los Angeles October 1965, J. S. Nader, ed. (U. S. Dept. of Health, Education, and Welfare. U. S. Public Health Service).

Stephens, E. R., and F. Burleson (1967), "Analysis of the Atmosphere for Light Hydrocarbons," J. Air Poll. Contr. Assoc., Vol. 17, pp. 147-153.

Stuhl, F., and H. Niki (1971), J. Chem. Phys., Vol. 55, p. 3904.

Thielke, J. F., et al. (1972), "Multiwavelength Nephelometer Measurements in L.A. Smog Aerosol: Correlation with Size Distributions," in Aerosols and Atmospheric Chemistry, G. M. Hidy, ed. (Academic Press, New York, New York).

Trijonis, J. C., and K. W. Arledge (1975), "Impact of Reactivity Criteria on Organic Emission Control Strategies in the Metropolitan Los Angeles AQCR," TRW, Incorporated, El Segundo, California.

Turner, D. B. (1969), "Workbook of Atmospheric Dispersion Estimates," AP-26, Environmental Protection Agency, Research Triangle Park, North Carolina.

Van de Hulst, H. C. (1957), Light Scattering by Small Particles (John Wiley and Sons, New York, New York).

Volman, D. H., and R. A. Gorse (1972), "Photochemistry of the Gaseous Hydrogen Peroxide-Carbon Monoxide Systems: Rate Constants for Hydroxyl Radical Reactions by Competitive Kinetics," Final Report, Project 5-143-2, University of California, Davis, California.

Vukovich, F. M., et al. (1976), "A Theoretical Study of the St. Louis Heat Island: The Wind and Temperature Distribution," J. Appl. Meteor., Vol. 15, pp. 417-440.

Whelpdale, D. M., and R. W. Shaw (1974), "Sulphur Dioxide Removal by Turbulent Transfer Over Grass, Snow, and Water Surfaces," Tellus, Vol. 26, pp. 196-205.

Whitbeck, M. R., et al. (1976), "A Kinetic Study of CH_3O_2 and $(CH_3)_3CO_2$ Radical Reactions by Kinetic Flash Spectroscopy," 12th Informal Conference on Photochemistry, National Bureau of Standards, Extended Abstracts, pp. K1-1 to K1-5.

Whitby, K. T., and B. Cantrell (1975), "Atmospheric Aerosols--Characteristics and Measurement," unpublished manuscript, Mechanical Engineering Department, University of Minnesota, Minneapolis, Minnesota.

White, W. H., and R. B. Husar (1976), "A Lagrangian Model of the Los Angeles Smog Aerosol," J. Air Poll. Contr. Assoc., Vol. 26, pp. 32-35.

Whitten, G. Z., and H. Hogo (1977), "Mathematical Modeling of Simulated Photochemical Smog," EPA-600/3-77-011, Environmental Protection Agency, Research Triangle Park, North Carolina.

Wilson, W. E., Jr., and A. Levy (1970), J. Air Poll. Contr. Assoc., Vol. 20, p. 385.

__________ (1969), "A Study of Sulfur Dioxide in Photochemical Smog II," 2nd Annual Progress Report to American Petroleum Institute, Project S-11.

Wilson, W. E., Jr., et al. (1973), "The Effect of Fuel Composition on Atmospheric Aerosol Due to Auto Exhaust," J. Air Poll. Contr. Assoc., Vol. 23, pp. 949-956.

Yanenko, N. N. (1971), Method of Fractional Steps (Springer-Verlag, New York).